Synthesis and Evaluation of Cyclen-Based Lanthanide Complexes for Luminescent Sensing and as MRI Contrast Agents

Jennifer K. Molloy

October 2010

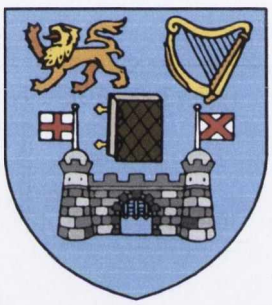

University of Dublin

Trinity College

Based on research carried out under the direction of

Prof. Thorfinnur Gunnlaugsson

A thesis submitted to the School of Chemistry,

University of Dublin, Trinity College for the degree of

Doctor of Philosophy

Declaration

This thesis is submitted for the degree of Doctor of Philosophy to the University of Dublin, Trinity College and has not been submitted before for any degree or examination to this or any other university. Other than where acknowledged, all work described herein is original and carried out by the author alone. Permission is granted so that the Library may lend or copy this thesis upon request. This permission covers only single copies made for study purposes, subject to normal conditions of acknowledgment.

Abbreviations

ADP	Adenine Diphosphate
AFM	Atomic Force Microscopy
AMP	Adenine Monophosphate
ATP	Adenine Triphosphate
AuNPs	Gold Nanoparticles
BAPA	N-bis-2-pyridyl methyl-6-amine
BOC	*Tert*-butyloxycarbonyl
$(BOC)_2O$	Di-*tert*-but-dicarbamate
br	broad
CD	Circular Dichroism
CPL	Circularly Polarised Luminescence
Cyclen	1,4,7,10-Tetraazacyclododecane
DCM	Dichloromethane
DLS	Dynamic Light Scattering
DMAP	Dimethyl aminopyridine
DMF	Dimethyl formamide
DMSO	Dimethyl sulfoxide
DNA	Deoxyribonucleic acid
DTPA	Diethylene triamine pentaacetic acid
d	doublet
ESI	Electrospray Ionisation
ESMS	Electrospray Mass Spectrometry
Et_3N	Triethylamine
EtOAc	Ethyl acetate
EtOH	Ethanol
GSH	Glutathione
H	Hours
IR	Infrared
HRMS	High Resolution Mass Spectrometry
Ln	Lanthanide

LMWT	Low Molecular Weight Thiols
MALDI	Matrix-Assisted Laser Desorption/Ionisation Spectrometry
MeOH	Methanol
m	Multiplet
MRI	Magnetic Resonance Imaging
nm	Nanometre
nta	4,4,4-trifluoro-1-(2-naphthyl) butanedione
NMR	Nuclear Magnetic Resonance
pH	$-\log[H_3O^+]$
pK_a	$-\log K_a$ where K_a is the acidity constant
ppm	Parts per million
ppb	Parts per billion
q	Quartet
RNA	Ribonucleic acid
s	Singlet
SPR	Surface Plasmon Resonance
t	Triplet
TEAP	Tetraethylammonium phosphate
TEM	Transmission Electron Microscopy
TFA	Trifluoro acetic acid
TLC	Thin Layer Chromatography
TOAB	Tetraoctyl ammonium bromide
tta	4,4,4 trifluoro thiophene butanedione
UV-Vis	Ultraviolet-Visible
VT	Variable Temperature

Abstract

This thesis entitled "*The Synthesis and Evaluation of Cyclen Based Lanthanide Complexes for Luminescent Sensing and as MRI Contrast Agents*" is composed of five chapters. In the first chapter the photophysical properties of lanthanide ions are introduced and examples of the formation of mono and dinuclear complexes of these lanthanide ions are discussed. The potential applications of these lanthanide based complexes are outlined using literature examples. This is followed by a detailed discussion of the synthesis and charaterisation of gold nanoparticles and their functionalisation and stabilisation. The potential of these functionalised nanoparticles as sensors, probes and MRI contrast agents as demonstrated in the literature is discussed, with particular emphasis on the functionalisation of gold nanoparticles with metal complexes.

The second chapter of this thesis discusses the development of dinuclear lanthanide complexes based on two synthetic strategies. The first describes the use of click chemistry to form dinuclear complexes with simple, clean reaction conditions. The formation of three different dinuclear complexes is discussed. The second strategy described is the attempted synthesis of Tröger's base-based dinuclear complexes. The formation of Troger's base-based ligands was attempted via various pathways which are outlined in this chapter. Also discussed is the formation of simple Tröger's base derivatives, designed from simple starting materials, for the potential formation of Tröger's base - based dinuclear complexes.

Chapter three gives a detailed description of the synthesis and characterisation of six chiral cyclen-based ligands, and their corresponding Eu(III) complexes. The synthesis of gold nanoparticles was carried out using the Brust method and the characterisation of these particles using TEM, DLS and UV-Vis spectroscopy is explained. The functionalisation of gold nanoparticles with the aforementioned complexes was carried out and the potential of these complexes to act as luminescent sensors on the surface of gold nanoparticles is assessed.

Chapter four describes the synthesis and characterisation of two ligands and their corresponding Eu^{3+}, Tb^{3+}, Gd^{3+} complexes. These Eu^{3+} complexes were analysed

photophysically in order to determine their ability to form ternary luminescent complexes with antennae such as **nta** and **tta**. The thiol based complexes anchored on the surface of gold nanoparticles are assessed with regard to the formation of luminescent ternary complexes. These systems are also analysed for their potential as MRI contrast agents by carrying out ^{1}H NMR NMRD studies, demonstrating their potential as MRI contrast agents both as the complexes alone and as their surface modified gold nanoparticle analogues.

All physical and synthetic procedures used in chapters two to four are detailed in chapter five. References are given in chapter six, and the appendices A.1 and B.1 detail the experimental data pertaining to chapters two to four.

Table of Contents

Acknowledgements

I would like to sincerely thank my supervisor, Prof. Thorri Gunnlaugsson for his help and advice over the past four years.

I would also like to thank the past and present members of the TG group for their help endless cups of tea!: Julien, Celia, Aline, Cidalia, Emma, Jon, Gary, Danni, Niamh, Doireann, Rebecca, Rob, Sam, Brian, Swagatha, Elaine, Laura, Dave and Dawn and the newest addition Joe. Thanks to Celia, Julien, Danni, Gary, Rebecca and Doireann for making the first couple of years a lot of fun in the TG group! And of course the original first years for making things interesting over the past three years !!

A sincere thank you to all the readers of various drafts of this manuscript, particularly Steve and Oxana and Sam who really put a lot of work into it.

I would like to especially thank Dr John O' Brien for all of his help over the years and all the technical staff, Dr. Manuel Reuther, Dr. Tom Mc Cabe, Dr. Bernard Jean-Denis and Dr. Martin Feeney, particularly recently for all the complexes ! I would also like to thank Dr. Dermot Brougham and his group in DCU for their help with the NMRD measurements.

Also to Christophe for making the four years of my phd a lot more fun and bearable, its always better to have someone to share the three in the morning writing experiences with and in the early days lots of nights out after work !

Most of all, I would like to thank my family for putting up with me for the past four years, particularly with all the late nights recently !! Havent been home too much !! So hopefully that will change over the next few weeks.

Chapter 1

Introduction

Chapter 1: Introduction

1.0 Introduction

This thesis focuses on the use of lanthanide ions in supramolecular systems for use as molecular sensors and as MRI contrast agents. The lanthanide ions have numerous characteristics that lend them to the study of optical imaging and sensing due to their photophysical characteristics in particular.[1] For this reason, this Chapter is divided into two sections, whereby the first section will discuss lanthanides and their photophysical properties, which allow their use in applications such as imaging. The properties of lanthanide ions and current research in the field of lanthanide chemistry has been widely discussed in the PhD theses of Andrew Harte and Niamh Murray and so only a brief discussion for understanding will be given in this introduction.[2] The development of such dinuclear complexes is discussed with recent advances in the literature in both macrocyclic dinuclear complexes and in supramolecular assemblies for dinuclear complexes. The majority of the research with lanthanide ions to date focuses on their behaviour in the solution state, however, there are only a few examples of such complexes immobilised on flat gold surfaces or the surface of a gold nanoparticle (**AuNPs**). Therefore, the second section will give an overall review of the field of **AuNPs**, discussing first the properties and characterisation methods of **AuNPs**, followed by their incorporation into systems for sensing and drug delivery leading towards the incorporation of metal complexes onto the surface of the nanoparticle and their applications in sensing and as contrast agents.

1.1 Introduction to Lanthanides

The lanthanide ions consist of the first period of the *f*-block metals from La to Lu. They have characteristic *4f* shell configurations and exhibit similar properties across the periodic table due to a regular decrease in the size of the atomic radii; known as the lanthanide contraction.[3] Their most stable oxidation state is 3+, particularly in water, and has the general electron configuration [Xe] $5d^16s^24f^n$ (n= 1-14).[4] The lanthanide ions possess high charge densities and demonstrate high electrostatic interactions due to their Lewis acidity and polarity. The lanthanides can display varied coordination numbers, from 6 to 12, the most common coordination states being 8 and 9 for ions such as Eu^{3+} and Tb^{3+}, which will be discussed further in Chapters 2- 4. Due to their Lewis acidity, the lanthanide ions show a preference for ligands, which are easily polarised and can act as Lewis bases. For this reason, lanthanides can easily interact with functional groups such as aliphatic amines,

carboxylic acids and amides. Ligands containing these moieties will be utilised throughout this thesis for the complexation of lanthanide ions. However, in the solution state, the lanthanides tend to utilise small solvent molecules to achieve the most stable coordination number of 9.[5] Solvent molecules (such as water or methanol) can act as coordinating ligands to the complex. However, they can also quench the luminescence of many of the lanthanide ions through vibrational deactivation, a phenomenon that will be further discussed in the next section as part of the photophysical properties of the lanthanides.

1.1.1 Photophysical Properties

The use of lanthanide ions for sensing and imaging has been much explored due to their interesting optical and coordination properties, particularly their luminescence.[6] Luminescence refers to the emission of energy as light from an electronically excited state and can refer to both fluorescence and phosphorescence.[7] Fluorescence is a spin allowed process, involving excitation to the singlet excited state and results in emission of a photon, which occurs usually within the nanosecond timescale. In contrast, phosphorescence refers to a spin forbidden process, which involves a change in spin multiplicity occurring on a timescale from 10^{-6} s^{-1} to a number of seconds.

The shielding of the lanthanide f-orbitals results in Laporte forbidden, f-f electronic transitions, which cause them to exhibit low extinction coefficients (0.5-3 dm^3 mol^{-1} cm^{-1}) for these lanthanide ions. Some of the lanthanide ions are more luminescent than others and their luminescent capabilities depend on the efficiency of the population of the excited state and how their non-radiative deactivation is minimised. The electronic [Xe]$4f^n$ (n = 0-14) configurations of lanthanide ions generates a rich variety of electronic levels. The quantum yields of the lanthanide emission are directly related to the energy gap between the lowest excited state and the highest vibronic level of the ground state. Gd^{3+}, Eu^{3+}, and Tb^{3+} possess the highest luminescence efficiency. They have high energy transitions between their lower excited state and their ground state *c.a.* ΔE_{Gd} ($^6P_{7/2} \rightarrow {}^7F_6$) = 32200 cm^{-1}, ΔE_{Eu} ($^5D_0 \rightarrow {}^7F_6$) = 12300 cm^{-1} and ΔE_{Tb} ($^5D_4 \rightarrow {}^7F_0$) = 14800 cm^{-1}, which reduces the energy transfer toward high frequency oscillators and allows an easier population of their excited states *via* energy transfer from the triplet states of different organic chromophores. They also exhibit long lived excited state lifetimes, which can lead to numerous applications as luminescent probes and sensors as, once excited, it can take much longer for the lanthanide emission to occur than that of the autofluorescence of the analyte (Figure 1.0).[7, 8] Another advantage of the lanthanides is that they exhibit narrow line-like emission bands, which contribute to the ease with which the emission can be detected.

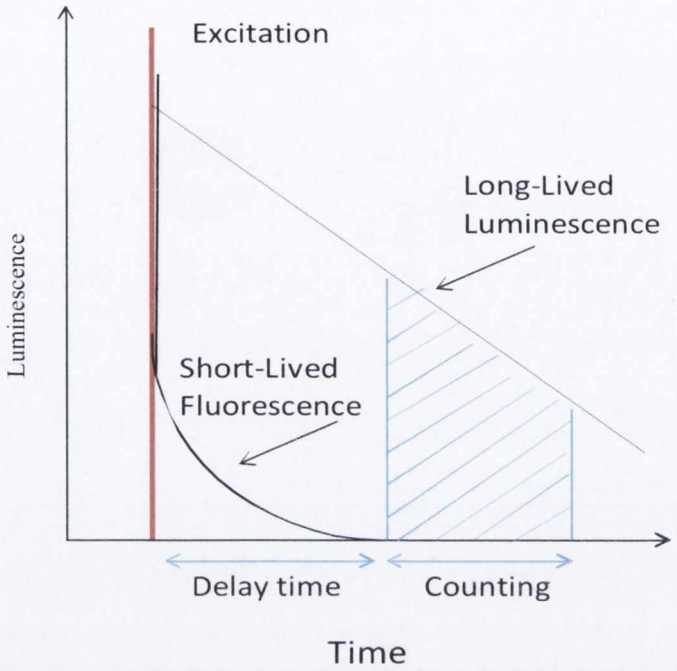

Figure 1.1: *Time resolved discrimination of the long lived luminescent lifetimes compared to that of the background autofluorescence*

Due to the low extinction coefficients discussed above, direct excitation of the lanthanides is inefficient as they are generally inert photophysically; exhibiting very low molar absorptivities and large band gaps between the excited and ground states.[9] Laser irradiation can provide sufficient excitation energy, if the radiation matches quite closely the energy difference between the lanthanide ion ground state and excited states. Argon ion laser excitation is suitable for the direct excitation of Eu^{3+} and Tb^{3+}, the lanthanides most often used for luminescent materials.[10] However, a more efficient and versatile method to sensitise the emission uses an external sensitising chromophore or antenna (Figure 1.1), which can transfer its own excited state energy to the lanthanide ion excited state. The antenna effect, as shown in Figure 1.2, overcomes the problem of low extinction coefficients, as an antenna or chromophore can be incorporated directly into the coordination environment of the lanthanide ions.

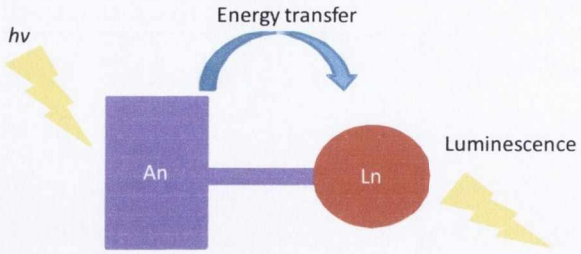

Figure 1.2: *Excitation of the lanthanide ion (Ln) by energy transfer from the antenna (An)*

The chosen antenna/chromophore should have a long lived triplet excited state, T_1, and the energy of the triplet state must be at least 1700 cm^{-1} above the energy of the lanthanide excited state, *i.e.* excitation of $^5D_0$ and $^5D_4$ for Eu^{3+} and Tb^{3+}, respectively. This ensures the transfer of sufficient energy to the lanthanide ion *via* intramolecular energy transfer.[11] Furthermore, the antenna must be in close proximity to the lanthanide centre to facilitate the energy transfer. The distance between the chromophore and the lanthanide ion must be no greater than $1/r^6$ in order to facilitate energy transfer, r being the distance between the lanthanide ion and the chromophore. It is also important that the energy of the chromophore is sufficiently high, in order to prevent or minimise back energy transfer from the lanthanide to the chromophore, as this can cause quenching of the lanthanide excited state.

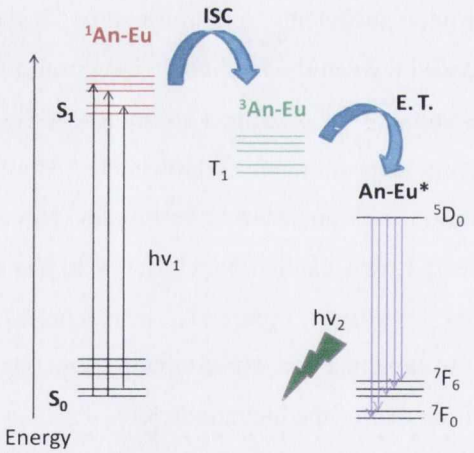

Figure 1.3: *Simplified Jablonski energy diagram for excitation of Eu(III) using the antenna effect*

The antenna effect utilises a chromophore, which absorbs the excitation energy, producing the singlet excited state S_1, as illustrated in Figure 1.3. Deactivation of the excited state, S_1, can occur *via* fluorescence emission or radiationless deactivations back to S_0. However, intersystem crossing (ISC) can also occur to the triplet excited state, T_1, of

the antenna. The process of ISC from a singlet to a triplet state is a forbidden process and can be enhanced by the heavy atom effect, with atoms such as Eu(III) or Tb(III), which induce intersystem crossing. The T_1 excited state can be quenched by singlet oxygen or can undergo energy transfer from the triplet state of the antenna to the lanthanide excited state (Ln*).[3] Subsequent deactivation of the lanthanide excited state results in emission as lanthanide luminescence.

There are two possible mechanisms for the transfer of energy between the triplet excited state of the antenna, T_1, to the lanthanide excited state, Ln*; these are the Förster and Dexter mechanisms. The Förster mechanism involves overlap of energy levels, whereby energy transfer occurs through space and has a distance dependence, $1/r^6$, r again being the distance between the lanthanide ion and the chromophore.[12] The Förster energy transfer process is, therefore, more efficient if this distance is reduced. The Dexter energy transfer mechanism involves an electron exchange between the excited chromophore and the lanthanide ion in a through bond interaction which has a e^{-r} dependence.[13]

As mentioned previously, the lanthanides can have coordination numbers as high as 12. If the number of coordination sites provided by the ligand is insufficient to fulfil the coordination requirement, solvent molecules such as water and methanol can complete the coordination sphere. The incorporation of high frequency oscillators, such as OH and NH, results in an important radiationless deactivation process, which contributes greatly to a decrease in the luminescence quantum yields (ϕ_f); the OH and NH oscillators effectively quench the lanthanide luminescence through vibrational deactivation of the excited state.[4a] This can be observed in aqueous solution, as the water molecules coordinate easily to the lanthanide ion, quenching the luminescence, which can be a problem in applications such as luminescent sensing, when carried out in aqueous solution. This disadvantage can, however, be exploited in the development of sensors for specific analytes, as these analytes (provided they have high affinity) can bind lanthanide ions, displacing water molecules and thus 'switch on' the luminescent response. This approach, as illustrated in Figure 1.4 using a β-diketone, will be discussed in detail in Chapter 3.

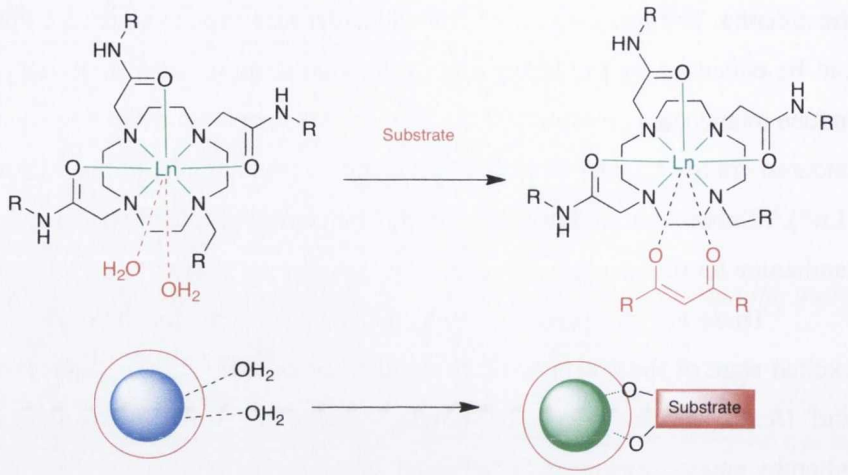

Figure 1.4: *Enhancement of the luminescence due to displacement of water molecules*

This quenching process can also be useful for a different reason, as it allows for the determination of the number of water molecules bound in the inner sphere of the lanthanide ion. The extent of the quenching of the luminescence is dependent on the number and proximity of the OH oscillators to the lanthanide. The number of metal bound water molecules, or the hydration state (q), can be calculated by measuring the metal centred luminescence lifetimes in H_2O and D_2O, respectively. The q value is calculated by using Equation 1, developed by Horrocks *et al.*,[14] and adapted by Parker *et al.*,[15] taking into account the effects of other oscillators such as NH and OH, which can quench the emission of the lanthanide ion. In equation 1, A is a proportionality constant, which gives a value for the sensitivity of the lanthanide ion to quenching by the metal bound water molecules.

$$q^{Eu3+} = A\,[\,(1/\tau_{H2O} - 1/\tau_{D2O}) - 0.075x - 0.25] \qquad \text{Eq. 1}$$

The value -0.25 is the correction represented by second sphere water molecules and -0.075x is a correction for NH oscillators attached to the complex that can deactivate the excited state. The properties of the lanthanides lend these metal ions to various applications as discussed previously, however, it is important to form stable complexes of these lanthanide ions in order to apply them to these various applications. The formation of such lanthanide complexes will be discussed in the following sections.

1.1.2 Formation of Lanthanide Complexes

The lanthanides, due to the properties discussed above, have proven to be interesting choices as probes for use in biological sensing and imaging. For this reason, this section will introduce the complexation of lanthanides using various ligands, the design of which

must take a number of criteria into consideration, such as kinetic and thermodynamic stability and the potential to fill the lanthanide coordination sphere, as mentioned in Section 1.1.1. An important aspect of lanthanide complexation is the stability of the complex, as, particularly for use in biological probes or sensors, the complexes need to be stable to avoid decomplexation. The release of lanthanides in the body can be potentially fatal due to their ability to form the hydroxide species, which precipitates in solution. Such stability is dependent on the type of ligand chosen for complexation.

The control of the stability and the functionality of the complexes is of the utmost importance. In order to ensure stability, a large number of different ligands were developed and were based on three different strategies:

1. Macrocyclic Approach
2. Podands
3. Self Assemblies

The most straightforward approach is the production of cyclic ligands based on macrocycles, which form extremely stable complexes. An example of such is tetraazacyclododecane (cyclen), which has been used in order to form complexes with high stability constants. These ligands are useful for the complexation of lanthanides due to the possibility of changing the functionalities on the arms of the macrocycle, allowing the development of large families of ligands with different functionalities, while also enabling the rigid control of the coordination environment.[7] In addition to cyclic ligands, polydentate acyclic ligands have also been shown to efficiently bind lanthanide ions. Examples of such acyclic and cyclic ligands include preorganised crown ethers, **1**, and cryptands, **2**,[3] predisposed ligands such as cyclen, **5**,[16] podands, **4**,[17] and self assembly processes with benzimidazoles, **3**,[18] and these have been used in order to form stable and useful complexes of lanthanide ions such as Eu^{3+}, Gd^{3+} and Tb^{3+}, Figure 1.5.

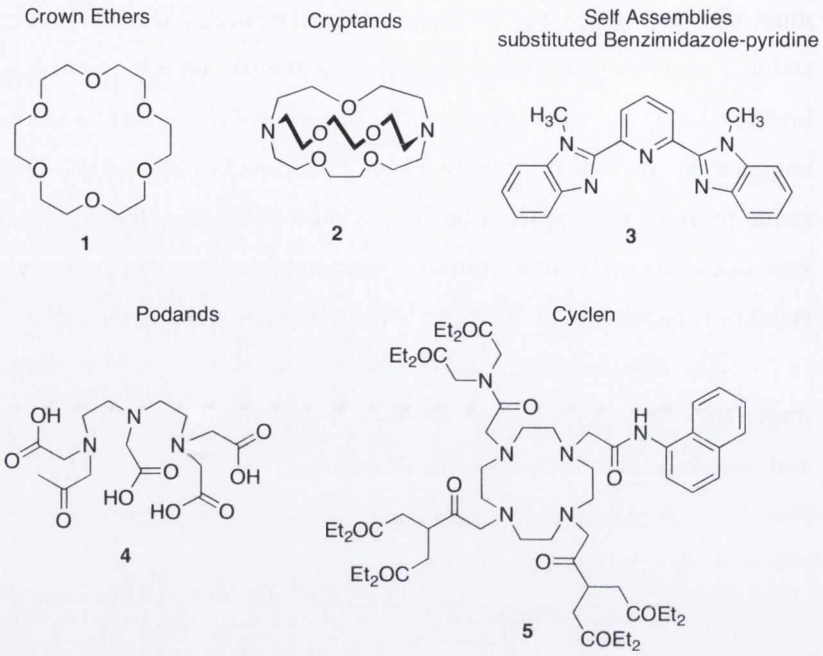

Figure 1.5: *Ligands **1**, **2**, **3**, **4** and **5** for the complexation of lanthanides based no different complexation strategies*

Mononuclear complexes based on these designs have been extensively researched for a variety of different applications such as imaging,[16] luminescent sensing,[19] RNA hydrolysis[20] and MRI contrast agents.[21] The properties and applications of various lanthanide complexes have been discussed extensively within the Gunnlaugsson group in the PhD theses of Dr. Doireann Moore,[20] Dr. Cidalia Santos,[22] Dr. Andrew Harte,[2a] Dr Joseph Leonard,[23] Dr. Floriana Stomeo[24] and Dr. Anne-Marie Fanning[25] and so will not be discussed as this has already been covered in great detail. The topic of dinuclear complexes has been briefly discussed in the theses of Dr. Andrew Harte and Dr. Doireann Moore, however, as the first Chapter of this thesis will focus on the development of dinuclear lanthanide complexes, this will be briefly discussed in this section.

1.1.3 Dinuclear Lanthanide Complexes

The development of dinuclear complexes for use in luminescence, both as imaging probes and ribonuclease mimics, has been targeted, with the potential of using the possible cooperativity of two metal ions in close proximity. The cooperativity of metal ions is not an unusual feature, particularly in nature, as the most common enzymes and biological markers use between two and several metal ions, examples being zinc, iron, copper, cobalt *etc.*, particularly in catalysis.[26] For this reason, dinuclear complexes are the first step towards the mimicry of functional polymetallic species. Recently, they have generated

great interest due to the possibility of controlling the geometry and shape with small adaptations to the spacer group.[27] For the purpose of this thesis, the dinuclear complexes discussed are based on the cyclen macrocycle. There are a wide variety of functional groups reported for the formation of dinuclear complexes, such as xylene spacers and pyridine spacers,[20] and alkyl chains,[28] which enable the formation of geometrically defined structures. Recently, lanthanide complexes exhibiting this possible cooperativity have been used in fields such as imaging and MRI as discussed below.

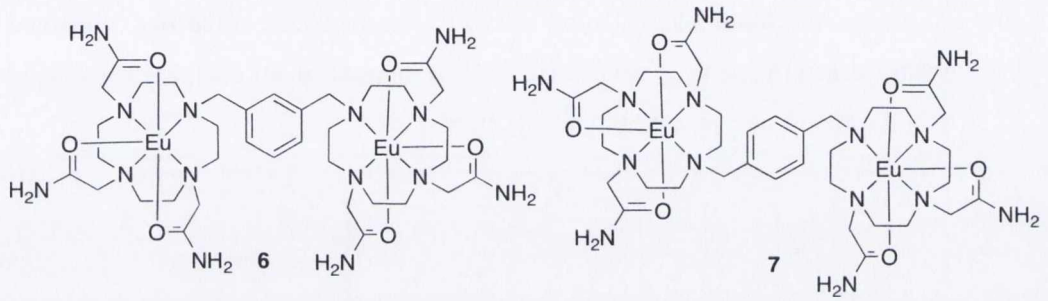

Figure 1.6: *Heptacoordinate dinuclear complexes* ***6*** *and* ***7*** *acting as potential ribonuclease mimics*

Moore *et al.*[20] and Nwe *et al.*[26] simultaneously demonstrated the RNA cleavage ability of the heptacoordinate cooperative dinuclear complexes, **6** and **7** respectively, Figure 1.6. These complexes were shown to have a large enhancement in activity compared to the mononuclear complexes indicating possible cooperativity between the metal ions in the hydrolytic process.

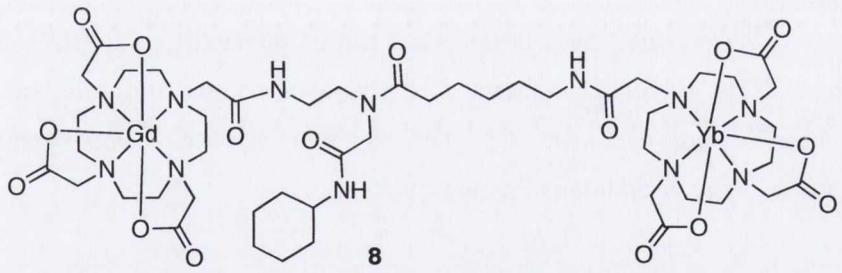

Figure 1.7: *Lanthanide dinuclear chelates*

Dinuclear Gd(III) chelates, such as **8** (Figure 1.7), have also been shown to be efficient MRI contrast agents.[29] These chelates exhibited both fast water exchange rates with the bulk solvent and slow tumbling rates, ensuring high relaxivity rates. The development of such MRI contrast agents will be further discussed in Chapter 4. These chelates were effective contrast agents as these complexes adopted a more rigid geometry and consisted of mixed Yt^{3+} and Gd^{3+} species. However, the main topic of interest in this chapter is the use of these dinuclear systems for lanthanide luminescence. Complexes

containing a benzophenone bridge were developed, which allowed sensitisation of each metal, while ensuring a rigid locked conformation.[30] Dinuclear lanthanide structures such as this have been utilized recently for the sensing of analytes, one such example being the development of a coordinatively unsaturated cationic dinuclear Tb^{3+} complex by Harte *et al.*,[31] can detect the presence of mono or bis-carboxylates in buffered aqueous solution at physiological pH. The Tb^{3+} complex has been shown to form a dinuclear pocket, in which the terephthalic acid can bind both lanthanide centres displacing the metal bound water molecules, resulting in an enhancement of the luminescence. This was confirmed by X-ray crystal structure analysis, which showed that the lanthanum complex contained two metal bound water molecules on each metal centre.

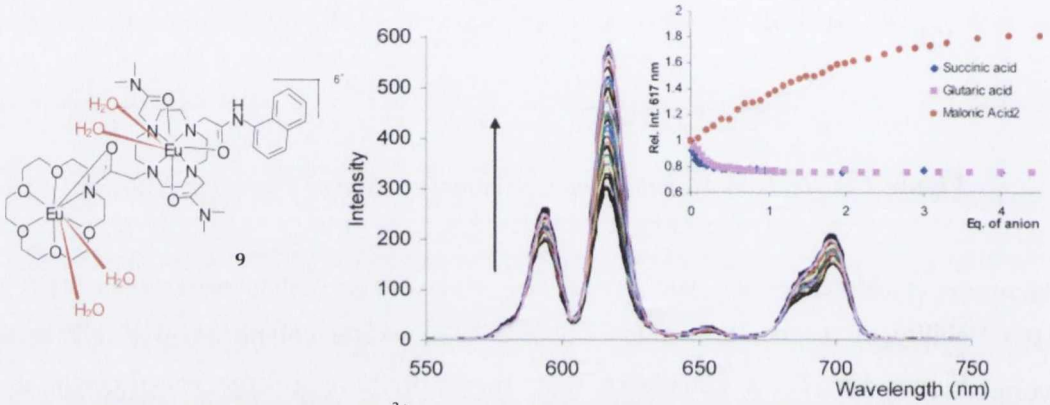

Figure 1.8: *Dinuclear Eu^{3+} complex, **9**, used as a sensor of aromatic carboxylates (right) switching on the luminescence of the lanthanide ion upon addition of malonic acid in HEPES buffer*

Plush *et al.*[32] have developed a similar dimetallic complex, **9**, with both a cyclen macrocycle and a crown ether attached *via* an acetamide arm, as a potential malonic acid sensor, shown in Figure 1.8. This complex showed selective enhancement of the luminescence on addition of malonic acid.

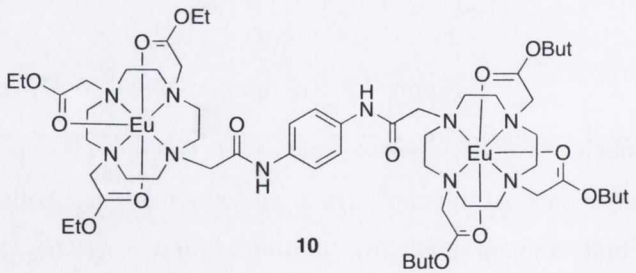

Figure 1.9*: Heterometallic complexes containing lanthanide ions in symmetrical binding pockets*

Following on from these results, Natrajan *et al.*,[33] developed various dinuclear systems including dimetallic lanthanide complexes, **10**, capable of containing different lanthanide ions in symmetrical binding pockets. This approach incorporated the sequential deprotection and complexation of an orthogonally protected ligand with a bridging acetamide unit. More recently, Jauregui *et al.*[34] have developed a new synthetic method, which allows for the formation of similar dinuclear complexes in a selective manner.

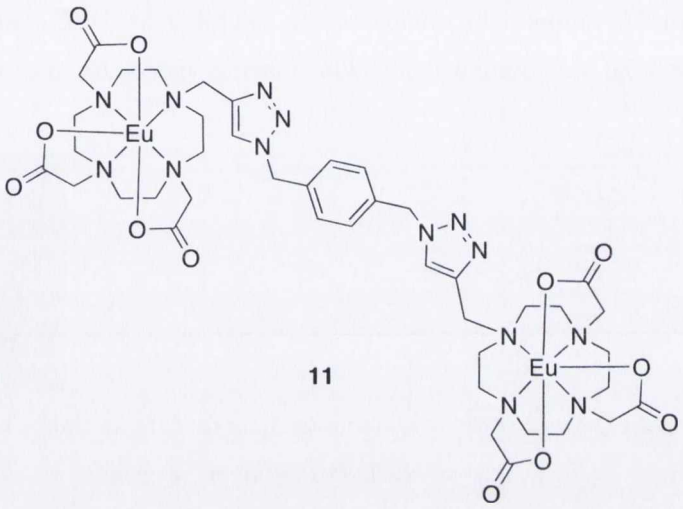

11

***Figure 1.10**: Dinuclear complex, **11**, utilising click chemistry as the strategy for formation of polymetallic complexes*

These complexes, such as **11**, were based on an alkyne framework, which can be used to generate polymetallic complexes with Eu^{3+} and Tb^{3+} ions using a Cu(II) click chemistry 1,3-Huisgen cycloaddition approach. 1,2,3 triazoles, which can be formed *via* a 1,3-cycloaddition between an azide and an alkyne (the so called 'click reaction'), have been shown to allow the development of a controlled dinuclear species. These dinuclear species based on the macrocyclic scaffold have been shown to be interesting, particularly for use in lanthanide luminescence. However, it is not only through the macrocyclic chemistry that the formation of dinuclear complexes can be achieved, but also through self-assembly of supramolecular polymetallic species.

1.1.4 Lanthanides in Supramolecular Chemistry

Another important facet of lanthanide complexation is the use of large acyclic polydentate ligands in order to wrap around the metal and fulfil the coordination sphere through supramolecular self-assembly. This templation needs to incorporate polydentate

ligands, which are capable of stable complex formation although, in general, this approach is less stable than the complexation using macrocycles.

This templation strategy has been used very effectively by Bünzli *et al.*,[35] who demonstrated the possibility of forming luminescent dimetallic bisbenzimidazole-based complexes or helicates. These bisbenzimidazole-based ligands have been shown to form stable, water-soluble triple stranded helicates with chromophoric or solubilising groups allowing variation of the functionality. For example, the addition of polyoxyethylene groups in **12**, Figure 1.11, increased the solubility of these complexes in water so they could be used as possible lanthanide imaging agents for the imaging of HeLa cancer cells.[35]

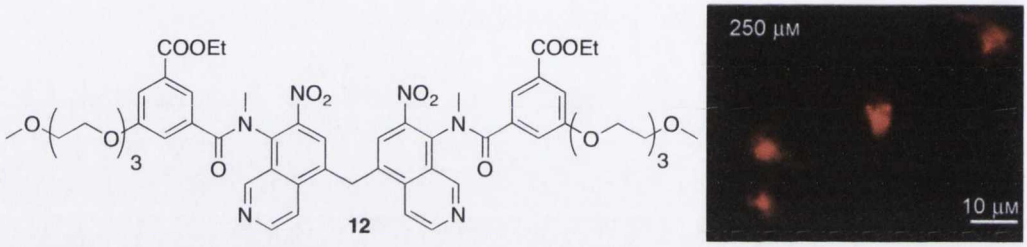

12

Figure 1.11: *Polyoxyethylene helicates such as **12**(left) confocal imaging of cells with helicates in the nuclei (right)*

The molecule, **12**, was shown to localize in the secondary endosomes and lysosomes that mainly co-localise with the endoplasmic reticulum, so that it lends itself to studies on a long timescale, especially as excitation wavelengths that are less damaging for living cells can be used (*e.g.* 405 nm). Albrecht *et al.*[36] have also shown the formation of triple stranded helicates, such as **13**, shown in Figure 1.12, through the use of templation with Eu^{3+} ions. These complexes demonstrated the efficient sensitisation of the metal ions using the acetal protected dicarboxylic acids with a phenyl chromophore on the end of each carboxylate.

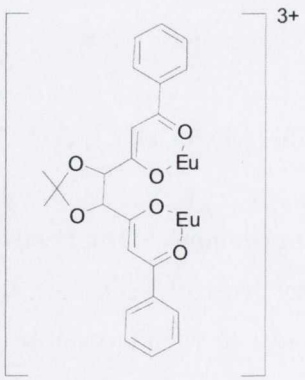

13

Figure 1.12: *Triple stranded helicates derived from acetal based ligands*

Piguet *et al.*[37] demonstrated the formation of heterometallic *d-f* hybrid water soluble helicates, **14**, based on a ruthenium/lanthanide conjugate, which demonstrated triple stranded helicate formation with both metals, as shown in Figure 1.13. The Ru(II) bidentate benzimidazol-2-yl-pyridine forms complexes that exhibit both *mer* and *fac* isomerisation. However, on addition of a lanthanide the isomerisation favoured the stabilisation of the *fac* isomer.

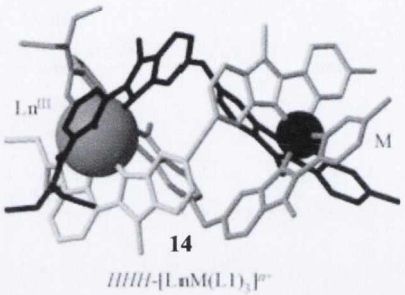

14

Figure 1.13: Dimetallic triple stranded helicates based on LRu[37]

The Gunnlaugsson group have previously developed chiral helicates based on a 2,6-pyridine dicarboxylic acid moiety, which lead to the formation of a triple stranded dimetallic helicate, using 3 strands of a 2,6-naphthylacetamide substituted pyridine.[38] The tuning of the bridges utilized for the formation of the helicates has been shown to change the possible orientation of the helicate, with both squeezed and stretched helicates possible depending on the nature of the spacer unit, this being confirmed using MM2 molecular modeling.

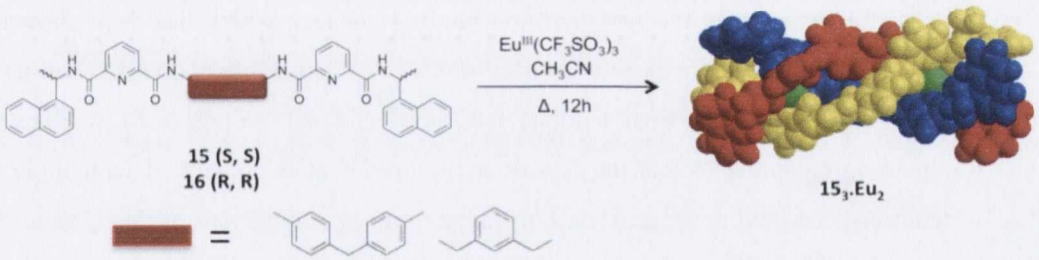

*Figure 1.14: Synthesis of dinuclear helicates based on 2,6-pyridine dicarboxylic acid, molecular modelling of helicate formed from ligand **15**(left)*

The most recent example of this work from the Gunnlaugsson group involves chiral triple stranded lanthanide helicates, **$15_3.Eu_2$**, based on a 2,6-pyridine dicarboxylic acid scaffold and a diphenylmethane linker in order to bridge the two metal centres.[39] These ligand threads were shown to form helicates with 2:3 binding stoichiometry, as shown in Figure 1.14, which was determined by fitting both UV-vis absorption titrations and luminescent titrations, using MM2 molecular modelling studies to confirm the wrapping of the three strands. This 2:3 stoichiometry was also confirmed by the titration of

$Eu(CF_3SO_3)_3$ with solutions of the ligand in acetonitrile, showing the 'switching on' of the luminescence with the addition of up to 0.66 equivalents of metal.

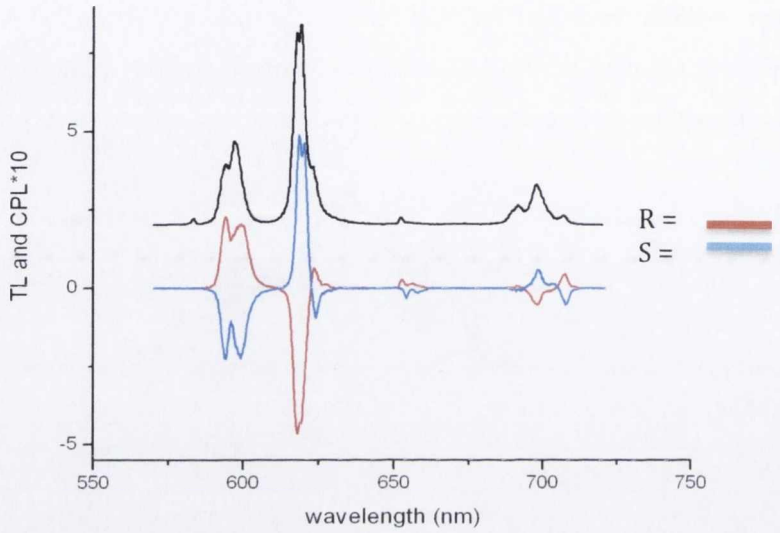

Figure 1.15: *CPL of lanthanide based helicates,* ***15$_3$.Eu$_2$*** *showing chirality of the excited state of both enantiomers*

The chirality of these helicates was observed using Circular Dichroism (CD) and Circularly Polarised Luminescence (CPL) studies, the latter of which demonstrated the chiral emission of the lanthanide complex, Figure 1.15. This has been shown with a number of helicates from the Gunnlaugsson group, such as those developed using a benzyl amine linker between the two pyridine binding pockets, which has been shown to form similar 2:3 complexes with Sm^{3+}, Tb^{3+} and Eu^{3+}.[39-40] Dinuclear complexes similar to those previously discussed in both sections 1.1.3 and 1.1.4 will be presented in Chapter 2. The remaining Chapters in this thesis will focus on the development of lanthanide complex functionalised gold nanoparticles. For this reason, the second part of this Chapter will give a review on gold nanoparticles (**AuNPs**) and their functionalisation, leading to the incorporation of lanthanide complexes onto the surface of gold.

1.2 Gold Nanoparticles

There is an increasing interest in the synthesis and applications of **AuNPs**, due to their biocompatibility, unique size and shape dependence and optoelectronic properties.[41] Nanoparticles have been designed in order to develop hybrid materials with novel properties.[42] In particular, **AuNPs** have become increasingly popular in the search for biocompatible functional surfaces, in order to act as catalyst carriers, functionalised

sensors and as imaging agents.[43] They have also been used in a wide variety of biological applications, some of which will be discussed in the following sections.

1.2.1 The Properties of AuNPs

An important property of **AuNPs** is their surface plasmon resonance (SPR) absorption band. This resonance is pronounced in metal nanoparticles because of the collective oscillations of the conduction band electrons.[44] Under irradiation, the plasma couples with the excitation light and produces an enhancement of the electromagnetic field of the nanoparticles.[45] Interaction with incident light and these oscillating electric fields produces light scattering and absorption. The SPR is expressed as a maximum in the electronic spectrum with its position dependent on the metal and the size of the nanoparticles. The SPR band for **AuNPs** of size 5 nm is observed at 520 nm. In general, nanoparticles smaller than 2 nm are referred to as clusters of gold. An increase in the size of **AuNPs** causes a red shift of the maximum absorption, for instance, nanoparticles of size 5 nm would be expected to have an SPR at 520 nm, whereas **AuNPs** of size 20 nm would shift the SPR to 530 nm.[46] The binding of analytes to the surface of the gold can have a direct effect on the SPR.[47]

Another important property of **AuNPs** is the inherent fluorescent properties of the gold.[47] An understanding of the extent to which the proximity of the gold will affect the luminescence of the compounds used to functionalise the **AuNPs** is important. Visible luminescence has been reported for water soluble **AuNPs**, however, upon the binding of fluorescent or phosphorescent materials to the surface of nanoparticles, fluorescent quenching can be induced due to electron transfer to the gold itself.[48] This is the basis for the fluorescent sensing, which will be discussed in Section 1.2.4.3, but firstly a review on the synthesis of **AuNPs** will be discussed in the following section.

1.2.2 The Synthesis of AuNPs

Chemical preparative methods for the formation of **AuNPs** consist of nucleation and growth of gold clusters from the reduction of a gold salt, such as terachloroaurate ($HAuCl_4.H_2O$). The important factors in this synthesis are the control of growth to a certain size and shape, the stabilisation in solution and the surface functionalisation of the gold.[49] There are a wide variety of synthetic pathways developed for the synthesis of small monodisperse nanoparticles. These mostly consist of the reduction of the gold by a reducing agent such as $NaBH_4$,[50] or citric acid,[51] followed by stabilisation of the

nanoparticulate gold by covalent attachment of a stabilising agent or electrostatic attraction of a salt to prevent aggregation.[52]

A very common method for the synthesis of **AuNPs** is the simultaneous reduction and stabilisation of the gold using a citrate salt such as sodium citrate. This method was first used by Turkevitch *et al.*,[49a, 51, 53] and has become a common method for the formation of water soluble **AuNPs**. This technique controls the size of spherical nanoparticles by altering the gold/citrate ratio. Higher ratios of citrate can generate smaller **AuNPs** due to the increased stabilisation. The citrate acts as a temporary stabiliser, which can be displaced with ligands such as thiols. In fact, the simultaneous addition of citrate and thiol causes reduction by the citrate with subsequent stabilisation by the thiols.

Brust *et al.*[50] developed a synthetic method for the formation of **AuNPs** in which, dilute solutions of the tetrachloroaurate were dispersed in a tetraalkyl ammonium bromide salt (TOAB) solution, in order to transfer the gold to the organic phase by surfactant stabilisation as depicted in Figure 1.16. Reduction by $NaBH_4$ in a mixed organic/aqueous solution can then be carried out. Subsequent stabilisation of these nanoparticles has been achieved in a number of different ways.

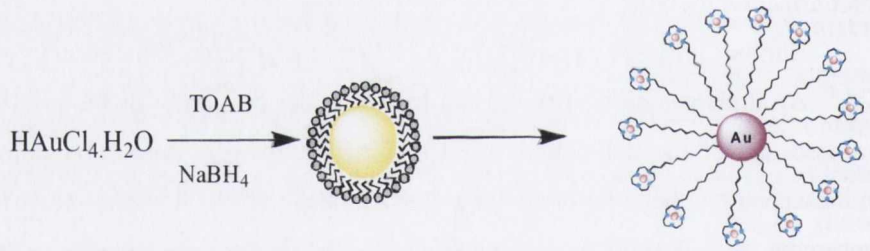

Figure 1.16: *Brust-Schiffrin synthesis of* ***AuNPs*** *by reduction of* $HAuCl_4.H_2O$ *using* $NaBH_4$

For example, stabilisation can occur either through covalent bonding of a stabiliser to the surface of the **AuNPs** themselves or through electrostatic interactions such as that discussed previously for the surfactant stabilised particles.[49b] Caruso *et al.*[52] showed that **AuNPs** could undergo phase transfer to the aqueous phase, through the stabilisation of the **AuNPs** with dimethylamino-pyridine (DMAP), replacing the need for covalent interactions in the stabilization process. However, the most effective method by which to generate stabilised **AuNPs** is to covalently bind ligands to the surface of the nanoparticle such as with **17**, shown schematically in Figure 1.17.[54] The two synthetic pathways outlined above remain today, the most common ways of synthesising 5-10 nm **AuNPs**. However, a number of alternative methods have recently been developed, which utilise various stabilizers or reducing agents such as polystyrene,[55] triphenyl phosphine,[56] amino acids,[57]

polyelectrolytes,[58] and biological substrates possessing amines functionalised at the terminus.[59]

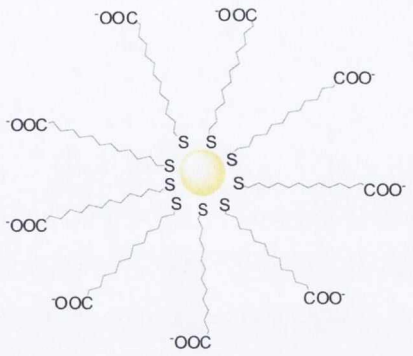

17

Figure 1.17: *Thiol stabilised* ***AuNPs***

The reversible formation and dissolution of nanoparticles can be facilitated using UV light with polyoxyethylene polymers and gold salts.[60] Irradiation with UV light yields the **AuNPs**, while switching off the UV light was sufficient to dissolve the **AuNPs** and yield $\mathbf{Au^{3+}}$. The comb-like polyoxyethylene polymer structure, which contains a sulfide moiety was found to be essential for this reversible formation and dissolution of the **AuNPs**. However, an approach more widely used is the incorporation of different stabilising units in order to ensure adequate stabilisation for a particular particle size. Vignolle *et al.*,[61] demonstrated a method in which **AuNPs**, functionalised with *N*-heterocyclic carbene ligands with various chains attached to the N position, could be rigidly controlled using the length of the chains attached to the *N*-heterocyclic carbene. Long flexible chains gave rise to the isolation of particles of size 6-7 nm in diameter, whereas rigid bulky isopropyl groups yielded smaller nanoparticles of size 2 nm.

More recently, laser ablation technology has been utilised for the formation of size controlled nanoparticles with very low concentrations of stabilising agent,[62] whereas the purification of nanoparticles has been recently attempted with differential centrifugation with a CsCl gradient. This yielded very interesting arrays of dimers and trimers, in excellent purity, such as that observed in Figure 1.18.[63] These citrate-synthesised nanoparticles were stabilized with 2-naphthalene thiol, and could be induced to aggregate in solutions of NaCl or CsCl. Solutions of varying density of CsCl with centrifugation allowed the synthesis of dimers and trimers, which could then be halted with addition of polymer coating, encapsulating the nanoparticles and allowing the separation of dimers and trimers in high purity. Considering the importance of structural intactness, which is critical for any nanoassembly, this offers a facile approach for the controlled assembly of **AuNPs**.

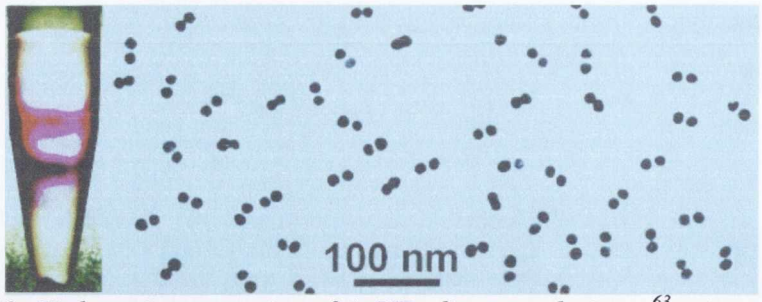

Figure 1.18: *High-purity separation of* ***AuNPs*** *dimers and trimers*[63] *using a CsCl gradient and centrifugation*

The use of thiacalixarenes demonstrates a different approach towards the development of stabilised **AuNPs** of small size. Here, amphiphilic thiacalixarenes act as both a stabiliser and a mild reductant, as the phenolic groups on the outer rim can be easily oxidized to form quinine groups facilitating the reduction of the metal ions.[64] By simply adjusting the ratio of Au/S, **AuNPs** of different sizes could be readily obtained in aqueous phase under mild conditions. However, in addition to the control of the synthesis and stabilisation, it is important to be able to characterise the properties of these nanoparticles with various techniques to assess size, shape and stability of such particles. The next section will discuss the characterisation techniques applied to these **AuNPs**.

1.2.3 Characterisation of AuNPs

With the development of the field of **AuNPs**, the ability to be able to fully characterise these particles accurately in solution and solid state has been of utmost importance. For this reason, the main characterisation techniques for **AuNPs** will be dealt with in the following sections. However, only those employed in Chapter 3 and 4 will be outlined in the next sections.

1.2.3.1 Transmission Electron Microscopy

Transmission Electron Microscopy (TEM) is utilized in order to analyse the size and distribution of particles.[65] This is achieved by imaging the gold core of the particles, which relies on the contrast between the high molecular weight gold and the carbon films on which the nanoparticles are deposited.

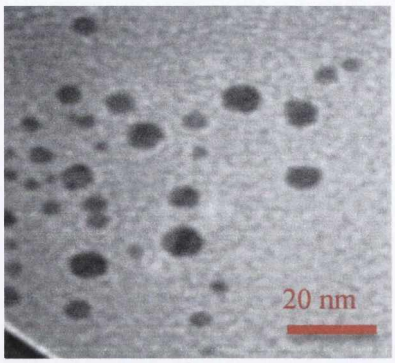

***Figure 1.19**: TEM images of **AuNPs** showing average size particles of 5-10 nm*

In general, carbon grids are used with no modification or with polymer coating such as Formvar. The technique is efficient, particularly for **AuNPs,** due to the high contrast between the carbon and gold. Figure 1.19 shows a TEM image of gold nanoparticles of approximate diameter 5 nm.

1.2.3.2 UV-Vis Absorption Spectroscopy

As previously discussed in Section 1.2.1, noble metal nanoparticles, particularly **AuNPs**, have well-known UV-Vis absorption properties; they display an SPR band in the UV-Vis absorption spectrum. The **AuNPs** are strongly size dependent and exhibit a visible colour change from red to blue as discussed above in section 1.2.1. The SPR band is red shifted when the **AuNPs** become aggregated in solution, as seen in Figure 1.20, showing the changes in the SPR with size from 50-200nm in diameter.[66]

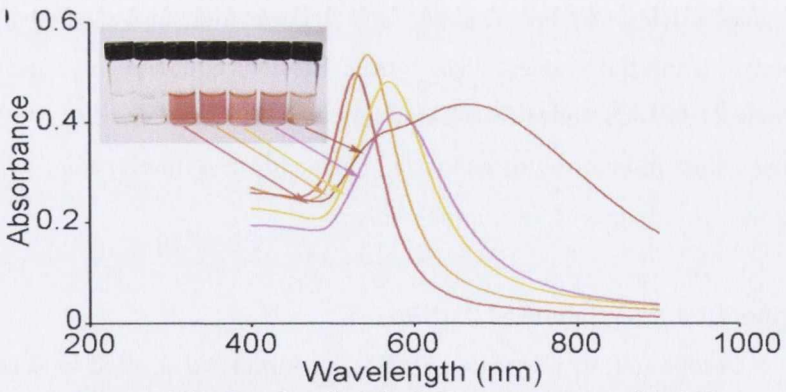

Figure 1.20**:SPR band of the UV-vis spectrum of **AuNPs

The size, concentration and aggregation level of **AuNPs** are all very important and so it is essential these properties can be easily analysed. A method for estimating these by UV-Vis absorption spectroscopy is utilized by fitting to the Mie model for spheres, previously discussed in section 1.2.1, when outlining the SPR, and taking into account the

Gans model for spheroids.[49a] Calibration of the SPR frequency allows an accuracy of about 6% for the size evaluation for different shaped and sized nanoparticles.

Section 1.2.3.3 Dynamic Light Scattering

Dynamic Light Scattering (DLS) is a technique, which allows the determination of characteristics such as molecular weight, zeta potential and the hydrodynamic radius from the diffusion coefficients of solutions of the nanoparticles.[67] This utilizes the back scattering of light from the sample and so can be used for the analysis of **AuNPs** as it measures the size and molecular weight of the particles and also possible aggregation and hydrodynamic radius with functionalised ligands, Figure 1.21.

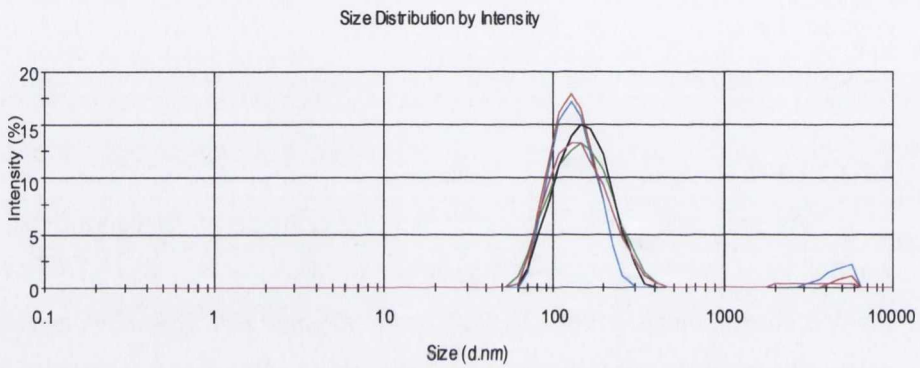

Figure 1.21: *DLS showing size distribution of* ***AuNPs*** *functionalised with thiols*

In this technique, the changes in the scattered light due to the Brownian motion of the nanoparticles can be measured and a correlation curve can be obtained from this response, using the mathematical Stokes Einstein equation to relate the diameter of the nanoparticles. DLS under flow conditions has also been envisaged by Katayama *et al.*,[68] for the online monitoring of nanosized chemicals in a flow system, which has been shown to be particularly useful for microchemistry.

Section 1.2.4 Functionalised AuNPs

Combining the properties of the nanoparticles discussed in Section 1.2.1 and 1.2.2, with the intrinsic functionalities of organic and biomolecular systems, by grafting them on the surface of nanoparticles, will yield hybrid materials with novel properties and functions.[42, 69] The preorganization of the receptors on the surface of the nanoparticles reduces their conformational flexibility (entropic contributions) and increases their effective concentration, thus forming hydrophobic self assembled monolayer-like

environments at the surface. Such functionalisation leads to the formation of materials with increased loading, which will be discussed in the following sections.

1.2.4.1: Chromophore Functionalised AuNPs

AuNPs, as discussed in previous sections, have interesting photophysical characteristics, which lend them to the fields of sensing and the development of alternative luminescent materials. The addition of chromophores to the surface of the gold nanoparticles can result in unique properties for both the metal nanoparticle and the functionalised organic ligand.

Thomas *et al.*[70] reported the formation of functionalised **AuNPs** with dyes or chromophores directly attached to the surface of the gold and examined the optical and luminescent properties of these dye conjugated nanoparticles. The addition of compounds, such as phenyl isothiocyanate and benzylamine, caused a change in the SPR of the **AuNPs**, with broadening of the SPR band, due to change in the surface properties.[70] The **AuNPs** can also alter the fluorescence and optical properties of dyes and chromophores such as porphyrins, pyrenes, and fullerenes.[70-71] The incorporation of fluorophores onto the surface of **AuNPs** can have a large effect on the singlet excited state of the fluorophores, by inducing quenching due to energy transfer to the metal.[72] The energy transfer depends on a number of factors, such as the size and shape of the **AuNPs**, the distance from the core and the flexibility and mobility of the functionalized units, such as that seen in fullerene **AuNPs** analogues.[73] These properties can be tuned in order to develop systems for potential applications in optoelectronic materials.

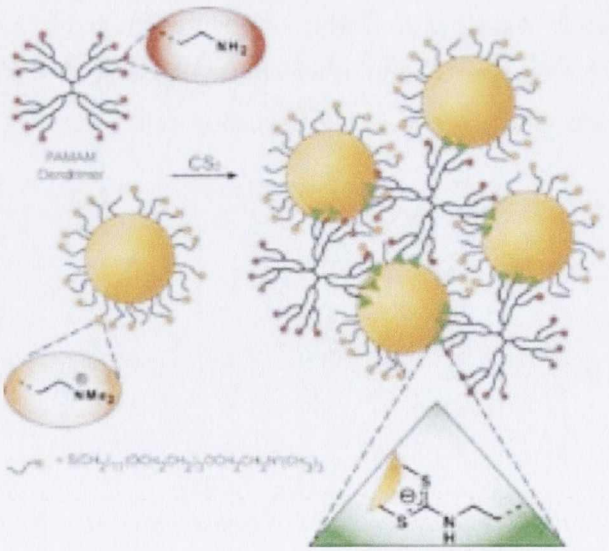

Figure 1.22: *Dendrimer stabilised* ***AuNPs*** *based on assemblies of PAMAM dendrimers*[74]

In fact, dendrimers have been shown to be of interest for the formation of stable compounds for use in optoelectronics and plasmonics.[70, 74] The attachment of dendrimers to the nanoparticle can be monitored by the fluorescence of the dendrimers, as formation of the nanoparticles by addition of $NaBH_4$ caused a decrease in their fluorescence due to the quenching by the gold core.[75] These strongly interlocked molecular branches provided high stiffness and rigidity and, since no back folding was possible, maximum exposure of the surface functionalities was achieved, resulting in careful control of the solubility of these macromolecules and consequently of the obtained **AuNPs** dendrimer hybrids.[76] These nanoparticles are of great interest, as attaching folic acid or fluorescein isothiocyanate to G-5 dendrimers with neutral charge surface area can allow specific targeting of cancer cells overexpressing folic acid receptors, demonstrating the benefits of functionalising gold nanoparticles with dendrimer assemblies. Stabilised **AuNPs** have recently been used for a number of applications, particularly the use of nanoparticles in drug delivery, which will be discussed in the following section.

1.2.4.2 AuNPs in Drug Delivery Systems and Anticancer Research

A key attribute of nanoparticles is their ability to act as nanoscale carriers. Drug delivery systems (DDS) can be used to regulate drug release, minimising side effects and improving therapeutic efficacy of conventional pharmaceuticals.[77] Monolayer protected **AuNPs** provide an excellent synthetic scaffold for the formation of DDS, due to their functional versatility, improved biocompatibility and low toxicity.[78] For example, the photoregulated release of caged anticancer drugs from the surface of **AuNPs** has been demonstrated by Agasti *et al.*,[79] who showed that the controlled release of fluorouracil, **19**, using a photocleavage reaction in which irradiation at 365 nm causes the cleavage of the drug molecule, allowing release into the cancer cell, Figure 1.23.

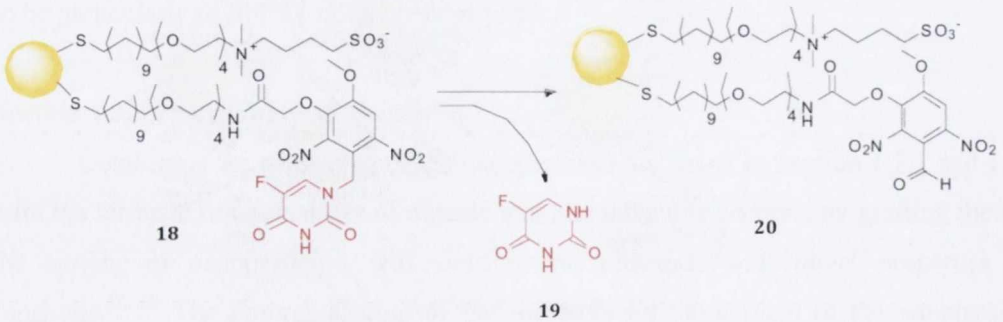

Figure 1.23: *Photoregulated release of caged anticancer drugs such as fluorouracil upon irradiation at 365 nm*

The fluorouracil conjugated **AuNPs**, developed and synthesised by Agasti *et al.*[79] for this study, possessed a gold core diameter of 2 nm and featured a surface functionality, comprised of a mixed self assembled monolayer of photocleavable fluorophores and zwitterionic thiol ligands. The two ligands possessed a common basic structure, where an alkyl segment was used to confer stability to the nanoparticle, while the tetraethylene glycol component provided water solubility and superior compatibility. An IC_{50} value of 0.7 μm (concentration of a drug required to inhibit viral replication by 50 %) was observed, on a per nanoparticle basis, upon irradiation of the sample, corresponding to 11.9 μm on a per drug basis. Nanoresponsive carriers for amines have also been demonstrated by Nakanishi *et al.*[80] These carriers, utilising simple deprotection chemistry, can incorporate amines, which can be released photochemically, and these have been shown to be efficient in *in vivo* studies for amines such as histamine.

Caged nanostructures utilised for the capture and release of drug molecules is a common theme exploited with nanoparticles.[81] This has involved the incorporation of molecules such as dyes and drugs, which are held in a hydrophobic pocket in the nanoparticle and then released by membrane mediated diffusion, without uptake of the carrier itself.[82] These cage-like nanostructures are functionalised with tetraethylene glycol chains as seen in the previous example, with zwitterionic terminal groups in order to ensure solubility, Figure 1.24. Shieh *et al.*[83] have demonstrated the ability to synthesise drug functionalised nanomaterials, with quantification of the number of drug molecules attached to the surface of the particle, as well as demonstrating that the properties of the drug itself are unchanged. These paclitaxel substituted particles have been found to be as efficient when stabilised on a solid platform as in solution.

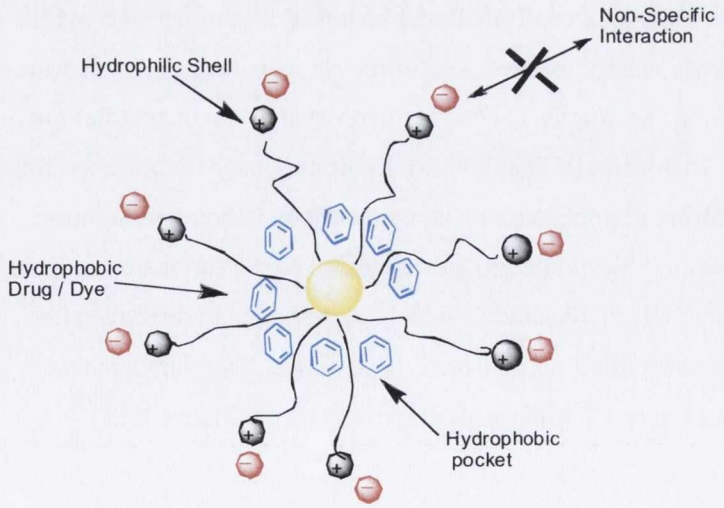

***Figure 1.24: AuNPs** based hydrophobic shells for potential drug delivery*

Following on from the process of drug delivery, an obvious succession is drug therapy and anticancer research. Entrapment of hydrophobic molecules in long thiol chains has proven to be an attractive option for cancer drug therapies, due to the hydrophobic pocket generated within the hydrophilic shells.[82] These allow non-specific interactions that cause release of the drug or dye into the cancer cells. However, optimising **AuNPs** for multifunctional diagnosis and therapy is still a great challenge. An interesting development has recently emerged in the detection of lung cancer in patients using **AuNP** arrays. These **AuNPs** were functionalised with 4-methoxy-toluenethiol, 2-mercaptobenzoxazole or 11-mercapto-1-undecanol and were shown to have detection limits of 2-10 ppb on exposure to formaledyhde and acetaldehyde, volatile organic compounds known to cause lung cancer.[84] These nanoparticles allowed detection of these markers in the exhaled breath of patients demonstrating the benefit of utilising these arrays. The sensing of analytes utilising functionalised **AuNPs** will be discussed in section 1.2.4.3.

1.2.4.3: Nanoparticles in sensing

Based on the state dependent (aggregation, redispersion) SPR absorption properties, fluorescent properties, as well as size and shape, **AuNPs** can be used for the sensing of metal ions, enzymes, proteins, oligonucleotides and other small molecules.[85] In particular, **AuNPs** are an attractive substrate for the development of colorimetric sensors due to high extinction coefficients, stability and easy functionalisation by organic ligands.[86] Furthermore, it has been shown that attachment of proteins to the surface of the gold changes the SPR band of the **AuNPs**, ensuring that any conformational change is observed in the SPR of the nanoparticles.[87] Upon exposure to solutions of differing pH, the protein undergoes conformational changes, folding at high pH but unfolding at low pH.[88] This consequently induced a colorimetric response, as a hypsochromic shift in the UV-Vis absorption spectrum was observed with changes in the surface energy of the particles.

Malonamide functionalised particles have also shown interesting possibilities for the colorimetric detection of lanthanide ions in aqueous solution.[89] Ligands functionalised with sodium thiosulfate groups can attach to the surface of the gold with another tail group of tetraethyl malonamide, which serves as a selective Ln^{3+} binding site. Acyclic malonamides such as this have been utilised for lanthanide ion detection and they are known to have a 2:1 binding of ligand to metal, Figure 1.25.[89]

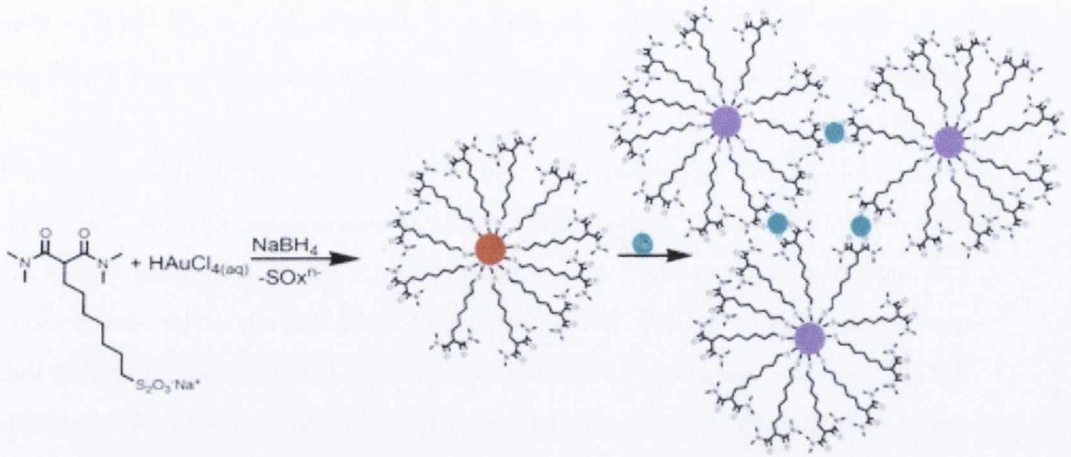

***Figure 1.25**: Colorimetric sensing of trivalent lanthanide ions by malonamide-functionalised **AuNPs**[89]*

Cross linking of particles due to this 2:1 binding of the malonamide causes changes in the SPR, and inducing a colour change from red to blue; colorimetrically detecting the presence of the lanthanide.

Recently, disulfide linked **AuNP**-based reagents for detecting small molecular weight thiols (LMWTs) have been developed utilising the strong S-Au bond.[90] In order to sense the presence of LMWTs, a disulfide bridge was prepared that was accessible to reduction by LMWTs, but not by higher molecular weight thiols.[90]

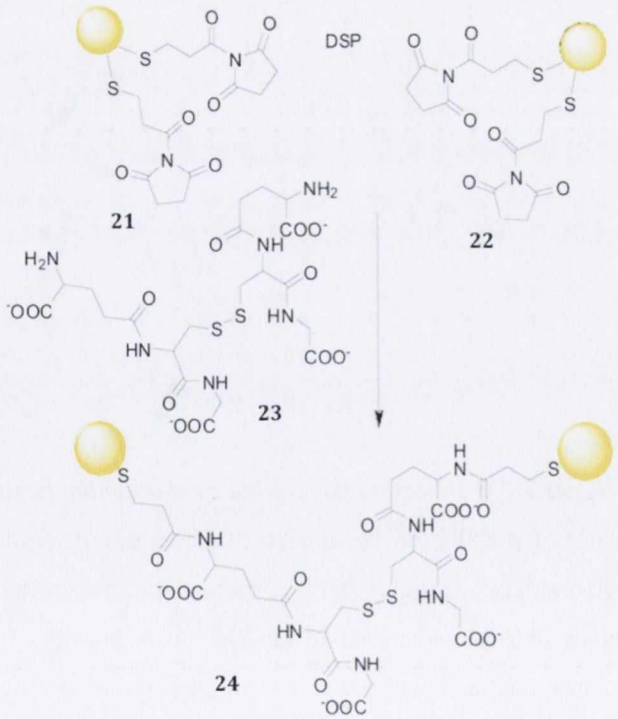

***Figure 1.26:** Synthesis of disulfide linked **AuNP** clusters*

This was possible as monodisperse **AuNPs, 21** and **22**, have different SPR properties than clusters, **24**, which provide a signal for the presence of the low molecular weight thiols, Figure 1.26.

Dong *et al.*[91] have investigated a new fluorescent method for the sensitive detection of biological thiols in human plasma using a near infrared dye FR 730. This sensing approach was based on the strong affinity of gold for thiols and the highly fluorescent quenching ability of **AuNPs**. In the presence of thiols, the dye underwent desorption from the gold surface, inducing a 'switching on' effect of the emission, enhancing the near IR signal dramatically. Such an effect in the near IR region leads to the possibility of the detection of thiols in biological samples.

The sensitive detection of analytes using **AuNPs** has been shown for a variety of different examples. A recent example of the use of such nanoparticles has been the formation of a luminescent switch for cyanide detection.[92] A key component of this sensor was that rhodamine attached to the surface of the gold was quenched due to efficient energy transfer to the gold itself. Cyanide is well known to dissolve metals such as Au and Ag and was used here with that in mind, as upon treatment of these rhodamine functionalised **AuNPs** with cyanide, the Au became etched and the rhodamine was released, with concurrent enhancement of the fluorescent signal as shown in Figure 1.27.

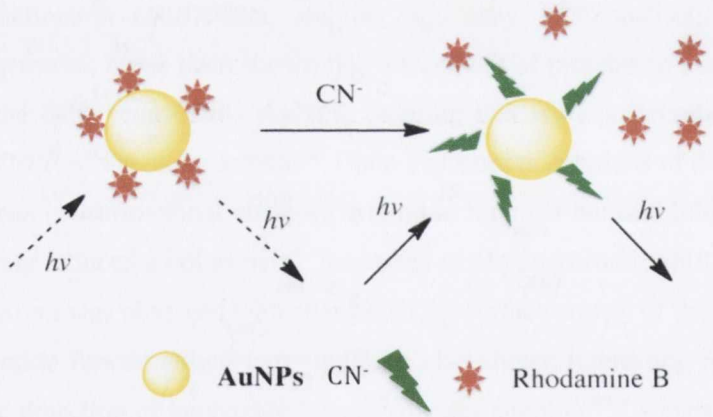

Figure 1.27: *Detection of cyanide by rhodamine functionalised* ***AuNPs***

The use of **AuNPs** for the sensing of melamine in solution has recently been shown to be highly beneficial, as the illegal incorporation of melamine into formula milk has been reported and is detrimental to infant health.[93] It is possible for melamine to control the assembly of cyanuric acid, which can form supramolecular hydrogen-bonded complexes, **27** between the melamine, **26**, and the cyanuric acid, **25,** Figure 1.28. The melamine-stimulated aggregation of **AuNPs** was evidenced by TEM images, which revealed

monodisperse nanoparticles in the absence of melamine and the formation of significant aggregation of nanoparticles in the presence of 1.5 μM melamine.

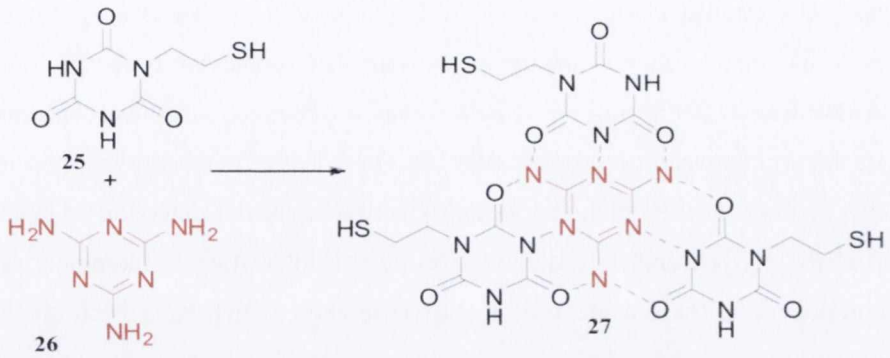

Figure 1.28: *Melamine sensing due to the presence of cyanuric acid with formation of hydrogen bonded systems,* ***27*** *with the melamine* ***26***

Fluorescent **AuNPs** based sensors for Cu^{2+} have also recently been developed, whereby highly fluorescent glutathione capped **AuNPs** showed Cu^{2+} binding, with the aggregation of **AuNPs** into larger aggregates indicative of Cu^{2+} complexation.[94] Glutathione (GSH), which is a natural peptide, was employed as a stabiliser and a gentle reducing agent in this one step synthesis of GSH capped fluorescent **AuNPs**. An indication of particle size of less than 2.5 nm was given by the SPR band in the UV-vis spectrum. However, upon introduction of EDTA to the sample (as a strong binder of Cu^{2+} ions), the formation of dispersed nanoparticles was observed by TEM imaging, indicating that the aggregation was significant of the Cu^{2+} complexation process. This method was found to be highly selective for the presence of Cu^{2+} ions; no fluorescent quenching was observed for any other divalent and trivalent ions.

The enhancement of estriol detection was also improved with the use of **AuNPs** as high mass labels conjugated to the primary antibody.[95] Various examples of sensing on the surface of nanoparticles have demonstrated the benefits of these systems. For instance, gold nanodot-based luminescent sensors have been developed for the detection of hydrogen peroxide and glucose.[96] These nanodots were bound with 11-mercaptoundecanoic acid as a stabilising agent and have been shown to be luminescent. In the presence of H_2O_2, oxidation of the thiol chain occurs, which caused disulfide bond formation, thus decreasing the number of units that were bound to the nanoparticle and so decreasing the luminescence, sensing the presence of H_2O_2. The use of such **AuNPs** as biological sensors, is an interesting possibility for the detection of DNA.

The detection of DNA using **AuNPs** has gained wide interest as the **AuNPs** allow increased sensitivity of the detectors. In particular, molecular beacon-functionalised

AuNPs have been tested as a dry reagent strip type nucleic acid biosensors.[97] These strips were shown to detect the presence of nucleic acids specifically. The ability to detect single-base mismatched DNA was eight fold greater with the **AuNPs** functionalised molecular beacons, than with the analogous dye-labelled molecular beacons. Similar designs of **AuNP**-based DNA probes, which serve as an electrochemical biosensor with a 1:1 interaction between tripodal **AuNPs** and DNA, have been observed, possibly highlighting this method for the efficient and highly active molecular detection of DNA. The utility of **AuNPs** in DNA and drug delivery has proven interesting in biological systems.[98] A key component of these systems is metal complexes, which have been shown to be widely present in the body, as imaging, sensing, and drug development candidates. For this reason the next section will discuss the potential of metal complex functionalised gold nanoparticles.

1.2.4.4 AuNPs functionalised with metal complexes

Metal complexes have long been shown to be interesting for various applications, such as luminescent sensing, as discussed already.[99] Nevertheless, there are few examples of metal complexes attached to the surface of **AuNPs**,[100] which is quite surprising considering the wide uses of metal complexes, particularly in the fields of sensing, biological imaging, energy conversion and RNA hydrolysis.[99] Moreover, the incorporation of metal complexes onto the surface of **AuNPs** is a highly interesting area within supramolecular chemistry, but, to date, is unexploited.

An interesting example, whereby metal complexes exhibit an increased efficiency upon nanoparticle attachment, is the development of nanoparticle stabilised zinc complexes carried out by Bonomi *et al.*[101] Zn^{2+} is the metal ion preferred by hydrolytic enzymes and it is non-toxic, redox inactive and bioavailable. Zn^{2+} complexes of *N*-bis-2-pyridyl methyl-6-amine (BAPA) derivatives have been found to be extremely efficient, due to cooperation between metal Lewis acid activation and H-bonding, for increased hydrolytic activity towards phosphate diesters. The reactivity gain, due to the confinement of the Zn^{2+} complex on the nanoparticle at pH 7, is quite important, hydrolysing bis-*p*-nitrophenyl phosphate (BNP) 100 times faster than the complex alone. The observed rate constant was found to be 3.6×10^{-5} s^{-1}, which is a 300,000-fold increase over the background reaction. It was anticipated that such high activity was found to be a direct result of a number of cooperative metals attached to the gold surface.

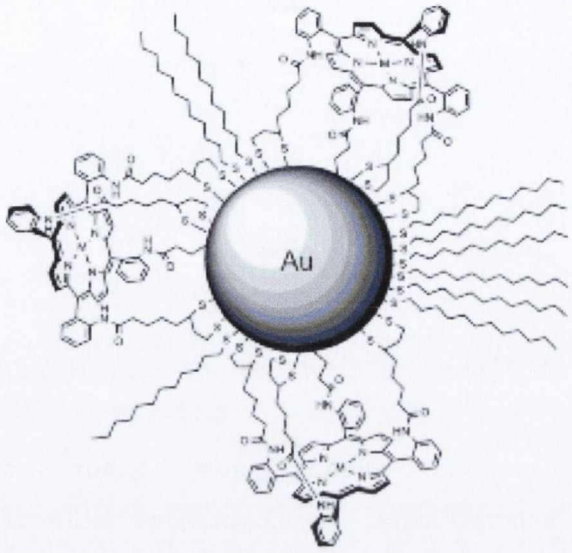

28

Figure 1.29: *Zinc porphyrin attached to* ***AuNPs, 28***[102]

Beer *et al.*[103] showed that disulfide-functionalised zinc metalloporphyrins, **28**, shown in Figure 1.29, self-assembled on **AuNPs** and as such, exhibited remarkable surface-enhanced anion binding affinities as compared to the free metalloporphyrin in solution. The ultimate aim of this work was to develop optical and redox-active, nanoparticle based anion sensors. Importantly, surface pre-organisation of the neutral zinc metalloporphyrin moiety significantly enhanced the coordination at the nanoparticle surface, to such an extent that the recognition in a mixed aqueous-organic solvent system was made possible. The increase in the association constant for anion recognition, observed upon confining the receptor to the surface, was also found to be significant. Furthermore, by preorganising the receptors on to the gold surfaces, their conformational flexibility was reduced and entropic contributions became more favourable. Solvation effects, associated with close packing of receptors in a dominantly hydrophobic self-assembled monolayer environment, was also thought to be important. The development of porphyrin based complexes has also been studied by Lindsey *et al.*,[71] who showed the synthesis and characterisation of a family of metalloporphyrin building blocks, which can be utilised for the formation of various optical and electronic devices.

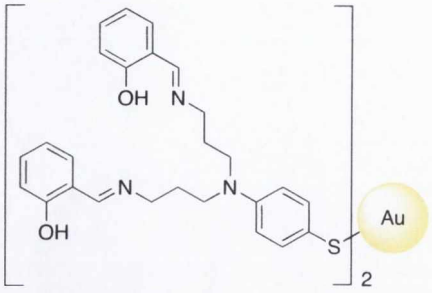

29

***Figure 1.30**: Schiff base based ligands, **29**, for iron complexation and functionalisation of gold surface*

Iron complexes, derived from Schiff bases such as Bis-(3-salicylideneaminopropyl)-amine], have been shown to efficiently functionalise the surface of **AuNPs**, Figure 1.27.[104] These iron complexes have been designed to interact with the **AuNPs**, through an ambidentate thiocyanate ligand or through a pendant thiol group, appended to the ligand. These derivatives, such as **29**, can then be tuned to stabilize the nanoparticle in solution, or to cause aggregation of the particles and consequently are potentially useful for the incorporation of Schiff base-based metal complexes with specific magnetic properties.

Concurrently, the recent development of ruthenium complex stabilised **AuNPs** is an interesting one, due to the potential of ruthenium-bipyridine and phenanthroline as active anticancer agents. In this case, the ruthenium complexes, were utilised in order to enhance the phase transfer properties of the nanoparticle systems.[105]

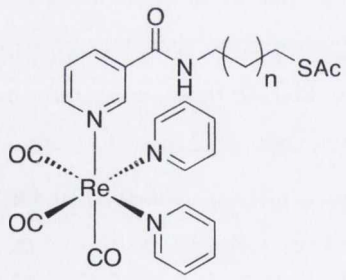

30

***Figure 1.31:** Rhenium complexes for the functionalisation of **AuNPs** to function as emissive fluorphores*

There is currently growing interest in incorporating metal complexes, previously shown to be useful as potential luminescent probes, onto the surfaces of **AuNPs**. For the logical design of an emissive fluorophore-**AuNPs** conjugate, an important consideration is the reduction in the efficiency of excited state quenching. A novel synthetic strategy was

reported recently to accessing functionalised rhenium complexes, such as **31** allowing attachment to small diameter **AuNPs**, Figure 1.31.[106] The resulting hybrid conjugates were found to be water soluble, and retained their MLCT emission characteristics, and consequently, represented a useful possibility for the future development of novel functionalised **AuNPs**, which have the potential to be exploited in a number of applications, including fluorescence microscopy and nanodevices. In addition to the use of metals such as zinc, iron, and rhenium, there has been significant interest in the development of lanthanide probes for the reasons already outlined in Section 1, such as their long lived excited state lifetimes, narrow line-like emission bands and luminescent capabilities.[3] The properties lend the lanthanide ions to functionalisation of complexes onto the surface of nanoparticles to combine both the properties of the lanthanide and the nanoparticle, which will be discussed in Section 1.2.4.6.

1.2.4.5 Lanthanide luminescent AuNPs

There are a number of research groups working on the development of luminescent nanoparticles based on the use of silica networks,[107] and silver nanoparticles,[108] which have shown interesting properties for use in the development of probes and MRI contrast agents, which will be discussed in Section 1.3.1. Recently, luminescent lanthanide (III) complexes, such as **31**, have also been incorporated into nanosized materials through doping of nanoparticles, Figure 1.32.[109]

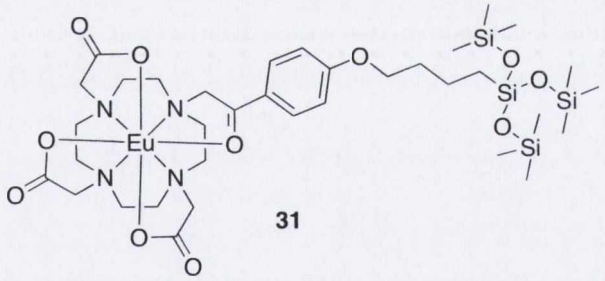

31

***Figure 1.32**: Lanthanide complexes doping the surface of silicon oxide nanoparticles for novel photophysical materials*

There is also a recent example in the literature of a europium complex, grafted onto the surface of organic dye-doped silica nanoparticles, which can detect the presence of anthrax, Figure 1.33.[110] In this case, the anthrax spores can be detected through the biomarker calcium dipicolinate with a sensitivity of 0.2 nM, showing the benefit of grafting these complexes to a surface. However, to the best of our knowledge, there are very few reports of lanthanide complexes grafted onto the surface of **AuNPs**.

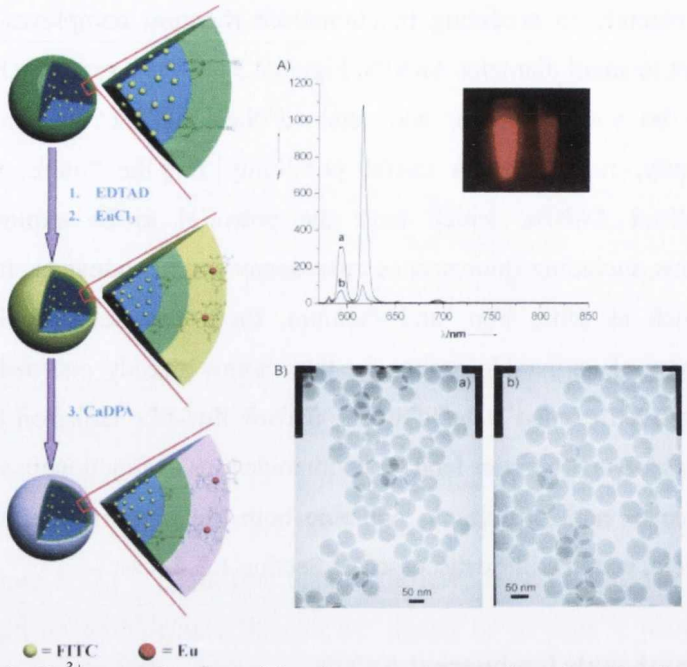

***Figure 1.33**: Eu^{3+} complex-based luminescent sensor functionalised on silica based nanoparticles for the detection of anthrax, A) Emission spectrum of Eu^{3+} complex showing distinctive red emission B) TEM images of silica based nanoparticles*[110]

One of the first examples of lanthanide luminescent **AuNPs** was demonstrated by Thomas *et al.*[111] which involved the development of a series of lanthanide complex functionalised **AuNPs** such as **32**, functioning as phosphorescent probes, possessing thiol derivatised bipyridines and dodecanethiols, Figure 1.34. This was used to prepare mixed monolayer functionalised **AuNPs**, with a diameter of c.a. 4 nm.

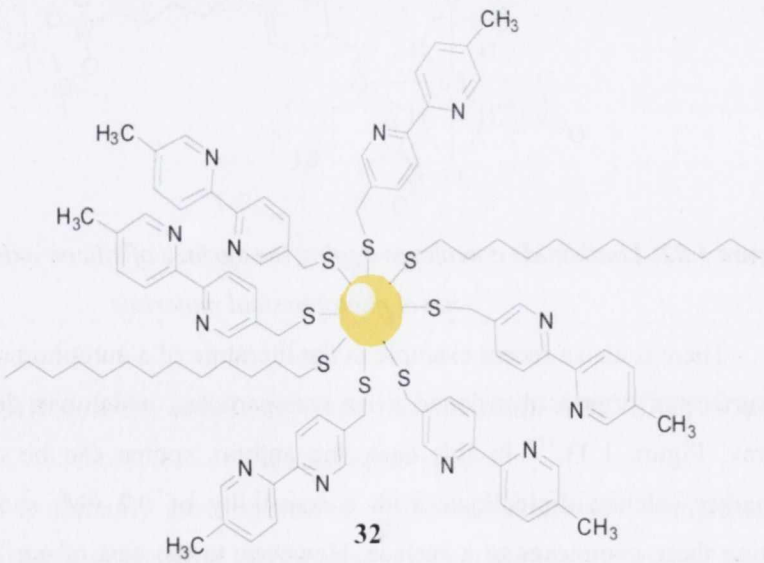

***Figure 1.34:** Bipyridine capped gold nanoparticles for the complexation of Eu^{3+} and Tb^{3+}*

One significant feature of these nanohybrid systems, such as **32**, was its high absorption coefficients due to the presence of approximately 340 molecules of coordinating bipyridine ligand per **AuNPs**. In fact, a 1:3 complexation stoichiometry was observed between the bypyridine ligand and the metal ion. The self-assembled structure observed in the TEM images for these systems, suggested that the lanthanides were possibly coordinating with the bipyridine groups on other nanoparticles causing bridging units between the nanoparticle systems. The displacement of the lanthanides for other cations was then used for the detection of metals, such as Cu^{2+} or Ca^{2+}. The binding of which "switched off" the lanthanide luminescence, thus forming highly efficient, diverse, cation sensors with a switch reliant on the luminescence of the europium and terbium. In fact, the formation of controlled aggregates showed that upon the addition of Cu^{2+} the system underwent aggregation, through the formation of a complex between two separate nanoparticles, resulting in the formation of cluster type aggregates. It is possible that such phosphorescent nanohybrid systems might have a wide range of applications in optoelectronic devices and supramolecular systems.[69a]

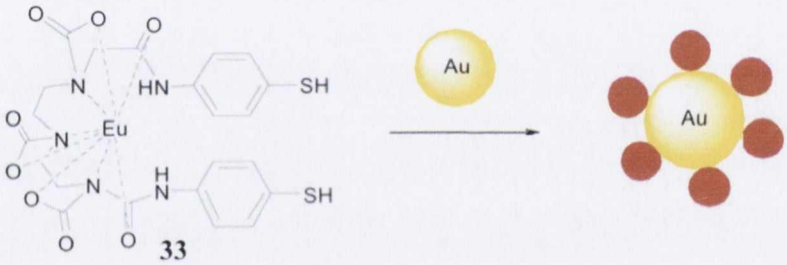

Figure 1.35: *Luminescent* ***AuNPs*** *functionalised with* ***33***

Another example of a lanthanide complex functionalised onto a **AuNPs** was reported by Lewis *et al.*,[112] whereby **AuNPs** were used as a scaffold in order to assemble multiple tailor-made europium complexes, **33**, Figure 1.35, yielding water soluble **AuNPs**. These displayed intense red Eu (III) luminescence upon excitation of the phenyl chromophores. The ligands chosen for the complexation of the lanthanides was diethylene triamine pentaacetic acid (DTPA), previously shown to form stable complexes with lanthanides. The ligand was then functionalised with two thiol moieties to ensure a rigid structural framework attached to the nanoparticle, *via* synthesis that involved the use of citrate as a reductant. This yielded water-soluble thiol capped gold colloids of 10 - 15 nm, which were shown to be luminescent, with a smaller than expected quenching of the luminescence of the lanthanide, due to the proximity of the lanthanide to the gold surface. Titration of the complex, **33**, into a solution of the **AuNPs** caused a bathochromic shift of

the SPR band, followed by an increase of the SPR band, showing the successful functionalisation of the particles by the europium complexes.

It is known that the quenching effect is lessened with the dense packing of the luminescent complexes onto the surface of the nanoparticle. However, it has been shown that the use of long chain thiols to maximise the distance from the gold surface, while still staying within the nanoparticle sphere, reduces this quenching effect.[70] For this reason, lanthanide complexes functionalised with thiols and a chain of 12 carbons length have been incorporated onto gold surfaces. Examples include that of Murray *et al.*[113] who demonstrated the ability to attach the lanthanide complexes, **34.Eu**, to flat gold surfaces and to 'switch on' the luminescence, by the formation of a ternary complex, through self-assembly between the complex and an antenna, **35**, Figure 1.36.

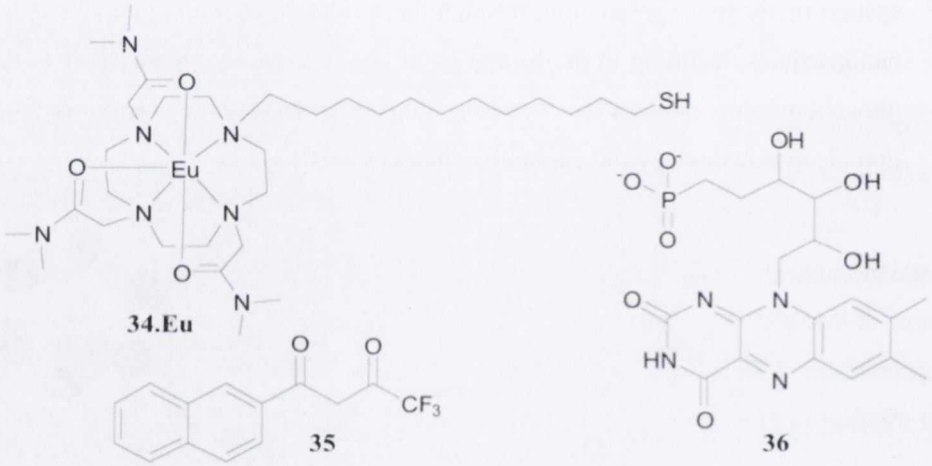

Figure 1.36: *Complex **34.Eu** which can form luminescent complexes with antenna, **35**, and can allow the sensing of phosphates, such as **36** by quenching of the luminescence*

The emission of the nanoparticulate system could then be 'switched off' by adding an antenna, such as **36**, that possessed an excited state energy that is too high to allow the energy transfer to the lanthanide (as stated in section 1.2.2, the antenna must be of sufficient energy to excite the lanthanide). The surfaces formed by evaporating a layer of gold onto mica disks, were also analysed by Atomic Force Microscopy (AFM), the ultimate goal of which was to create possible dual functioning sensory systems (using both AFM and luminescence). The surface of the gold was imaged as being islands of gold with grain sizes of 100 nm, which changed significantly on the functionalisation by the complex. This has demonstrated that monothiol conjugated cyclen complexes, possessing a coordinatively unsaturated Eu(III) centre, can be used to develop a luminescent lanthanide based self assembled monolayer on a gold surface.

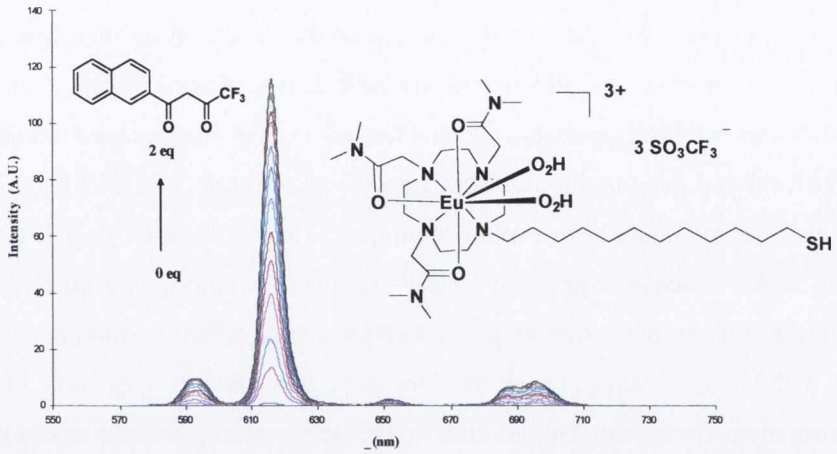

Figure 1.37: *Luminescent* ***34.Eu-AuNPs*** *(1 x 10^{-5} M) "switched on" upon addition of 4,4,4-trifluoro-1-(2-naphthyl)-1,3-butadione* ***(nta)*** *in HEPES buffer*

With the same system, Massue *et al.*[114] reported the heptadentate macrocyclic Eu(III) cyclen conjugate possessing an alkyl thiol, **34.Eu**, shown in Figure 1.37, which enabled the adsorption of the complex onto the surface of **AuNPs** for the formation of small water soluble **AuNPs**. The development of such lanthanide luminescent **AuNPs** was carried out with the aim of developing sensors for biologically relevant molecules, such as phosphate anions. The formation of ternary complexes, or a self-assembly, between the complex, **Eu.34**, on the **AuNPs** and an external β-diketonate antenna, **nta**, **35**, at pH 7.4, resulted in a dramatic enhancement in the luminescence or a 'switching on' of the signal, depicted schematically in Figure 1.38. These complexes served as efficient detectors for adenosine monophosphate (AMP), adenosine diphosphate (ADP), adenosine triphosphate (ATP), which in displacement assays, showed the removal of the antenna leading to the quenching of the lanthanide luminescence.

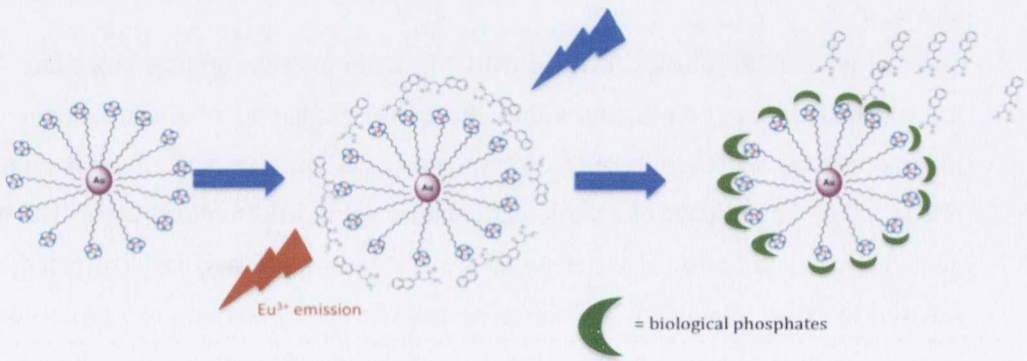

Figure 1.38: *Schematic representation of lanthanide luminescent Eu-**AuNPs**, functioning as sensors for ADP, ATP and AMP*

The behaviour of the aforementioned system was also investigated as a function of pH in aqueous solution, whereby the pH behaviour was analysed by monitoring changes in the absorption spectrum of **34.Eu** and the SPR band, as well as the fluorescence and the lanthanide emission spectrum. The changes in the fluorescence emission were quite significant and exhibited a blue shift in alkaline solution. The SPR band also experienced slight hyperchromism at low pH, which upon a further increase in pH, was shown to blue shift, which could be attributed to aggregation in solution. The Eu(III) emission arising from the self assembly formation on **AuNPs** was significantly modulated as a function of pH, with biggest changes observed in the $J = 2$ band, which is sensitive to the coordination environment of the lanthanide, and so shows the binding of the antenna directly to the inner coordination environment of the metal.[115] These results demonstrated the pH driven self-assembly of the ternary complex between the complex **Eu.28** and antenna, **29**, which results in a luminescent emission.

Lanthanide complexes, as seen in section 1.2.4.6, have become increasingly useful in various types of imaging and sensing, due to the increased stability, efficiency and loading on the surface of nanoparticles.[99] This is ideal for the development of imaging agents such as MRI contrast agents as this, in general, requires a concentration of higher than 1.0 mM. For this reason, MRI contrast agent-functionalised **AuNPs** have been developed by a number of research groups. The following section is focused on the development of Gd(III)-based contrast agents for Magnetic Resonance Imaging (MRI) attached to gold surfaces. A full description of relaxivity, contrast agents and their use in multimodal imaging will be discussed in more detail in Chapter 4.

1.3: Development of Magnetic Resonance Imaging contrast agents attached to gold surfaces

Magnetic Resonance Imaging (MRI) is a non-invasive clinical procedure, based on the magnetic fields of protons within the body, producing two dimensional views of internal organs or tissue.[116] MRI depends upon the enhancement of local proton water relaxation in the presence of a particular contrast agent. MRI contrast agents can markedly alter the relaxation rates of water protons in tissues where they are distributed, which is referred to as the relaxivity, r_1. Contrast agents can be divided into two groups depending on whether they cause a change in the T_1 (longitudinal relaxation time, which is the time taken for the protons to realign with the external magnetic field) or T_2 (tranverse relaxation time, which is the time taken for the protons to exchange energy with the other nuclei),

which are known as positive or negative contrast agents, respectively. In general, contrast agents that have an effect on the T_1 tend to be paramagnetic agents such as Gd^{3+} and Mn^{2+}, whereas T_2 agents tend to be superparamagnetic agents, such as iron oxide nanoparticles.[117] The values for the increase in T_1 or T_2 are used to determine the efficiency of a contrast agent and consist of contributions from both inner sphere and outer sphere relaxation mechanisms, and this phenomenon will be discussed further in Chapter 4.

If a contrast agent must be added in order to obtain better resolution, there are a number of important factors, which must be taken into consideration, one of which involves the efficiency of the contrast agent. Due to the low sensitivity of the MRI technique it is necessary to measure the relaxivity at quite high concentrations, which is not ideal for *in vivo* analysis.[118] For this reason, the use of systems such as micelles and aggregates has been a recent focus, due to the lower loading of contrast agent required.[119] A potential method to increase the relaxivity of the sample is to anchor the complexes on a substrate, which is very slow moving or tumbling such as dendrimers, carbohydrates or proteins.

Nanoparticles that act as very efficient contrast agents, with relaxivities of above 20 $mM^{-1}s^{-1}$, have been previously developed based on the T_2, the tranverse relaxation time. In general, this is due to contribution from bulk nanoparticle materials and results in high relaxivity values. Many attempts to develop efficient contrast agents on silica nanoparticles,[120] and iron oxide[121] have shown interesting results. The utilisation of iron oxide nanoparticles resulted in superparamagnetic nanoparticle arrays, which have very high relaxivity, developed by Brougham *et al.*[122] The combined relaxivity of the iron oxide nanoparticles resulted in high relaxivity values, suggesting the iron particles are acting in a cooperative way, *i.e.* as part of a supramolecule, instead of individual particles. Corr *et al.*[123] developed such superparamagnetic nanoparticles based on the iron oxide structure, which gave rise to relaxivities of 22.5 $mM^{-1}s^{-1}$. Glyconanoparticles, based on carbohydrates functionalised on the surface of iron oxide nanoparticles, have also been shown as efficient T_2 relaxation agents for the imaging of neurological tissue.[124]

1.3.1 Gadolinium based contrast agents attached to nanoparticles

Relaxivity using lanthanide ions relies on the ability of the lanthanide ion, in this case Gd^{3+}, to dramatically decrease the relaxation time of the H_2O molecules in solution. Alone, H_2O has a relaxation time of approximately 2.5 seconds, however, with the addition of a contrast agent most typically in the form of Gd^{3+} complexes, the relaxivity of the H_2O

protons undergo very swift relaxation, as shown schematically in Figure 1.39. This allows much higher contrast between diseased and healthy tissues, thus enhancing the MRI signal.

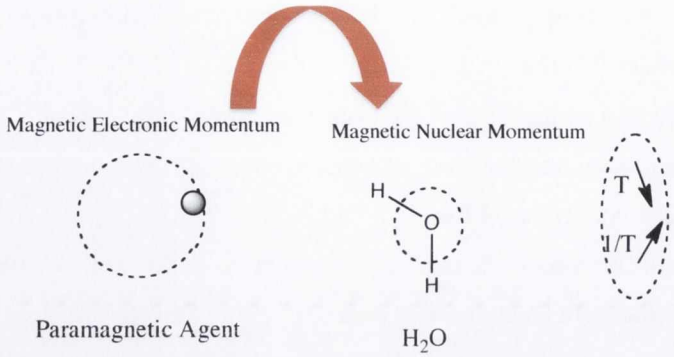

Figure 1.39: *Effect of a paramagnetic ion on H_2O relaxivity*

In order for this to occur, at least one H_2O molecule must be bound in the inner coordination sphere of the Gd^{3+} ion, which will then undergo rapid exchange with the H_2O molecules of the surrounding solution, affecting the relaxation time of the bulk H_2O. In general, the higher the number of H_2O molecules directly bound to the metal centre, the more efficient the relaxivity of the complex. However, this must be balanced with the stability of the complexes themselves, as it is important not to allow release of free gadolinium species into the body, as these are extremely toxic due to exchange with Ca(II) and precipatiation of the Gd^{3+} due to formation of the hydroxide complex. Therefore, the most efficient contrast agents are those, which have at least one or two metal bound H_2O molecules and consequently the choice of ligand in these systems is important. Clinically used analogues of Gd^{3+} complexes, such as Gadomelitol, in addition to other Gd^{3+} based contrast agents, accounts for 30% of all MRI imaging carried out to date.[117] This Gd DOTA based system with large hydrophilic groups has been shown to have a relaxivity of 39 $mM^{-1}s^{-1}$.

The development of lipid-, micelle- or nanoparticle-based contrast agents have the potential to give very high relaxivity values, due to the high concentration of the contrast agent required. This has been recently reported by Mulder *et al.*[125] wherein they emphasised the important impact liposomal nanoparticles, micelles and nanocrystals have on increasing the sensitivity and efficiency of MRI contrast agents. In particular, compounds which allow micelle formation seem to give rise to extremely high relaxivity values.[126]

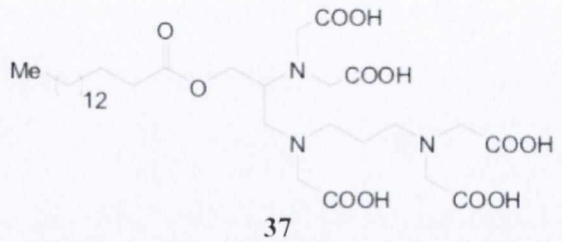

37

Figure 1.40: *An example of an amphiphilic Gd^{3+} chelate* ***37***

An alternative way to increase the relaxivity, by decreasing the tumbling rate of the complex, is through self-assembly of amphiphilic Gd^{3+} chelates to form micelles. Toth *et al.*,[127] developed an example of such amphiphilic gadolinium chelate based on (hydroxymethylhexadecanoyl ester) ethylene propylenetriaminepentaacetic acid, the tumbling of which was slowed through attachment of **37** to a 16-carbon lipophilic arm, which was reported and compared to the activity of previous micelles formed, Figure 1.40. Furthermore, Meade *et al.*,[128] formed Gd^{3+}-based multimeric contrast agents, which can be grafted onto a cyclodextrin surface using click chemistry, in order to increase the possible relaxivity.

The formation of larger assemblies or micelles, have been shown to dramatically increase the activity of MRI contrast agents, with up to 100 fold enhancement of the relaxivity. However, there are an increasing number of reports on the incorporation of T_1 contrast agents onto the surface of nanoparticles, and on solid supports in order to form more efficient systems.[129] Much effort has been devoted to the development of such particles, which are biocompatible, water soluble and easily removed from the body. Attachment of these systems onto nanoparticles ensured a high concentration of contrast agent per nanoparticle. This ensured high activity at a lower loading such as that observed for the Gd complex functionalised nanoparticles by Debouttiere *et al.*,[130] where values of 585 $mM^{-1}s^{-1}$ were observed per particle compared to 3.0 $mM^{-1}s^{-1}$ for the complex alone.

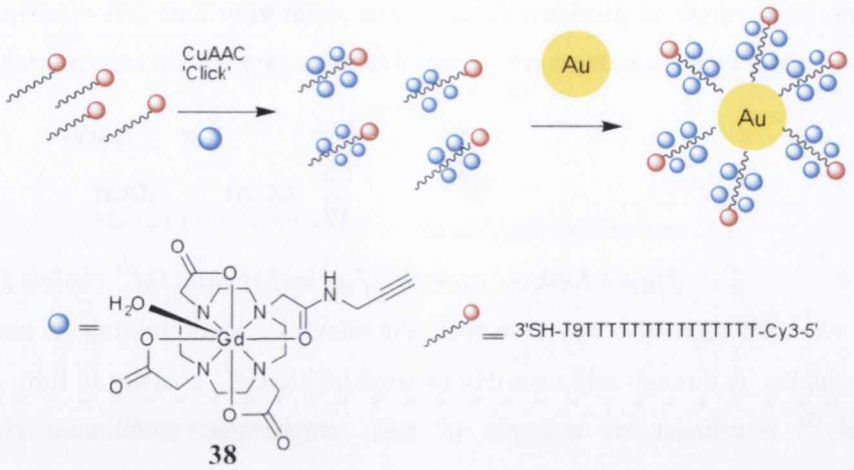

Figure 1.41: *Synthesis of click chemistry based Gd hybrids*

Recently, multimodal Gd^{3+} enriched DNA hybrids, such as those seen in Figure 1.41, have been synthesised, in order to obtain enhanced contrast with facile cell uptake and long term retention.[131] In particular, conjugating **AuNPs** functionalised with DNA hybrids and attaching Gd^{3+} complexes, such as **38**, shown in Figure 1.41, showed a twofold increase in the relaxivity per Gd^{3+} from 3.2 $mM^{-1}s^{-1}$ to 8.7 $mM^{-1}s^{-1}$. In fact, Kim *et al.*[132] developed a DTPA glutathione conjugate attached to a **AuNP** surface, which demonstrated relaxivity values of 1.87 x 10^{-5} $mM^{-1}s^{-1}$ and 3.02 x 10^{-5} $mM^{-1}s^{-1}$ for the longitudinal and tranverse relaxivities r_1 and r_2, respectively. Importantly, the functionalised nanoparticles were found to be stable and non toxic in *in vitro* tests.

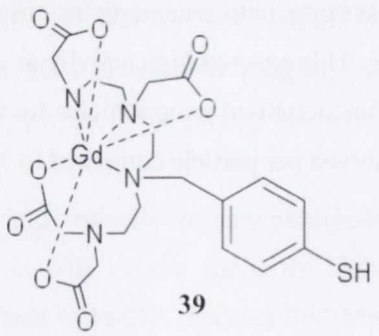

Figure 1.42: *Complex **39** for the functionalisation of **AuNPs***

Most recently, Helm *et. al.*[133] developed lanthanide complexes, **39**, grafted onto the surface of a **AuNP**, which showed very high relaxivity values for the system. The gold core was found not to contribute to the overall magnetic moment. Two different ratios of gold to ligand were used and both systems gave similar relaxivity values. These nanoparticle-based MRI contrast agents were found to yield relaxivities of 60 $mM^{-1}s^{-1}$.

Further to this, Penades *et al.*[134] developed glyconanoparticles, which are effectively multivalent sugar coated gold nanoclusters and were shown to exhibit even higher relaxivity values, Figure 1.43.

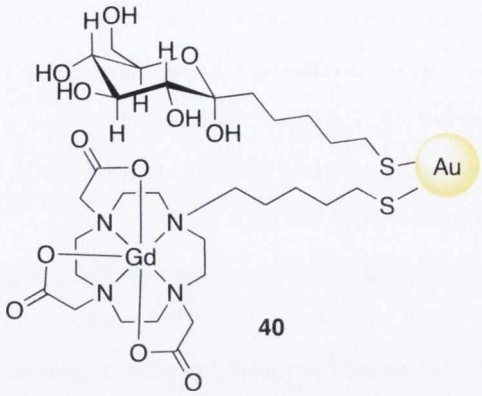

40

Figure 1.43: *Paramagnetic glyconanoparticles based on* ***40*** *as potential MRI contrast agents*

The sugar coating confers water solubility and biological activity on the nanoparticles and have also been shown to be non toxic and thus effective for biological assays. This study proposed combining the glyconanoparticle with Gd-DOTA complexes in which to develop new paramagnetic probes. In general, the incorporation of a suitable glycoconjugate and a Gd^{3+} chelate, has been shown to enhance the relaxivity properties of the Gd^{3+} chelate. In this study, the paramagnetic nanoparticles were prepared using different ratios of thiol-sugar (glucose galactose, lactose) conjugates and tetraazacyclododecane triacetic acid. The results indicate that grafting a complex onto a nanocluster is not enough to cause a dramatic difference in the relaxivity, however, the incorporation of different sugars led to changes in the relaxivity values. The most efficient system was found to contain galactose, which yielded relaxivities over 20 $mM^{-1}s^{-1}$; which is an enhancement of over 6 times that shown by commercial contrast agents. As a result, the addition of these systems to nanoparticles greatly increases the capacity of the system to act as an MRI contrast agent.

1.4 Conclusion:

This chapter has given a brief introduction to the properties of lanthanides, particularly their luminescent properties for development of probes and imaging agents. Such topics have been previously discussed in the theses of Dr. Doireann Moore, Dr. Andrew Harte and Dr. Niamh Murray, consequently, to aid the reader it was deemed necessary to give a brief discussion on the properties of lanthanide chemistry and give only

a few examples of current work. The characteristic properties of the lanthanides were described followed by the brief discussion on the development of lanthanide chemistry, particularly the formation of dinuclear complexes based on lanthanides. The formation of heterometallic dinuclear complexes *via* click chemistry and selective functionalisation of cyclen has also been discussed. Dinuclear complexes can also be formed *via* supramolecular assembly, for this reason the formation of dinuclear complexes with triple stranded helicates was reported, with the use of these helicates in applications such as imaging and sensing.

The next section contained a review of **AuNPs**, including the synthesis of **AuNPs** *via* citric acid stabilization and the Brust-Schiffrin method, their stabilisation and subsequent functionalisation by molecules such as thiols *via* covalent bonding, or electrostatic interactions with salts such as citric acid. The characteristic properties of these nanoparticles with different functional groups attached were fully discussed. However, the main focus of this discussion on **AuNPs** has been towards the incorporation of metal complexes, particularly lanthanides, onto the surface of the gold. Metal complexes with transition metals such as rhenium, iron and zinc are particularly useful for applications such as RNA hydrolysis, sensing and imaging. The focus of this thesis is on lanthanide complexes attached to **AuNPs,** and so the functionalisation of the gold surface and the resulting properties of the **AuNP-Ln** hybrids were discussed. Particularly, it is the formation of the Eu^{3+} luminescent **AuNPs** that was of interest, with examples of a complex, which can function as a sensitive sensor for substrates, such as biological phosphates ADP *etc*. both on **AuNPs** and gold flat surfaces.

The final topic of this introduction was the formation of Gd^{3+} complex-functionalised **AuNPs** as potential MRI contrast agents. There are a number of examples in the literature of Gd^{3+}-functionalised **AuNPs**, which have demonstrated high relaxivity. These complexes have been shown to increase the sensitivity of MRI contrast agents due to higher loading and proximity of a large number of metal ions.

Section 1.4.1: Work Described within this thesis

Building on work already carried out within the Gunnlaugsson group; the aim of the first part of this thesis, which will be discussed in Chapter 2, is to investigate the formation of two types of dinuclear lanthanide complexes the overall design of which is shown schematically in Figure 1.44. The two types of linkers to be discussed are one based on the use of click chemistry for the facile formation of heterometallic species. The second

design is based on the formation of Tröger's Base-based dinuclear complex using both the rigidity and potential chirality of the Tröger's Base bridge.

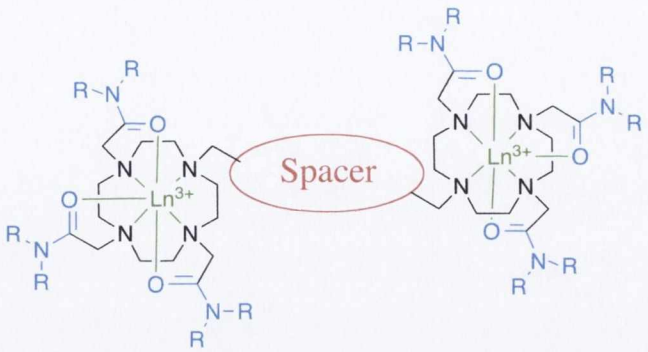

***Figure 1.44**: Dinuclear complexes with varied spacer groups*

The second topic, which spans Chapters 3 and 4, will discuss the incorporation of lanthanide complexes onto **AuNPs** for two different applications, the first being the incorporation of chiral lanthanide complexes, such as **41.Eu and 42.Eu**, onto the surface of **AuNPs** and evaluation of the sensing ability of these complexes for binding of carboxylates, such as 4,4,4-trifluoro-1,3-butadione leaning towards the sensing of chiral substrates. These chiral lanthanide luminescent **AuNPs** have been analysed using Transmission Electron Microscopy (TEM), Dynamic Light scattering (DLS), Circularly Polarised Luminescence (CPL) and Circular Dichroism (CD) studies as well as luminescent titrations with anions.

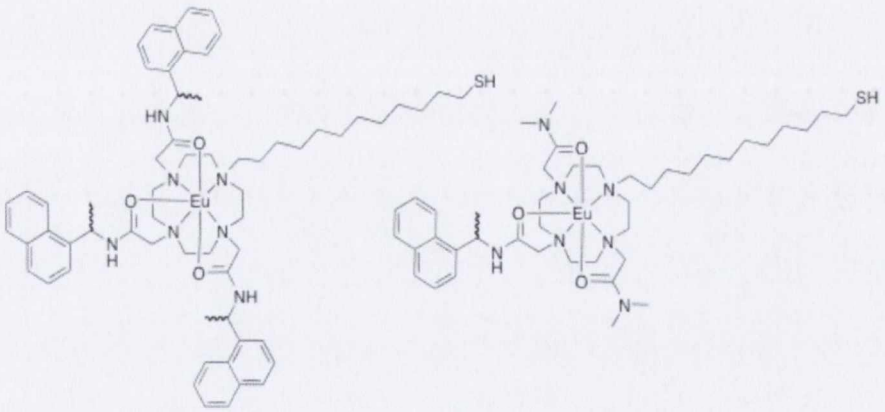

41R.Eu
41S.Eu

42R.Eu
42S.Eu

Figure 1.45: Structure of complexes **41.Eu** and **42.Eu** for the functionalisation of chiral luminescent **AuNPs**

The second application involves the incorporation of a mononuclear Gd^{3+} complex, **43**, onto the surface of the gold *via* a long chain thiol, utilising the higher loading of Gd^{3+} per nanoparticle to increase the sensitivity of the imaging agent, in order to

demonstrate the potential use as MRI contrast agents and were analysed using a wide variety of techniques such as DLS, TEM, NMRD, NMR and UV-vis spectroscopy.

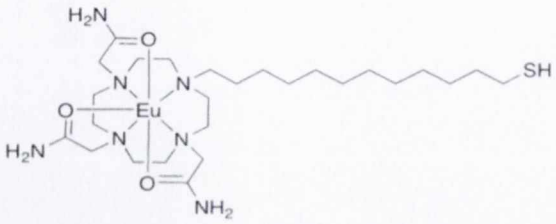

43

Chapter 2

Cyclen-based Dinuclear Lanthanide Complexes

Chapter 2 Cyclen Based Dinuclear Lanthanide Complexes

2.1 Introduction

Lanthanide cyclen based chemistry is a diverse field of research, which is employed in various applications such as in luminescent sensing, imaging, RNA hydrolysis, and MRI contrast agents within the last few decades.[135] It relies on advantageous physical properties, in particular photophysical properties, such as the long lived emission, line-like emission bands while the lanthanide ions also exhibit fast relaxation times.[136] Lanthanide chemistry has been utilised most widely as mononuclear complexes for various applications in recent years. However, polymetallic macrocyclic analogues have been unexploited, possibly due to the challenges of the design and complicated synthesis of polymetallic analogues with specific properties with only a few examples of complex polymetallic lanthanide based systems.[137]

The use of dinuclear complexes, particularly in RNA hydrolysis and in luminescent probes is due to the enhanced response from polymetallic species (multiple metals within the one unit), possible cooperativity between two metal centres and potential formation of heterometallic species.[138]

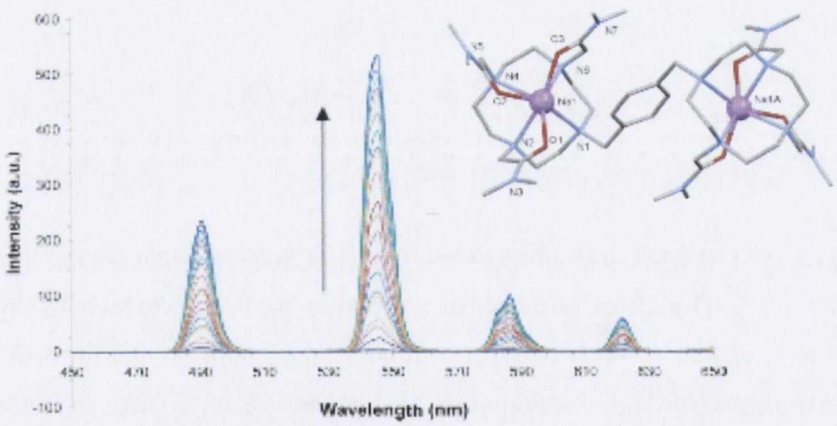

***Figure 2.1**: The dinuclear Tb^{3+} complex exhibiting "switching on" of the Tb^{3+} luminescence upon addition of terephthalic acid, binding between the two metal ions and displacing the metal bound water molecules*

In the Gunnlaugsson research group, the synthesis of cyclen based dinuclear lanthanide complexes has been shown to be useful in the development of novel sensors in Figure 2.1.[139] The presence of two metal centres presented the possibility of different binding modes, such as that shown by Harte *et al.*,[140] in Figure 2.1, who demonstrated the successful binding and hence, the luminescent sensing of terephthalic acid by the dinuclear

complex, which involved binding of both carboxylates of the terephthalic acid by the dinuclear complex at physiological pH.

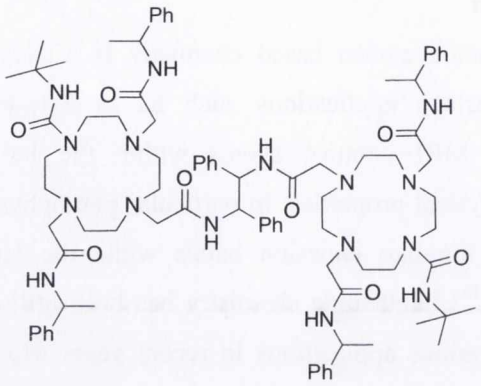

44

Figure 2.2: *Ligand **44** synthesised for the formation of dinuclear complexes*

Murray *et al.*[141] also recently developed chiral dinuclear complexes, which formed different steroisomers due to the orientation in solution of the phenyl rings in the bridge of the complex, Figure 2.2. These complexes based on **44**, upon the addition of anions were found to demonstrate a CPL response for achiral carboxylates such as HCO_3^- showing the chiral sensing of these substrates.

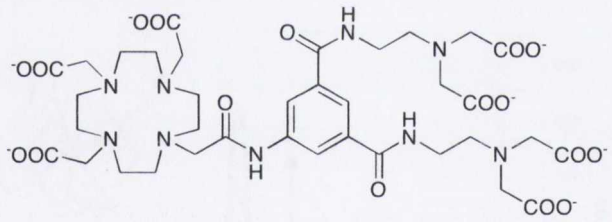

45

Figure 2.3: *Bifunctional ligand for both MRI and luminescent probes*

The design of dinuclear complexes has been demonstrated by Angolevski *et al.*, who prepared **45**, with two different chelating groups for the formation of heterometallic complexes.[142] The development of ligands, such as **45**, as shown in Figure 2.3, demonstrates the potential formation of heterometallic complexes with dual functionality. These molecules can undergo complexation of the Gd^{3+} ion *via* the cyclen macrocycle, however, the complex can also undergo complexation of Eu^{3+} or Yb^{3+} *via* the carboxylates on the opposite terminus of the molecule. This can allow the molecule to function as both an MRI contrast agent *via* the Gd^{3+} and also as a luminescent probe *via* the chelated Eu^{3+} centre.[142]

The traditional synthetic methods associated with the formation of more complicated cyclen based analogues are both difficult, expensive and time consuming,

therefore in this Chapter we will focus on the development of novel synthetic approaches for the formation of dinuclear lanthanide complexes and their design, synthesis and characterisation will be discussed in the following sections.

2.2 Design of Dinuclear complexes

The synthesis and analysis of dinuclear lanthanide complexes will be investigated based on different bridges to link the two structural units. These linkers have been chosen to incorporate moieties with useful characteristics, which will contribute to the properties of the complexes themselves, or allow facile reaction conditions and the utilisation of a variety of functional groups as shown in Figure 2.4.

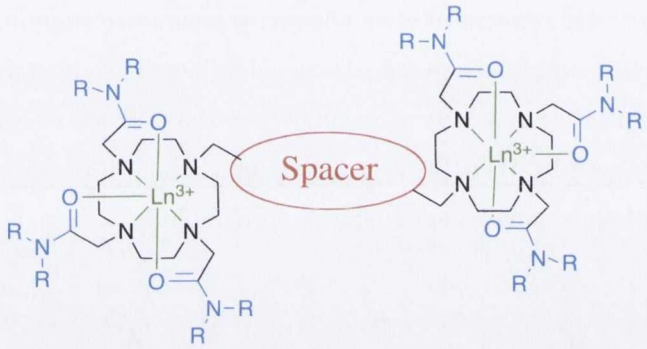

***Figure 2.4**: Design of dinuclear lanthanide complexes*

These dinuclear complexes have incorporated a macrocyclic unit based on cyclen, which has been shown to be an efficient chelator for lanthanide ions.[143] Acetamide arms will be utilised, as they are capable of partially fulfilling the coordination sphere of the lanthanide ion, forming a stable complex. The bridge will be important to the design of these complexes, as if the bridge brings the complexes into too close proximity it could cause self-quenching of the luminescence. Also, as shown by Dr. A. Harte and Dr. D. Moore, the flexibility or rigidity of the bridge can be influential on the properties of the complex.[2a, 20] For these reasons, the incorporation of two different bridges will be investigated in this Chapter, based on two synthetic strategies: **a) Cu(II) catalysed 1,3 dipolar "click" chemistry and b) Tröger's Base formation.**

The initial target for the formation of dinuclear complexes utilised Cu(II) catalysed click chemistry, which is a method developed by Sharpless *et al.*[144] in order to describe certain types of reactions, which will be discussed in detail in the following sections.

2.2.1 Click Chemistry

Click chemistry refers to a series of reactions that obey specific rules, such as being stereospecific, high yielding and involve simple experimental methods.[145] In general, they should also make use of environmentally friendly conditions, either solvent free or aqueous conditions and should avoid complicated isolations. Examples of these click chemistry reactions are 1,3-dipolar cycloadditions, Diels Alder additions and opening of strained ring systems, such as epoxides.[146] The development of this reaction has been particularly successful with the 1,3-Huisgen reaction, which is a 1,3-dipolar cycloaddition between an alkyne and an azide. This click reaction can be promoted by the presence of a copper catalyst and generates a 1,3 triazole moiety during the process of the reaction.[144]

The establishment of click chemistry as an interesting means of clicking two units together with simple chemistry, discussed in detail by Sharpless *et al.*[144, 146] has been manipulated in the synthesis of macrocycles, sensors, and polymers.[144, 147] Chow *et al.*[148] have considered the benefits of utilising the click chemistry motif in the development of oligotriazoles and polytriazoles, shown in Figure 2.5.

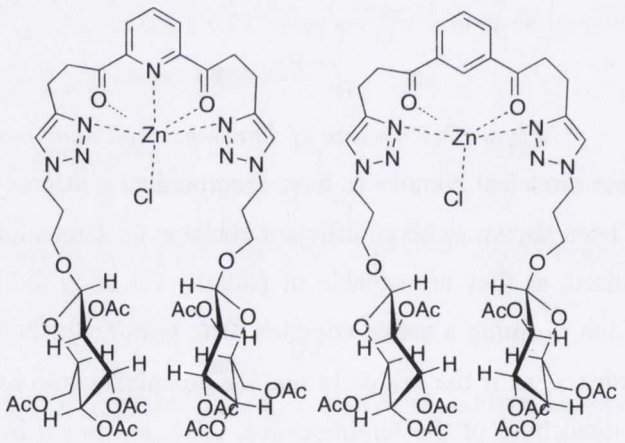

46 **47**

Figure 2.5**: Zinc complexes of triazole based ligands, **46** and **47

The triazole itself can be shown to have interactions with the surrounding molecules, through the H-bond donor-acceptor nature of the triazole ring, which in this case is shown coordinating the zinc metal in the formation of zinc complexes, **46** and **47**, shown in Figure 2.5. Larger polymeric structures have shown that the triazole does not have the same influence in long polymeric chains as the triazole itself would be too small to observe significant interactions.[148]

Recently, the development of lanthanide based click analogues has become prominent with Hulme *et al.*[149] attempting the addition of a chromophore to sensitise the

lanthanide emission *via* quick and simple reactions instead of complicated isolation and purification. This reaction was also chosen by Lowe and Faulkner *et al.*[138] as the means to generate dinuclear complexes with flexible triazole-based linkers, as discussed in Chapter 1.

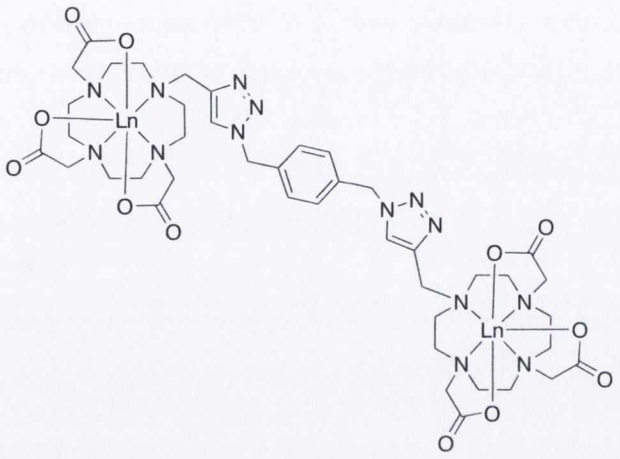

48.Ln

***Figure 2.6**: Dinuclear cyclen based lanthanide complex, **48.Ln**, synthesised via click chemistry*

The formation of a 1,3-triazole unit between an azide and an alkyne in Figure 2.6, yielded the dinuclear complex, **48.Ln**, demonstrating the ability to 'click' mononuclear complexes together in order to form a dinuclear complex selectively. The click reaction provides a facile method for the incorporation of a chromophore into lanthanide complexes and enables the potential formation of heteronuclear complexes, which can confer dual functionality to the complexes, such as demonstrated by Jauregui *et al.*[138b]

For these reasons, click chemistry was chosen as a novel means to develop dinuclear complexes, both with and without appended choromphores, with the potential for the development of novel luminescent probes. The design, synthesis and characterisation of these systems will be discussed in sections 2.3.1, 2.3.2, 2.3.3.

2.3 Synthesis and Characterisation of Click Chemistry precursors

The synthesis of the precursors followed the design specified for the formation of dinuclear complexes in Figure 2.4, Section 2.2. This involved the incorporation of two macrocyclic units linked by a bridging unit, in this case a triazole-based bridge. With the aim of forming dinuclear lanthanide complexes *via* click chemistry, the precursors **51** and **52** were targeted. The click reaction requires both an alkyne moiety and an azide. Our design consisted of the mono-alkylation of cyclen with the alkyne arm.

2.3.1 Synthesis and Characterisation of 51 and 52

The first ligand targeted was a simple cyclen macrocycle with one alkyne and three acetamide arms in order to form a stable Ln^{3+} complex. This complex could then be reacted *via* click chemistry with a suitable azide, possibly attached to another cyclen lanthanide complex, allowing the formation of mixed metal complexes.

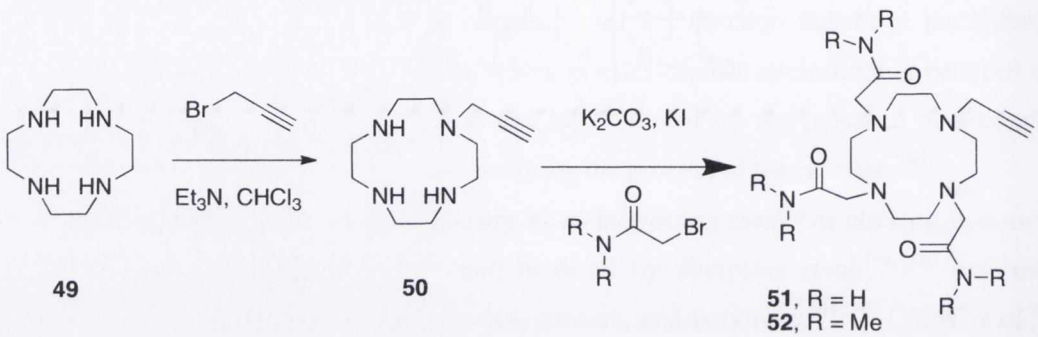

Scheme 2.1**: Synthesis of amide-based ligand **51** and **52

The first step was the synthesis of the alkyne, **50**, which was formed by monoalkylation of the cyclen macrocycle, **49**, with propargyl bromide, using a method developed and widely used in the Gunnlaugsson group, shown in Scheme 2.1.[150] Stirring of four equivalents of cyclen with propargyl bromide in NEt_3 at 65 °C, followed by extraction into $CHCl_3$, and washing with 1 M KOH solution, yielded the monosubstituted **50,** as a yellow oil in 96 % yield, Scheme 2.1.

The successful formation of **50** was observed by ^1H NMR ($CDCl_3$, 400 MHz) analysis, which showed the expected resonances of the monosubstituted product with the resonance of the alkyne CH proton at approx 2.3 ppm as a broad singlet, Figure A.1, Appendix A. The remaining CH_2 protons of the cyclen macrocycle and of the alkyne arm appeared as a broad multiplet from 2.5-3.5 ppm. The successful formation of **50** was also confirmed by HRMS, with the species found with a m/z of 211.1917 for $C_{11}H_{23}N_4$, corresponding to the calculated mass of 211.1223.

This monosubstituted analogue was then functionalised with *N*-bromoacetamide over 7 days, refluxing with 3.3 equivalents of K_2CO_3, filtered through celite to remove the inorganic salts, removal of solvent under reduced pressure, followed by an extraction into $CHCl_3$ yielded **51** as a yellow oil, 55 % yield, Scheme 2.1. HRMS confirmed the presence of the tetrasubstituted product, **51**, with mass obtained 404.2380 for $C_{17}H_{31}N_7O_3Na$, which was further confirmed with ^1H NMR ($CDCl_3$, 400 MHz) analysis, indicating the appearance of the cyclen CH_2 protons at 2.5 ppm, with the NH resonances visible at 5.8 ppm and 8.2 ppm, Figure 2.7.

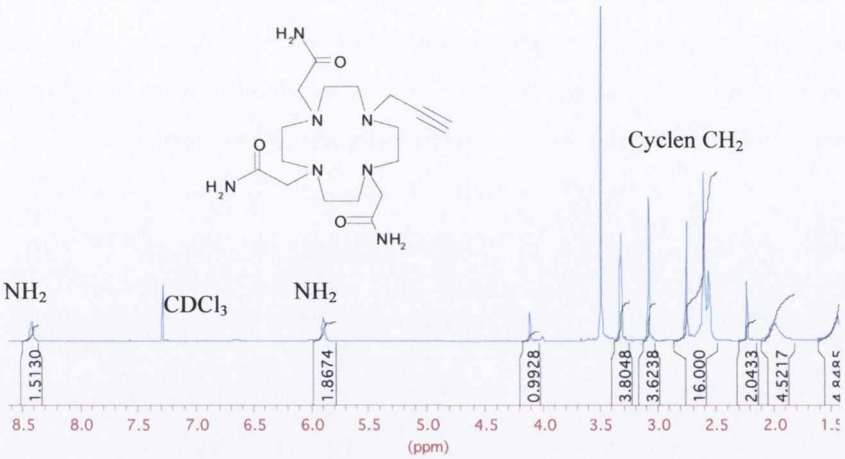

Figure 2.7**: ^1H NMR spectrum ($CDCl_3$, 400 MHz) of **51

There was a possibility that the amide arms could cause potential difficulties with the catalysis due to the tendency for Cu(II) to prefer binding to NH moieties. Potentially, the use of α-chloro-*N,N*-dimethyl acetamide arms, instead of *N*-bromoacetamide, could increase the yield and ease of reaction during later steps. For this reason the synthesis was also carried out with α-chloro-*N,N*-dimethyl acetamide according to Scheme 2.1.

Compound **50** was alkylated with α-chloro-*N,N*-dimethyl acetamide in the presence of K_2CO_3 and KI under reflux over 7 days, followed by filtration through a plug of celite and washing with 1 M KOH solution and H_2O, giving **52**, as a yellow oil, 58**%** yield. The ^1H NMR ($CDCl_3$, 400 MHz) spectrum of the ligand again showed the alkyne proton and cyclen protons as seen before, with the CH_3 and CH_2 of the arms shown among the protons of the macrocycle, Figure A.2, Appendix A. Mass spectrometry showed the formation of the product, **52**, which was observed for $C_{23}H_{44}N_7O_3$ at 466.3484. This synthesis allowed the isolation of simple alkyne functionalised macrocycles, **51** and **52**, however, the next section discusses the formation of chiral ligands possessing a chromophore which could lead to novel chiral click chemistry dinuclear complexes.

2.3.2 Synthesis and Characterisation of 53

The ligands synthesised in the previous section possessed simple acetamide arms for the complexation of the lanthanide within the macrocycle. The main aim of this research was the development of potential luminescent probes, utilising click chemistry to form dinuclear lanthanide complexes, however, these complexes did not possess a chromophore. As discussed in Chapter 1, the lanthanide ions experience low extinction coefficients and f-f forbidden transitions, which means the most efficient way to excite the lanthanide is through indirect excitation of an antenna using the antenna effect. For this

reason, the next ligand was designed to incorporate three naphthyl chromophores, capable of exciting the lanthanide ion *via* energy transfer processes. Additionally, each naphthyl moiety contained a chiral centre, which also would confer chirality on the complexes potentially allowing the metal centered emission to be recorded.

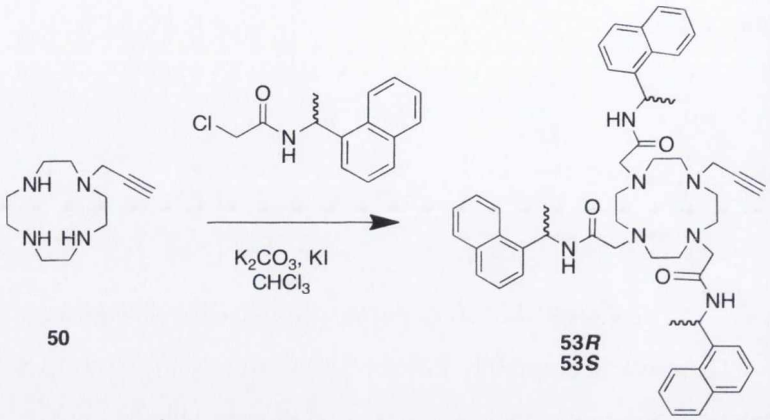

Scheme 2.2**: Synthesis of ligand **53R and 53S

The synthesis of **53** was carried out in a similar manner to that of **51** and **52**, Scheme 2.2, from the monosubstituted cyclen, **50**, which was reacted with 3.3 equivalents of α-chloro-naphthyl acetamide (both *R* and *S* enantiomers) in the presence of K_2CO_3 and KI and refluxed overnight in $CHCl_3$, followed by filtration to remove the inorganic salts. The solvent was removed under reduced pressure and the resulting residue purified using column chromatography with alumina (CH_2Cl_2/MeOH 95:5 as gradient), to yield the desired products, ***53R*** and ***53S*** as brown oils in 37 and 40% yields, respectively.

The ^{1}H NMR spectrum ($CDCl_3$, 400 MHz) of the ligand confirmed the formation of the product, with the naphthyl protons visible at 7-8.5 ppm, with the distinctive CH of the naphthyl arm shown at 6.5 ppm, Figure 2.8. The ^{1}H NMR spectrum ($CDCl_3$, 400 MHz) of the second enantiomer is shown in Figure A.3, Appendix A. Also, the cyclen protons and methyl protons of the chiral centre were observed as broad multiplets from 1.5-3.0 ppm. This acetamide CH and CH_2 protons show a 1:2 ratio of the resonances demonstrating the presence of the required product.

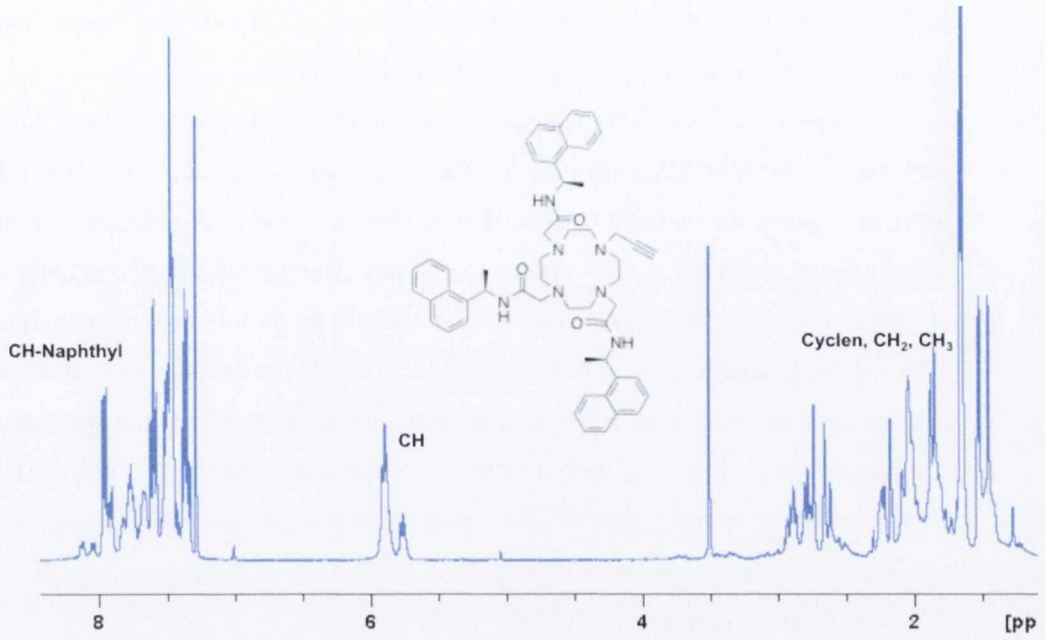

Figure 2.8**: [1]H NMR spectrum ($CDCl_3$, 400 MHz) of ligand **53

The ^{13}C NMR ($CDCl_3$, 100 MHz) resonances also show this 1:2 ratio of the carbonyl carbons and the acetamide CH_2 carbon resonances. The successful formation of the product was also confirmed by HRMS, which showed the tetrasubstituted product 844.4911 for $C_{53}H_{62}N_7O_3$ corresponding to the calculated mass being 844.4914.

Next the optical activity of the ligand **53**, was investigated using Circular Dichroism (CD). CD spectroscopy, is a technique, which measures the difference in the absorption of left-handed versus right-handed polarised light.[151]

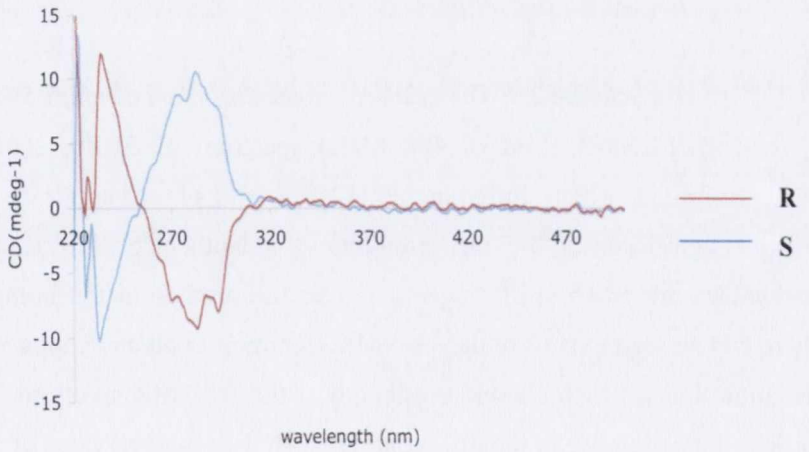

***Figure 2.9**: CD spectrum of **53R and 53S** in MeOH*

The CD spectra were first recorded for ligand **53*R*** and **53*S*** in MeOH and are shown in Figure 2.9. The band of the $S_0 \rightarrow \pi\pi^*$ transition of **53*R*** and **53*S*** was observed to

respond to polarised light with the same magnitude, which indicates that the enantiomers were isolated without changes to the chiral centres.

Having synthesised the ligands **51**, **52** and **53** and characterised them fully, the next step was to prepare these ligands for the 1,3-Huisgen cycloaddition. The 1,3-Huisgen reaction requires the use of a Cu(II) catalyst. However, the click reaction with the ligands alone caused problems as the catalyst Cu(II) has strong association constants for cyclen and so it proved necessary to prevent the macrocycle from binding to the Cu(II) catalyst.[138] This will be further discussed in Section 2.4.1. To achieve this, the ligands **51**, **52** and **53** were complexed with $Ln(CF_3SO_3)_3$. The next section will discuss the formation of each complex with the lanthanide ions in order to prevent complexation by the Cu(II) during the click reaction.

2.3.3 Synthesis of complex 51.Eu and 52.Eu

The complexation of **51** with Eu^{3+} was carried out with 1.1 equivalents of $Eu(CF_3SO_3)_3$, stirring in MeOH at 65 °C overnight, followed by removal of solvent under reduced pressure, dissolved in MeOH (1 mL) and precipitated out of swirling diethyl ether to give the product, **51.Eu**, as a yellow oil, Scheme 2.3.

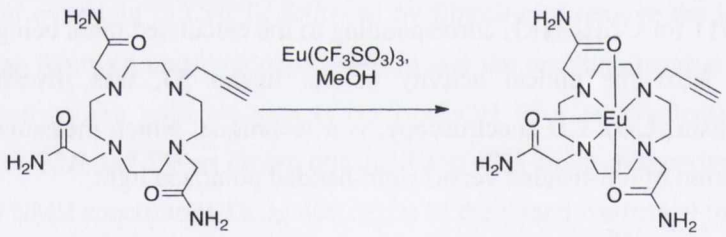

51 **51.Eu**

Scheme 2.3**: The synthesis of the europium complex **51.Eu

The ^1H NMR (MeOD, 400 MHz) spectrum of **51.Eu**, showed the axial and equatorial protons which shifted in the ^1H NMR with a broad spectrum from + 20 ppm to - 20 ppm significant of the incorporation of a lanthanide shift reagent, Appendix A. Lanthanides are NMR shift reagents and so the protons in the immediate coordination sphere can be seen to shift in the ^1H NMR spectrum. Lanthanide ions also give rise to fast relaxation times, which causes broadening of the ^1H NMR spectrum. Mass spectrometry confirmed the presence of the Eu^{3+} complex with the observed value of 551.1472.

The lanthanide complexation of **52** was carried out in an identical manner to that of ligand **51**, using both $Eu(CF_3SO_3)_3$ and $Tb(CF_3SO_3)_3$, which gave rise to **52.Eu** and **52.Tb**, respectively, by refluxing the corresponding salts in MeOH overnight followed by

precipitation from swirling diethyl ether to give yellow oils, in quantitative yields in both cases, Scheme 2.4.

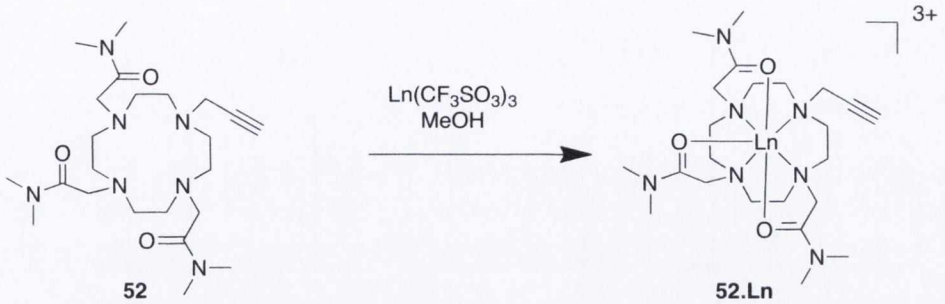

***Scheme 2.4**: The synthesis of the complexes **52.Ln** (Ln = Eu, Tb)*

The ^{1}H NMR spectrum (MeOD, 400 MHz) of **52.Eu**, as shown in Figure 2.14, demonstrates the complexation of ligand **52** and the shifting and broadening of the spectrum due to the presence of the paramagnetic Eu^{3+} metal with resonances from 31 ppm to -25 ppm being observed, Figure 2.10. The presence of conformational isomers due to speed of relaxation on the NMR timescale as a result of the presence of the lanthanide ion causes the number of resonances to be larger than expected for the europium complex.[152] Elemental analysis was attempted for the ligands and complexes but they proved too hygroscopic to allow accurate elemental analysis to be obtained.

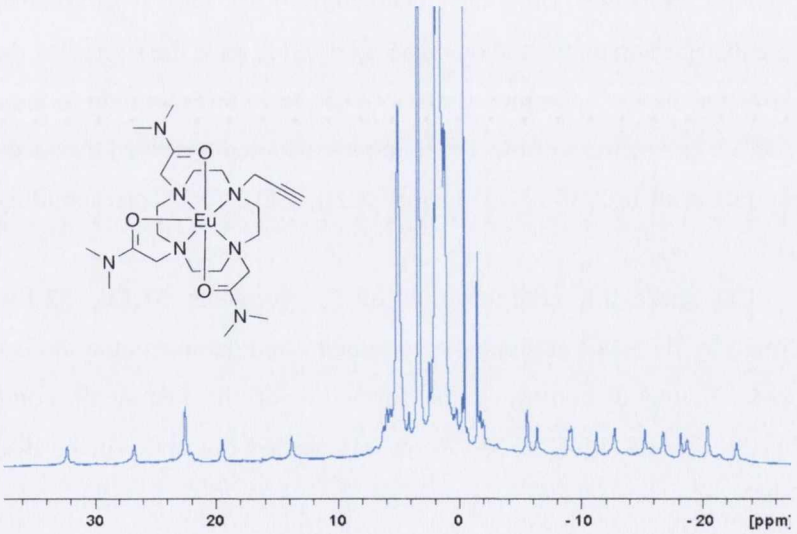

Figure 2.10**: ^{1}H NMR (MeOD, 400 MHz) of complex **52.Eu

The ^{1}H NMR spectrum (MeOD, 400 MHz) of the Tb^{3+} complex was also observed and due to the paramagnetic nature of the Tb^{3+} ion caused much more dramatic shifting of the complex in the ^{1}H NMR.

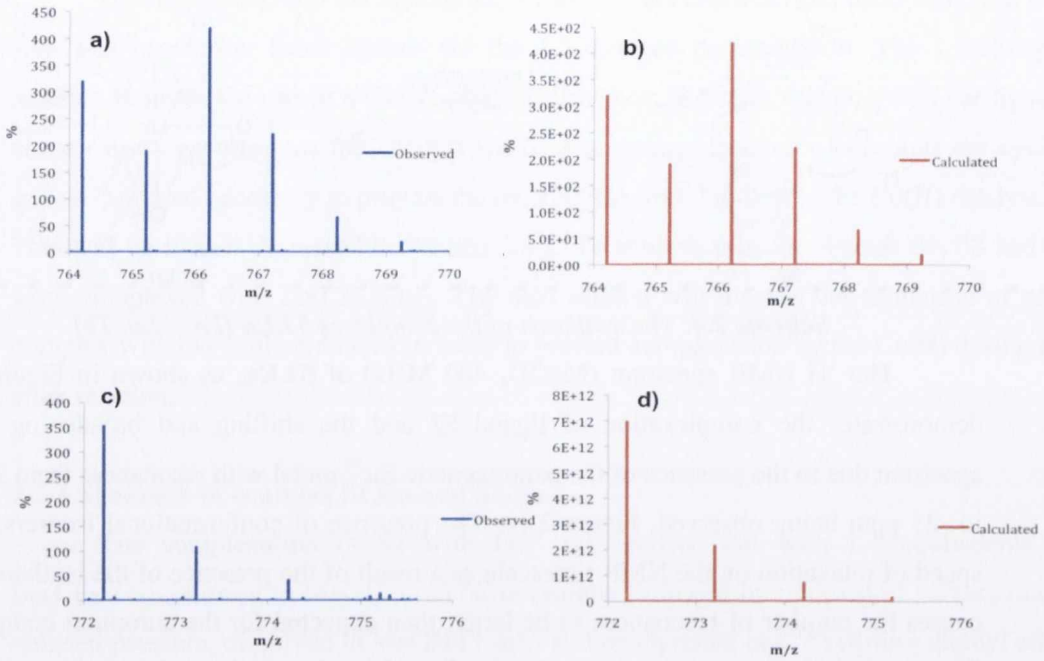

***Figure 2.11**: Isotopic distribution for **52.Eu:** a) Observed and b) Calculated and **52.Tb:** c) Observed and d) Calculated in MeOH in ESI*$^+$

The complexes were also characterised by mass spectrometry and the typical isotopic distribution pattern, shown in Figure 2.11, gave the signal for the expected mass at 766.2103 for the Eu^{3+} complex $C_{24}H_{42}N_7O_6F_3SEu$ corresponding to the calculated mass of 766.2082. The spectrum of the Tb^{3+} complex also demonstrated the successful formation of the product with m/z of 772.2144 for $C_{24}H_{42}N_7O_6STbF_3$ corresponding to the calculated mass of 772.2123.

The successful complexation of the products **51.Eu**, **52.Eu** and **52.Tb** was confirmed by ^{1}H NMR and mass spectrometry and demonstrated the isotopic distributions required. Having demonstrated the formation of the lanthanide complexes **51.Eu** and **52.Eu**, the complexation of **53** (*R*, *S*) was carried out and will be discussed in the next section.

2.3.4 Synthesis and Characterisation of complexes of 53.Eu (*R*, *S*)

The lanthanide complexes of **53*R*.Eu and 53*S*.Eu** were formed using the same synthetic strategy, by refluxing the corresponding ligand with 1.1 equivalents of $Eu(CF_3SO_3)_3$ under argon in CH_3CN for 18 hours. The complexes were then precipitated

from swirling diethyl ether and dried under vacuum to yield brown oils in quantitative yields.

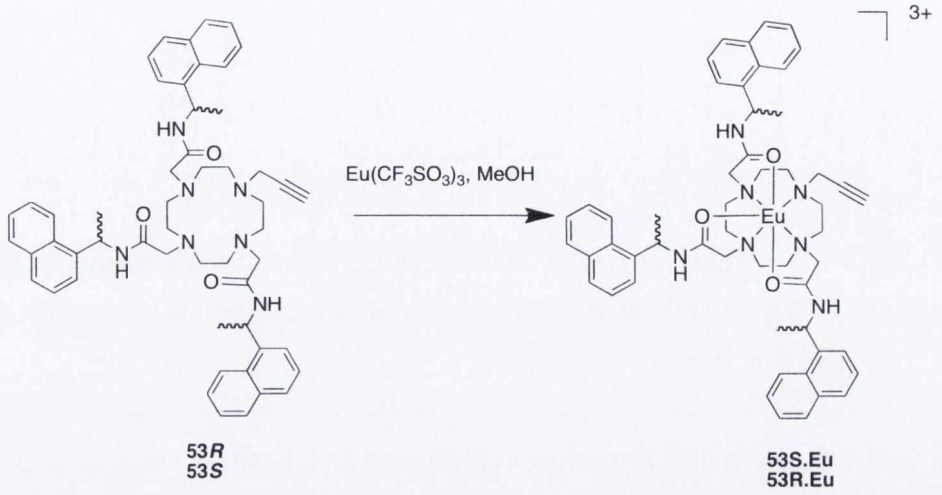

Scheme 2.5**: The synthesis of complex **53.Eu (R, S)

As can be seen in the ^{1}H NMR (MeOD, 400 MHz), the complexation of this ligand was very effective, showing shifting and broadening of the resonances between +25 ppm and – 25 ppm, Figure 2.12. The ^{1}H NMR for the second enantiomer is shown in Figure A.5, Appendix B.

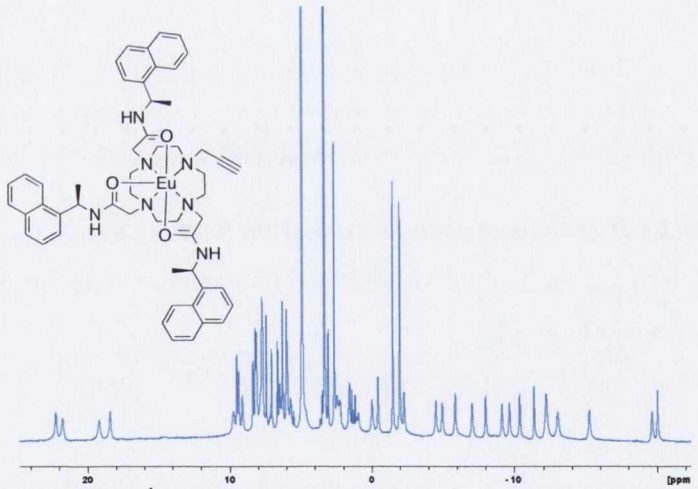

Figure 2.12**: The ^{1}H NMR spectrum (MeOD, 400 MHz) of complex **53R.Eu

The mass spectrometry of the complexes were obtained and demonstrate the peak found m/z 1144.3495 for $[M\text{-}H^{+}+CF_3SO_3^{-}]^{+}$ corresponding to the calculated m/z 1144.3439. The isotopic distribution of the species is shown in Figure 2.13.

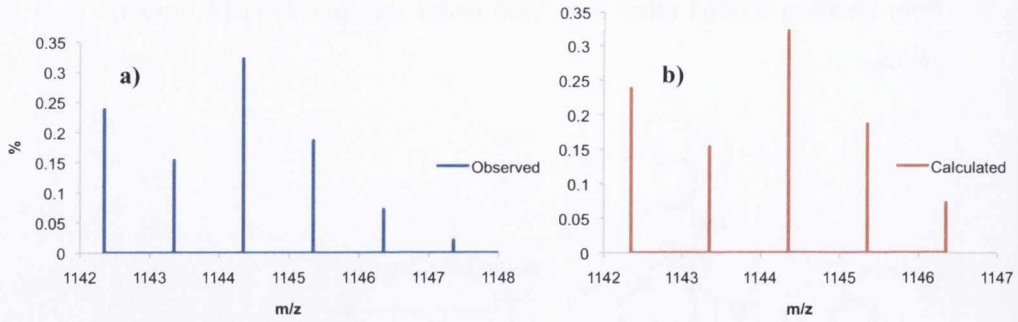

***Figure 2.13**: **a)** MALDI of **53.Eu b)** Calculated spectrum in MeOH*

Having synthesised the aforementioned complexes, the next section discusses their photophysical characterisation.

2.3.5 Photophysical Properties of 51.Eu and 52.Eu and 52.Tb

The photophysical characterisation of **51.Eu, 52.Eu and 52.Tb** was carried out in MeOH. The UV-Vis absorption spectrum of **51.Eu** was recorded at 1 x 10^{-5} M, and demonstrated very weak bands due to presence of the triple bond and the high energy transition of the carboxylates, shown in Figure 2.14.

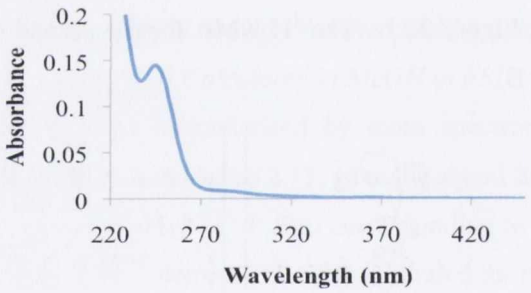

***Figure 2.14**: UV-Vis absorption spectrum for **51.Eu** (c = 1 x 10^{-5}M) in MeOH,*

Excitation into λ_{max} at 250 nm yielded the luminescence emission of the complex **51.Eu,** which is shown in Figure 2.15.

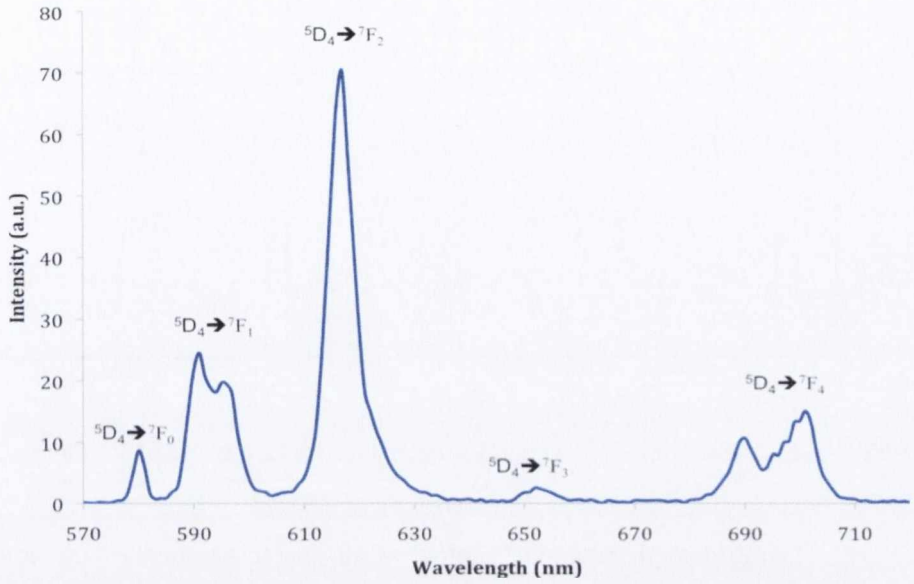

***Figure 2.15**: Eu^{3+} emission spectrum of **51.Eu** ($c = 1 \times 10^{-5}M$) in MeOH, $\lambda_{ex} = 254$ nm*

The complexes, **51.Eu** and **52.Eu** were also analysed photophysically, recording first the UV-Vis absorption spectrum. The UV-Vis spectrum of **52.Eu** and **52.Tb** illustrated in Figure 2.15, similar results to that of **51.Eu** with weak bands observed for the triple bond and the carbonyl moieties.

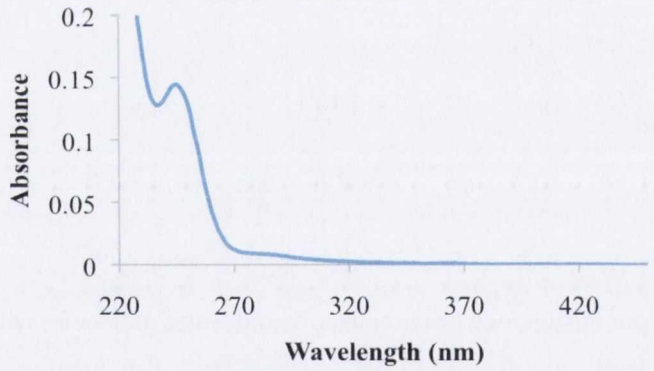

***Figure 2.16**: The UV-Vis absorption spectrum of **52.Eu** and **52.Tb** ($c = 1 \times 10^{-5}M$) in MeOH*

Without a chromophore, only weak sensitisation can occur, however, it was possible to obtain the emission through excitation of the high energy carbonyl band centred at 250 nm and the weak alkyne bands in the UV-Vis absorption spectrum. Excitation into the UV-vis absorption at 250 nm yielded the emission spectrum, which can be seen in Figure 2.16 for both the Eu^{3+} and Tb^{3+} emission.

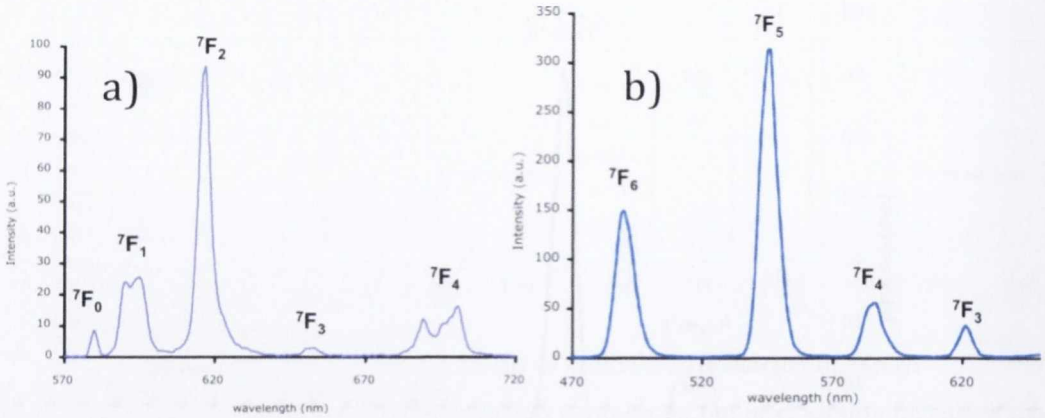

***Figure 2.17**: Eu^{3+} and Tb^{3+} emission spectra for a) **52.Eu** and b) **52.Tb** ($c = 1 \times 10^{-5}$M) in MeOH, λ_{ex} at 250 nm.*

Having demonstrated the photophysical characterisation of the complexes using UV-Vis absorption spectra and luminescence emission, the next step was to determine the luminescent lifetimes and hydration states of the complexes.

2.3.6 Calculation of the hydration state (q) of 51.Eu and 52.Eu

The coordination sphere of the lanthanides can be fulfilled by solvent or water molecules as discussed in Chapter 1 which can cause quenching of the luminescence by vibrational deactivation.

i) $$q^{Eu(III)} = 2.1\ [\ (1/\tau_{H2O} - 1/\tau_{D2O})] \qquad \textbf{Eq. 1}$$

ii) $$q^{Eu(III)} = 1.2\ [(1/\tau_{H2O} - 1/\tau_{D2O}) - 0.25 - 0.075x] \qquad \textbf{Eq. 2}$$

iii) $$q^{TbIII} = 5\ [(1/\tau_{H2O} - 1/\tau_{D2O}) - 0.06] \qquad \textbf{Eq. 3}$$

In our design, one or two metal bound water molecules could coordinate to the Eu^{3+} ion. This can be confirmed by calculation of the q value determined from the lifetimes of the Eu^{3+} and Tb^{3+} emission in solution, using Eq. 1, Eq. 2 or Eq. 3 in MeOH/MeOD and in H_2O/D_2O solutions, respectively.[14a]

***Table 2.1**: Lifetimes and q values of **51.Eu**, **52.Eu** and **52.Tb** in H_2O and D_2O*

Complex	τ_{H2O} (ms)	τ_{D2O} (ms)	q (± 0.5)
51.Eu	0.40	1.5	2.0
52.Eu	0.405	1.47	2.4
52.Tb	1.41	1.91	0.68

The prefix 2.1 is a proportionality constant that mirrors the sensitivity of the europium to quenching by metal bound water molecules. The complex seen above gave q values of 2, which correlates well with similar compounds from the literature.

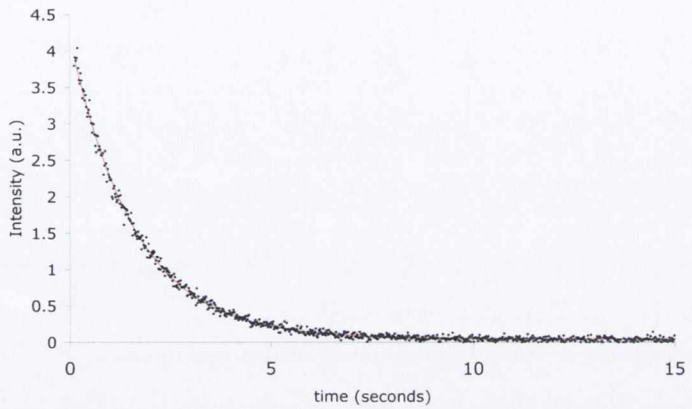

***Figure 2.18**: Plot of luminescent decay of **52.Eu**, fit to a monoexponential decay in H_2O*

The lifetime measurements showed a monoexponential plot, demonstrating the presence of one luminescent species in solution, shown in Figure 2.17. The calculation of the lifetimes of **52.Eu** was carried out in H_2O and D_2O and demonstrated a monoexponential decay with values for the lifetime of 0.405 ms and 1.47 ms for H_2O and D_2O respectively, shown in Figure 2.17. This corresponds to a hydration state or q value of approximately 2, calculated according to the Eq. 1 developed by Parker *et al.* showing that the complexes contained two metal bound water molecules. The lifetimes of the **51.Eu** and **52.Eu** were found to be 0.40 and 0.41 ms respectively, which was expected for complexes such as these with two metal bound water molecules.[140] Having shown the photophysical characterisation of **51** and **52,** the next step was to employ the previous methods to study the complex **53**.

2.3.7: Photophysical Characterisation of 53.Ln

The photophysical characterisation of **53*R*.Eu** and **53*S*.Eu** was carried out in MeOH. The UV-Vis absorption spectrum of **53.Eu *(S, R)*** was recorded at 1 x 10^{-5} M, and displayed a maximum at 281 nm, which was attributed to the S_0 - $\pi\pi^*$ transition of the naphthalene chromophore with the distinctive three fingered absorption, Figure 2.18.

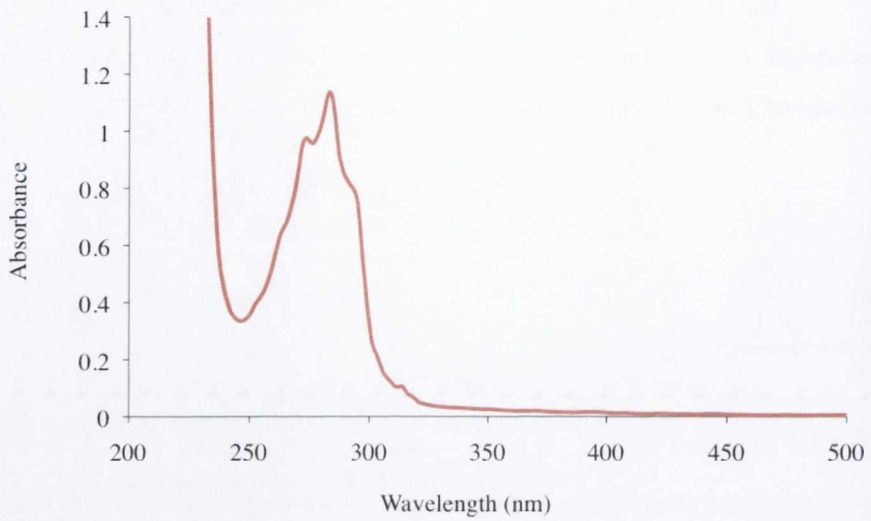

Figure 2.19: *UV-vis absorption spectrum of* ***53S.Eu*** *($c = 1 \times 10^{-5}$M) in MeOH*

The excitation of **53.Eu**, both *R* and *S* enantiomers, at 281 nm into the $S_0 \rightarrow \pi\pi^*$ transition of the naphthalene moiety yielded the ligand centred fluorescence emission shown in Figure 2.20.

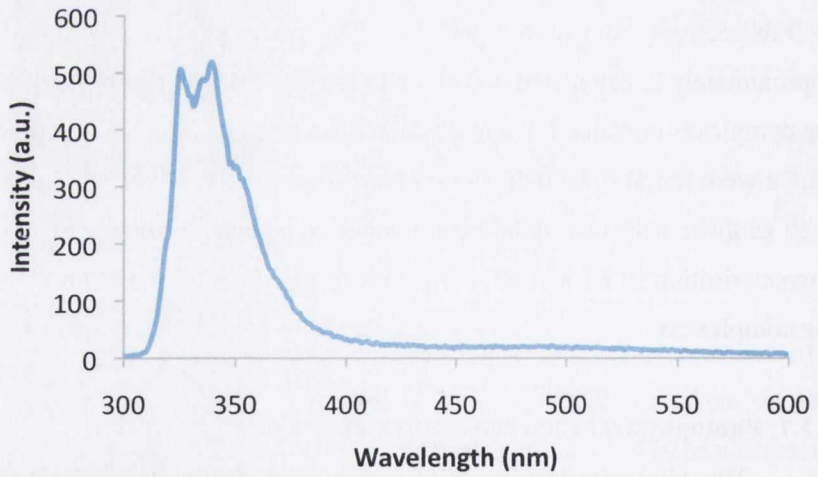

Figure 2.20*: Fluorescence emission spectrum of* ***53S.Eu*** *($c = 1 \times 10^{-5}$M) in MeOH, λ_{ex} = 281 nm*

Excitation into the $\pi\pi^*$ transition of the naphthalene absorption band also resulted in the sensitisation of the lanthanide centred emission, which demonstrated population of the lanthanide excited state *via* energy transfer from the excited state of the naphthyl antenna to the $^5D_0$ accepting level of t he lanthanide, Figure 2.21.

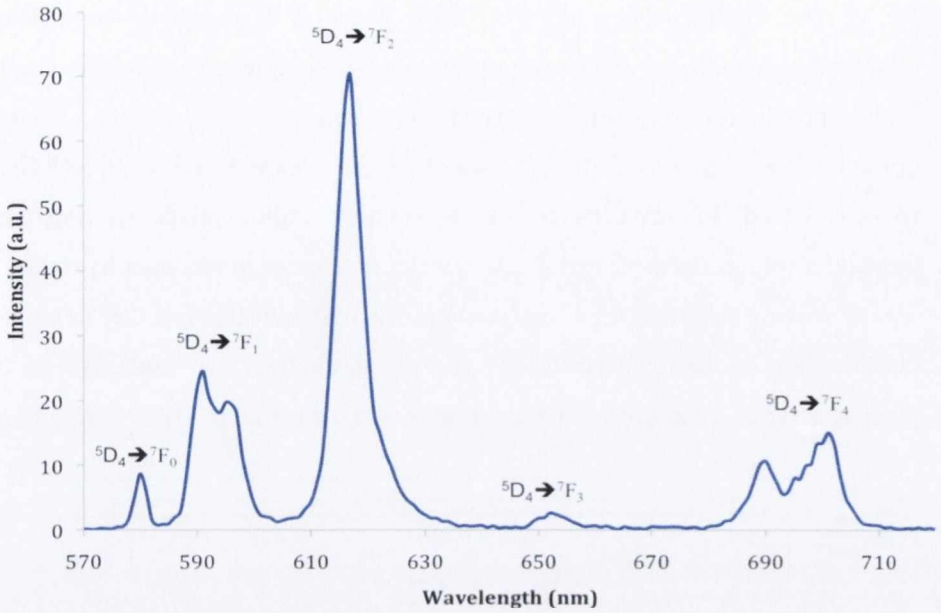

***Figure 2.21**: Eu^{3+} centred emission of **53S.Eu** ($c = 1 \times 10^{-5}$M), $\lambda_{ex} = 281$ nm*

The Eu^{3+} emission spectrum can act as a fingerprint for determination of the Eu^{3+} coordination pattern. These bands centred at 575, 593, 616, 651, and 695 nm respectively, represent the deactivation of the $^5D_0$ excited state to the ^7F_J (J = 0-4 respectively) states as shown in Figure 2.20.

After complexation of **53** (R and S) with Eu^{3+} and photophysical evaluation of the resulting complexes, it was important to analyse the lifetimes and thus the *q* value or hydration state, which will be discussed in the next section.

2.3.8 Determination of the lifetimes and *q* values of 53.Eu

The complexes **53*R*.Eu** and **53*S*.Eu** were heptadentate and in a similar manner to that observed for **51.Eu** and **52.Eu,** the coordination sphere could be filled with solvent molecules. The hydration state was calculated from the luminescent lifetimes decays of the complexes, however, in this case the complexes showed low solubility in H_2O and for that reason the hydration states were calculated using MeOH and MeOD with Equation 2 as discussed for **51.Eu** and **52.Ln**.

Table 2.2: Lifetimes and q values of 53R.Eu and 53S.Eu in MeOH and MeOD

Complex	τ_{MeOH} (ms)	τ_{MeOD} (ms)	q (±0.5)
53*R*.Eu	0.569	1.67	1.7
53*S*.Eu	0.560	1.69	1.8

The lifetimes observed for **53.Eu** *R* and *S* enantiomers were similar to those observed in Section 2.3.6, demonstrating that the complexes behaved in a similar manner with longer lifetimes due to the more efficient sensitisation of the Eu^{3+}, from the naphthyl chromophore. The hydration or *q* value of the complexes **53*R*.Eu** and **53*S*.Eu**, were found to be 1.7 and 1.8 respectively, in methanolic solution, demonstrating the complexes contained approximately 2 metal bound water molecules in the inner hydration sphere.

Having characterised the complexes photophysically, the next step was the confirmation of the retention of the chirality throughout the synthesis and complexation processes. The CD spectrum of the complex was measured in MeOH for both enantiomers.

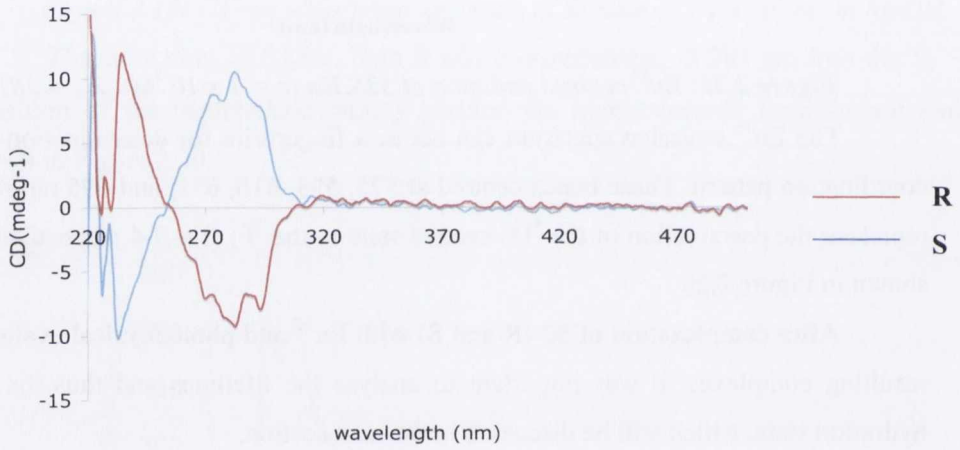

***Figure 2.22**: CD spectrum of **53R.Eu** and **53S.Eu** in MeOH*

As demonstrated for the ligand, the CD spectrum obtained in MeOH for both the enantiomers of **53.Eu** showed the naphthyl antenna significant of the $S_0 \rightarrow \pi\pi^*$ with opposite enantiomers retained throughout the complexation process.

Having synthesised complexes **51.Eu**, **52.Ln** and **53.Eu** and characterised them *via* NMR, mass spectrometry, IR and photophysical measurements the next section discusses the possible formation of dinuclear complexes *via* the Click 1,3-Huisgen cycloaddition.

2.4 The Click reaction

The formation of the click complexes requires the presence of copper catalyst, an azide, alkyne and a reducing agent, such as sodium ascorbate. Firstly, the azide must be safely synthesised as aromatic azides can be explosive. The azides used were based on simple aromatic bromides, which were generated by stirring benzyl or xylyl bromides

overnight under argon with 3 eq. of NaN_3 followed by basic extraction. The work up of these reactions is important as azides can be explosive in acidic conditions. However, after a number of attempts it was discovered that the most efficient method for the formation of the azide, involved in situ synthesis by stirring at room temperature with NaN_3, followed by addition of the click reagents without isolation of the azide.

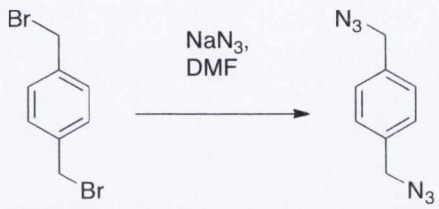

54 **55**

***Scheme 2.6**: The synthesis of the azide **55**, using sodium azide in situ*

The azide was synthesised by dissolving di-bromo para-xylene in DMF followed by the addition of NaN_3, Scheme 2.6, and the resulting mixture was stirred overnight to ensure formation of the azide after which the complex and catalyst were added, Scheme 2.6. This avoided the product azide, **55**, from becoming potentially explosive during the work up. The final step was to attempt click chemistry with the molecules synthesised in the previous sections as will be discussed in the next section.

2.4.1 Synthesis of 56.Eu

The click chemistry reaction was attempted with the ligand **51**, **52** and **53** itself as it was expected to allow formation of the click triazole. However, as discussed in Section 2.4.2, upon addition of the catalyst, the Cu(II) immediately became complexed in the cyclen macrocyclic cavity, and would become inert for the purpose intended as the catalyst could not associate with the triple bond as required. For this reason, we used the complexes formed in the previous sections in the click reactions.

After formation of the complex, the click reaction was attempted by first using *in situ* formation of the azide in DMF. The Eu^{3+} complex, **51.Eu**, was dissolved in 5 mL of DMF followed by the addition of $CuSO_4.5H_2O$ and sodium ascorbate and stirred at room temperature for three days, shown in Scheme 2.7. The solvent was removed under reduced pressure to yield an oily residue and mass spectrometric analysis was obtained. This showed no evidence for the formation of the desired product, **56.Eu**. Upon examination of the ^1H NMR ($CDCl_3$, 400 MHz) of the isolated fraction, no resonance was observed for the

triazole bridge as the expected resonance for the triazole proton should appear at approximately 8 ppm.

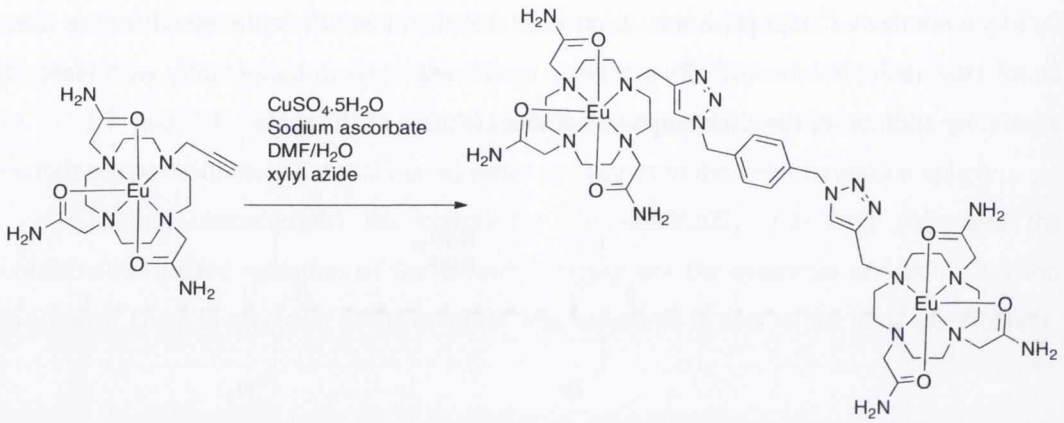

51.Eu **56.Eu**

Scheme 2.7**: Synthesis of dinuclear complex **56.Eu

Due to the failure of this reaction to form the desired triazole product, **56.Eu**, a number of subsequent reactions were carried out with the attempt to form the triazole bridge required using various modified experimental procedures from the literature, as shown in Table 2.3.

Table 2.3: Attempted click conditions with complex 51.Eu

Click No.	Eq. of Cu	Solvent	Eq. of NaAsc	Time	Temp
1	0	Toluene	0	o/n	120°C
2	1.3	DMF/H_2O	3.9	o/n	25°C
3	0.06	$EtOH/H_2O$	0.6	o/n	80°C
4	1.3	DMF/H_2O	3.9	o/n	90°C

However, no product was observed during each of these attempts by mass spectrometry and ^1H NMR, so it was thought that the NH_2 arms could possibly interfere with the catalytic activity of the Cu(II) required for the formation of the triazole. It was then attempted to utilize complex **52.Ln** as this could possibly result in less interference with the reaction itself. These results for this investigation will be discussed in the next section 2.4.2.

2.4.2: Click reaction of 52.Ln (Ln = Eu, Tb)

Due to the poor results obtained for the attempted synthesis of **51.Eu** above, the click reaction was attempted using **52.Eu** and **52.Tb**.

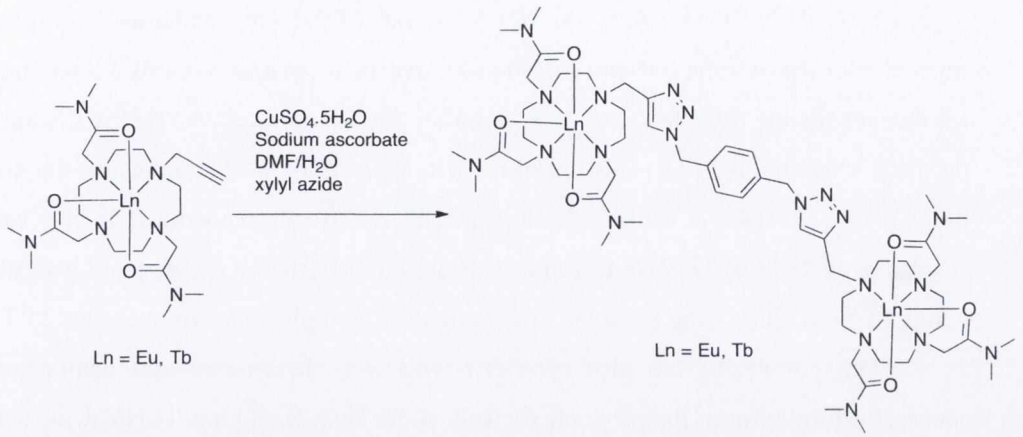

52.Ln **57.Ln**

Scheme 2.8**: Click reaction using **52.Ln** (Eu, Tb) in the presence of xylyl azide to give **57.Ln

As shown in Scheme 2.6, the azide was synthesised *in situ* after which the complex, **52.Ln** and sodium ascorbate, were added to the solution in DMF, followed by the addition of $CuSO_4$ in H_2O. The resulting mixture was stirred for 48 hours, during which the solution turned blue/green showing reduction of the copper metal, washing with ether to remove the excess azide and precipitation out of swirling diethyl ether, yielded the products **57.Eu** and **57.Tb** as yellow oils in 46% and 51% yield, respectively.

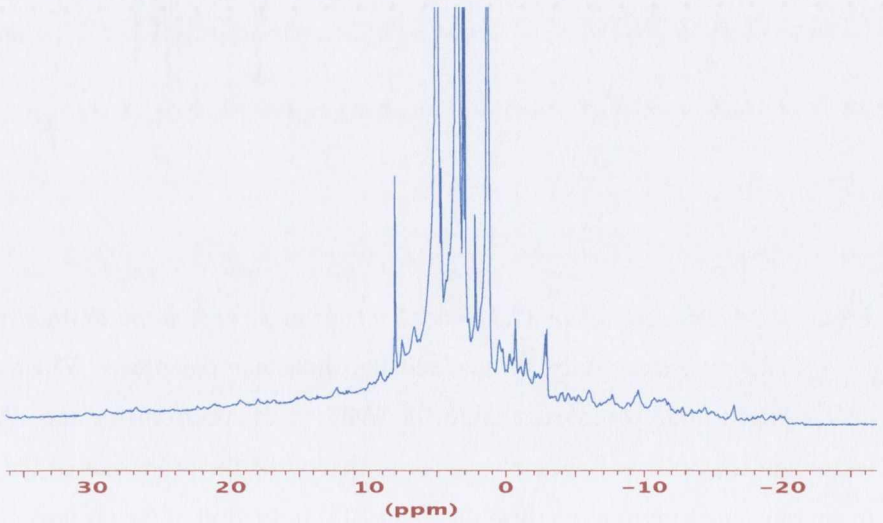

Figure 2.23**: ^{1}H NMR spectrum (MeOD, 400 MHz) of **57.Eu

^{1}H NMR (MeOD, 400 MHz) analysis of both **57.Eu** and **57.Tb** were carried out. The shifts in the ^{1}H NMR spectrum of the Eu^{3+} complex suggested formation of the dinuclear click complex due to the more symmetrical nature of the resonances, shown in Figure 2.21. ^{1}H NMR (MeOD, 400 MHz) analysis of the Tb^{3+} analogue demonstrated the formation of the product through shifting of the resonances and contains a lower number of resonances for the dinuclear complex, possibly due to the more symmetrical nature of the product, Appendix A. The mass spectrometric analysis of **57.Ln** indicated the signal for the **51.Tb**, at 2031.4130 for $C_{58}H_{93}N_{20}O_{18}F_{12}S_4Tb_2$ corresponding to the calculated spectrum of 2031.4175. The isotopic distribution pattern for the species was observed, which is significant of the presence of the dinuclear complex, shown in Figure 2.23.

The HRMS of the product **57.Eu** was also determined and demonstrated the successful formation of the product. As well as the HRMS and the ^{1}H NMR the success of this reaction could also be determined from the IR with the stretch at 1600 cm^{-1} experiencing a sharp increase compared to that of the starting material **52.Ln**, possibly from the formation of the triazole.

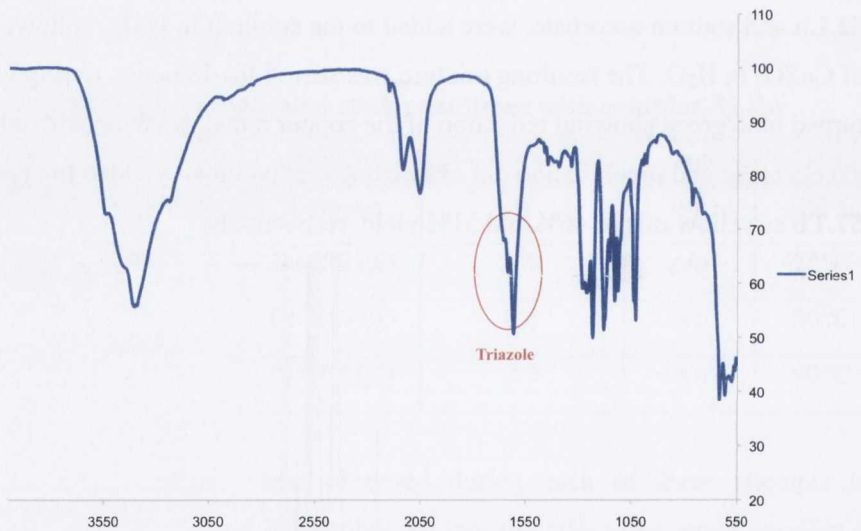

***Figure 2.24**: IR spectrum of **57.Tb** with the triazole stretch in the IR highlighted in red*

Having successfully synthesised the dinuclear complexes **57.Eu** and **57.Tb** and characterised these complexes using ^{1}H NMR, mass spectrometry and IR, the complexes were then characterised photophysically to determine the properties of the click analogues in solution and to further confirm the successful formation of the product.

2.4.2.1 Photophysical Characterisation of 57.Eu and 57.Tb

Initially, the complexes, **57.Ln**, were analysed by recording the UV-Vis absorption spectra. This shows in the UV-Vis absorption spectrum, Figure 2.25, the band at 250 nm corresponding to the weak absorption of the carbonyls can be seen. In comparison to that of the precursor in Figure 2.14, a second weak shoulder at 450 nm is observed in the UV-Vis absorption spectrum of the product and the triazole linker of the dinuclear complex, respectively.

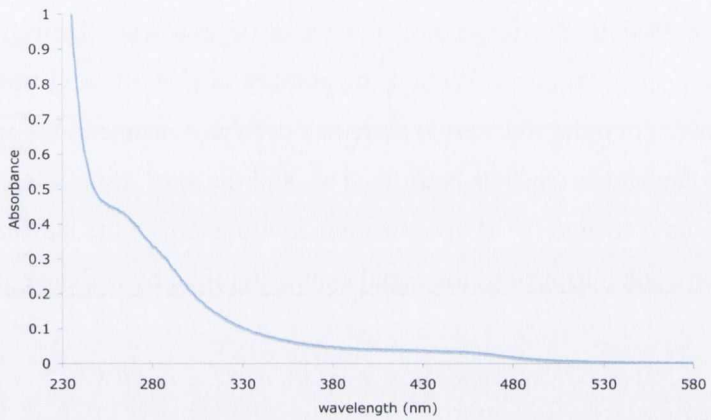

Figure 2.25: *UV-Vis absorption spectrum of* ***57.Eu*** *($c = 1 \times 10^{-5}$M) in MeOH*

Excitation at 250 nm and at the weak shoulder at 450 nm, caused indirect excitation of the lanthanide ion with the luminescence of the Tb^{3+} metal further demonstrating that the shoulder at 450 nm belongs to the absorption of the triazole and not to an MLCT state associated with the possible presence of the copper metal in solution.

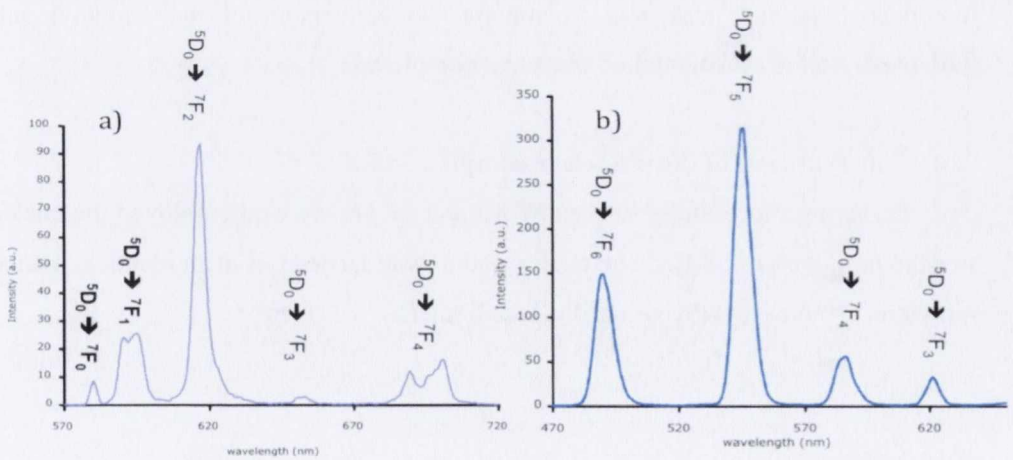

Figure 2.26: *Phosphorescence spectra of a) Eu^{3+} for* ***57.Eu*** *and b) Tb^{3+} for* ***57.Tb*** *in MeOH, ($c = 1 \times 10^{-5}$M), λ_{max} =250 nm*

Triazole-based cyclen lanthanide complexes have previously demonstrated the possibility of the coordination of the triazole proton to the lanthanide.[138] For this reason, the next section will determine the lifetimes and number of metal bound water molecules for the resulting complexes.

2.4.2.2 Calculation of *q* values and lifetimes of 57.Ln

As discussed for the previous complexes, the luminescence lifetimes allow the calculation of the hydration states fitting the rate of decay to a monoexponential function. As discussed in Section 2.3.6, a *q* value of two was obtained for **52.Eu** and **52.Tb**, however, after the click reaction the number of metal bound water molecules was again determined in order to assess if there had been any change in the coordination environment of the lanthanide ion. For both the Tb^{3+} and the Eu^{3+} complexes the luminescence decay suggested a change in the coordination environment of the lanthanide due to coordination of the triazole nitrogen to the metal centre signified by a change in hydration state from 2 to 1.

Table 2.4: Lifetimes and q values of 57.Eu and 57.Tb in H2O and D_2O

Complex	τ_{H2O} (ms)	τ_{D2O} (ms)	q (±0.5)
57.Eu	0.855	1.6	1.14
57.Tb	1.36	1.89	0.73

This result further suggests the successful formation of the triazole based dinuclear complex. The next task was to attempt the conversion of the naphthyl substituted complexes to the triazole linked dinuclear complexes.

2.4.3 The synthesis of the dinuclear complex 58.Eu

Having successfully formed **57.Eu** and **57.Tb**, we next employed the click reaction for the formation of **58.Eu**. The click reaction was carried out in an identical manner to the previous complexes with both of the enantiomers.

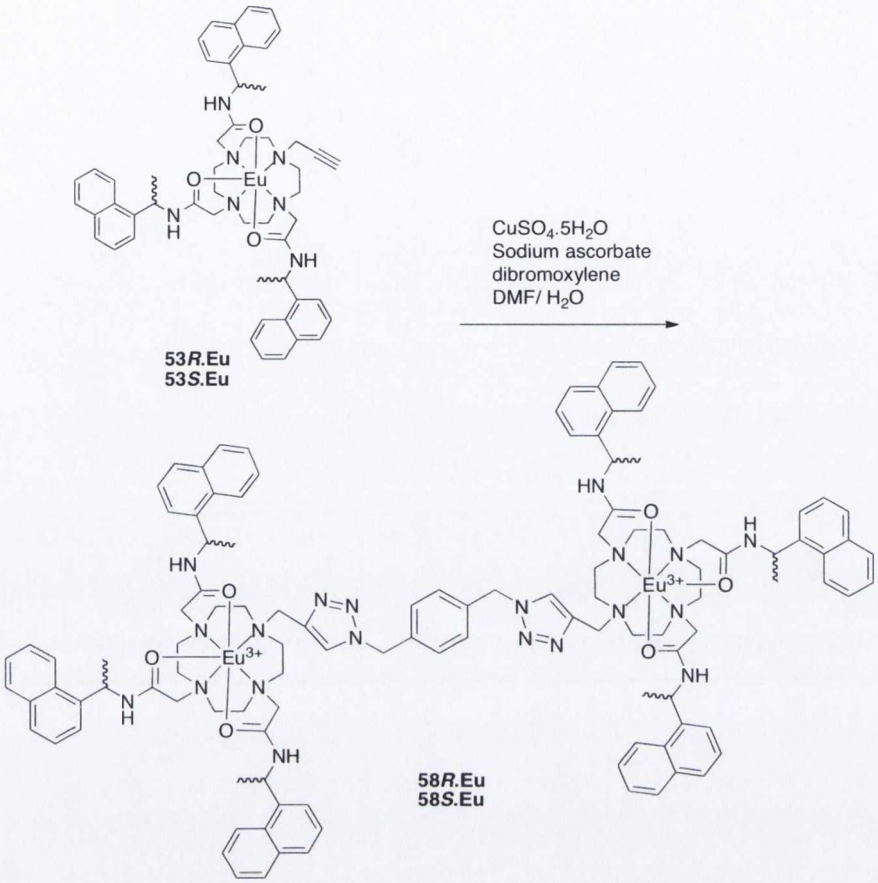

Scheme 2.9**: Synthesis of click complex **58.Eu (R, S)

This involved *in situ* preparation of the azide and addition of the complex with $CuSO_4$ and sodium ascorbate. The complex was refluxed overnight, followed by precipitation from H_2O to yield **58.Eu** as a brown oil in 55% yield. Shifts in the ^1H NMR (MeOD, 400 MHz) spectrum of the resulting complex **58.Eu** demonstrate that complexation occurred with the resonances appearing more defined possibly due to the higher symmetry of the dinuclear complex, Figure 2.27.

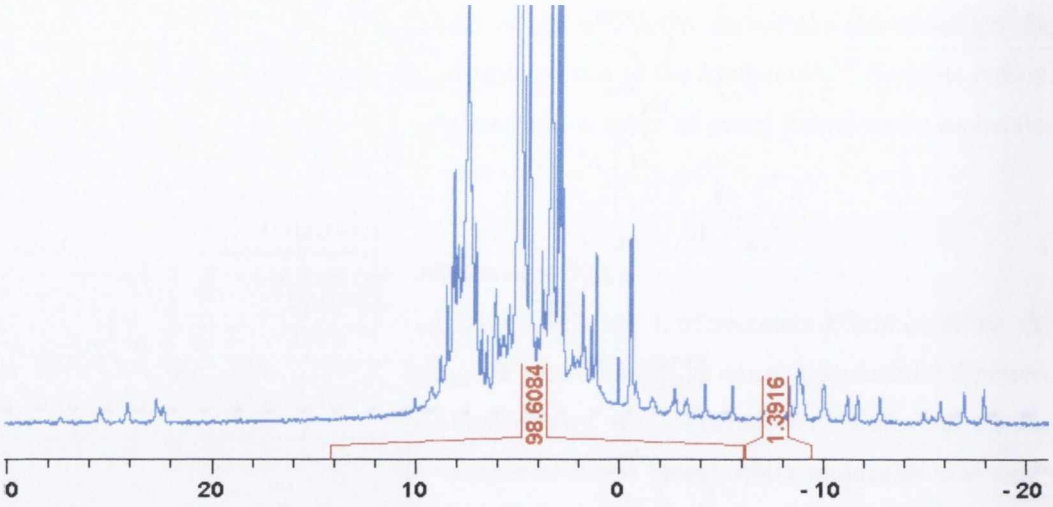

Figure 2.27**: ^{1}H NMR (MeOD, 400 MHz) spectrum of **58.Eu

The presence of the triazole can be identified using IR spectroscopy as the triazole stretch appears at approximately 1600 cm^{-1} as shown for **58.Eu**, Figure 2.28.

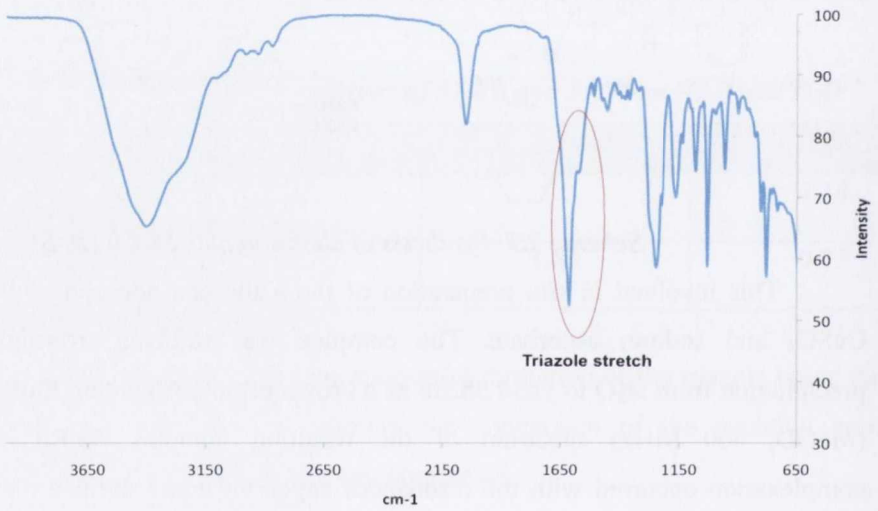

***Figure 2.28**: Infrared spectrum of **58.Eu** showing triazole stretch at 1600 cm^{-1}*

Also, the use of mass spectrometry demonstrated the isotopic distribution of the complex in methanolic solution, significant of the presence of the dinuclear complex, shown in Figure 2.29 for the species M + 4triflates/2 for the 2^{+} charged complex showing that this click reaction was successful in the formation of dinuclear chiral click complex. The same results were observed for the R isomer.

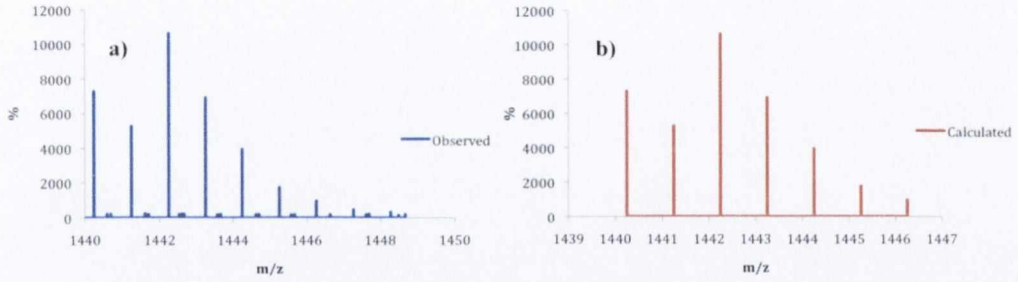

***Figure 2.29**: Mass spectroscopic analysis showing **a)** complex **58.Eu** b) Calculated spectrum*

Having successfully synthesised and characterised the complexes **58.Eu**, *R* and *S*, the next step was to determine their photophysical properties.

2.4.3.1 Photophysical characterisation of 58.Eu

Following the formation of **58.Eu** it was necessary to characterise this complex photophysically. Initially a UV-Vis absorption spectrum was recorded displaying the ππ* transition attributed to the naphthyl group of the complex demonstrating that the UV-Vis absorption spectrum remained unchanged throughout the click procedure.

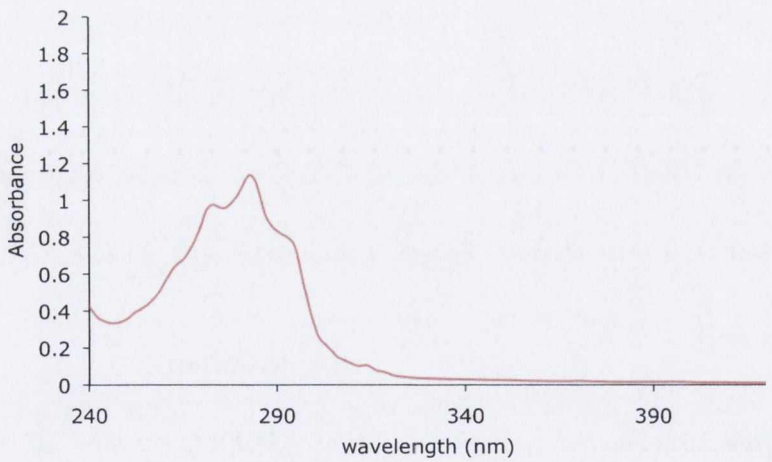

***Figure 2.30**: UV-Vis absorption spectrum of **58.Eu** in MeOH (1 x 10^{-4} M) with naphthyl band at 281 nm*

Excitation into the $S_0 \rightarrow \pi\pi^*$ transition of the naphthyl chromophore gave rise to the ligand centred fluorescence, which demonstrated a strong fluorescent band at 345 nm corresponding to the fluorescence of the complex itself. This again corresponded to that of the starting material although slight differences can be observed in the shape of the band.

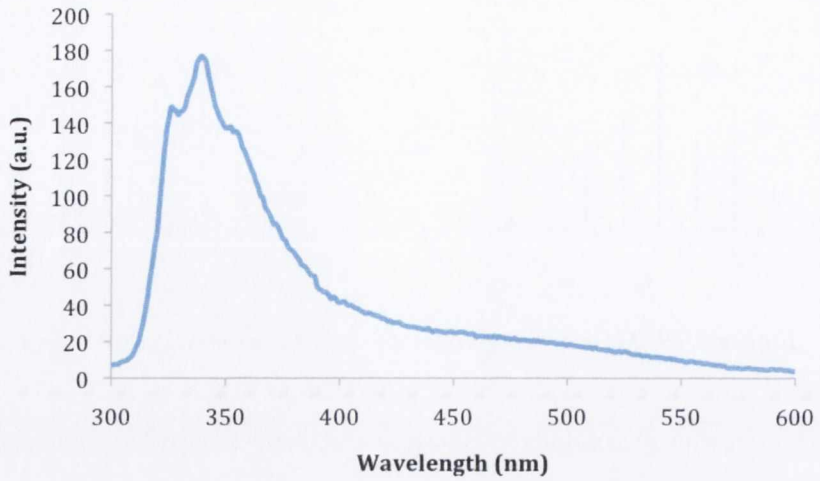

Figure 2.31: *The fluorescence emission spectrum of* ***58.Eu*** *in MeOH,* λ_{max} *= 281 nm*

Excitation into the $S_0 \rightarrow \pi\pi^*$ transition also yielded the phosphorescence emission of the Eu^{3+}, which is shown in Figure 2.32. This was quite different to that of **53.Eu** with the transition at $J = 0$ observed to be quite intense signifying the symmetry of the molecule upon formation of the dinuclear complex.

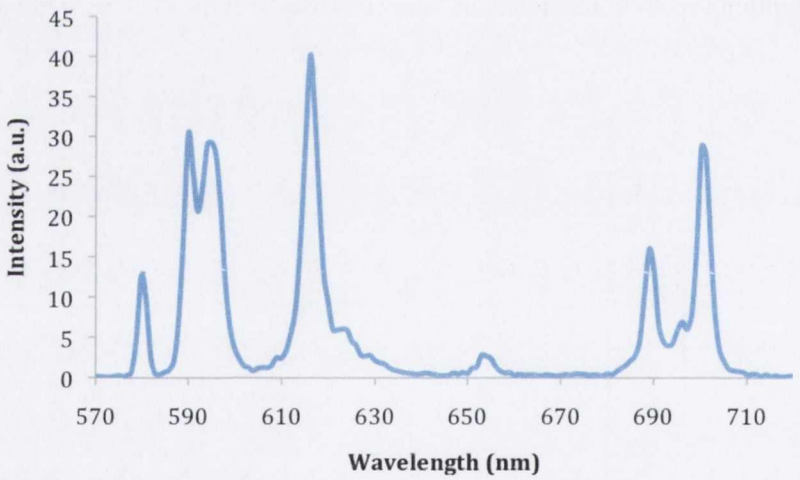

Figure 2.32: *The* Eu^{3+} *emission spectrum of* ***58.Eu*** *(*$c = 3 \times 10^{-5}$*M) in MeOH,* λ_{max} *= 281 nm*

The phosphorescence emission of the complex **58.Eu** also allowed the calculation of the luminescent lifetimes or decay of the luminescent emission which was carried out in MeOH and MeOD and allowed the calculation of the hydration state of the molecule as discussed for the previous complexes.

Table 2.5: *Lifetimes and q values of* ***58.Eu*** *in MeOH and MeOD*

Complex	τ_{MeOH} (ms)	τ_{MeOD} (ms)	q (±0.5)
58*R*.Eu	0.72	0.82	0.36
58*S*.Eu	0.69	0.87	0.62

The lifetimes determined for the complex **58.Eu** demonstrated changes in the coordination environment of the lanthanide. Upon calculation of the hydration state or *q* value of the complex it was found to contain approximately one metal bound water molecule significant of the binding of the triazole NH to the Eu^{3+}. This was further evidence that the click reaction was carried out successfully for the complex **58.Eu**.

In summary the complexes **51.Eu**, **52.Ln** and **53.Eu** were synthesised and characterised photophysically. The click chemistry has been successfully carried out on three different complexes and the products **57.Ln** and **58.Eu** (*R*, *S*). The click reaction, although allowing for the facile development of dinuclear complexes, formed a bridging unit was quite flexible and was not known to provide good luminescence properties. Also the click reaction has been widely used in the fields of organic synthesis, luminescence and even nanoparticles. For this reason the next step was to utilize the Tröger's base unit to click monotopic ligands together in order to allow simple two-step synthesis of possible dinuclear lanthanide complexes, discussed in the following sections.

2.5 Tröger's base linkers for development of dinuclear systems

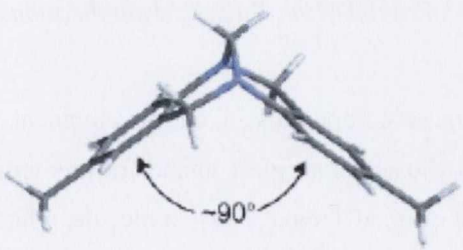

The Tröger's Base is a chiral rigid diamine with two aromatic rings stacked perpendicular to each other.[153] This inherent chirality and V-shaped structure makes these molecules ideal candidates for use in a wide variety of areas. Recently designed Tröger's Base derivatives include polysubtituted analogues, macrocycles such as Trögerophanes, crown ether derivatives, heterocyclic analogues, metal complexes and supramolecular structures, which can be used as receptors for acyclic substrates, aromatic amides and cyclic amides as well as chiral resolving agents.[153-154]

The Tröger's Base was discovered by Julius Tröger's in 1887 when he reacted paratoluidine with formaldehyde in the presence of HCl. Spielman *et al.*[155] discovered the

structure of the Tröger's Base unit and its chirality in 1935, which is due to the two stereogenic nitrogens atoms of the diazocine bridge. This was further confirmed by X-Ray diffraction studies by Wilcox *et al.*,[156] in 1985. The molecule is rigid with a dihedral angle of approximately 90 ° between the two aromatic rings, which can be varied depending on the substituents on the aromatic ring.[153] Tröger's base is an ideal ligand for supramolecular chemistry as it combines the important elements of chirality, rigidity, aromaticity and a variable dihedral angle between the two aromatic moieties.[154b, 157] Both the chirality and the rigidity of this ligand could potentially give the dinuclear complex very interesting properties. For this reason, it was chosen as an ideal linker for a dinuclear cyclen based lanthanide complex, as it could, due to its shape, bring the lanthanide ions in close proximity to each other. The development of Tröger's base naphthalimide compounds such as **59-62**, have been carried out in the Gunnlaugsson group previously by Dr. Emma Veale.[158] These molecules showed efficient binding for DNA, which was further confirmed by UV/Vis, Fluorescence, CD and thermal denaturation studies, all of which showed its interaction with calf thymus DNA.

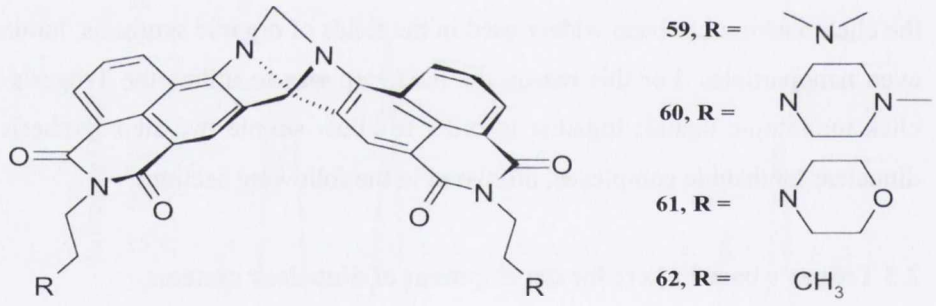

Figure 2.33: *Tröger's Base developed for anticancer applications*

Partly due to the success of these compounds in the development of anticancer agents, the Tröger's Base moiety was chosen as an ideal ligand for this project. The first step is to carry out the synthesis of the original Tröger's base molecule, which is shown in the following section.

2.6 Synthesis of Tröger's Base 68

In the literature, there are many variations on the Tröger's base synthesis, where each utilise a carbon equivalent, formaldehyde, (although other carbon equivalents can be used, such as formate) and a strong acid such as trifluoroacetic acid (TFA, although other acids can be used such as HCl). The proposed mechanism is highlighted in Scheme 2.12,

the exact mechanism of the Tröger's base formation is yet unknown but mass spectrometric measurements of various intermediates suggest this mechanism.[159]

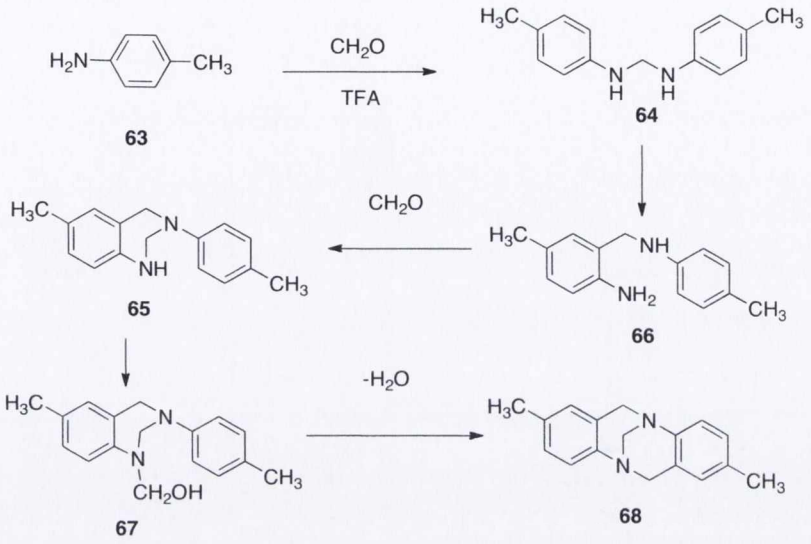

***Scheme 2.10**: Mechanism for the formation of Tröger's Base, **68** using formaldehyde and H^+*

A number of acids were attempted, such as HCl and acetic acid but less efficient Tröger's base formation was observed under these conditions. For this reason, the synthetic pathway chosen for the synthesis of Tröger's base utilised TFA and formaldehyde. The formation of **68** (Scheme 2.11), required 1 equivalent of *p*-toluidine, **63**, 2 equivalents of formaldehyde stirring in excess TFA overnight at room temperature. TFA was removed under reduced pressure and the resulting residue was dissolved in $CHCl_3$. Washing with H_2O yielded **68** as an orange solid in 65 % yield.

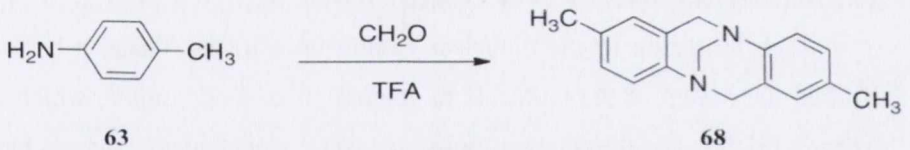

Scheme 2.11: *Synthesis of **68***

Analysis of **68**, using ^1H NMR ($CDCl_3$, 400 MHz) demonstrated the presence of the characteristic methylene protons of the Tröger's base, Figure 2.34. The bridged methylene unit H_c resonates as a singlet in the ^1H NMR at 4.65 ppm, while the 2 protons adjacent are not equivalent and are split due to the stereogenic nitrogens in the diazocine bridge and resonate as separate doublets at 4.2 ppm, H_a and 4.8 ppm, H_b, highlighted in Figure 2.34 in red.

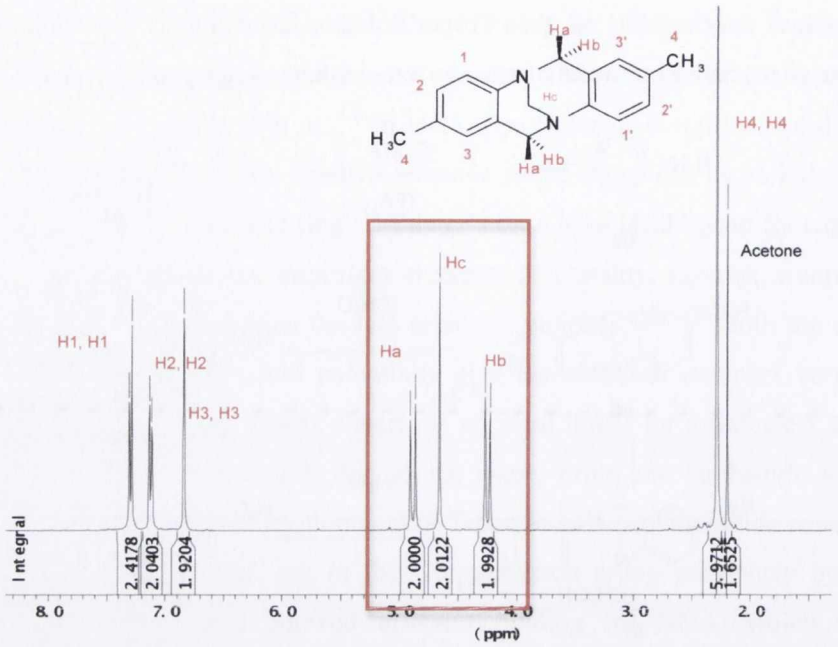

***Figure 2.34**: The ^{1}H NMR ($CDCl_3$, 400 MHz) spectrum of the Tröger's base, **68**, with emphasis on the CH_2 protons of the diazocine bridge highlighted in red*

The remaining resonances in the ^{1}H NMR ($CDCl_3$, 400 MHz) spectrum are the six aromatic protons, which appear as singlet and two doublets between 6.8-7.3 ppm and the methyl signal is distinctive at 2.2 ppm. The formation of **68** was also confirmed by ^{13}C NMR analysis and mass spectrometry. Both the shape and the rigidity of this Tröger's base unit could prove very interesting for the development of dinuclear lanthanide complexes. The following section will discuss the results for this investigation.

2.6.1 Macrocyclic derivatives of Tröger's Base

The formation of the dinuclear complexes utilising Tröger's base chemistry first required the design of the molecule to contain an aromatic amine, which could form the Tröger's bridge. The three target molecules were heptadentate Troger's base macrocyclic derivatives, **69,** and **70**, and an octadentate derivative, **71**, as shown in Figure 2.35. The heptadentate derivatives would allow the complex to contain two metal bound water molecules, which could lend these complexes to the potential sensing of carboxylates as was discussed in Chapter 1. The derivatives **69** and **70** were based on the use of a nitrobenzyl substituent to form the Tröger's Base bridge shown in Figure 2.35. The second derivative demonstrated the use of an acetamide-based linkage forming an octadentate ligand.

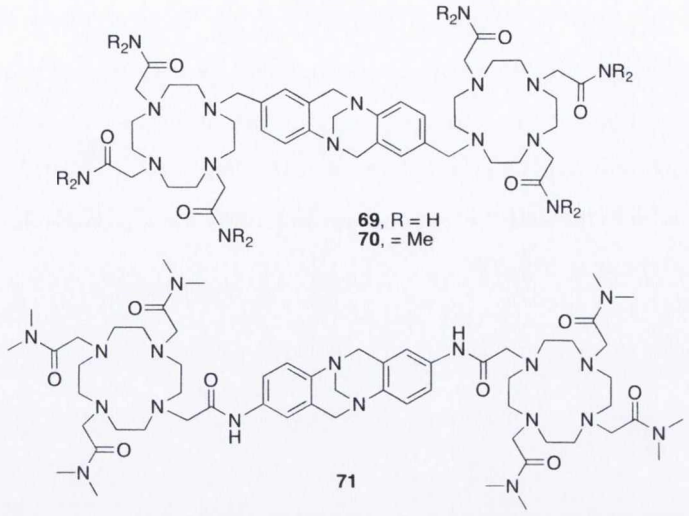

***Figure 2.35**: The two target molecules, heptdentate **69**, **70** and octadentate **71** for the formation of Trogers Base based dinuclear complexes*

The first target molecules and the most interesting for the purpose of luminescent sensing were **69** and **70** due to the potential presence of metal bound water molecules, which could form ternary complexes with analytes.

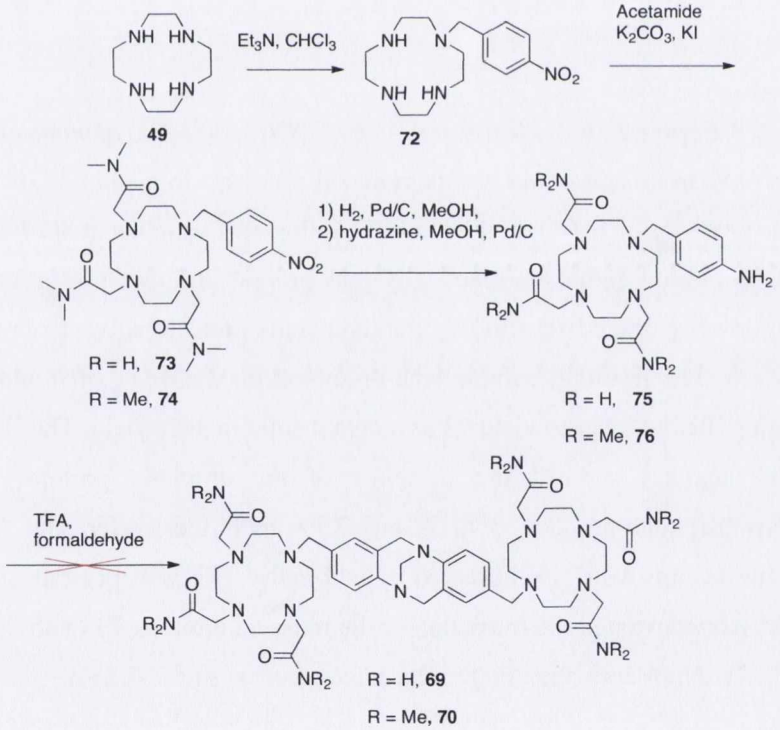

***Scheme 2.12**: Synthesis of Tröger's base targets **69**, **70** from 4-Amino benzyl bromide*

The first step was to ensure alkylation of the macrocycle, **49**, with the nitrobenzyl arm through a monosubstitution reaction,[150] which was carried out by stirring nitrobenzyl bromide and Et_3N with 4.1eq of cyclen overnight in $CHCl_3$ at 65°C, Scheme 2.12. Basic

work up to remove excess triethylamine yielded **72**, as a yellow oil in 24 % yield. The ^{1}H NMR ($CDCl_3$, 400 MHz) of **72** showed the formation of the desired product with the aromatic protons of the nitrobenzyl group resonating as two doublets and the cyclen CH_2 as a broad multiplet, 2-3 ppm, Figure 2.36. The formation of **72** was also confirmed by HRMS, which showed the product at 308.2086 for $C_{15}H_{26}N_5O_2$, with the corresponding calculated mass at 308.2087.

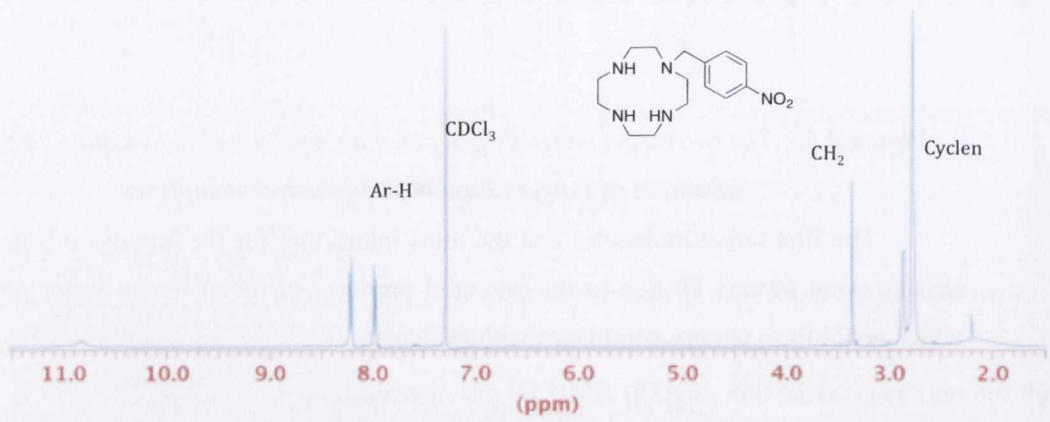

***Figure 2.36**: ^{1}H NMR spectrum ($CDCl_3$, 400 MHz) of monosubstituted 72*

N-Bromoacetamide was then added dropwise to a solution of **72** in $CHCl_3$/MeOH in the presence of K_2CO_3 and KI at 0 °C, followed by stirring at 80 °C for 1 week to ensure full substitution as this is a kinetically slow process, following its progress by ESI MS. The solution was filtered to remove inorganic salts and the solvent removed under reduced pressure. The resulting residue was dissolved in MeOH (1 mL) and precipitated out of swirling diethyl ether to yield **73** as a cream solid in 44% yield. The ^{1}H NMR ($CDCl_3$, 400 MHz) analysis showed the presence of the aromatic protons, as shown for the monosubstituted product at 8.12 and 7.39 ppm, the cyclen and CH_2 protons of the acetamide arms were also observed upfield in the ^{1}H NMR spectrum shown in Figure 2.37. HRMS demonstrated the formation of the required product, **73**, with the signal at 501.4297 for $C_{21}H_{34}N_8O_5$ corresponding to the calculated mass of 501.2550.

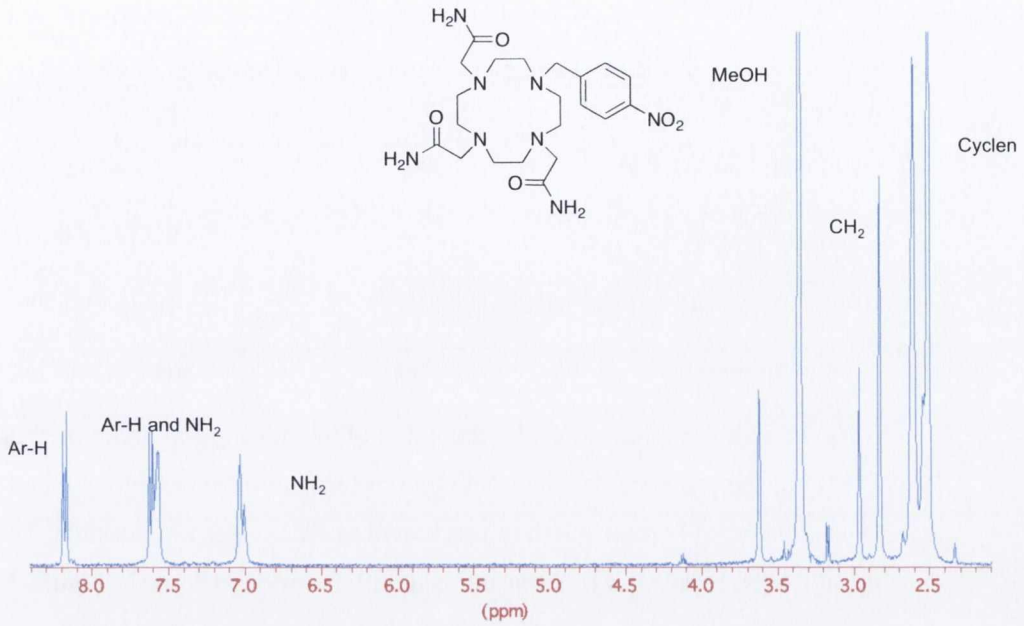

***Figure 2.37**: [1]H NMR (MeOD, 400 MHz) spectrum of ligand 73*

In order to form the amine, the product **73** was reduced under three atm. with H_2 using 10 % Pd/C as catalyst. The filtration of the catalyst and removal of solvent allowed the isolation of a brown residue. However, ^{1}H NMR ($CDCl_3$, 400 MHz) analysis, showed that the benzyl arm had been cleaved, which was a possible outcome due to the benzyl group being known as a successful protecting group for the synthesis of trisubstituted cyclen.[160] As an alternative reduction, **73** was reacted with hydrazine and Pd/C as catalyst in EtOH solution. The solution was filtered through a plug of celite and the solvent removed under reduced pressure, dissolved in $CHCl_3$ and washed with H_2O to determine if the benzyl group was intact, this yielded the amine without the benzyl group showing that cleavage had again occurred.

We then repeated these reactions using **74** as the starting material. Compound **72** was alkylated with α-Chloro-*N,N*-dimethyl acetamide in the presence of K_2CO_3 and KI in CH_3CN followed by filtration, washing with 0.1 HCl (2 x 10 mL) and 0.1 KOH (2 x 10 mL) and H_2O (2 x 10 mL), dried over $MgSO_4$, filtered and the solvent removed under reduced pressure to yield the product **74** as a brown oil, 75 % yield. ^{1}H NMR analysis demonstrated the formation of the product, Appendix A, which was confirmed by ^{13}C NMR analysis and mass spectrometry.

Table 2.6: The reduction attempts for formation of **69**

Reduction conditions	Successful	Cleavage or reduction
H_2, 1 atm and 3 atm, Pd/C MeOH	No	Cleavage of the nitrobenzyl group
Ammonium formate	No	Partial reduction and then cleavage
Hydrazine monohydrate	Partially	Reduction and then cleavage
Sodium dithionate	No	Cleavage of the nitro benzyl group

Again with the synthesis of **76**, reduction of the nitro group under pressure utilising Pd/C (10%) in the presence of either ammonium formate or hydrazine, yielded the amine and cleaved the benzyl group and thus attachment to cyclen was not possible. The ^{1}H NMR (MeOD, 400 MHz) spectrum of the water layer after work up shown in Figure 2.38, shows that only the substituted acetamide macrocycle was isolated. This had been previously shown to be efficient as a protecting group for the formation of tribsubstituted cyclen analogues, by Morrow *et al.*[160] Conversely the ^{1}H NMR (DMO-d_6, 400 MHz) spectrum of the $CHCl_3$ solution, after washing with H_2O, removal of solvent under reduced pressure showed the cleaved the nitrobenzyl group expected but did contain any resonances corresponding to the cyclen macrocycle.

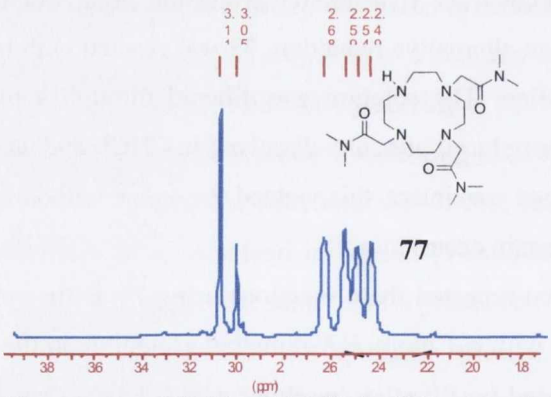

***Figure 2.38**: ^{1}H NMR spectrum ($CDCl_3$, 400 MHz) of **77** upon cleavage of nitrobenzyl group*

Effectively, the formation of the desired amines, **75** and **76**, was not successful and hence the formation of **69** and **70** could not be achieved using this strategy. Consequently we turned our attention to the synthesis of **71**, which would not allow facile cleavage of the acetamide linkage.

2.6.2 Synthesis of 71

Due to the problems associated with the benzyl linkage, an alternative synthesis was attempted utilising the nitro acetamide instead of the nitrobenzyl group.

The synthesis of **71** is shown in Scheme 2.12 and targeted the formation of the amine **80**, which was the key intermediate in the formation of **71**, and had previously been carried out in the Gunnlaugsson laboratory by Dr. Cidalia Santos for the formation of cyclen based anion sensors.[19] The synthesis involved the initial formation of the α-Chloro amide, and was achieved by addition of chloroacetyl chloride with stirring at 0 °C to a solution of the 4-nitroaniline and Et_3N in CH_2Cl_2 followed by an acid/base extraction, the desired product as a brown oil in 85 % yield.

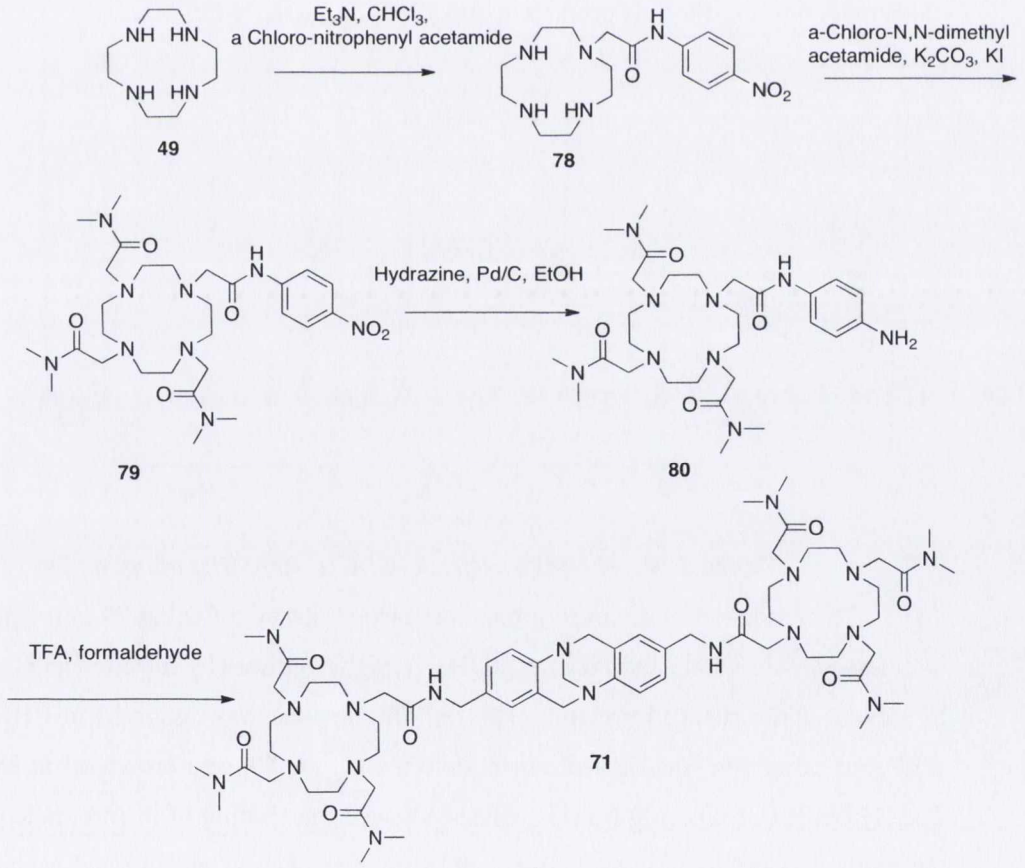

Scheme 2.13: *Synthesis of Trögers Base* ***71***

This was then stirred overnight with 4.1 equivalents of cyclen in the presence of Et_3N in $CHCl_3$, which yielded **78** in quantitative yield after extraction into $CHCl_3$ and washing with H_2O. The ^1H NMR ($CDCl_3$, 400 MHz) analysis showed the presence of the cyclen protons at 2.76 ppm as a broad multiplet, and the aromatic resonances show two doublets at 8.20 ppm and 7.99 ppm. HRMS confirmed the formation of the monosubstituted product with the mass observed at 351.2133 for $C_{16}H_{27}N_6O_3$ corresponding to the calculated mass of 351.2145.

This product, **78**, was then alkyated with α-chloro-*N,N*-dimethyl acetamide in the presence of K_2CO_3 and KI and stirred overnight, followed by filtration of the inorganic salts and removal of solvent under reduced vacuum. The resulting residue was dissolved in $CHCl_3$, washed with 0.1 M KOH yielding the product, **79**, as a brown oil, 75 % yield. The ^1H NMR (400 MHz, $CDCl_3$) spectrum, Figure 2.39, showed the formation of the tetrasubstituted ligand, **79** with observed resonances in a 2:1 ratio for the CH_2 of the arms, while the ^{13}C NMR showed the required number of resonances, which confirmed the successful formation of the product, **79**, and was further demonstrated by HRMS with the exact mass observed for the product at 606.3728 for $C_{28}H_{48}N_9O_6$.

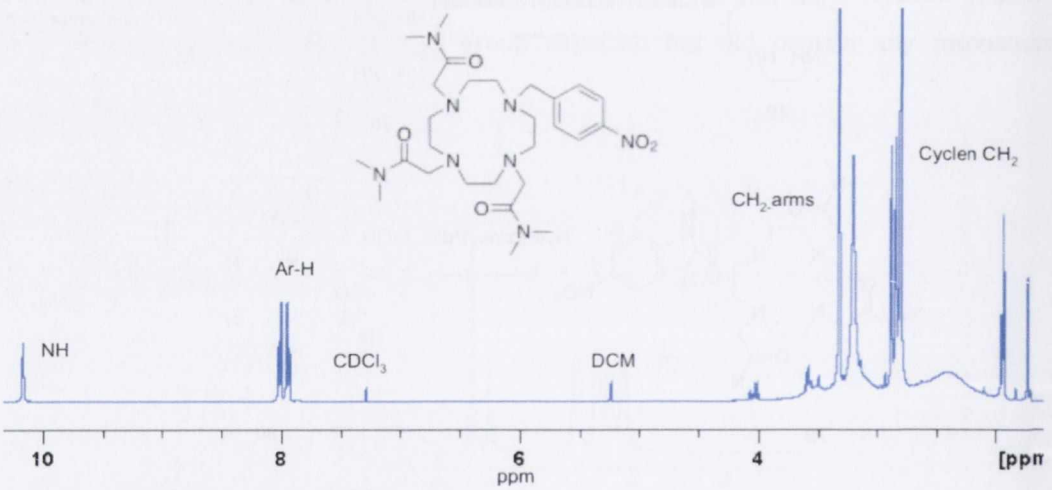

Figure 2.39: *^1H NMR spectrum ($CDCl_3$, 400 MHz) of ligand **79***

The reduction of the nitro group was carried out by refluxing **79** in the presence of hydrazine monohydrate and Pd/C in EtOH overnight followed by filtration and the removal of solvent under reduced pressure. The resulting residue was dissolved in $CHCl_3$ and an acid/base extraction was carried out to yield the amine, **80**, as a brown oil in 88 % yield. The ^1H NMR ($CDCl_3$, 400 MHz) analysis, showed the shifting of the aromatic protons of the aromatic ring downfield, Figure 2.40. Moreover, the cyclen ring and acetamide CH_2 and CH_3 protons remained unchanged in the ^{13}C NMR. Mass spectrometric analysis also

confirmed the presence of the product, **80** with HRMS showing the mass at 576.3996 for $C_{28}H_{50}N_9O_4$.

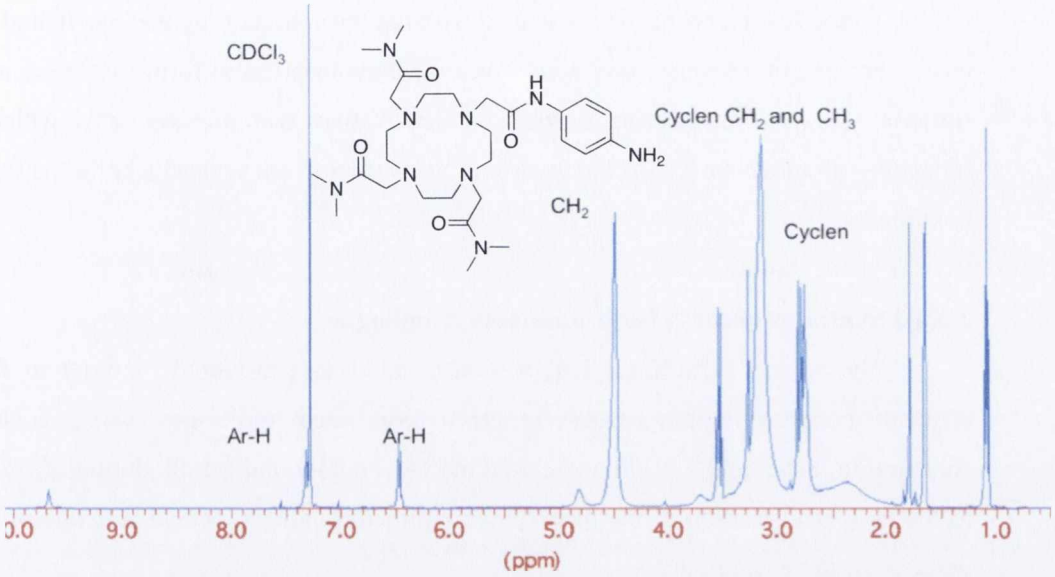

Figure 2.40**: [1]H NMR spectrum ($CDCl_3$, 400 MHz) of amine **80

The final step in the synthesis shown in Scheme 2.12, was to form the Tröger's Base derivative **71**. This was carried out using the same conditions as discussed previously using TFA and 3 equivalents of formaldehyde. The TFA was removed under reduced pressure and the crude product was isolated as a yellow oil, by extraction and washing with water. The mass spectrometric analysis of this product demonstrates the presence of the product with the signal observed at 1187.7853 for $C_{59}H_{99}N_{18}O_8$ with the calculated mass at 1187.7893. Unfortunately, ^{1}H NMR analysis of **71**, was ambiguous as it showed the presence of the Tröger's base diazocine bridge, but also showed a large number of CH_2 protons possibly corresponding to excess starting material. Due to this **71** was then purified using column chromatography with CH_2Cl_2/MeOH and EtOAc/Hexane as eluents. However, each attempt to isolate **71**, including column chromatography, size exclusion chromatography, reverse phase column chromatography was found to show no improvement in the ^{1}H NMR spectrum, in some cases causing degradation of the product. This suggested that this molecule perhaps allowed Tröger's base formation but showed degradation during isolation of the product. Due to time constraints this was not developed further. Having failed to isolate **71** in pure form it was next attempted to form the dinuclear complex from smaller Troger's Base derivatives containing halides or α-Chloroamides which could allow alkylation of the macrocycle, the synthesis of which will be discussed in the next section.

2.6.3 Formation of smaller Tröger's Base Derivatives

Following the problems associated with the formation of ligands **69**, **70** and **71**, low molecular weight Tröger's base derivatives were synthesised to form the linker required. Initially, attempts to synthesise Tröger's base derivatives with dibromo arms, which would be simple to attach to the cyclen molecule were carried out and will be discussed in the next section.

2.6.3.1 Synthesis of the 2,8-dibromomethyl analogue

The bromo substituted Tröger's base, **83**, was considered in order to facilitate efficient conversion into larger Tröger's base-based molecules using nucleophilic substitution, Scheme 2.13. This would be the ideal compound for alkylation of cyclen due to the ease of alkylation of the macrocycle with alkyl halides, and so was one of the first derivatives to be attempted.

The synthesis involved the reduction of 4-nitro-benzylbromide at one atmosphere of H_2 pressure, catalysed by 10% Pd/C, Scheme 2.13 to give **82**. The *p*-amino benzylbromide, was subsequently reacted with formaldehyde (1.5 eq.) and TFA at 0 °C overnight. However, after work up, which involved an extraction into $CHCl_3$ and washing with H_2O, no resonance corresponding to the methylene protons were visible in the ^1H NMR ($CDCl_3$, 400 MHz) spectrum.

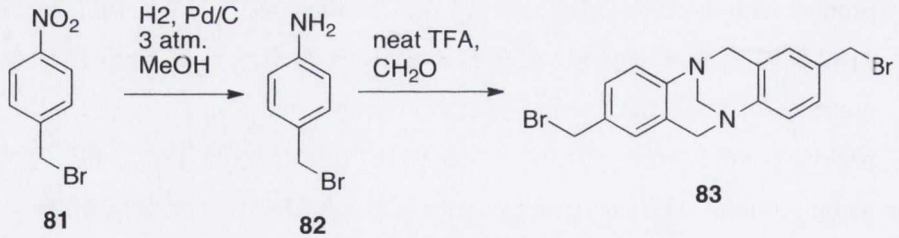

81 **82** **83**

Scheme 2.14**: Synthesis of bromomethyl substituted Tröger's Base, **83

Instead, a signal was observed upfield at approximately 2 ppm, which signified the formation of a methyl group integrating for 3 protons. The formation of **83** was therefore unsuccessful. This was not entirely unexpected as results have shown that a benzyl linkage with a halogen can result in cleavage of the benzyl group. Further attempts to synthesise this ligand using milder reduction conditions were unsuccessful, as although the amine was isolated, according to ^1H NMR ($CDCl_3$, 400 MHz), the product was impure. When purification was attempted using column chromatography on flash silica (eluting phase

CH_2Cl_2/MeOH gradient of 1-30 %), the methylene protons 3-4 ppm disappeared, suggesting that degradation had occurred on the column.

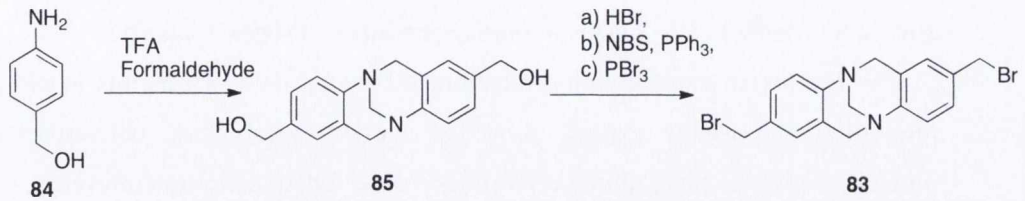

Scheme 2.15: *Attempted Synthesis of* ***83***

An alternative synthetic route for the formation of **83** involved the bromination of the diol Tröger's base, **85**. 4-Amino benzyl alcohol, was reacted with neat TFA and formaldehyde to form the desired product **85**, which was extracted into $CHCl_3$ and washed with water to give the product as a brown oil, 51 % yield. Again various reactions were attempted to form the bromide such as bromination with HBr, NBS and PBr_3 however, this did not allow for the isolation of the product as each synthesis caused the alcohol to either degrade or remain unreacted.

The third attempt to form **83** was to brominate the original Tröger's base, **62**. The first procedure involved a 16 h reaction stirring benzoyl peroxide and NBS in CCl_4 at room temperature under argon. However, this attempt was unsuccessful again due to degradation of the starting material.

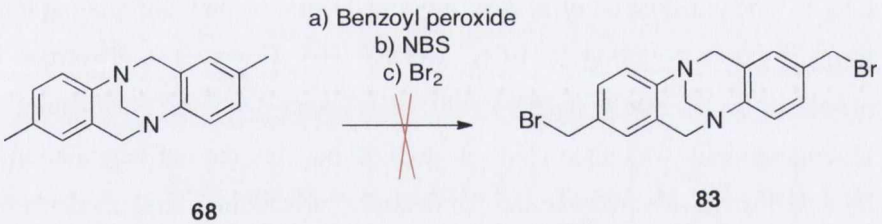

Scheme 2.16: *Attempted Synthesis of* ***83***

The NBS reaction was also attempted overnight at 80 °C. However, both attempts showed no evidence for the formation of **83** in the ^1H NMR spectrum but did suggest that the starting material **68** had degraded. Each attempt to brominate the Tröger's Base, **68**, caused partial or complete degradation of the starting materials. This suggested that the benzyl bromide was not an ideal target for the formation of dinuclear complexes. Recently, 4-Amino benzyl bromide was made commercially available, however, at 3000 euro for 5.0 g of starting material, it was not feasible for research purposes. For these reasons the next step was to synthesise a series of simple Tröger's base derivatives for the potential

formation of α-chloro amides for the functionalisation of the cyclen macrocycle with the overall target again being the formation of **71**.

2.6.3.2 Synthesis of the 2,8-bismethanamine based Tröger's base 87

The target was the amine substituted Tröger's base, **87**, as this would provide an interesting and useful starting point for many Tröger's base derivatives and could potentially give α-chloro amide derivatives for the functionalisation of cyclen.

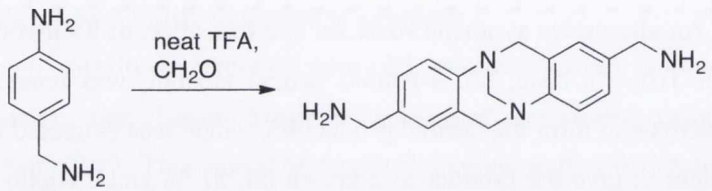

86 **87**

Scheme 2.17: *Synthesis of* ***87***

It was anticipated that the two nucleophilic amines in the compound may cause problems in this synthesis. 4-Amino benzylamine, **86**, was reacted with formaldehyde in neat TFA for 16 h at room temperature. After removal of the TFA under reduced pressure and basification up to pH 12 by the addition of 1 M NaOH, the product was extracted into $CHCl_3$. The purification of **87** was attempted using column chromatography on flash silica using a gradient elution (CH_2Cl_2: MeOH/NH_3). However, unidentified impurities were observed in ^1H NMR ($CDCl_3$, 400 MHz) analysis after purification and so column chromatography was attempted on alumina but this caused degradation of the Tröger's base derivative. Despite varying temperature, stoichiometric equivalents of CH_2O and the reaction time, **87** could not be isolated in pure form according to ^1H NMR ($CDCl_3$, 400 MHz) analysis. Further attempts to purify **87** *via* trituration with methanol, water, $CHCl_3$ and by using column chromatography on flash silica did not lead to improvements in the yield or purity of **87**. Therefore a different synthetic pathway was considered for the formation of **87**, shown in Scheme 2.18.

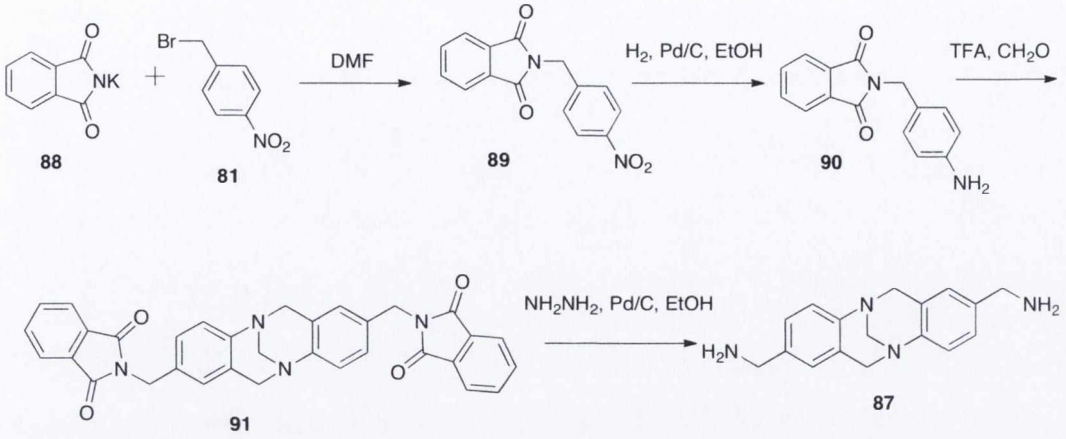

Scheme 2.18**: Synthesis of Tröger's base amine **87

The first step in the synthesis involved the generation of the phthalimide protected amine, **86**, by stirring potassium phthalimide, **88**, with 4-nitro benzylbromide **81** in DMF overnight. Dissolving the reaction mixture in H_2O and extraction into EtOAc/ toluene (2:1), followed by washing with water yielded **89** as white crystals in a 64 % yield. The ^1H NMR spectrum ($CDCl_3$, 400 MHz) demonstrated the formation of the product with the CH_2 visible at 4.95 ppm. ^{13}C NMR ($CDCl_3$, 400 MHz) and mass spectrometry confirmed the formation of product **89**. Reduction of the nitro group by hydrogenation at 3 atm with Pd/C yielded **90**, as yellow crystals in quantitative yield. The product formation was confirmed by ^1H NMR and ^{13}C NMR analysis. The HRMS also demonstrated the formation of the product with the mass observed for the ligand **90** at 253.1700 for $C_{15}H_{12}N_2O_2$, which was calculated to be 253.0977. Stirring **90** with 3 equivalents of formaldehyde and TFA, removal of solvent under reduced pressure and subsequent extraction of the residue into $CHCl_3$ with washing with H_2O, gave rise to the formation of **91** in 30 % yield as a brown oil. This compound was deprotected by stirring with neat hydrazine at 80 °C overnight, extracted into $CHCl_3$ and washed with water, giving **87,** as a yellow oil, in 61 % yield.

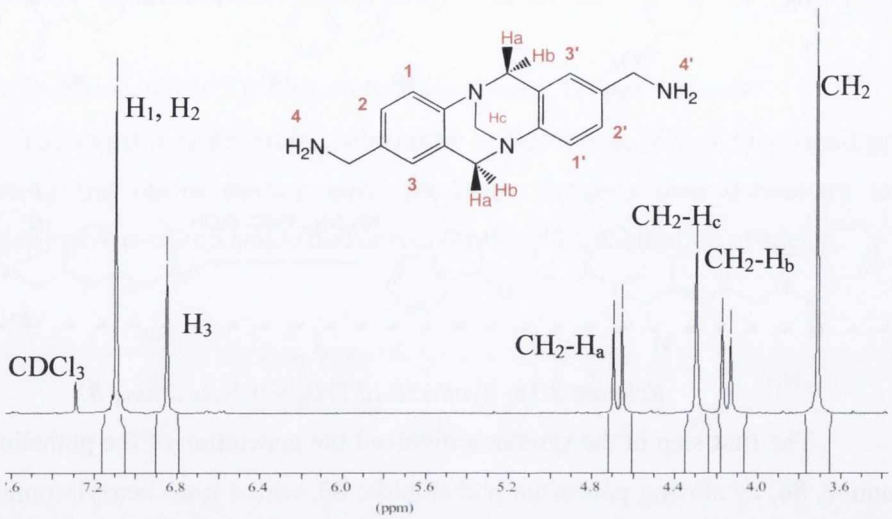

Figure 2.41: *^{1}H NMR spectrum ($CDCl_3$, 400 MHz) of* ***87***

^{1}H NMR ($CDCl_3$, 400 MHz) analysis of **87**, showed the expected set of resonances for the methylene protons of the Tröger's base peaks as three doublets resonating between 4-5ppm, Figure 2.41. The formation of **87** was further confirmed by ^{13}C NMR analysis, mass spectrometry and IR. This starting material could be utilised as a building block for the formation of Tröger's base macrocyclic ligands using the formation of α-chloro amides, which will be discussed with the formation of **92**.

The bis-acetamide Tröger's base **92** (Scheme 2.19) was developed as this could potentially react with cyclen to form the linker needed for the formation of the dinuclear complex.

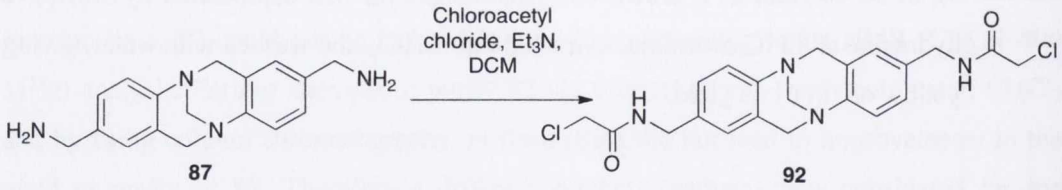

Scheme 2.19: *Synthesis of* ***92***

To achieve this, the diamine **87**, was stirred with NEt_3 in $CHCl_3$ at -10 °C with dropwise addition of chloroacetyl chloride over one hour at -10 °C, followed by stirring overnight at room temperature. Extraction into $CHCl_3$ and washing with H_2O did not yield **92** when analysed by ^{1}H NMR spectroscopy. The aqueous layer was reduced to a yellow

residue under reduced pressure and precipitated from MeOH, to give rise to the product **92**, as a white solid, 2% yield.

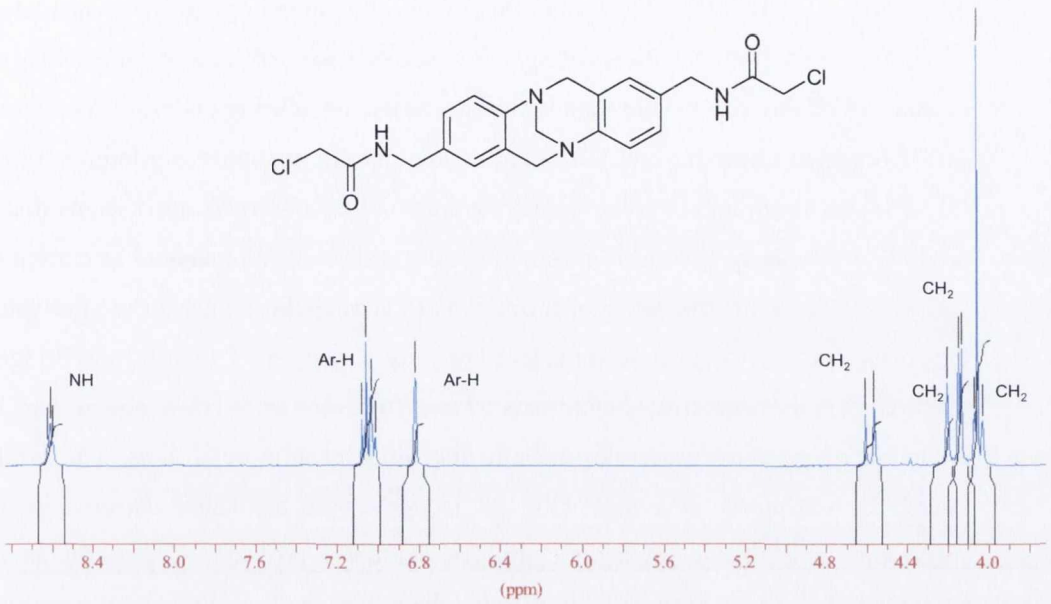

Figure 2.42: *^{1}H NMR spectrum (DMSO-d_6, 400 MHz) of* ***92***

Upon analysis of the ^{1}H NMR spectrum (DMSO-d_6, 400 MHz), the product observed was the anticipated acetamide **92**, as the methylene peaks for the diazocine bridge were observed as well as the peaks for the two methylene units, which could be seen at 4.06 ppm and 4.13ppm, Figure 2.42. The product **92** was only formed in 3 %, yield, due to the difficulties with extraction, and the synthesis was irreproducible, despite varying temperature, reaction time and solvent. Even though the yield was low, there was sufficient ligand to carry out a simple alkylation of triBOC protected cyclen. This procedure involved stirring **92** and triBOC cyclen (1.1 eq.) overnight at reflux, followed by filtration of the inorganic salts and extraction of this residue into $CHCl_3$ and washing with water. Removal of the solvent under reduced pressure yielded a yellow oil. The ^{1}H NMR ($CDCl_3$, 400 MHz) showed the characteristic broad cyclen peaks as a large multiplet at 2-3 ppm and the distinctive CH_2 region for the Tröger's base diazocine bridge, shown in Figure A.8, Appendix A.

However, the product was isolated in such small quantities that it was difficult to proceed to the next step so the remaining α-chloro-acetamide, **92**, was further reacted with 3.3 equivalents of trisubstituted cyclen functionalised with three α-chloro-*N,N*-dimethyl acetamide, **77**, in order to determine if this reaction was viable. Compound **92** was refluxed overnight with K_2CO_3 and KI and **77** in order to alkylate the macrocycle. The ^{1}H NMR

spectrum (DMSO-d_6, 400 MHz) suggested the successful formation of the product with aromatic and CH_2 protons indicative of product formation. The HRMS of the product was observed at 1237.8018 for $C_{61}H_{102}N_{18}O_8Na$ corresponding to the calculated mass 1237.8026. However, the ^1H NMR spectrum showed the presence of excess CH_2 and CH_3 resonances of the macrocycle potentially due to excess starting material. As demonstrated for **71** repeated isolations and purification attempts did not show any improvement in the ^1H NMR spectrum and in some cases degradation was observed, so it seems this product possibly degrades upon column chromatography and so isolation cannot be carried out.

In this section the potential formation of macrocyclic Tröger's Base derivatives was the focus in order to generate dinuclear complexes with the Tröger's base bridge. These reaction were unsuccessful. Compounds **69** and **70** demonstrated cleavage of the CH_2 upon reduction of the nitro group despite utilising mild reaction conditions. The synthesis of ligand **71** was more successful with the Tröger's base formation detected in the mass spectrometric analysis, however again this synthesis proved unsuccessful as repeated attempts to isolate the pure **71** demonstrated the presence of excess aliphatic protons in the ^1H spectroscopic analysis. For this reason the formation of smaller Tröger's Base derivatives was attempted based on the dibromo derivative. These reactions were again unsuccessful due to the difficulty in reducing the nitro group without causing cleavage of the CH_2 of the molecule. The final attempt to form **71** was carried out through the formation of the α-chloro amide, **92** for the alkylation of cyclen, however this molecule was formed in low yield and although alkylation of trisubstituted cyclen was attempted the product **71** could not be isolated in pure form.

The next section discusses preliminary work on the formation of simple Tröger's Base derivatives for potential use as sensors using a simple Tröger's Base amine derivative 87 and a carboxylic acid derivative the synthesis of which will be discussed in the next section.

2.7 Preliminary Work on Functionalised Tröger's base derivatives

Having demonstrated the difficulties involved in the synthesis and isolation of target molecules **69**, **70**, **71**, the potential of smaller Tröger's base molecules was realised for the formation of functional small molecules. The next step was to determine the possibility of the formation of simple functionalised Tröger's based moieties, utilising the amine previously synthesised, **87**, and a simple carboxylic acid derivative, the synthesis of which will be discussed in the next section.

2.7.1 Synthesis of 94

Having previously synthesised the amine **87** in Section 2.6.3.2, the carboxylic acid substituted Tröger's Base, **94** was synthesised as this molecule could be used as a building block for the formation of a variety of Tröger's Base derivatives. This synthesis was first attempted directly from the 4-Amino benzoic acid, **93,** using TFA and formaldehyde as shown in Scheme 2.19. Difficulties were encountered in the synthesis of **94**, possibly from the electron withdrawing nature of the carboxylic acid, which may hinder electrophilic aromatic substitution, making the aromatic amine weakly nucleophilic and the product formation was not observed.

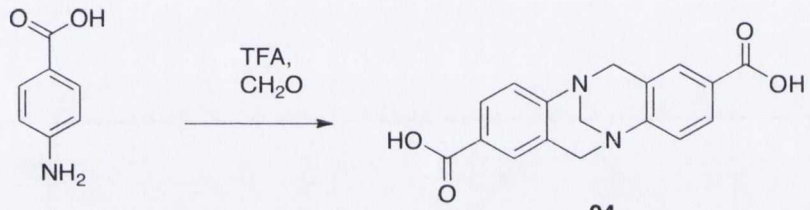

93 **94**

Scheme 2.20: *Synthesis of* ***94***

As the carboxylic acid was very difficult to generate directly, another synthetic pathway was needed for its formation. Compound **94** could be synthesised using a basic hydrolysis of the diester **96**. The first step was to synthesise the 4-amino methyl benzoate, **95**, from 4-amino benzoic acid, **93**, which is commercially available. 4-amino benzoic acid was dissolved in methanol and refluxed overnight with 2 eq. of H_2SO_4. Extraction into $CHCl_3$ yielded pink crystals, **95**, in an 80 % yield. ^1H NMR and mass spectrometry confirmed the isolation of product **95**. Compound **95** was dissolved in TFA and formaldehyde and stirred overnight at 25 °C; followed by removal of the solvent and subsequent extraction into $CHCl_3$, which yielded the ester, **96**, that could be recrystallised from methanol in 60 % yield.

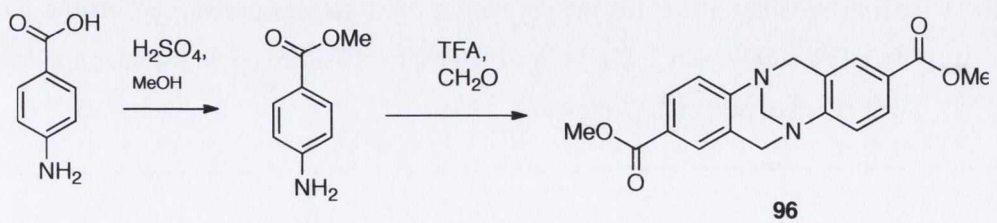

93 **95** **96**

Scheme 2.21: *Synthesis of* ***96***

The formation of **96** was confirmed by ^{1}H NMR ($CDCl_3$, 400 MHz) analysis, ^{13}C NMR ($CDCl_3$, 100 MHz) and mass spectrometry.

Single crystals of **96**, were grown by slow evaporation of $CHCl_3$ overnight from a suspension of the compound in MeOH. They were suitable for X-ray diffraction analysis, and the crystal structure is shown in Figure 2.44(left) was obtained by Dr. T. McCabe. Selected bond lengths and angles are also summarised in Table A.1, Appendix A. The view of the crystallographic b axis of the packed structure of **96** is shown in Figure 2.44 (right). As can be seen, the packing of **96** occurs with the aromatic moieties stacked perpendicular to each other, which can be very important in their development as sensors. The bond angle in the diazocine bridge, which controls the shape of the Tröger's base as seen in Table 1 is 111°.

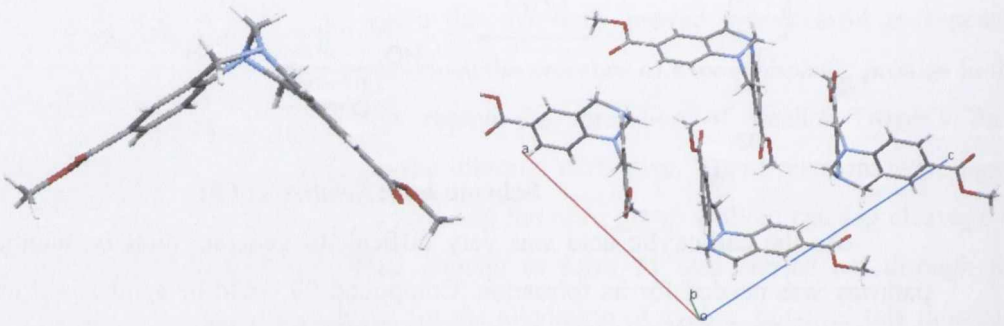

Figure 2.44: *Crystal structure and packing of* **96**

This ester **96** was then subjected to basic hydrolysis. This was carried out using 20 eq. of NaOH in ethanol and H_2O stirring overnight at room temperature. The product precipitated upon addition of 1 M HCl adjusting the pH to 5-6. This was collected by suction filtration to yield the carboxylic acid **94** in 65 % yield. ^{1}H NMR (DMSO-d_6, 400 MHz) IR and ^{13}C NMR (DMSO-d_6, 100 MHz) and mass spectrometry were used to confirm the formation of the desired carboxylic acid.

The synthesis and characterisation of the amine and carboxylic acid Tröger's base could possibly allow for the formation of structures derivatised on the terminus of the Tröger's base which lends these structures to possible supramolecular applications and this will be discussed in the following section.

2.7.2 Synthesis of 97

The coupling of simple Tröger's Base-based analogues, which allow the formation of varied arms on the terminus of the Tröger's base *via* the carboxylic acid, **94**, could lead to the formation of functional smaller Tröger's Base derivatives. The peptide coupling reaction with 1-ethyl-3-(3-dimethylaminopropyl)carbodiimide (EDCI) and hydroxybenzotriazole (HOBt) was carried out with 4-ethylamino-morpholine.

The synthesis was carried out by dissolving the carboxylic acid, **94**, and 4-Amino ethyl morpholine, in dry THF with hydroxybenzotriazole (HOBt), and stirring for 15 min under inert atmosphere at 0 °C. This was followed by the addition of EDCI, Et_3N and DMAP, which was stirred for a further 30 min at 0 °C and then at room temperature overnight.

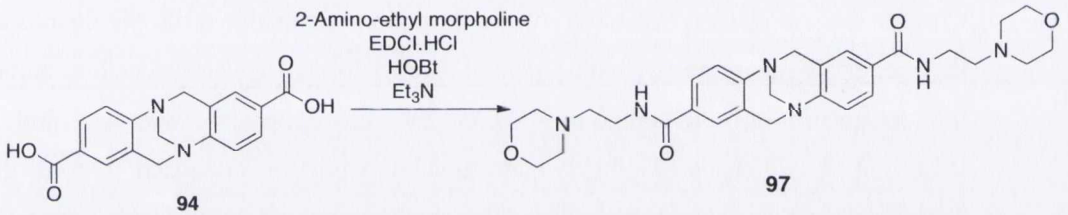

Scheme 2.22**: Synthesis of morpholine analogue of Tröger's base, **97

The reaction mixture was filtered, the solvent removed under reduced pressure and the residue extracted into $CHCl_3$, followed by washing with HCl (0.1 M) and NaOH (0.1 M) to isolate **97** as a white oil, 38 % yield.

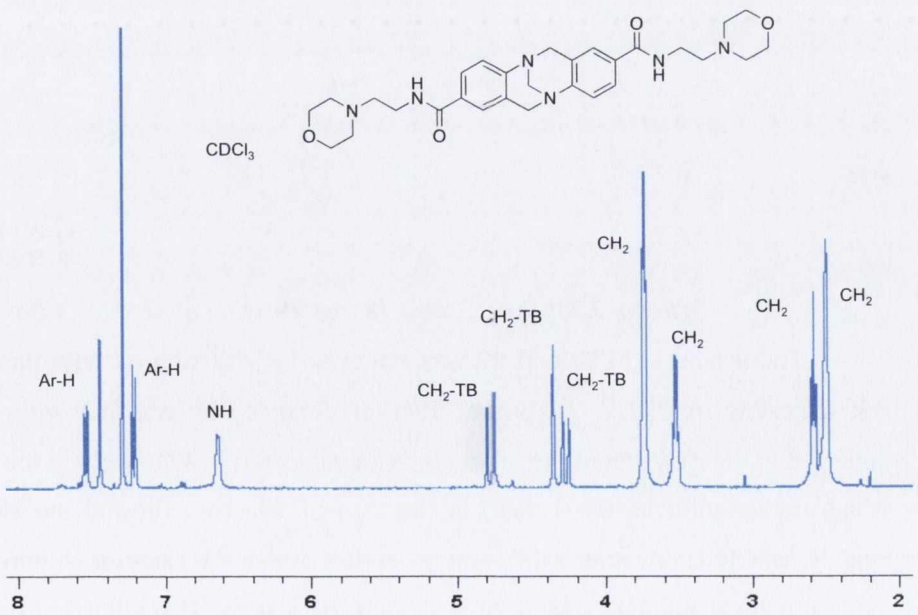

Figure 2.45**: ^1H NMR spectrum ($CDCl_3$, 400 MHz) of **97

Upon ^{1}H NMR analysis ($CDCl_3$, 400 MHz,) **97** was found to contain the necessary resonances with the morpholine moiety visible at 2.5 ppm and also the CH_2 of the diazocine ring appeared at 4-5 ppm. The Tröger's Base diazocine bridge distinctive of the CH_2 protons can be seen between 4-5 ppm. The ^{13}C NMR ($CDCl_3$, 100 MHz) shows the expected carbon resonances. The successful formation of the product was also confirmed by the observation of the signal significant of the product **97** at 535.3039 for $C_{29}H_{39}N_6O_4$ corresponding to the calculated spectrum at 535.3033. These results demonstrate the facile formation of functionalised Tröger's base derivatives. The next section will discuss functionalisation of the Tröger's base amine analogue, **87**.

2.7.3 Functionalised Tröger's Base derivatives from 87

Although the formation of cyclen based dinuclear derivatives was the focus of this Chapter it could also be expanded for the formation of functional ditopic ligands based on the Tröger's base amine, **87,** with potential affinity for various guests such as anions. With this design in mind, the compounds **98** and **99** were synthesised with a central Tröger's Base unit, to which two isothiocyanate moieties were functionalised to form thioureas. Thiourea based compounds have long been shown to exhibit anion sensing properties with the binding pocket of the urea acting as a host for anions such as hydrogenphosphate and chloride.[161] Furthermore the self-assembly of two different ligands wrapping around two guests can be envisaged, therefore potentially forming anion-templated supramolecular boxes.

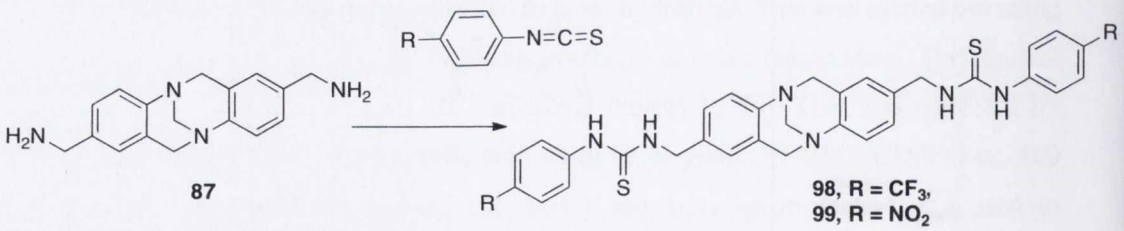

Scheme 2.23: *Synthesis of* ***98*** *and* ***99*** *using the Tröger's Base* ***87***

The synthesis of **98** and **99** was achieved by refluxing **87** with the corresponding isothiocyanate in $CHCl_3$ overnight. Filtration followed by washing with $CHCl_3$ several times led to the isolation of the products as a white solid in 43% yield in the case of **98** and as an orange solid in 40 % yield in the case of **99**. This allowed the isolation of two ligands, which demonstrated different properties due to the electron withdrawing effect of the terminal substituent. Ligand **98** was analysed first by ^{1}H NMR spectroscopy (DMSO-d_6, 400 MHz), which demonstrated the presence of the urea resonances appearing as broad

singlets at 9.81 ppm and 8.32 ppm, Figure 2.46. The diazocine protons, as assigned before, resonated between 4.1 - 4.6 ppm with the distinctive pattern characteristic of the diazocine bridge. The protons of the nitrophenyl unit resonated as two doublets at 7.71 ppm and 7.63 ppm. ^{13}C NMR (DSMO-d_6, 150 MHz) demonstrated the presence of the quaternary carbon of the CF_3 group at 180 ppm. HRMS confirmed the presence of the product at 641.1740 for $C_{31}H_{29}N_8O_4S_2$ corresponding to the calculated mass of 641.1753.

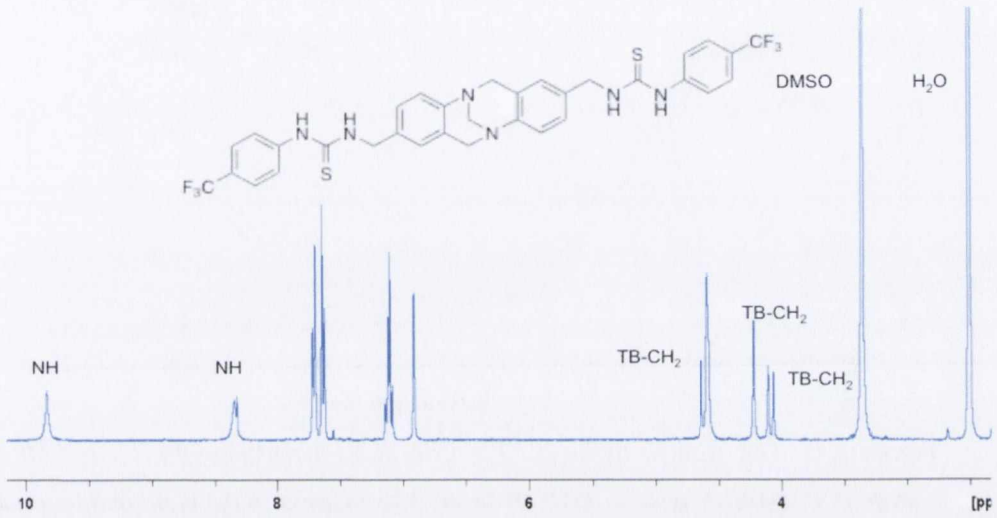

Figure 2.46**: ^1H NMR spectrum (DMSO-d_6, 600 MHz) of **98

^1H NMR (DMSO-d_6, 600 MHz,) analysis of **99** demonstrated the formation of the thiourea with the appearance of the NH thiourea protons downfield at 10.12 ppm and 8.56 ppm, shown in Figure A.11, Appendix A. The distinctive diazocine bridge of the Tröger's Base was observed between 4-5 ppm. ^{13}C NMR (DMSO-d_6, 150 MHz) showed the C-NO_2 group downfield at 146 ppm with the carbon resonances of the thiourea shown at 180 ppm.

The UV-Vis absorption spectrum of each of the compounds **98** and **99** was analysed, and showed different absorption profiles due to the different electron withdrawing nature of the nitro compared to the CF_3 analogue. The nitro analogue demonstrated a large band at 360 nm, whereas the spectrum for the CF_3 analogue showed a blue shifted band at 285 nm due to the higher energy absorption of the CF_3 phenyl group. This also caused the two compounds to show vastly different activity as anion binding agents.

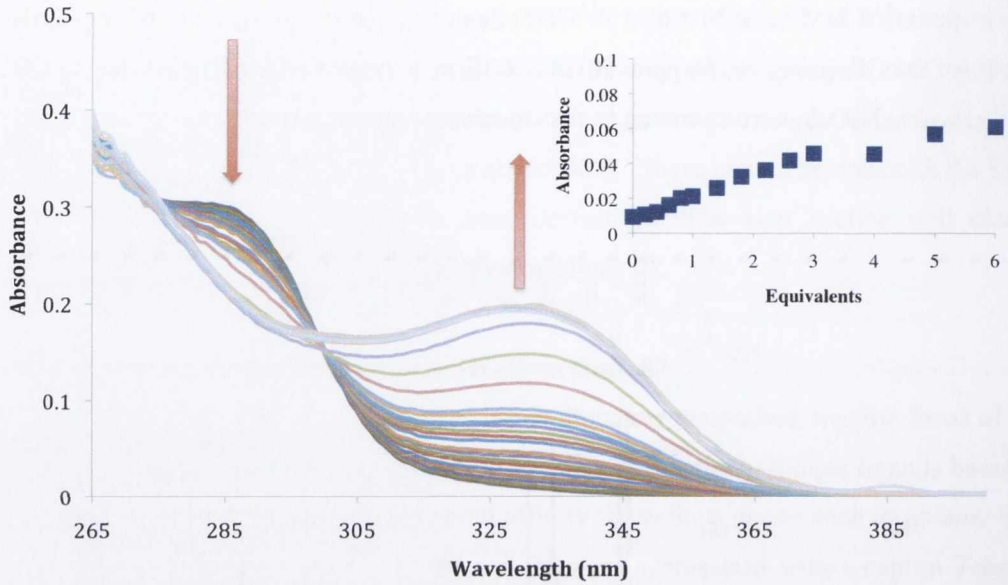

Figure 2.47: *The changes in the UV-Vis absorption spectrum of* ***98*** *(1 x 10^{-5} M) upon the addition of TBA hydroxide in DMSO.* ***Inset:*** *The changes in the band at 336 nm upon the addition of hydroxide*

The UV-Vis absorption spectrum of **98** demonstrated the presence of the band for the thiourea at 285 nm. Upon titration with various anions such as fluoride and phosphate no changes were observed in the UV-Vis spectrum. However, upon addition of hydroxide large changes were observed with the band at 285 nm disappearing and the band at 330 nm appearing up to the addition of two equivalents of hydroxide, as shown in Figure 2.47. This would suggest **98** undergoes deprotonation and not anion binding due to the changes observed occurred only upon the addition of hydroxide.

Conversely, the changes in **99** show dramatic differences in the UV-Vis absorption spectrum upon the addition of various anions. The changes of **99** in the UV-Vis absorption spectrum in DMSO upon the addition of the TBA salt of fluoride are shown in Figure 2.49. This demonstrates the appearance of a band at 487 nm, which was attributed to the ICT and experienced a hyperchromic shift upon the addition of up to 10 equivalents, while the band at 360 nm experienced a hypochromic shift.

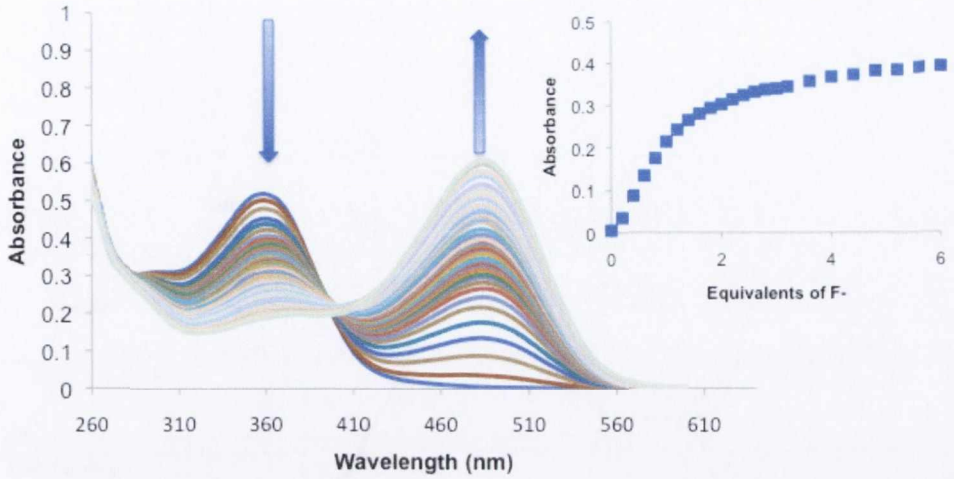

Figure 2.49: *The changes in the UV-Vis absorption spectrum of* ***99*** *in DMSO (1 x 10^{-5}M) upon the addition of TBA fluoride.* ***Inset:*** *Plot of absorbance at 487 nm versus the number of equivalents of TBA fluoride added.*

An isosbestic point was observed up to the addition of 10 equivalents at 410 nm. The band at 487 nm was plotted as a function of the number of equivalents of anion added as shown in the inset in Figure 2.49. This demonstrated a 1:1 binding of the anion and ligand. However upon fitting using SPECFIT™ the convergence was achieved with both the 1:1 and the 2:1 species present in solution. The binding constants for the fitting of **99** with fluoride, hydroxide and phosphate for both the 1:1 and the 2:1 species, are shown in Table 2.6.

The changes upon the addition of hydroxide to the ligand **99** behave in a similar manner to that of fluoride and are shown in Figure A.12, Appendix B.

Table 2.7: *Speciation and binding constants for* ***98*** *and* ***99*** *upon the addition of OH, PO_4^{3-} and F^-*

Ligand	Log β of 1:1	Log β of 2:1
99 and phosphate	0.039 ± 7.08	6.68 ± 0.22
99 and Fluoride	5.88 ± 0.07	9.03 ± 0.11
99 and OH	6.42 ± 0.31	11.25 ± 0.31

Upon the addition of phosphate to **99,** different behaviour was observed potentially due to the lower pKa of the anion. The band at 360 nm experienced a bathochromic shift

with a concomitant hyperchromic shift due to potential hydrogen bonding of the anion to the ligand.

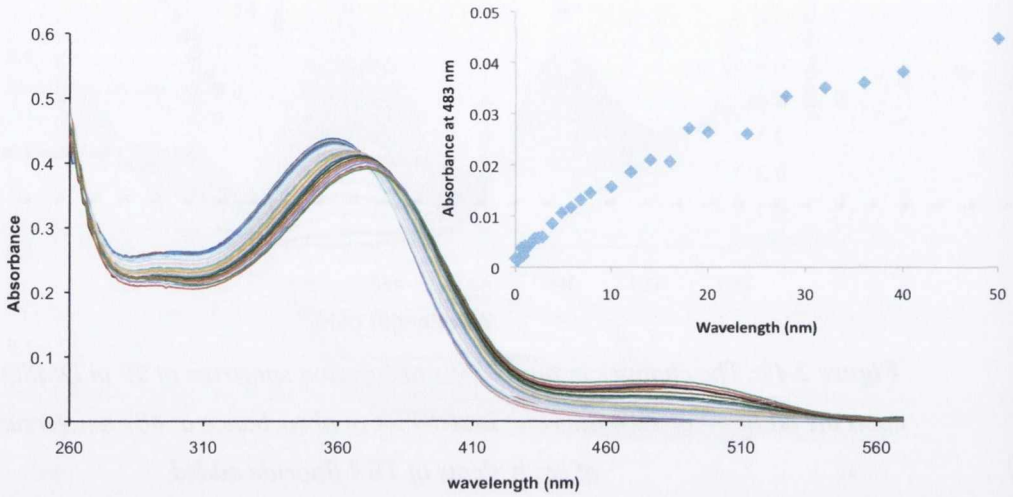

Figure 2.46: *The changes in the UV-Vis absorption spectrum of* ***99*** *($c = 1.56 \times 10^{-5}M$) upon addition of TBA phosphate.* ***Inset:*** *The plot of the absorbance at 483 nm versus the number of equivalents of TBA phosphate added.*

The changes observed for the ligands **98** and **99** suggest that ligand **99** forms hydrogen bonded complex with the phosphate anion but experiences deprotonation for the remaining anions such as hydroxide and fluoride. This however, was not observed for ligand **98** which demonstrated no response except in the case of OH, which suggested deprotonation. These molecules have demonstrated the potential for smaller Tröger's Base derivatives in supramolecular chemistry and the potential anion binding utilizing these Tröger's Base molecules.

2.8 Conclusion:

This chapter focused on the design of dinuclear complexes based on two different moieties. The first was the utilization of click chemistry in order to develop novel dinuclear lanthanide complexes, **57.Eu**, **57.Tb** and **58.Eu**. Three different precursors were synthesised and fully characterised and their photophysical properties analysed. The successful formation of 3 dinuclear lanthanide complexes was confirmed by ^{1}H, ^{13}C NMR spectroscopy and mass spectrometry. Photophysical characterisation was carried out on both the precursors and the dinuclear "clicked" complexes, which exhibited luminescent properties similar to the mononuclear species. The use of the metal bound water molecules

allowed further confirmation of the formation of the product with the number of water molecules decreasing due to binding of the triazole to the lanthanide centre.

The second possible method for the formation of dinuclear complexes, was the utilization of a Tröger's base bridge which displays a rigid chiral diazocine ring, which could prove interesting for the conformation of the complexes. The formation of the Trögers base-based macrocyclic complex proved challenging and a number of attempts to form **69** and **70** were unsuccessful. The formation of **71** however was detected in the mass spectrometric analysis but attempts to purify this ligand were unsuccessful. The formation of smaller Tröger's Base derivatives was targeted and the α-chloroamide **92** was isolated, however again functionalisation of cyclen macrocycle with the Tröger's Base was unsuccessful. Several smaller Tröger's Base derivatives were then synthesised and characterised. Compounds **87** and **94** were further derivatised to isolate functionalised Tröger's bases, of which **98** and **99** could be developed as efficient sensors for the presence of anions. Sensor **99** demonstrated sensing of fluoride and phosphate in DMSO solution with binding constants of 3.892 and 5.88 for phosphate and fluoride respectively. This emphasizes the potential of these molecules for supramolecular chemistry and lends these functionalities to the possible formation of a family of thiourea and urea based anion sensors based on Tröger's Base.

Chapter 3

Chiral Lanthanide Luminescent Gold Nanoparticles

Chapter 3: Chiral lanthanide luminescent gold nanoparticles

3.1 Introduction

As discussed in the Introduction, the lanthanide ions possess varied and interesting photophysical characteristics, such as line-like emission bands and long-lived excited states, the latter of which can be exploited using time-resolved luminescence spectroscopy.[18] Complexes utilizing these characteristics have been developed in Chapter 2, with the formation of novel dinuclear lanthanide complexes as potential luminescent probes. Recently, this field has progressed to the use of materials science to further develop the potential of such systems.[162] For example, novel research in the field of nanomaterials has shown the potential of incorporating organic or metal-organic molecules on inorganic substrates such as flat gold or gold nanoparticles (**AuNPs**) as shown in Chapter 1.[113, 163] These sensors have utilized the maximal loading of active material on the gold surface. However, there are only a few examples of lanthanide luminescent architectures functionalised on to gold surfaces despite the potential applications. In this Chapter, the development of lanthanide-based sensors was focused on the synthesis of cyclen lanthanide complexes and the functionalisation of these complexes onto **AuNPs**.

The development of sensors using cyclen-based macrocycles can be carried out using three main strategies: i) the displacement of metal bound water molecules from the lanthanide ion, switching on the luminescence of the system, ii) the binding of an external antenna to the complex, quenching the emission or iii) the binding of antenna to the complex and causing switching on of the luminescence, shown schematically in Figure 3.1. In this Chapter, the design of lanthanide-based sensors will focus on the first strategy, which involved the enhancement of the lanthanide emission with the displacement of metal bound water molecules by an analyte, Figure 3.1 (i). The presence of OH oscillators can effectively quench the luminescence of the lanthanide, deactivating the excited state through non-radiative processes. Although potentially a disadvantage, this characteristic lends itself to the field of molecular sensing, as displacement of these metal bound water molecules by the analyte removes this vibrational deactivation and 'switches on' or enhances the luminescence of the lanthanide ion.[164]

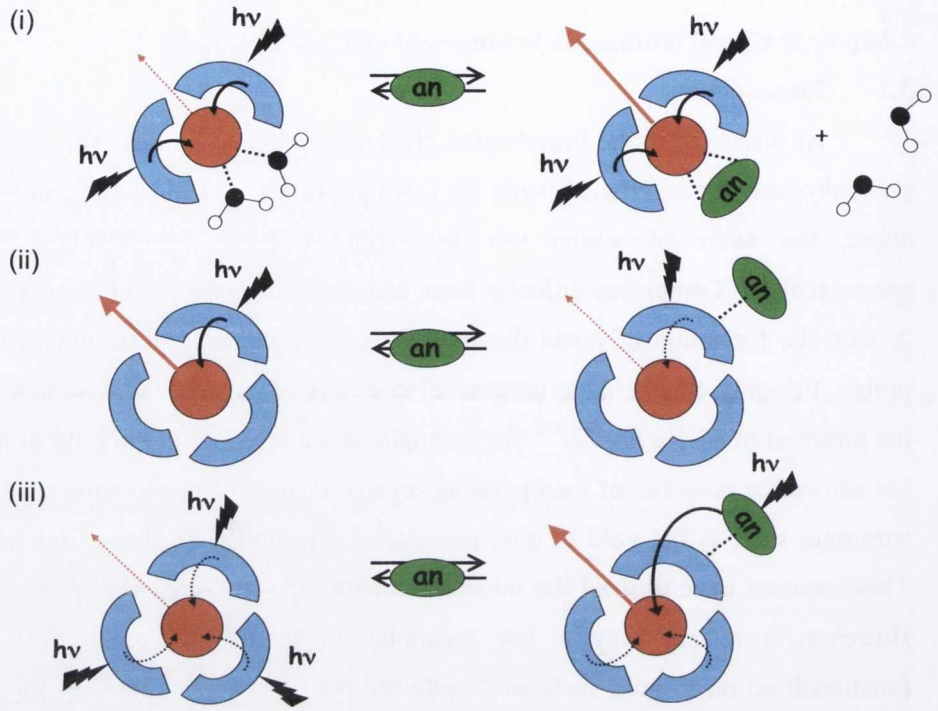

***Figure 3.1**: Three possible processes for the sensing of analytes using cyclen based lanthanide complexes i) displacement of metal bound water molecules or contribution of an analyte by ii) quenching the lanthanide luminescence iii) sensitising the lanthanide luminescence*[165]

The displacement of the solvent molecules responsible for the deactivation process must be enthalpy favoured. Due to the Lewis acid nature of the lanthanide ion, suitable analytes must possess basic properties and contain one or several good donor atoms, such as oxygen or nitrogen. Examples of such analytes are carboxylates or β-diketonates. Furthermore, these analytes can also contain a chromophore, which greatly enhances the luminescence by sensitising the excited states of the lanthanide ion *via* the antenna effect. Previously, cyclen based lanthanide complexes have been seen to be sensors of malonic acid, terephthalic acid, acetates, and phosphates such as those outlined in Figure 1.7.[140] This has been observed by Cantuel *et al.*,[166] who demonstrated the design of a tethered naphthyl acetic acid chromophore, which upon cleavage can actively displace the water molecules switching on the lanthanide luminescence, showing potential in drug delivery applications. These examples emphasise the ability of lanthanide complexes to sense analytes through the displacement of water molecules. The potential of this class of compounds for the formation of nanomaterials as specific luminescent probes is the central focus of this Chapter. The following sections will discuss the synthesis of lanthanide complexes and the tuning of their luminescence in the presence of β-diketonates and

carboxylates to form intelligent nanomaterials for further application in the fields of chemosensing.

The ability of these tethered cyclen-based lanthanide complexes for the sensing of analytes depends on their design. Moreover, one has to ensure the incorporation of the lanthanide complexes onto the surface of **AuNPs** occurs with little quenching or disturbance of the properties of the complexes themselves. Consequently, the design of the cyclen derivative is essential in order to minimize the quenching effect due to the nanoparticle. This has been shown to be possible in the Gunnlaugsson group with the incorporation of a cyclen-based sensor **28.Eu** onto the surface of the gold.[167] This demonstrated that the incorporation of a C_{12} chain onto the cyclen moiety limited the quenching of the lanthanide luminescence by the gold surface and prompted the design of sensors, **41** and **42**, which could be functionalised on the surface of **AuNPs**.

3.2 Design of the Sensors

The development of lanthanide luminescent **AuNPs** begins with the design of the complex to be attached to the gold surface. The lanthanides, despite the inherent advantages for biological sensing, have been shown to be toxic when uncomplexed. Therefore it is necessary to develop ligands, which allow for the formation of complexes that are both thermodynamically and kinetically stable under physiological conditions. Functionalised 1,4,7,10-tetraazacyclododecane (Cyclen) has been shown to be a very stable macrocycle for the complexation of the lanthanides as discussed in Chapter 1, where the use of carboxylate or acetamide arms provides the coordination environment for the formation of hepta and octadentate ligands.[168] A key component in the development of sensors based on this design, was discussed in previous papers,[169] using coordinatively unsaturated lanthanide complexes, designed in such a way that the high coordination requirements of the lanthanides are fulfilled by the use of labile metal bound water molecules. This design originally used by Parker *et al.*[170] will be utilized for the development of luminescent sensors.

The central focus of this chapter was the formation of lanthanide functionalised **AuNPs** for potential application as chiral luminescent probes. Within the Gunnlaugsson group chiral luminescent helicates and bundles have been successfully formed utilising simple chiral naphthyl chromophores as discussed in the formation of the helicates in Chapter 1.[39-40] Thus the same naphthyl moieties were chosen for the design of these cyclen-based complexes not only because they bring chirality to the system but they also allow sensitisation of Eu^{3+} emission. The requirements for the surface functionalisation of

the **AuNPs** is the incorporation of a C_{12} thiol chain of 12 carbons to minimize quenching of the luminescence, as discussed in Chapter 1. We believe that these properties are optimal for the formation of luminescent chiral lanthanide complexes, and for this reason these chromophores were functionalised onto the **AuNPs**. The vital aspect of this design was the potential for these complexes functionalised on the **AuNPs** to act as chiral luminescent sensors such as demonstrated by Bruce *et al.*[164a, 171]

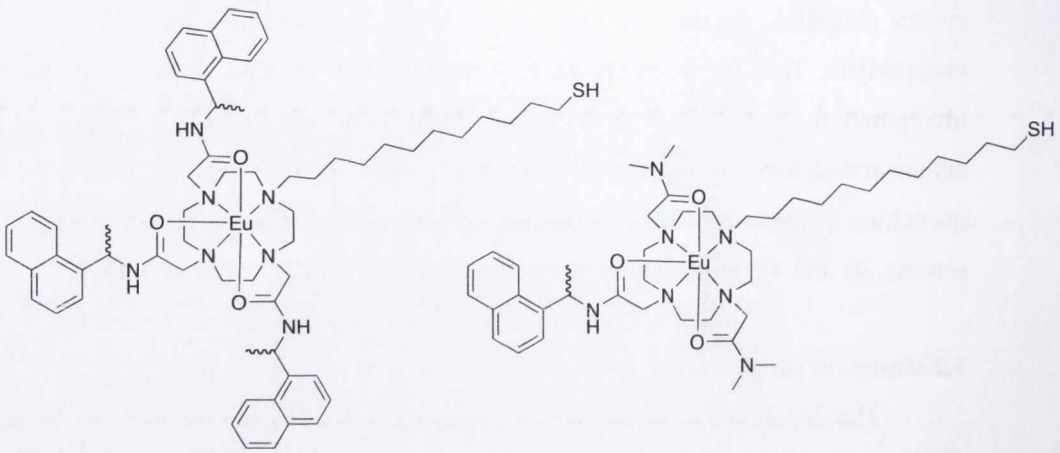

41*R*.Eu
41*S*.Eu

42*R*.Eu
42*S*.Eu

With all of this in mind, the complexes **41.Eu** and **42.Eu** were chosen as targets for these chiral lanthanide complexes. The ideal distance from the nanoparticle is approximately 12 carbon lengths as this has been found to minimize quenching of the lanthanide luminescence by the gold surface.[167a] For this reason, the first step in the synthesis of **41** and **42**, was the formation of an alkyl thiol chain using the commercially available dibromododecane, followed by incorporation into the cyclen structure, which was finally reacted with the 2-chloro-*N*-(1-naphthalenylethyl)]-acetamide, utilized to act as a sensitizing antennae. This was followed by complexation to form the corresponding europium complexes.[172] The above synthesis is described in the next sections.

3.3 The synthesis of 41

The thiol chain, **102**, was synthesised following a method described by Yokokawa *et al.*,[173] by stirring a solution of 1,12-dibromododecane, **100,** in CH_3CN with potassium thioacetate for three days, Scheme 3.1.

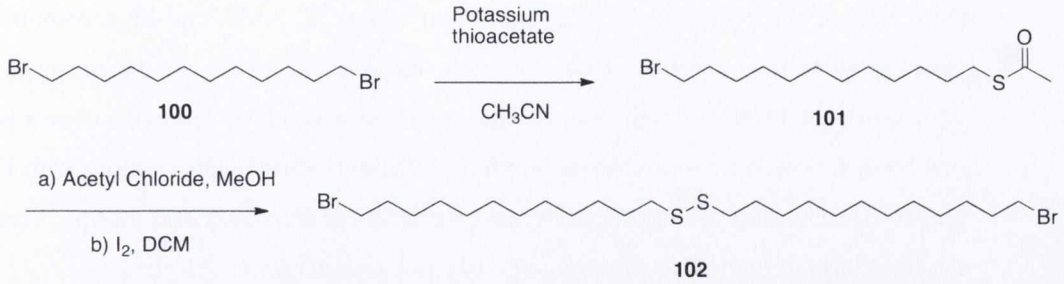

Scheme 3.1: *The synthesis of* **102**

After removal of CH_3CN under reduced pressure and column chromatography (using hexane/ethyl acetate, 95:5 as eluent), the desired product was isolated in 53 % yield. Both ^1H NMR ($CDCl_3$, 400 MHz) and ^{13}C NMR ($CDCl_3$, 100 MHz) analysis demonstrated the successful formation of the product **101**, Figure B.1, Appendix B. This product was then deprotected by dropwise addition of **101** into a solution of acetyl chloride in MeOH, cooled to 0 °C, and stirred overnight. The removal of solvent under reduced pressure, yielded the product as an intermediate, which was immediately dissolved in CH_2Cl_2 and oxidised by iodine, to give the disulfide, **102**, which was isolated after aqueous work up to yield a yellow solid in 47% yield.

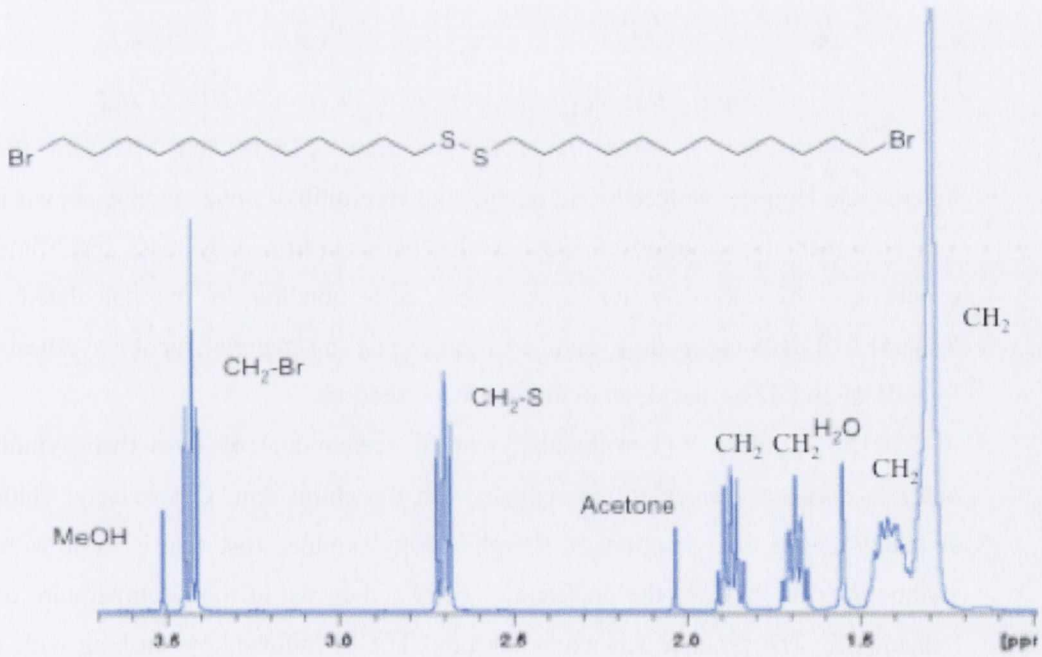

Figure 3.2*: ^1H NMR spectrum ($CDCl_3$, 400 MHz) of* ***102***

^1H NMR analysis ($CDCl_3$, 400 MHz) showed the formation of the product **102**, Figure 3.2, with the CH_2 located in proximity to the thiol and the bromide showing significant upfield shifts in comparison to that of the CH_2 in the centre of the chain. The

formation of the product was also confirmed using ^{13}C NMR and high resolution mass spectrometry. The disulfide, **102**, was then dissolved in $CHCl_3$ in the presence of four equivalents of Et_3N and four equivalents of cyclen was added dropwise over a period of one hour, followed by refluxing the mixture overnight. Subsequent washing with 1M KOH and H_2O, according to the procedure developed in the Gunnlaugsson group,[174] resulted in the formation of the bis-cyclen product, **103**, as a yellow oil in 70% yield.

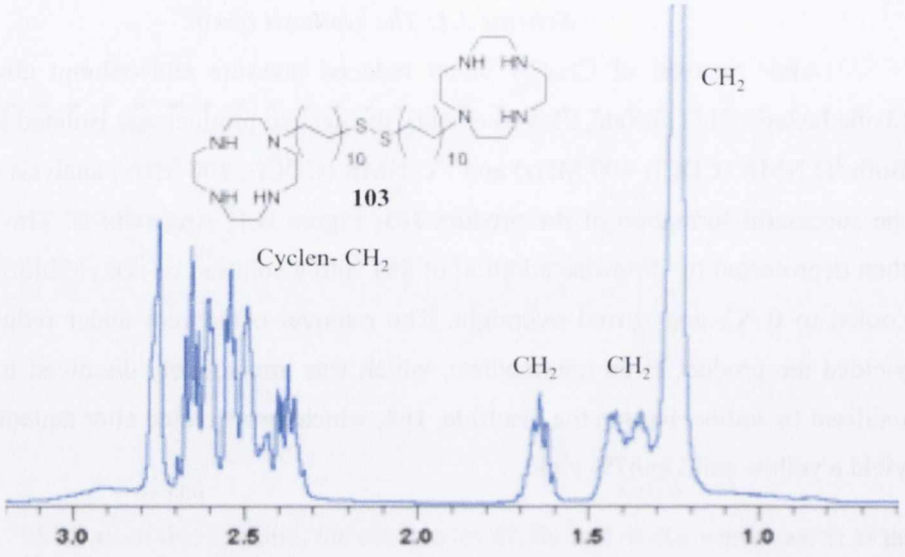

Figure 3.3: *^1H NMR spectrum ($CDCl_3$, 400 MHz) of* ***103***

The distinctive broad ^1H NMR spectrum ($CDCl_3$, 400 MHz) of the cyclen macrocycle coupled with the long chain, lead to multiple broad signals, shown in Figure 3.3. However, the isolation of **103** has also been confirmed by mass spectrometry with exact mass of 743.6529 for $C_{40}H_{86}N_8S_2$, corresponding to the calculated mass of 743.6417.[174] This compound was then used as starting material for the synthesis of both ligands **41** and **42** as discussed in the following sections.

The 2 chloro-*N*-(1-naphthalenylethyl)] acetamide, **105**, was then synthesised in order to alkylate the cyclen macrocycle with the chiral arm. Chloroacetyl chloride was added dropwise to a solution of 1-naphthylethyl amine, **104**, (carried out with R or S enantiomers) at 0 °C, in the presence of Et_3N and stirred at room temperature overnight, Scheme 3.2. The product was extracted into CH_2Cl_2, followed by washing with 1M HCl, 1M KOH and H_2O, before removal of the solvent under reduced vacuum to yield the product, **105**, as a dark brown solid, 80 % yield.

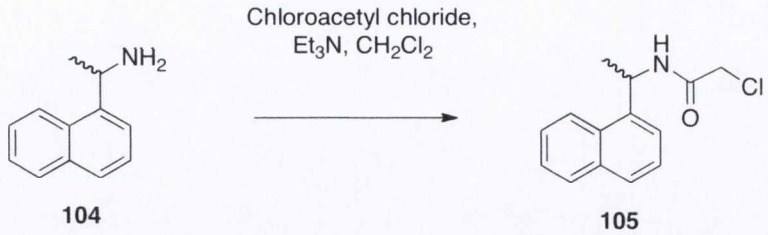

104 105

Scheme 3.2**: The synthesis of **105

The ^{1}H NMR spectrum ($CDCl_3$, 400 MHz) demonstrated the formation of the desired product, **105**, with the CH of the naphthyl group at 5.94 ppm and the CH_2 of the acetamide linkage observed at 4.05 ppm, Figure 3.4. ^{13}C NMR showed the CH_2 in the DEPT-135 at 42.1 ppm, which appeared after reaction with chloroacetyl chloride.

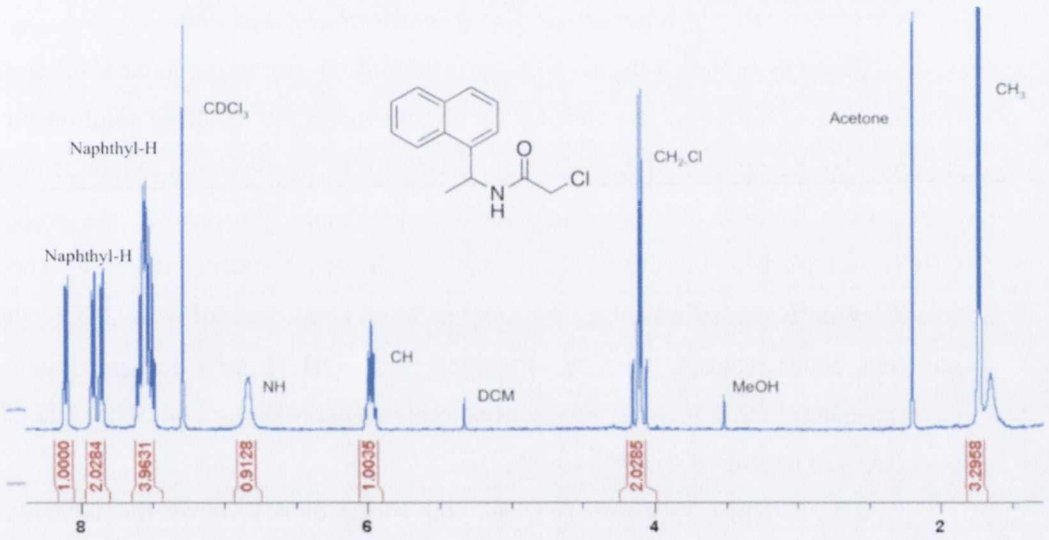

Figure 3.4**: ^{1}H NMR spectrum ($CDCl_3$, 400 MHz) of **105

Mass spectrometry further confirmed the formation of the product, **105**, with exact mass observed of 270.0343 for $C_{14}H_{14}ClNO$ corresponding to the calculated mass of 270.0662. Having successfully synthesised the α-chloro amide, the next step was to incorporate this into the cyclen macrocycle *via* alkylation of the cyclen amine, according to Scheme 3.3.

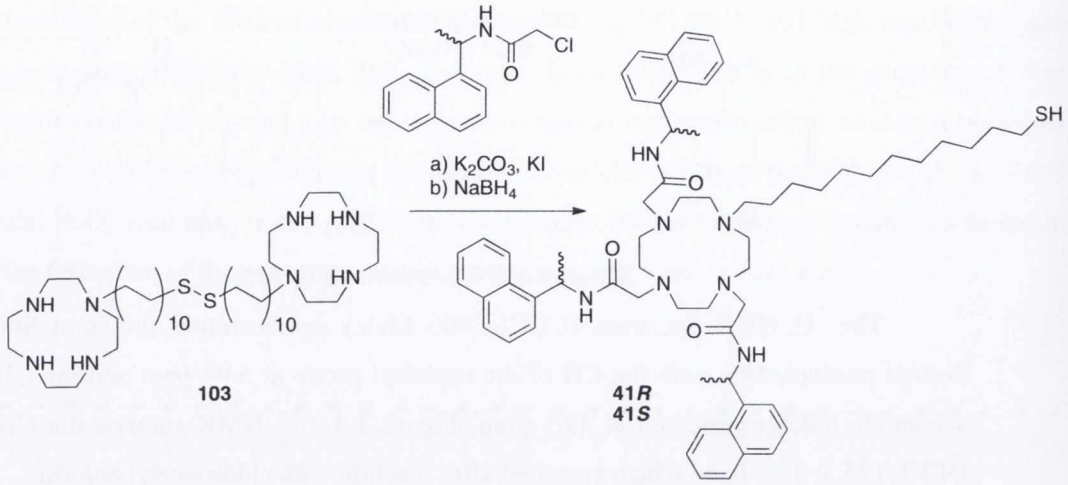

Scheme 3.3**: The synthesis of **41R** and **41S

This was achieved by the addition of **105** dropwise to a cooled solution of **103** in the presence of 6.6 eq. of KI and K_2CO_3 and refluxing the resulting solution for 1 week, followed by the addition of $NaBH_4$, with vigorous stirring overnight to reduce the disulfide bond. After removal of solvent under reduced pressure, the residue was redissolved in $CHCl_3$ and washed with 1M HCl to remove unreacted starting material. The aqueous solution was then basified using 1M KOH solution and extracted with $CHCl_3$, the solvent removed under reduced pressure, dissolved in MeOH (1 mL) and precipitated out of swirling diethyl ether to yield **41** after column chromatography with 95:5, CH_2Cl_2/MeOH gradient, as a brown oil in 35 % yield.

The ^1H NMR spectrum ($CDCl_3$, 400 MHz) of **41**, shows the formation of the product with the naphthyl protons resonating between 7 and 10 ppm, Figure B2 and B.3, Appendix B. The CH_2 protons of the chain and the cyclen macrocycle form broad multiplets both due to the number of protons associated and also due to the amorphous nature of the oil. In the ^{13}C NMR the resonances of each carbon was detected, the acetamide arm CH_2 were shown to resonate at 38.2 ppm. The resonances for the CH_2 acetamides were observed, as well as those of the chain carbons at 27.3-29.4 ppm, with the naphthyl carbons appeared at 122.9-129.1 ppm. The mass of the ligand was observed in the mass spectrometric analysis at 1006.6348, which was attributed to the $[(M+2H)^+/2]^+$ signal for $C_{62}H_{84}N_7O_3S$ corresponding to the calculated spectrum at 1006.6356 as shown in Figure 3.5 with the isotopic distribution.

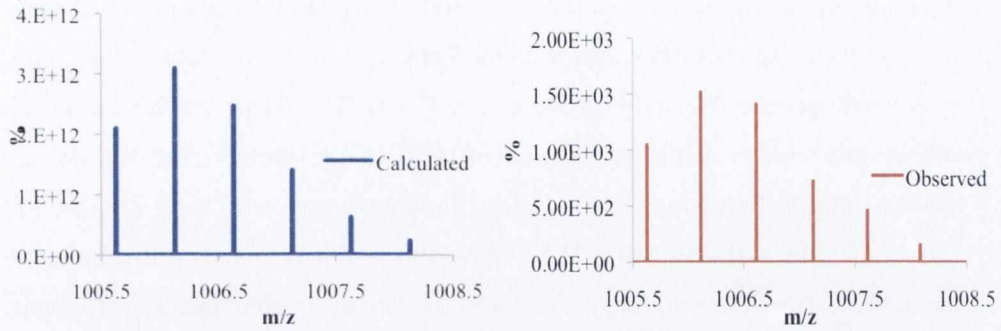

***Figure 3.5**: a) MALDI spectrum of **41R**, b) Recalculated spectrum of* $[(M+2H)^+/2]^+$

The synthesis and characterisation of two enantiomers of the trisubstituted ligand **41** were carried out and shown to be successful. ^1H NMR ($CDCl_3$, 400 MHz) demonstrated the successful formation of the product, which was confirmed by mass spectrometry.

3.4 Synthesis and Characterisation of Model Compound 106

It had been envisaged that the SH moiety might be able to bind to the metal centre (through possible displacement of the metal bound water molecules). Consequently, in order to highlight the potential effect of the thiol on the lanthanide coordination environment, ligand **106**, with an alkyl chain was synthesised. The synthesis follows the same route as for **41**, beginning with the synthesis of the monosubstituted cyclen ligand **107**, Scheme 3.4.

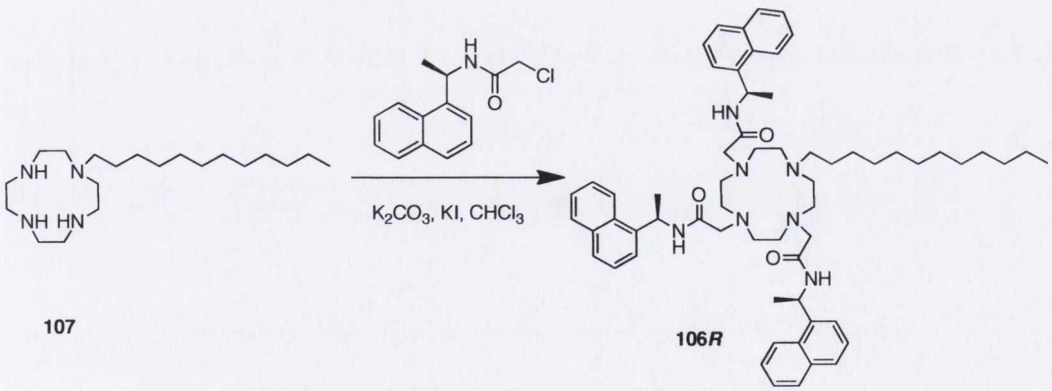

Scheme 3.4:** Synthesis of model compound **106

The monosubsituted cyclen ligand, **107**, was synthesised by addition of 4 equivalents of cyclen, 4 equivalents of Et_3N and 1 equivalent of bromododecane. The solution was washed with 0.1 M KOH solution and yielded the product **107**, as a yellow oil

in 49% yield. ^{1}H NMR ($CDCl_3$, 400 MHz) confirmed the formation of the monosubstituted ligand with the CH_2 protons of the chain and the cyclen resonating at 1.32 ppm and 2.38 ppm respectively. HRMS confirmed the formation of the product at 341.3639 with the calculated ligand at 341.3644 for the species $C_{20}H_{45}N_4$. **105** (*R* or *S* enantiomers), was then added dropwise to a stirred solution of **107,** in the presence of K_2CO_3 and KI and subsequently refluxed for 7 days. After filtration to remove inorganic salts, followed by extraction with 1 M HCl and 1 M KOH, washing with H_2O and removal of solvent under reduced pressure, the resulting residue was purified using column chromatography (95:5 % DCM/MeOH gradient) to yield **106** as a brown oil in 33 % yield. The successful formation of the desired product was confirmed using ^{1}H NMR spectroscopy, Figure 3.6. The α-CH proton of the N-(1-naphthalenylethyl) acetamide can be seen at 5.5 ppm. The cyclen area is also much more well resolved with the cyclen protons showing characteristic broad cyclen peaks. ^{13}C NMR ($CDCl_3$, 100 MHz) showed the naphthyl CH carbons resonating between 127.7 and 123.1 ppm and the CH_3 of the long alkyl chain at 14.1 ppm. Mass spectrometry demonstrated the successful formation of the product with the exact mass 996.6447 for $C_{62}H_{83}N_7O_3Na$ agreeing with the calculated value 996.6455.

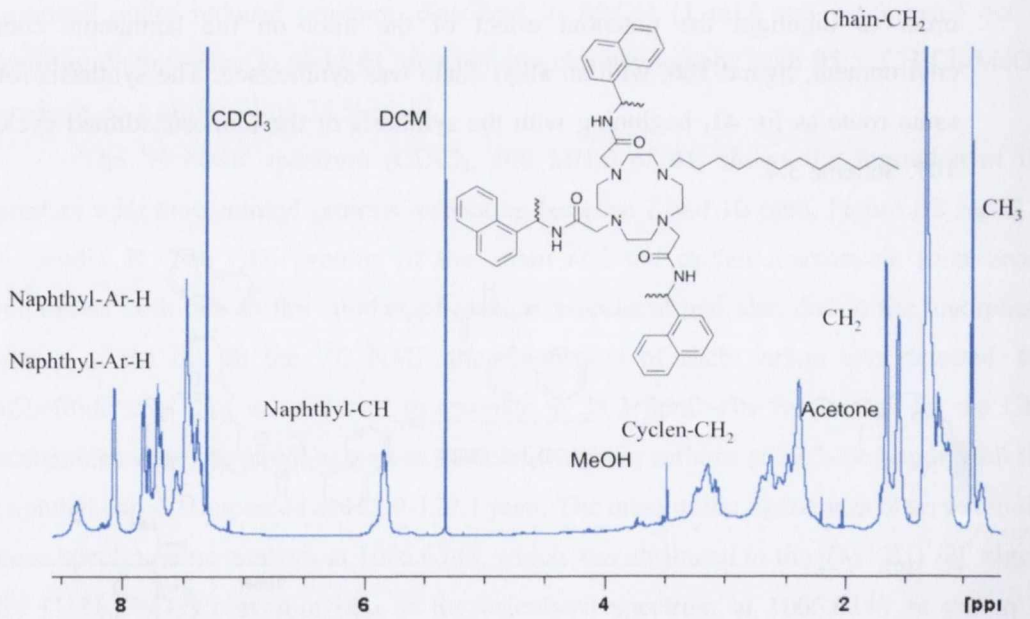

Figure 3.6**: ^{1}H NMR spectrum ($CDCl_3$, 600 MHz) of model compound **106

Having carried out the successful synthesis of both the ligand **41*R*** and **41*S*** and also the model compound **106**, the next step was to carry out the synthesis of the monosubstituted product, **42**.

3.5 Synthesis and Characterisation of 42*R* and 42*S*

The synthesis of ligands **42*R*** and **42*S*** was more challenging than the synthesis of **42**. To achieve the synthesis of the desired product two synthetic pathways were considered.

1) **stepwise synthesis *via* successive alkylations (Method A)**

2) **One pot synthesis (Method B)**

3.5.1 Method A- Synthesis and Characterisation of 42*S*

The first pathway involved the synthesis of **42*S*** as shown in Scheme 3.5, starting with monosubstitution of the cyclen macrocycle followed by addition of the alkyl chain. Monosubstitution of **49** was achieved by stirring Et_3N in $CHCl_3$ in the presence of 2 chloro-*N*-[(1-naphthalenylethyl)] acetamide, **105*S*** by stirring overnight. The organic layer was washed with 1 M KOH followed by removal of solvent under reduced vacuum, yielded **108,** in high purity and in quantitative yield.

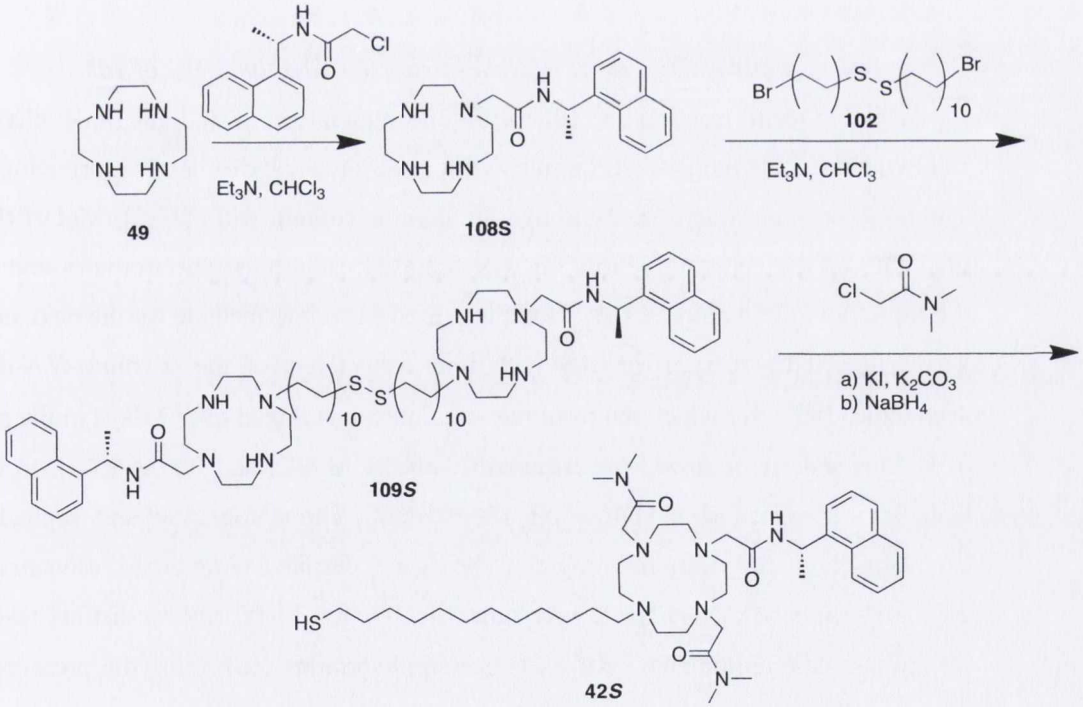

***Scheme 3.5**: Stepwise synthesis of **42S** via successive alkylations*

The ^1H NMR spectrum ($CDCl_3$, 400 MHz) showed the successful formation of **108**, with the CH_2 protons of the naphthyl acetamide appearing at 3.25 ppm, shifted from the peaks of the starting material **105**, which resonated at 4.05 ppm, Figure 3.7. The ^{13}C NMR

spectrum ($CDCl_3$, 100 MHz) showed the carbon resonances of the acetamide CH at 11.2 ppm shifted from the resonance of the starting material at 45.2 ppm demonstrating alkylation of the cyclen macrocycle. Mass spectrometry confirmed the formation of the product with a signal at 384.2755 for $C_{22}H_{34}N_5O$ corresponding to the calculated mass 384.2763.

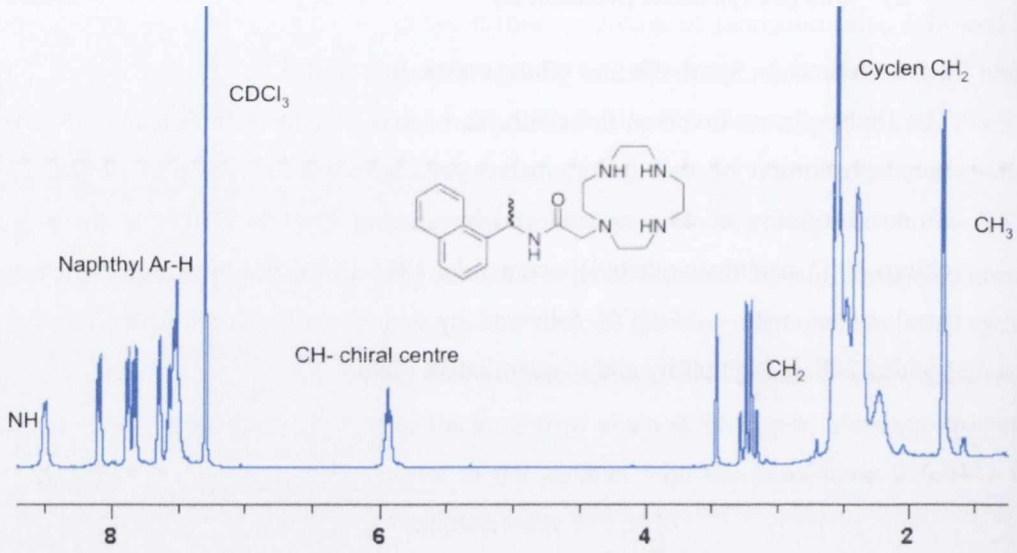

Figure 3.7: *The ^1H NMR spectrum ($CDCl_3$, 400 MHz) of* ***108***

Subsequent reaction of **108** with one equivalent of the disulfide chain, **102**, following the same monosubstitution conditions discussed above, lead to formation of **109**. The brown residue was passed through an alumina column with CH_2Cl_2/MeOH (95:5) as gradient and the resulting yellow oil was analysed using mass spectrometry and showed the formation of the product **109**, which was used as an intermediate for the next step. This was achieved by reaction of **109** with four equivalents of the α-chloro-*N,N*-dimethyl acetamide, **105**, after which the resulting solution was refluxed over 7 days in the presence of K_2CO_3 and KI, followed by extraction with 0.1 M HCl and 0.1 M KOH, in order to isolate the product as a yellow oil after column chromatography and sephadex size exclusion chromatography in 3 % yield. The ligand, despite having broad resonances in the aliphatic region of the ^1H NMR spectrum (MeOD, 400 MHz), shows distinct resonances for the aromatic region and for the CH acetamide protons confirming the presence of the naphthyl chromophore.

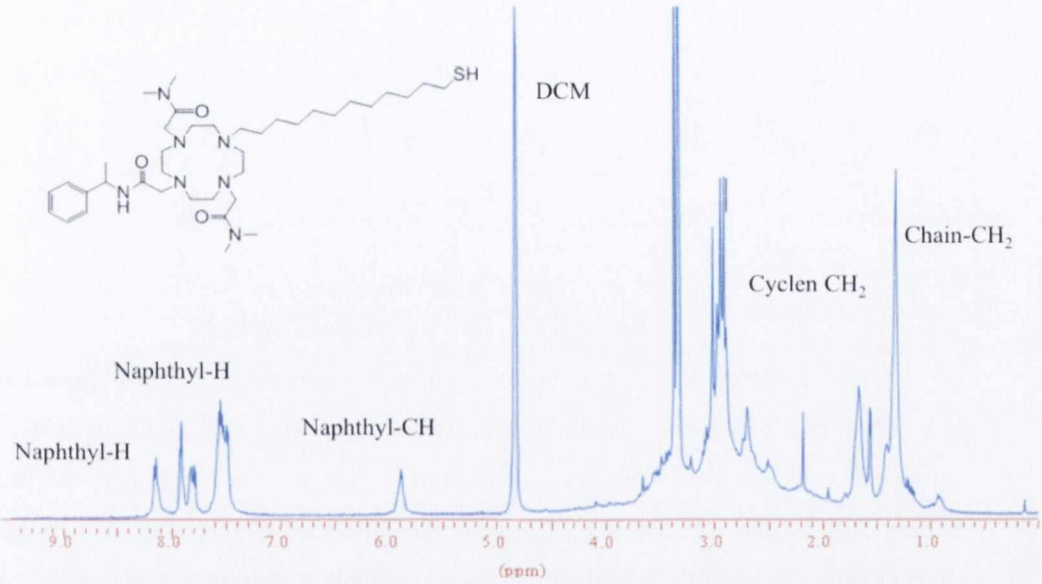

***Figure 3.8**: [1]H NMR spectrum (MeOH, 400 MHz,) **43S** enantiomer of ligand*

The broadening of the ^{1}H NMR spectrum (MeOD, 400 MHz) has been attributed to possible conformational change and folding in solution, Figure 3.8. The ^{13}C NMR spectrum (MeOD, 100 MHz) demonstrated the formation of the product as the CH_3 carbons of the acetamide arms were observed at 29 ppm. Also, the CH_2 carbon resonances of the chain and the acetamide arms were observed between 28.4 ppm and 57.1 ppm. Mass spectrometry confirmed the formation of the product with the signal observed at 753.5369 for $C_{42}H_{71}N_7O_3S$, corresponding to the calculated value of 753.5339. Having used the procedure for the multiple step alkylation of the cyclen macrocycle the next step was to demonstrate the one pot synthesis of the other enantiomer.

3.5.2 Method B- Synthesis and Characterisation of 42*R*

Method B utilised the starting material **103**, for the synthesis of the monosubstituted cyclen macrocycle and then attached the 2-chloro-*N*-(1-naphthalenylethyl) acetamide, **105** and α-chloro-*N,N*-dimethyl acetamide arms in a one pot reaction, avoiding successive purification steps.

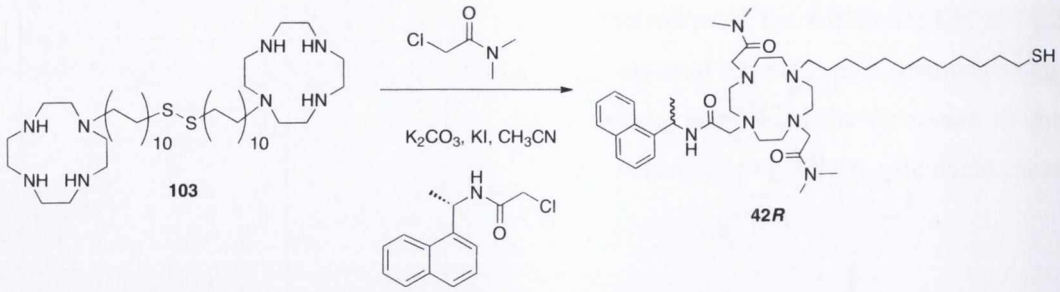

Scheme 3.6**: One pot synthesis of **42R

The first step was to form **103**, as shown in Scheme 3.1 and discussed in section 3.3. This chain was subsequently alkyated using two equivalents of **105** and four equivalents of α-chloro-*N,N*-dimethyl acetamide in a one pot reaction in the presence of excess K_2CO_3 and KI in order to tetraalkylate the macrocycle. Purification by column chromatography (CH_2Cl_2/MeOH 95:5 gradient) followed by size exclusion chromatography on sephadex in MeOH, yielded ***42R*** in 15 % yield. The ^{1}H NMR spectrum of the ligand, Figure 3.9, was similar to that seen in Figure 3.8, which correlates with both the ***R*** and ***S*** enantiomers. The ^{13}C NMR spectrum also showed the correct number of carbon resonances confirming the formation of the product. Mass spectrometry further confirmed the successful formation of the product, with the mass found to be 753.5369 for the species $C_{42}H_{71}N_7O_3S$, agreeing with the calculated mass of 753.5339.

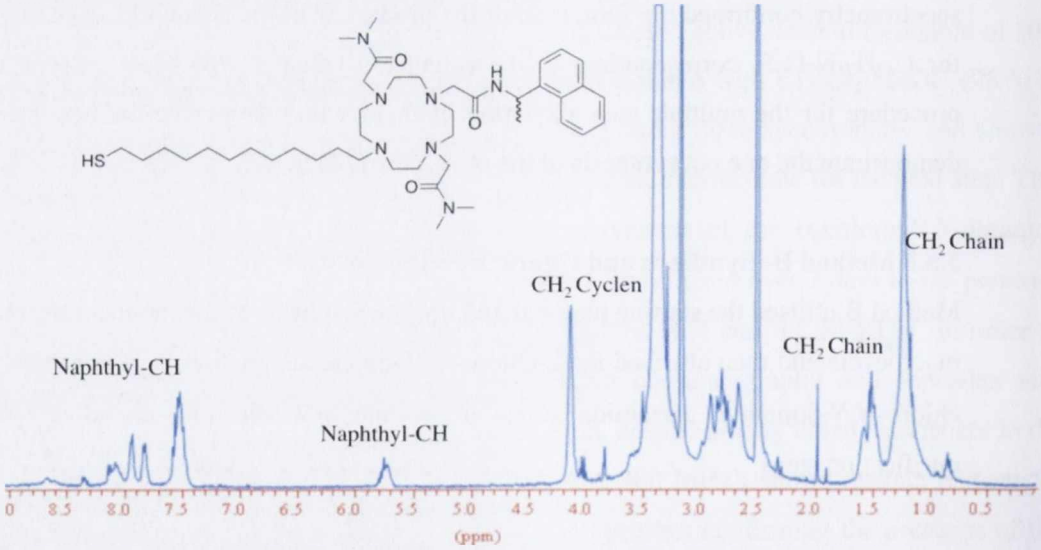

Figure 3.9**: ^{1}H NMR spectrum (400 MHz, DMSO-d_6) of **42R

The synthesis of **42** was carried out successfully for both *R* and *S* enantiomers however, the one pot synthesis was found to be more efficient as this yielded the product in 15 % yield compared to 3 % yield. Also, the one pot process required column chromatography to be carried out once, whereas the multiple step synthesis required

purification at each step. As mentioned for **41** there is a possibility that the thiol could coordinate to the metal centre. For this reason, the next step was to synthesise the model compound **110** for the monosubstituted system.

3.6 Synthesis of model compound 110

The alkyl analogue of **43** was also developed, replacing the thiol chain with a simple alkyl chain in order to compare the binding of metal bound water molecules.

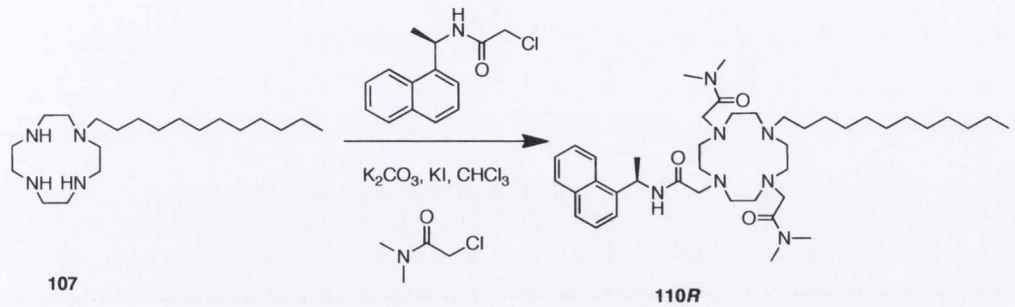

Scheme 3.7**: Synthesis of model compound **110R

Bromododecane was refluxed in CH_3CN overnight with 4 eq. of cyclen and Et_3N yielding the monosubstituted product **107**, which correlated with the ^1H NMR spectrum ($CDCl_3$, 400 MHz) and mass spectrometric analysis observed for the synthesis of **106,** in Scheme 3.4. A one pot synthesis with consecutive additions of **105** in the presence of K_2CO_3 and α-chloro-*N,N*-dimethyl acetamide was performed in order to alkylate the remaining positions on the macrocycle. The product was isolated by filtration through a plug of celite, extraction into $CHCl_3$ and washing with 1M HCl and 1M KOH solution, solvent was removed under reduced pressure and the product was precipitated from swirling diethyl ether to yield **110*R***, as a yellow oil in 80 % yield. The formation of the desired product **110*R*** was clearly evidenced in the ^1H NMR spectrum, as shown previously with the characteristic resonances of the CH_2 and naphthyl protons of the arms. Mass spectrometry confirmed the ligand formation with mass observed at 722.5695 for the species $C_{42}H_{72}N_7O_3$, corresponding to the calculated spectrum at 722.5697.

The two target molecules **41** and **42** were successfully synthesised and isolated along with the model compounds **106*R*** and **110*R***. The synthesis and characterisation of the corresponding Eu^{3+} complexes were also carried out and will be discussed in the following section.

3.7 Complexation of 42 (*R, S*), 43 (*R, S*), 106*R* and 110*R*

The lanthanide complex **41*R*.Eu** was formed by refluxing the ligand with 1.1 equivalents of Eu $(CF_3SO_3)_3$ under argon in CH_3CN for 18 hours. The complex was precipitated from swirling diethyl ether and dried under vacuum to yield **41*R*.Eu** as a brown oil in 86 % yield.

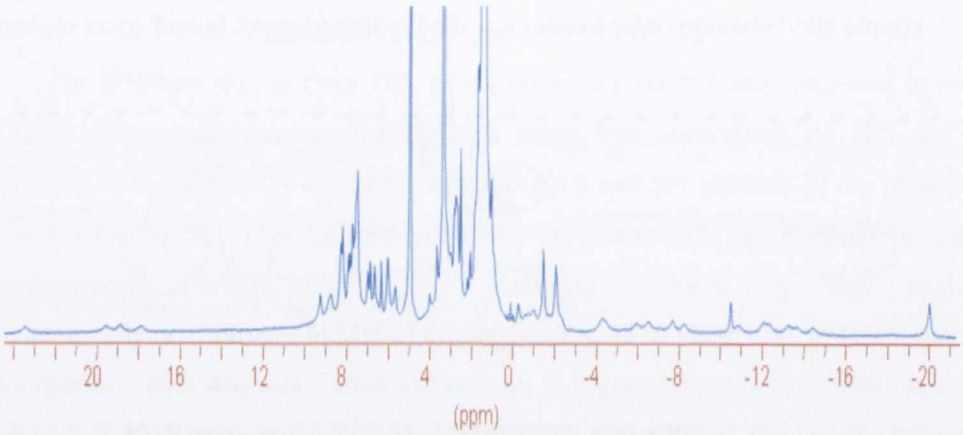

Figure 3.10**: ^1H NMR spectrum ($CDCl_3$, 400 MHz) of complex **41R.Eu

The successful formation of the product was confirmed by ^1H NMR ($CDCl_3$, 400 MHz) analysis. In this case, the axial and equatorial protons of the cyclen ring, as well as the acetamide CH_2 and naphthyl protons, were shifted by the europium centre. Mass spectrometric analysis is an important tool for the determination of complexation as the isotopic distribution pattern shows the distinctive signals of the Eu^{3+}, Figure 3.11.

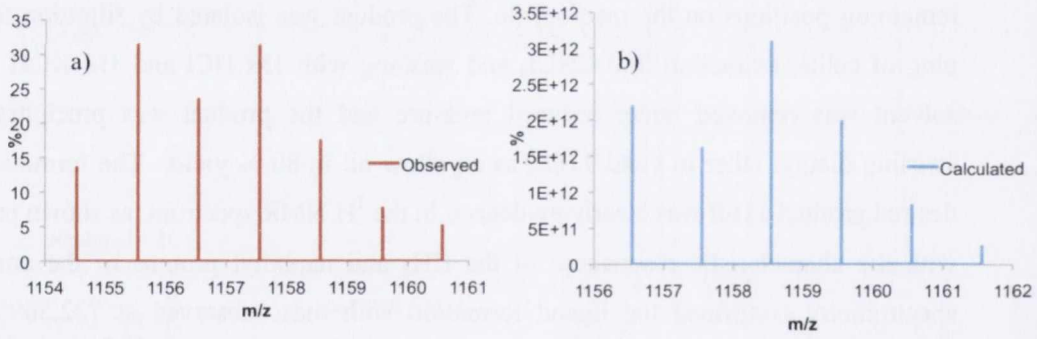

***Figure 3.11**: a) MALDI spectrum of **41R.Eu** and b) Calculated spectrum for $C_{62}H_{83}EuN_7O_3S$*

Mass spectrometry showed the presence of exact mass at 1158.5535 for $C_{62}H_{83}EuN_7O_3S$ corresponding to the calculated mass 1158.5491. Complexation of the **42*S*** enantiomer was carried out using identical conditions. The same result was observed for the R enantiomer, which can be seen in the ^1H NMR of the complex (Appendix B) and confirmed by mass spectrometry with the isotopic distribution of the Eu^{3+} ion.

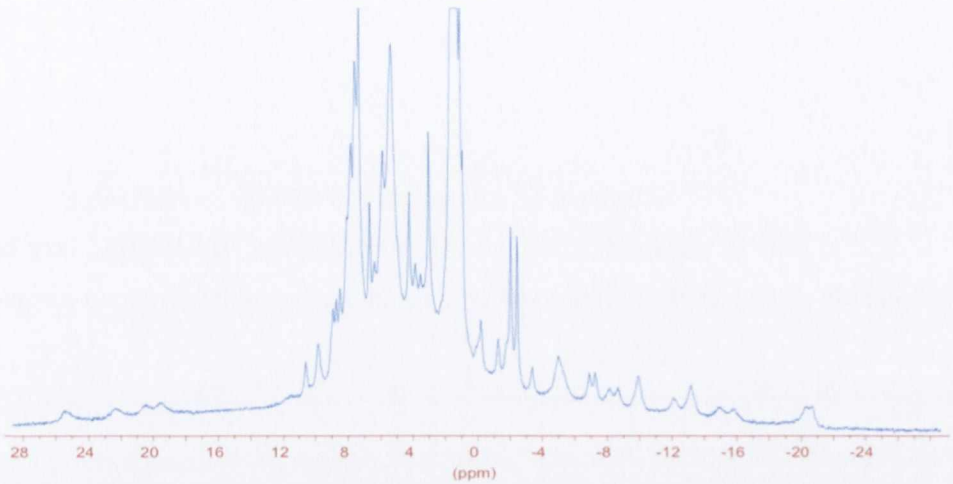

Figure 3.12: *^{1}H NMR spectrum (MeOD, 400 MHz)* ***of 106.Eu***

Complexation of **106** was carried out using similar experimental conditions followed by precipitation from swirling diethyl ether to yield a yellow oil, 23 % yield, Figure 3.12. The ^{1}H NMR spectrum (MeOD, 400 MHz) again showed shifting of the axial and equatorial protons from 20 ppm to -20 ppm. The mass spectrometric analysis confirmed the formation of the product with the species observed at 1124.5651 for $C_{62}H_{81}N_7O_3Eu$ with calculated mass at 1124.5613 and the isotopic distribution pattern of the Eu^{3+} was observed in Figure 3.13.

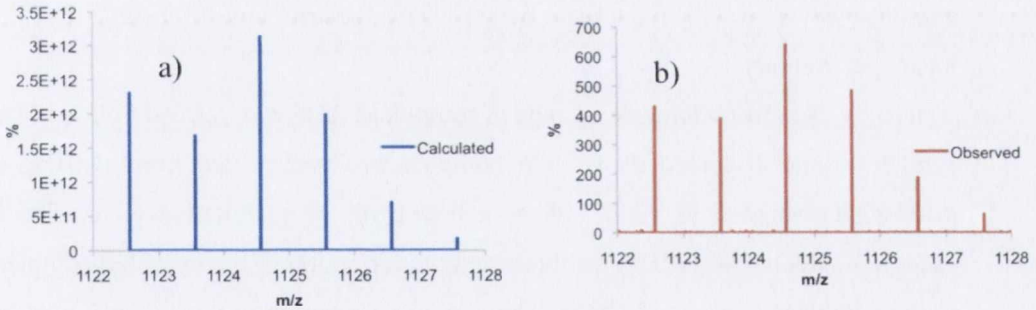

Figure 3.13*: a) Calculated spectrum of* ***106R*** *and b) MALDI spectrum of* ***106R***

The lanthanide complexes of **42*S*** and **42*R*** were formed in a similar manner, by refluxing ligand, **42**, with 1.1 equivalents of $Eu(CF_3SO_3)_3$ under argon in MeOH for 18 hours. The complex was precipitated from swirling ether and dried under vacuum to yield **42.Eu** as a brown oil in 15 % yield and 86% yield for the *R* enantiomer and *S* enantiomers respectively.

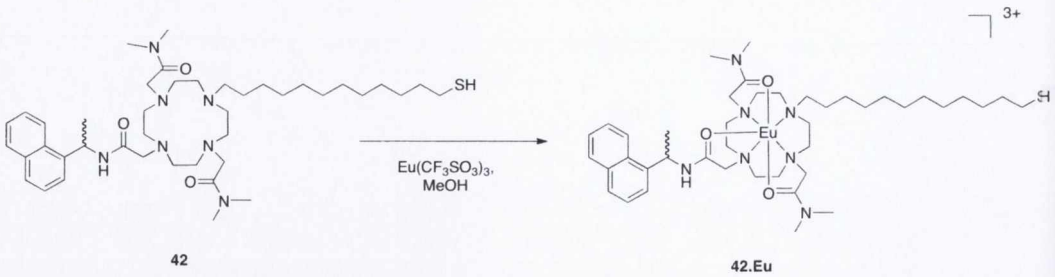

***Scheme 3.8**: Complexation of **42** with Eu $(CF_3SO_3)_3$*

The ^{1}H NMR spectrum (MeOD, 400 MHz) of **42*S*.Eu** was very broad with the greatly shifted axial and equatorial protons, indicative of the europium complexation.

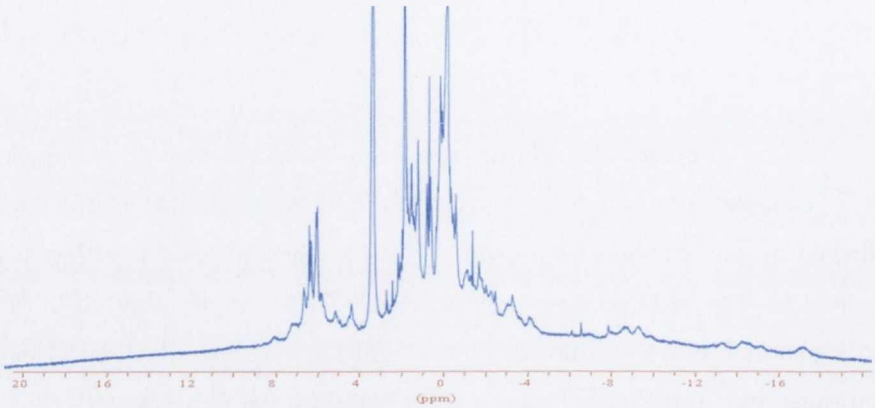

Figure 3.14:** ^{1}H NMR spectrum (MeOD, 400 MHz) of **42.Eu

Complexation of **42*R*** was carried out in an identical manner to that of **42*S*.Eu**, refluxing in CH_3CN overnight with 1.1 eq. of the metal salt. This again yielded the complex, which was characterised by ^{1}H NMR spectroscopy (Appendix B) and also by mass spectrometry.

The Eu^{3+} complex of model compound **110** was formed following the same synthetic route discussed above. The complex was precipitated from swirling ether and dried under vacuum to yield **110**, as a brown oil in quantitative yield. The ^{1}H NMR spectrum (MeOD, 400 MHz) demonstrated the formation of the expected complex, similar to the complexes discussed above. The complex formation was also confirmed by HRMS with the observed signal at 1022.4272 for $C_{43}H_{70}N_7O_6F_3SEu$ corresponding to the expected value of 1022.4273.

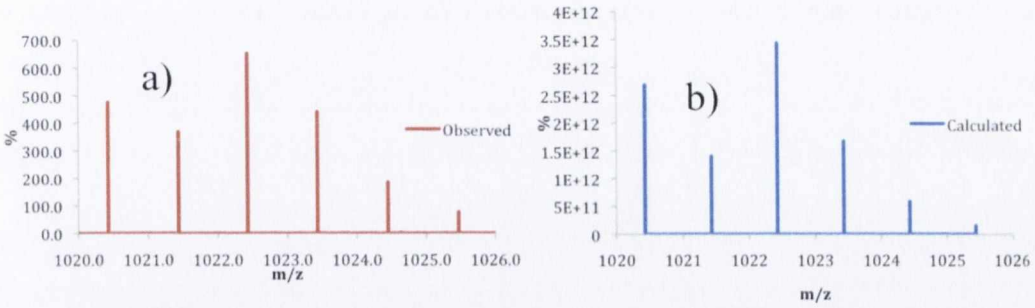

Figure 3.15**: a) MALDI spectrum of **110R.Eu** b) Calculated spectrum of **100R.Eu

The synthesis and characterisation of the complexes **41.Eu**, **42.Eu, 106.Eu** and **110.Eu** was successfully achieved and confirmed by ^{1}H NMR and high resolution mass spectrometry. The next section will discuss the photophysical evaluation of these complexes.

3.8 Photophysical Characterisation of 42.Eu

The photophysical characterisation of **42*R*.Eu** and **42*S*.Eu** (1 x 10^{-5} M) were carried out in MeO and displayed a λ_{max} at 281 nm, which was attributed to the $S_0 \rightarrow \pi\pi^*$ transition of the naphthalene chromophore with the distinctive three fingered absorption.

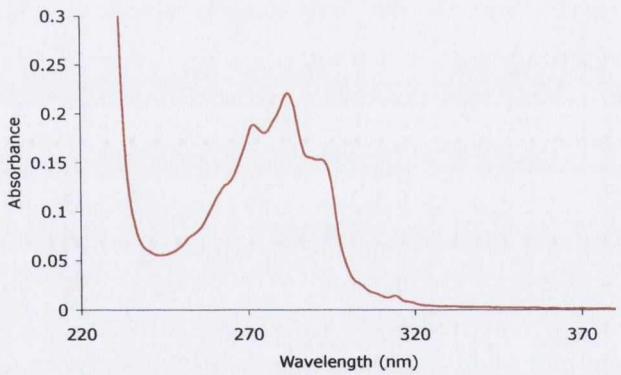

***Figure 3.16**: UV-Vis absorption spectrum of **42R.Eu** (c =1 x 10^{-5}M) in MeOH*

Excitation into the naphthyl chromophore, λ_{max} at 281 nm, yielded the ligand centred fluorescence emission spectrum of **42.Eu**, Figure 3.17.

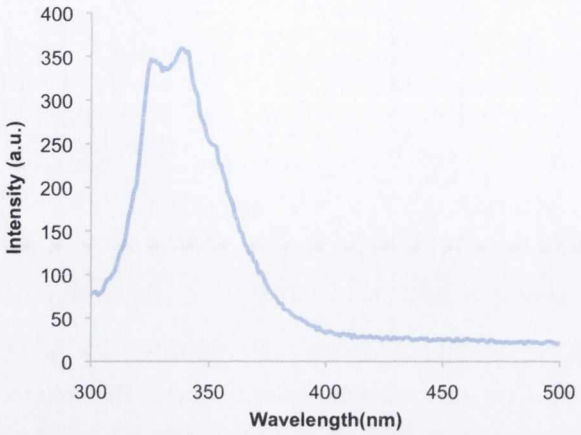

***Figure 3.17**: The fluorescence emission spectrum of **42.Eu** ($c = 1 \times 10^{-5}$ M) in MeOH*

Excitation into the naphthalene absorption band also resulted in the sensitisation of the Eu^{3+} centred emission, which demonstrated the population of the lanthanide excited state *via* energy transfer from the excited state of the naphthyl antenna to the $^5D_0$ accepting level of the Eu^{3+}, Figure 3.18. The Eu^{3+} emission spectrum can act as a fingerprint for determination of the Eu^{3+} coordination pattern.

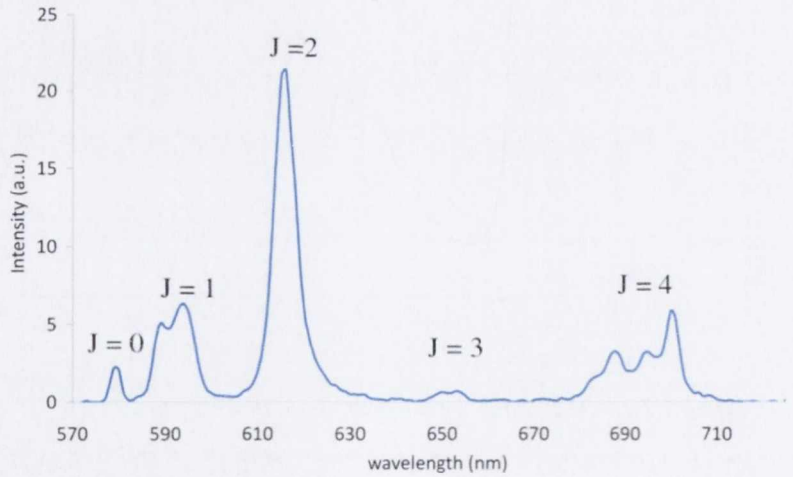

***Figure 3.18**: The Eu^{3+} emission spectrum of **42.Eu** ($c = 1 \times 10^{-5}$ M), $\lambda_{max} = 281$ nm*

These bands centred at 575, 593, 616, 651, and 695 nm respectively, represent the deactivation of the $^5D_0$ excited state to the ^7F_J (J = 0-4 respectively) ground states as shown in Figure 3.18. It is interesting to note the presence of the $J = 0$ transition, which is formally forbidden and so can sometimes remain unseen in the emission spectrum. It may gain intensity due to J mixing with the ligand orbitals and its oscillator strength, in general,

is sensitive to the ligand field and symmetry. The intensity of the magnetic dipole allowed $J = 1$ transition is relatively independent of coordination environment. The $J = 2$ and $J = 4$ transitions are very sensitive to the ligand field, especially to the nature and polarisability of the axial donor. The photophysical characterisation of the complexes **42.Eu** (*R*, *S*) is discussed in the following sections.

3.9 Photophysical characterisation of 42*R*.Eu and 42*S*.Eu

Analysis of the UV-Vis absorption spectra for **42*R*.Eu** and **42*S*.Eu** showed similar behaviour with the naphthyl band maximum located at 281 nm (Appendix B). Excitation at this wavelength yielded the characteristic Eu^{3+} emission spectrum (Appendix B). This complex exhibited lower extinction coefficients, 2645 $cm^{-1}M^{-1}$, due to the lower number of naphthyl antennae attached to the macrocycle, compared to that of **41.Eu**, which gave extinction coefficients of 12286 $cm^{-1}M^{-1}$ at 281 nm. The photophysical characterisation of **41.Eu-AuNPs** was carried out in MeOH, however, in the case of **42*R*** and **42*S***, the complexes were fully water-soluble, thus, the pH behaviour of these complexes was investigated in H_2O.

3.9.1 Photophysical analysis of 42.Eu, as a function of pH

Photophysical studies were first carried out using UV-Vis absorption spectroscopy and have shown a weak hypochromic effect of the $S_0 \rightarrow \pi\pi^*$ absorption band at 281 nm, while the p H is increased, however, overall the complex does not experience any major changes as a function of pH.

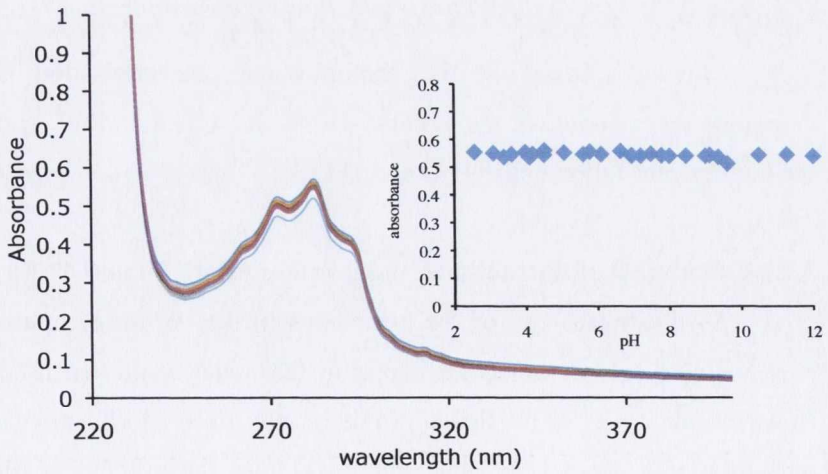

***Figure 3.19**: UV-Vis absorption spectrum **of 42.Eu** (c = 1 x 10^{-5} M) in H_2O using TEAP as ionic strength (0.1 M) as a function of pH. **Inset:** Absorbance versus pH at 281 nm*

This was shown to be reversible when the titration was carried out over a wide pH range from basic to acidic, demonstrating similar changes.

The ligand-centred fluorescence of the complex undergoes very little change with pH, showing a small steady decrease in intensity upon basification of the system, Appendix B. However, these changes remain quite small as was observed for the UV-Vis absorption and thus, the complex was stable in a wide pH range, Figure 3.19.

The behaviour of the luminescence has also been investigated over a wide pH range and the results were similar to those obtained for the UV-Vis absorption spectrum. No major changes were recorded upon pH variation however, when the pH evolves from 2-12, a decrease of the emission intensity at 615 nm was recorded between pH 2-4 and then remains stable from 4-12, which is indicative of the complex stability at physiological pH. This results were also found to be reversible in aqueous solution, between 4-12.

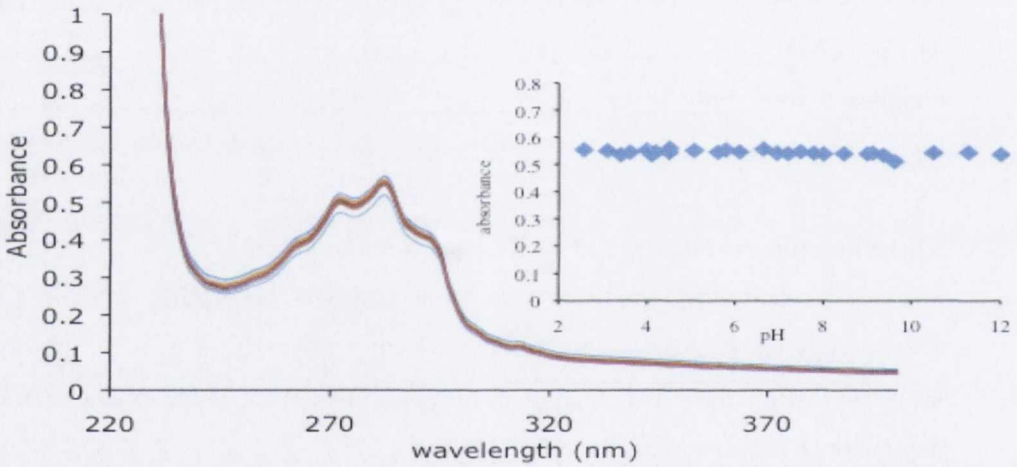

Figure 3.20: *The changes in the Eu^{3+} emission of* ***42.Eu*** *as a function of pH,* ***Inset:*** *Changes at 615 nm as a function of pH. Blue: Forward titration 2-12. Red: back titration from 12-2*

Having carried out the photophysical characterisation it was necessary to determine the lifetimes of the systems **41.Eu** and **42.Eu** and the hydration state based on the luminescence lifetimes in H_2O and D_2O.

3.9.2 Calculation of the lifetimes and *q* values for 41.Eu and 42.Eu

As illustrated, one of the key points in the design of luminescent probes is the presence of the H_2O molecules bound to the metal centre as discussed in Section 3.1. However, the cavity of the ligand provides only seven coordination sites for the Ln^{3+} ion, four from the macrocycle itself and three from the acetamide arms. As a result, the remaining coordination sites are filled with solvent molecules (*e.g.* H_2O). As discussed in Chapter 1 and 2, this hydration state or *q* value can be determined from the lifetimes of the

Eu ($^5D_0$) emission in solution, using Equations 1 and 2 in H_2O/D_2O and MeOH/MeOD respectively.[175] The emission decays were fit to a monoexponential function, indicating the presence of a unique luminescent species in solution

Table 3.1: *Calculation of the number of metal bound water molecules*

Complex	$\tau_{solvent}$ (ms)	$\tau_{Deuterated\ solvent}$ (ms)	q (±0.5)
41*R*.Eu	0.752	1.578	1.5
41S.Eu	0.831	1.702	1.3
42*R*.Eu	0.608	1.057	1.1
42S.Eu	0.61	1.06	1.2
106.Eu $_{model}$	0.70	1.61	1.7
110.Eu $_{model}$	0.61	1.33	1.9

In the case of **41**, **42** and **110** the lifetimes calculated in H_2O and MeOH yielded $\tau_{solvent}$ = 0.75 ms, 0.61 ms and 0.61 ms respectively, which suggest that the behavior of each complex in solution is similar. This has been further confirmed by the calculation of the number of metal bound water molecules shown in Table 3.1. The complexes, **41.Eu** and **42.Eu**, gave *q* values of less than two.[169, 176] However, the complex without the thiol present was also analysed, as one explanation for the low *q* value is loose coordination of the thiol to the metal centre due to possible folding of the chain.

The *q* values of approximately two obtained for the complexes **106** and **110**, suggests that the thiol is coordinating to the metal centre or at least there is a sufficient interaction that the thiol can partially displace the water molecules. Also it is possible that the chain is flexible enough that the chain can fold causing the coordination sites of the lanthanide to be blocked or so sterically hindered that further coordination to the lanthanide is not possible. With the hydration state determined the chirality of the complexes have been investigated by CD and circularly polarised luminescence (CPL), and the results from these investigations will be presented in the next two sections.

3.9.3 Circular dichroism studies of the complexes 41.Eu and 42.Eu

Initially, the optical activity of the complex **41.Eu** was investigated using CD spectroscopy, a technique that measures differences in the absorption of left-handed versus right-handed polarised light, which arises due to structural assymmetry.[176]

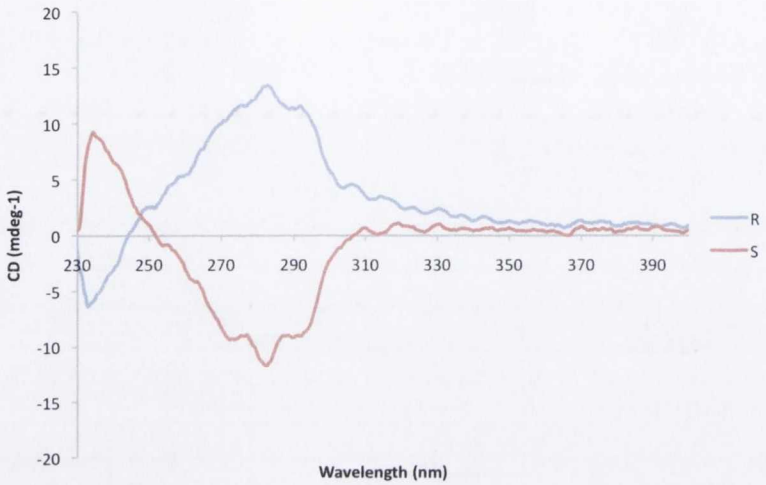

***Figure 3.21**: CD spectrum of **41R.Eu** and **41S.Eu** in MeOH*

The CD spectra were first recorded for ligand **41*R*** and **41*S*** in MeOH and are shown in Figure 3.18. The band of the S_0- $\pi\pi^*$ transition of **41*R*** and **41*S*** were observed to respond to polarised light with the same magnitude, which confirms the enantiomerically pure isolation of ligands **41*R*** and **41*S***.

The same measurements performed on the complexes **42*R*.Eu** and **42*S*.Eu** demonstrated similar results as observed for **41.Eu**. **42*S*.Eu** showed a positive CD band of the opposite sign than that observed for **42*R*.Eu**, which confirms the retention of the chirality of the architecture upon complexation. Moreover, the results obtained for the second enantiomer confirmed those obtained for **41*R*.Eu**, and thus the enantiomeric purity of the complexes.

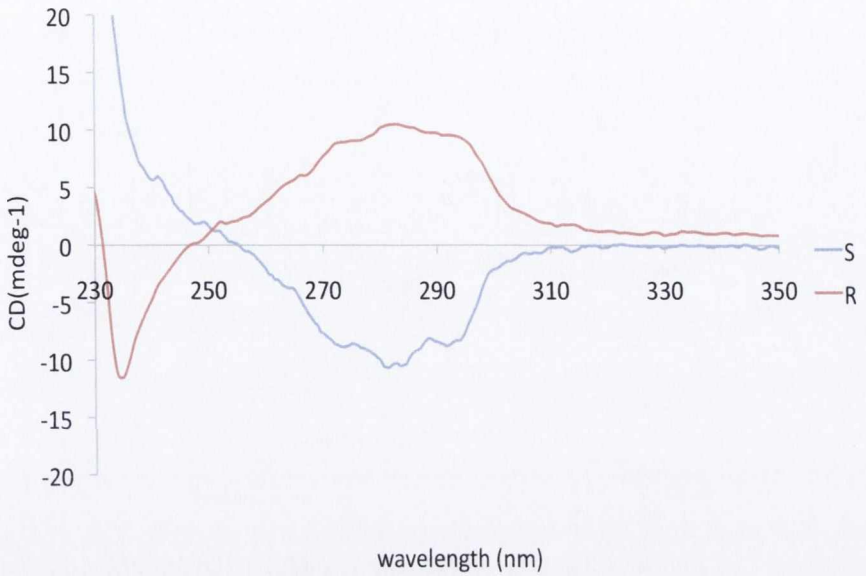

Figure 3.22: *CD spectrum of* ***42R.Eu*** *and* ***42S.Eu*** *in MeOH demonstrating the chiral naphthalene band of the complex*

Once the CD spectrum showed the presence of the chiral lanthanide complex the next step was to determine if the circularly polarised luminescence (CPL) could be detected, *i.e.* the chiral emission of the complex due to excitation and energy transfer from a chiral chromophore, which is discussed in the following section.

3.9.4 Circularly Polarised Luminescence Studies of 41.Eu and 42.Eu

CPL spectroscopy is a technique, which measures the polarised emission from an excited state of a luminescent architecture.[177] Similar to the chirality of the ground state of the complex, which is determined by CD, this allows the determination of the chirality of the excited state.[165] All of the CPL measurements were carried out by Dr. Robert Peacock in Glasgow University. In this case, it has already been shown in Figure 3.21 and 3.22, that the naphthalene chromophore is chiral and exhibits a distinctive band in the CD spectrum. Excitation into the naphthalene band, at 281 nm, causes energy transfer to the Eu^{3+} ion excited state as shown above in Figure 3.18. CPL utilises the nature of the polarised light, exciting the sample to cause energy transfer in a chiral manner to the europium centre. The CPL is much more sensitive to changes in intensity provoked by the geometry of the complexes.

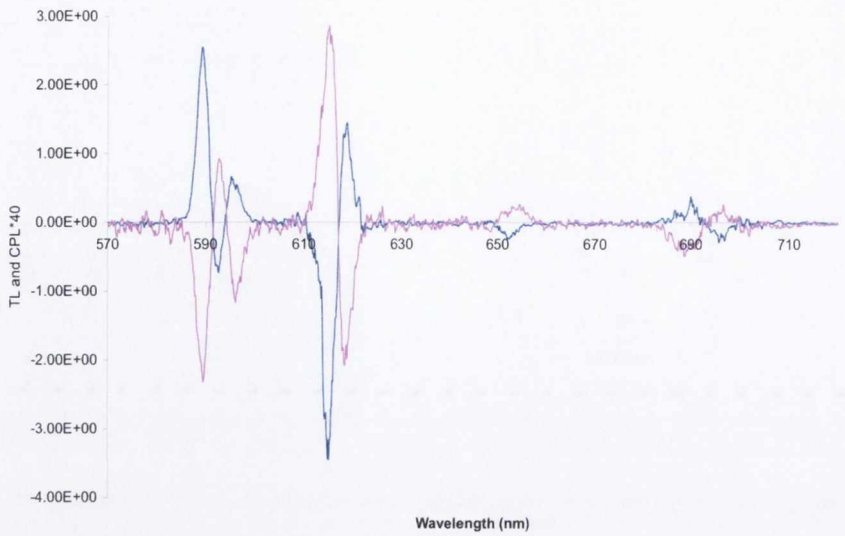

Figure 3.23: *CPL of* ***41R.Eu*** *and* ***41S.Eu*** *in MeOH,* λ_{max} *= 281 nm*

The CPL of the complex **42.Eu** could not be recorded accurately due to the lower luminescence intensity, which can be due to an insufficient energy transfer or low ε. Consequently, the resulting luminescence intensity was not sufficient to generate an intense CPL signal. To the contrary, complex **41.Eu** successfully showed the CPL luminescence due to the larger number of chromophores. This spectrum shows the *R* and *S* enantiomers overlaid with the splitting of the $J = 2$ band, particularly noticeable as this band is characteristic of the coordination sphere. Having investigated the chiral nature of the complexes, the next step was to examine the potential of these molecules as sensors.

3.10 Sensing of carboxylates using 41(*R,S*). Eu and 42(*R,S*).Eu

As discussed at the beginning of this chapter, the aim of this project was to develop luminescent sensors through the displacement of metal bound water molecules as depicted in Figure 3.1(i).[169] The photophysical characteristics of these complexes were first investigated in Section 3.10, including the calculation of the *q* values from the luminescence lifetimes and were found to possess one metal bound water molecule. It was then possible that displacement of these metal bound water molecules could be achieved with the addition of analytes, which possess strong binding affinity for the lanthanide ion, such as carboxylates and phosphates.[178] The first analytes used for these titrations were the simple acyclic carboxylates, such as citric acid and malonic acid as these have been shown to bind *via* the formation of 4-5 member rings.[32] These simple carboxylates were chosen as they had previously been shown to displace the metal bound water molecules of cyclen lanthanide complexes and enhance the luminescence.[162a] As expected, the UV-Vis

absorption spectrum of the complex, **41.Eu** and **42.Eu** remained unchanged upon the addition of malonic acid, succinic acid, acetate and phosphate and indicated that the anions did not give rise to perturbations in the ground state properties of the complex. Similar behavior was observed in the ligand centred fluorescence as can be seen in Figure 3.24.

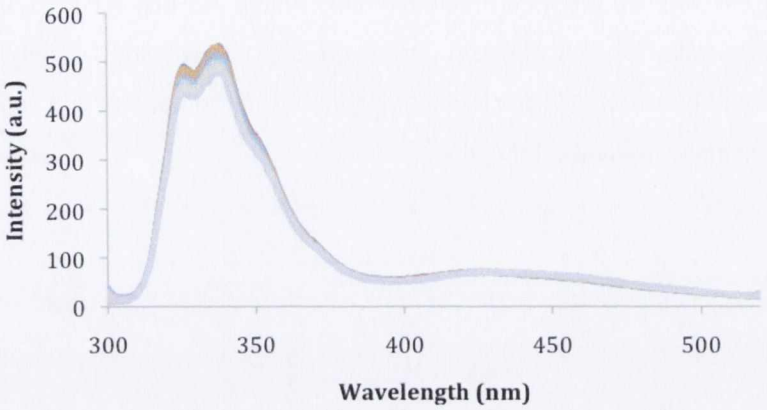

***Figure 3.24**: The changes in the fluorescence emission spectrum of **42.Eu** ($c = 1 \times 10^{-5}$M) in MeOH λ_{max} = 281 nm, upon the addition of malonic acid 0-10 equivalents*

As shown in Figure 3.25, the titration of **42.Eu** with malonic acid shows an enhancement of the time delayed emission of the Eu^{3+} until one equivalent. The same results could be obtained from analytes such as hydrogen phosphate.

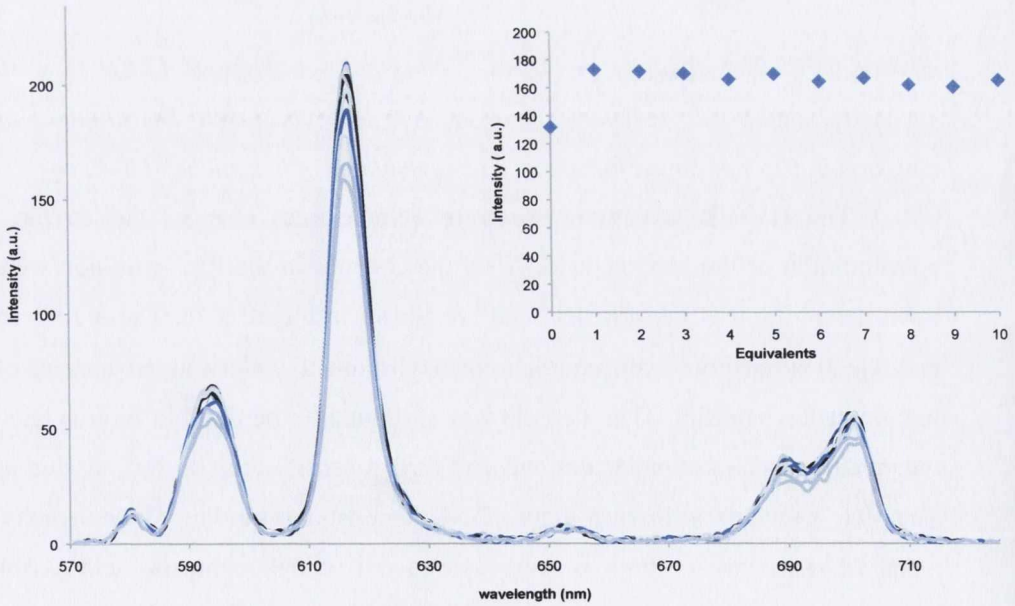

***Figure 3.25**: The changes in the Eu^{3+} emission spectrum of **42.Eu**, λ_{max} = 281 nm, upon the addition of malonic acid. **Inset:** The changes at 615 nm upon the addition of malonic acid*

However, the changes observed for such acyclic, non-aromatic carboxylates were miniscule and so alternative analytes possessing a chromophore were used in order to more efficiently sensitise the luminescence of the Eu^{3+}.

The analytes utilised for these titrations were benzoic acid and terephthalic acid, which have been reported previously as efficient antenna for the sensitisation of the Eu^{3+} excited state.[162b] Benzoic acid due to the simple aromatic carboxylate, which had been shown to bind and displace two metal bound water molecules due to the bidentate nature of the antenna was utilised initially

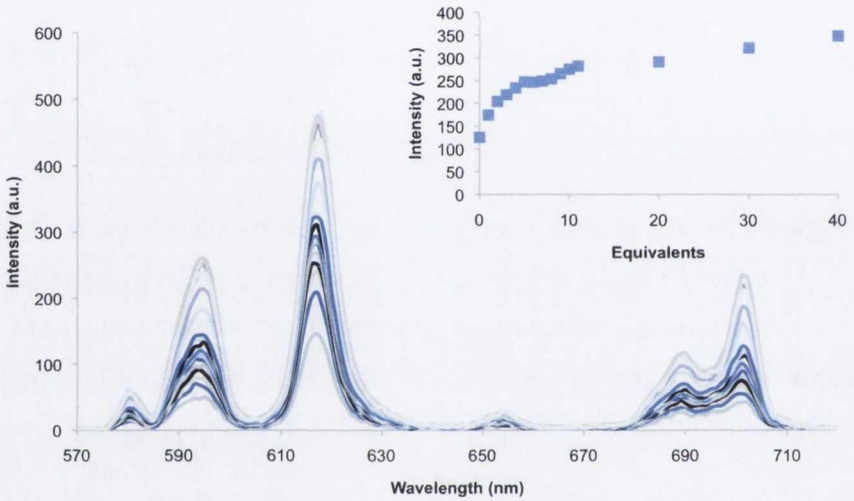

Figure 3.26: *The changes in the Eu^{3+} emission spectrum of* ***43.Eu*** *(1 x 10^{-5}M) with successive additions of benzoic acid, λ_{max} = 281 nm.* ***Inset:*** *The changes of the Eu^{3+} emission at 615 nm versus the number of equivalents of benzoic acid 0-40 eqs*

The UV-Vis absorption spectrum demonstrates changes due to the increasing concentration of the benzoic acid. Also, the changes in the Eu^{3+} emission were recorded upon the addition of benzoic acid and are shown in Figure 3.26. The Δ J =2 band at 615 nm, which is sensitive to the coordination environment, underwent an increase of 274 % in luminescence intensity. This increase was attributed to the benzoic carboxylate displacing the metal bound water molecules and also further sensitisation of the emission of the Eu^{3+}. The plot, shown as an inset in Figure 3.26, demonstrates binding of the carboxylate to the metal centre. Similar titrations were carried out with terephthalic acid as this antenna contains two carboxylates which could show different binding stoichiometry to the other carboxylates, as observed by Harte *et al.*[140] with the binding of terephthalic acid to a dinuclear complex. Upon the addition of terephthalic acid in aqueous buffered solution, the

UV-Vis absorption spectrum again underwent changes due to the absorbance of the antenna itself at 250 nm, Figure 3.27.

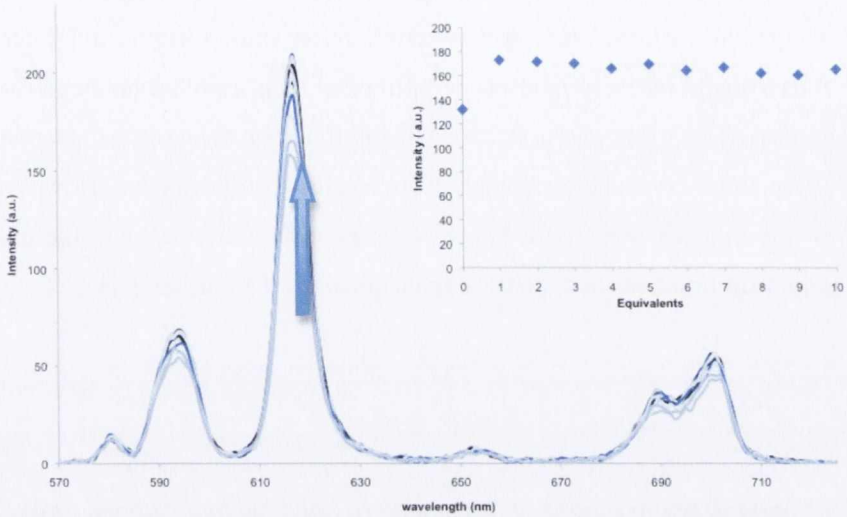

Figure 3.27: *The changes in the UV-Vis absorption spectrum of* ***42.Eu*** *(1 x 10^{-5} M) in HEPES buffer (pH 7.4, 0.1 NaCl ionic strength) with consecutive additions of terephthalic acid 0-5 eqs*

The excitation into the naphthyl band at 281 nm upon addition of terephthalic acid yielded the emission of the Eu^{3+} as shown in Figure 3.28, which demonstrates the efficient displacement of the metal bound water molecules and the efficient sensitisation of the Eu^{3+} excited state by the antenna.

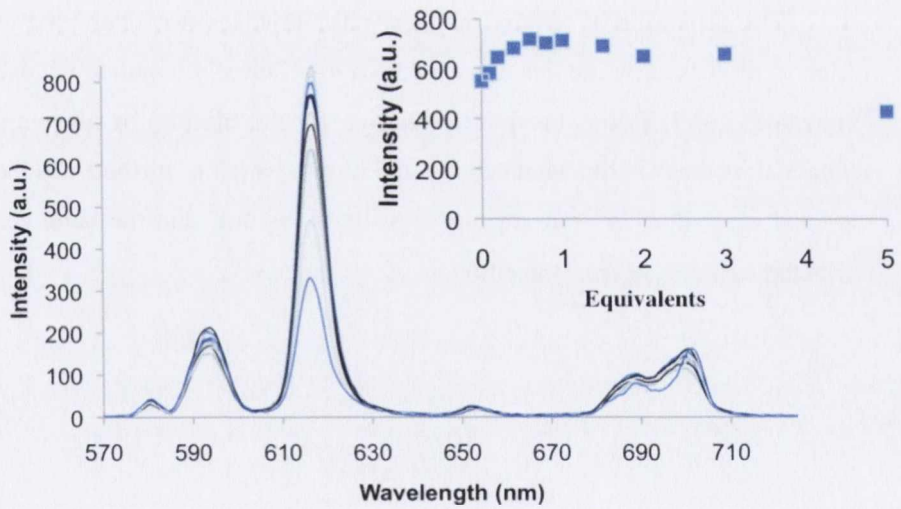

Figure 3.28*: The changes in the Eu^{3+} emission spectrum of* ***42.Eu*** *(1 x 10^{-5}M) in HEPES (pH 7.4, 0.1 NaCl ionic strength) upon the addition of terephthalic acid, λ_{max} = 281 nm.* ***Inset:*** *Plot of intensity at 615 nm versus theaddition of 0-5eqs of terephthalic acid*

The isotherm, shown as an inset in Figure 3.28, demonstrates the binding of 0.5 equivalents of antenna to the complex showing that two binding sites of the analyte allowed coordination of two complexes per terephthalic acid due to the potential of the terephthalic acid to provide two coordiantion sites, forming a 1:2 ternary complex. The enhancement of the luminescence of the Eu^{3+} was quite pronounced for the analytes which possessed a chromophore, due to contribution from the external antenna to the sensitisation of the metal centred emission upon coordiation of the antenna. However, the next step was to use analytes, which are known to very efficiently populate the excited state of Eu^{3+}, demonstrating a more dramatic enhancement of the luminescence.[177]

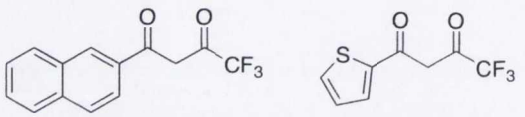

nta tta

Figure 3.29: *Structures of 444- trifluoro naphthyl butanedione (**nta**) and 4,4,4 trifluoro thiophene butanedione (**tta**)*

Previously, in the Gunnlaugsson group, the use of diketonate antenna, such as **nta** and **tta** (Figure 3.29) have been shown to be very efficient for the formation of luminescent ternary complexes of Eu^{3+}.[167b] For this reason, the same antenna were chosen for these measurements as, not only do they cause displacement of the metal bound water molecules, they also demonstrate additional sensitisation of the Eu^{3+} luminescence.

3.11 Formation of ternary luminescent complexes of 41.Eu with nta and tta

The formation of ternary luminescent complexes was attempted with **nta** and **tta**, which as discussed before, have been shown to efficiently populate the excited state of the lanthanide. The UV-Vis absorption spectrum for the titration of **nta** with **41.Eu** shows a sequential increase in the band centred at 330 nm, which is attributed to the **nta** itself, with the band centred at 245 nm attributed to the $S_0 \rightarrow {}^1\pi\pi^*$ and the band centred at 330 nm attributed to the $S_0 \rightarrow {}^3n\pi^*$ transition.

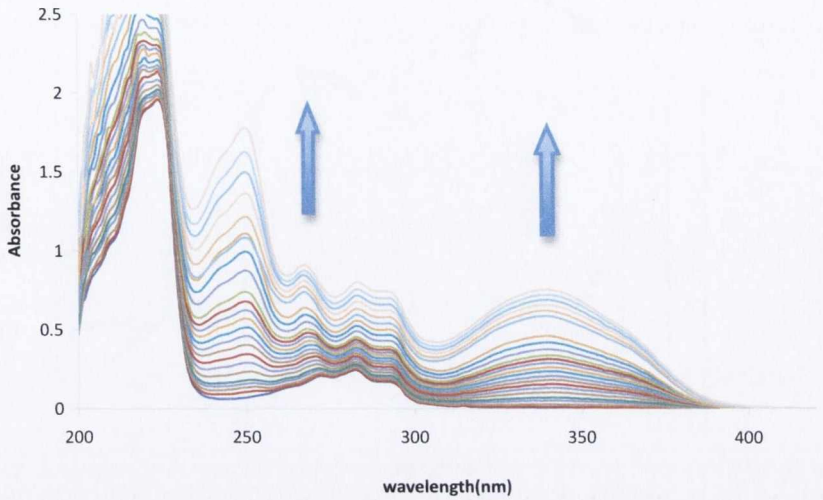

***Figure 3.30**: The changes in the UV-Vis absorption spectrum **of 41.Eu** (c = 1 x 10 $^{-5}$ M) in MeOH upon the addition of **nta** from 0-4.5 equivalents.*

The investigation of the effects of the addition of **nta** was also studied using fluorescence and time delayed emission. Firstly, upon addition of **nta** as shown in Figure 3.31, the fluorescence emission arising from the singlet excited state of the naphthyl moieties of the complex, extending from 300 - 400 nm, was significantly quenched, characteristic of the $S_0 \rightarrow \pi\pi^*$ deactivation of the naphthyl moiety. This deactivation is due to the competitive processes of ISC and energy transfer with the fluorescence highlighted in Figure 3.31.

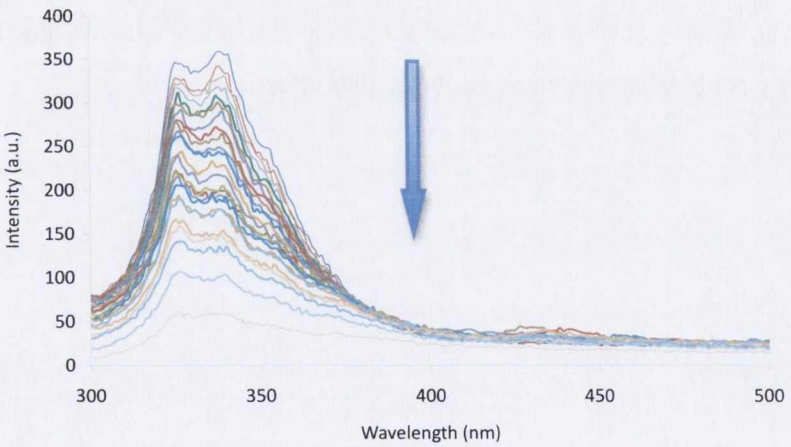

Figure 3.31**: Changes in the fluorescence emission spectrum of **41.Eu** in MeOH (c =1 x 10 $^{-5}$ M) , λ_{max} = 281 nm, upon the addition of **nta

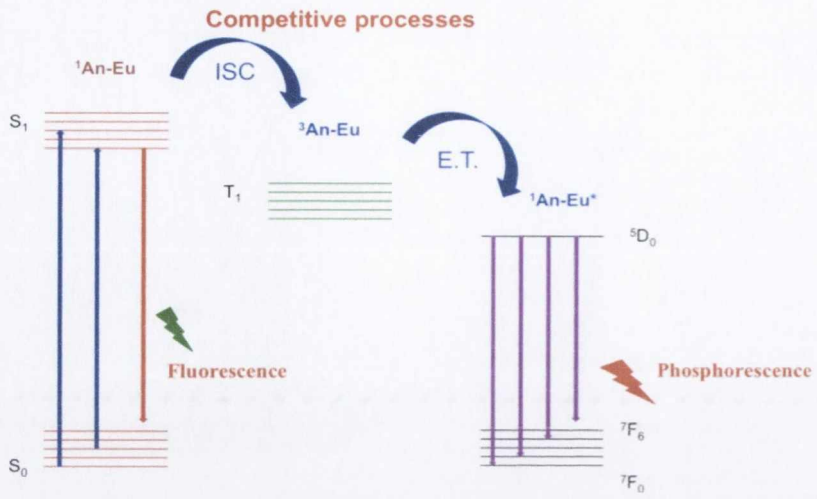

Figure 3.32: *Competitive processes yielding the fluorescence and phosphorescence of the metal complex.*

As expected, the displacement of H_2O and sensitisation of the Eu^{3+}, upon the addition of **nta**, was observed by monitoring the Eu^{3+} centred luminescence, due to the displacement of the metal-bound water molecules. The chromophoric antenna populates the excited state of the lanthanide efficiently and so can also be shown to contribute to the emission. This can be observed in Figure 3.32, where the isotherm plotted shows a stoichiometry of 1:1.

The titration of **nta** with complex **42.Eu** shows an enhancement of the Eu^{3+} emission intensity as a function of **nta**, evolving towards a maximum upon the addition of one equivalent. Also, as can be seen in Figure 3.33, a decrease in the luminescence was observed after reaching the saturation of the remaining sites on the Eu^{3+} centre. This decrease could be attributed to the inner filter effect.

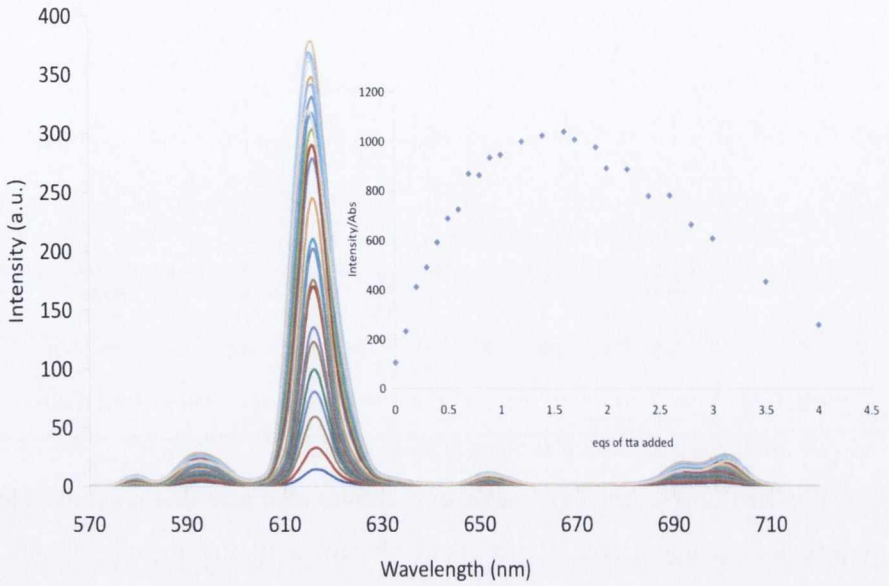

Figure 3.33: *The changes in the Eu^{3+} phosphorescence spectrum upon titrating* ***41.Eu*** *($c=1 \times 10^{-5}M$) with* ***nta****, 0-6 equivalents in MeOH, λ_{max} = 281 nm.* ***Inset:*** *Binding isotherm, emission intensity at 615 nm versus equivalents of* ***nta***

Similar results were observed for the titration of **41.Eu** with **tta**, which are shown in Figure B.10, Appendix B. These titrations were carried out in MeOH, however for potential applications, as luminescent probes *in vivo*, it is necessary to carry out measurements in more competitive media. Measurements were therefore carried out on **42.Eu**, in HEPES buffer (pH 7.4, ionic strength 0.1 M NaCl), which will be discussed in the next section.

3.12 Formation of luminescent ternary complexes of 42.Eu using tta

The same experiments carried out above, were also performed on **42.Eu** using both **nta** and **tta**, the structures of which are shown in Figure 3.29. The titration of **42.Eu** with **nta** is shown in Figure xx, Appendix B. These titrations were carried out in MeOH due to the insolubility of **tta** in aqueous solution. The UV-Vis absorption spectrum was recorded upon the addition of aliquots of **tta**, which shows similar results to that of **41.Eu,** with the band at 350 nm attributed to the absorption band of the **tta,** Figure 3.34.

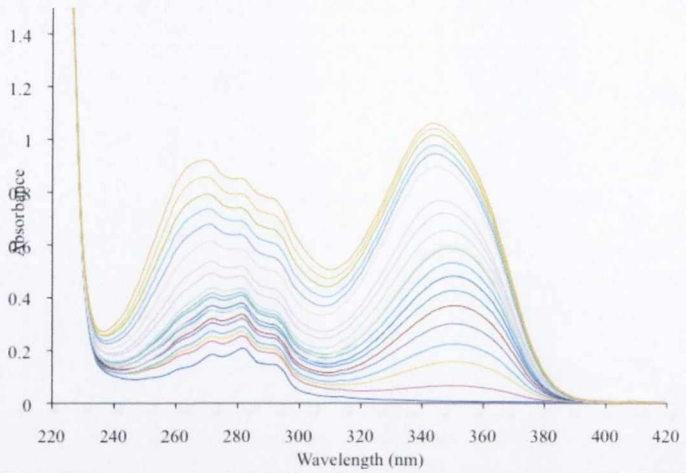

Figure 3.34: *The changes in the UV-Vis absorption spectrum of* ***42.Eu*** *(c = 1 x 10 -5 M) in MeOH upon the addition of 0-5 equivalents of* ***tta***

The fluorescence emission spectrum was also recorded upon the addition of **tta** and experiences a quenching of the band attributed to the ligand centred emission upon addition of **tta**, Figure 3.35. This is due to the more efficient energy transfer to the lanthanide upon sensitisation shown schematically in Figure 3.32, causing a decrease in the fluorescence and a corresponding increase in the luminescence of the lanthanide. The plot of the fluorescence at 339 nm versus the equivalents of **tta** shown in Figure 3.35 demonstrates the quenching of the fluorescence emission.

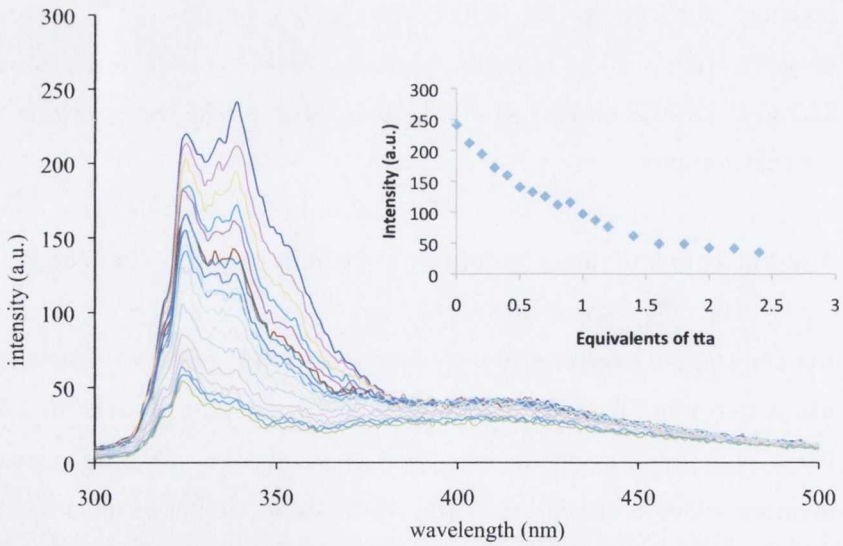

Figure 3.35*: The changes in the fluorescence emission spectrum of* ***42.Eu*** *in MeOH (1 x* 10^{-5} *M),* λ_{max} *= 281 nm, upon the addition of* ***tta****.* ***Inset:*** *Plot of equivalents of* ***tta*** *versus the intensity at 339 nm*

Upon the addition of **tta**, the Eu^{3+} emission spectrum arising for **42.Eu,** was monitored to determine the binding of the diketonate to the lanthanide ion, Figure 3.36. As

before, large emission enhancements were observed, most pronounced for the $\Delta J = 2$ band, centred at 615 nm, which was plotted as a function of the number of equivalents of antenna added, inset, Figure 3.36. The analysis of Figure 3.36 showed that up to the addition of one equivalent of **tta** the emission shows successive increases, after which it demonstrates quenching of the emission. The 1:1 binding stoichiometry was again observed for the complex upon addition of the bidentate antenna **nta**, which demonstrated the displacement of the metal-bound water molecules and external sensitization by the added antenna. The luminescent intensity after the addition of one equivalent experienced quenching due to the inner filter effect, which was also observed for **41.Eu**.

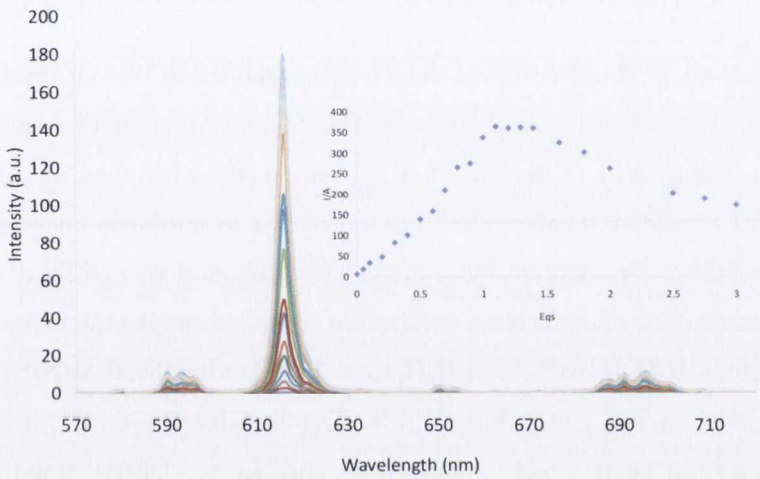

Figure 3.36: *Evolution of the Eu^{3+} phosphorescence spectrum of* ***42.Eu*** *($c=1 \times 10^{-5}M$) upon the addition of* ***tta*** *0-6 equivalents in MeOH, λ_{max} = 281 nm.* ***Inset:*** *Binding isotherm of the transition at 615 nm versus the equivalents of* ***tta*** *added.*

Having developed the aforementioned complexes for the binding of anions, such as carboxylates, and demonstrated that these analytes successfully displace the metal bound water molecules, we next focused our attention to the determination of a method for the synthesis the **AuNPs**, which will be discussed in the following sections.

3.13 Synthesis of Functionalised Gold Nanoparticles

The synthesis of the **AuNPs** was achieved *via* a number of different synthetic routes. Methods such as the Brust-Schiffrin method and citric acid stabilization were utilized, which have been widely reported in the literature to be successful for the formation of small size and monodispersed **AuNPs**.[179] These different attempts are detailed below in methods 1-5. The most successful method utilized was a modification of the Brust-Schiffrin methodology[179a], Scheme 3.9, however all methods attempted will be discussed.

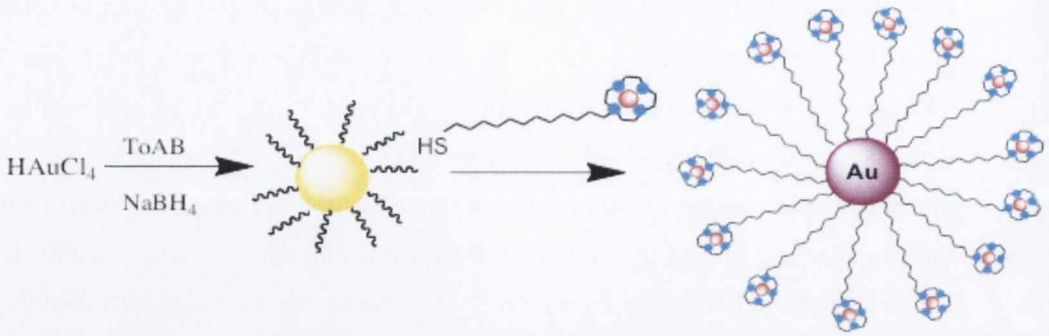

Scheme 3.9: Synthesis of **AuNPs** using the Brust Schiffrin method

3.13.1 Method 1: Modified Brust-Schiffrin method using DMAP stabilisation[179a]

The Brust-Schiffrin method showed successful formation of 5 nm nanoparticles and has been widely used in the literature.[179a] This method involved the use of an aqueous solution of tetrachloroaurate which was transferred to a toluene phase using TOAB as a phase transfer agent. Once in the toluene layer, the gold was reduced using an aqueous solution of $NaBH_4$. The two phases were then separated and the toluene phase washed with 0.1 M H_2SO_4, H_2O, 0.1M NaOH, H_2O, to yield the unstabilised **AuNPs.** DMAP was then added to the solution as a stabilizer as a phase transfer agent and stirred overnight. The phases were separated and the water layer contained the DMAP stabilised nanoparticles was obtained with the SPR absorption band appearing at 500 nm, Figure 3.36. TEM of the DMAP stabilized particles also demonstrated the stability and monodispersity and formation of approximately 5 nm sized particles.

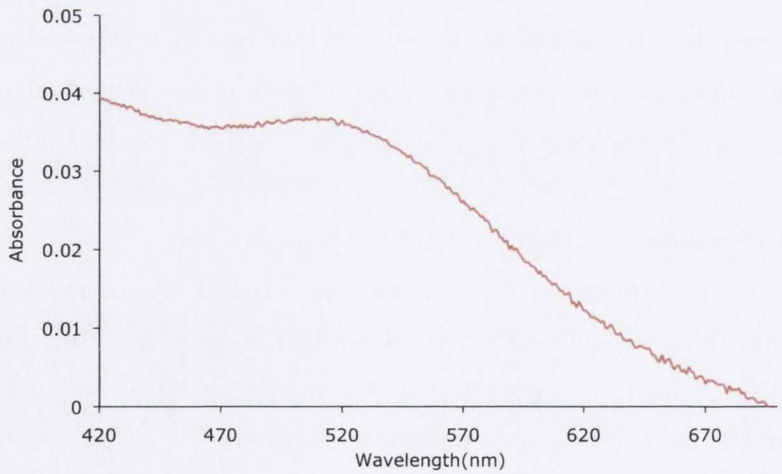

Figure 3.37: *UV-Vis absorption spectrum of DMAP-stabilized* ***AuNPs*** *showing SPR band centred at 520 nm.*

The position of the SPR band is important as the optical properties of **AuNPs** are strongly size dependent and the size can be related to the λ_{max} of the SPR band in the absorption spectrum. While 5-10 nm particles display an SPR band centred around 520 nm, aggregation leads to a significant red shift of the SPR band. However, difficulties were encountered upon exchange of the DMAP on the surface of the particles with the thiols, either **41.Eu** or **42.Eu**, as size exclusion chromatography did not isolate the **AuNPs** functionalised with the thiols, instead DMAP remained bound to the surface of the **AuNPs**.

3.13.2 Method 2: Modified Brust-Schiffrin method using direct complex stabilisation[179a]

Solution of the tetrachloroaurate in water was stirred vigorously and a solution of TOAB (0.05 M) in toluene was added to the solution and stirred vigorously for 30 min after which the solution was separated and the toluene layer washed with H_2O (20 ml). Approximately 0.09 mmol solution of the nanoparticles in toluene was added quickly to a solution of the thiol **42.Eu**. This was stirred for 5 min and a freshly prepared solution of the $NaBH_4$ (0.2 M) in water was added drop wise to allow the gold to be reduced slowly. However, immediate aggregation shown by dark black or purple precipitate was observed upon addition of the $NaBH_4$. No stabilization of the gold by the thiol was observed. A UV-Vis absorption spectrum of the sample showed no band at 520 nm usually observed for stabilised samples as explained in the introduction, nanoparticles much larger or much smaller than 5-100 nm do not exhibit an SPR band.

3.13.3 Method 3: Citric Acid[180]

Tetrachloroaurate was added to a boiling solution of sodium citrate and stirred for 48 hours, Scheme 3.10.

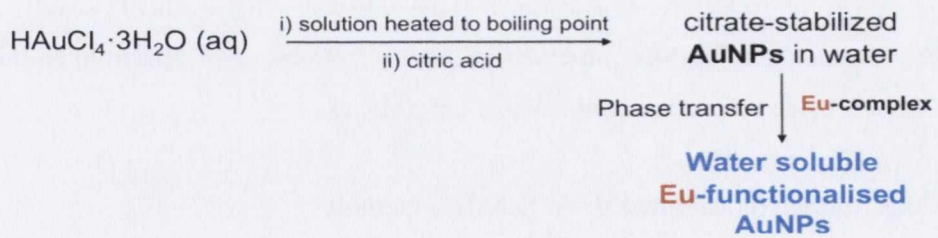

Scheme 3.10: *Synthesis of* ***AuNPs*** *via the citric acid stabilization in aqueous solution*

A UV-Vis absorption spectrum was obtained, which showed the SPR absorption band centred at 520 nm, which is significant of the monodisperse nanoparticles without aggregation. However, addition of the thiol, **42.Eu**, and continual monitoring of the UV-

Vis absorption spectrum show the gradual aggregation of the particles showing insufficient stabilisation.

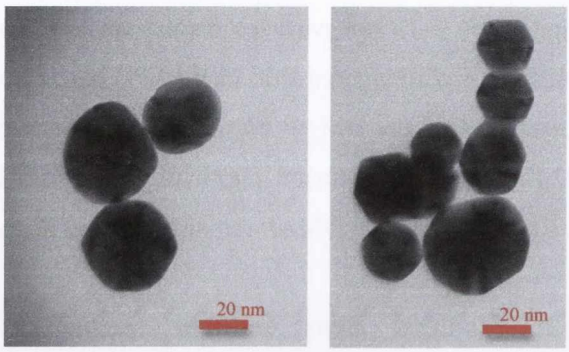

Figure 3.38: *TEM image demonstrating particles of size 20-50 nm with the citric acid synthetic method*

TEM images show the particle size is much greater than that expected for this method with particles as large as 50 nm before aggregation occurred, Figure 3.38.

3.13.4 Method 4: Modified Brust Schiffrin Method

Tetrachloroaurate (88.6 mg) in aqueous solution (10 mL) were stirred in a small flask. TOAB (0.23 g) in toluene was added slowly and the mixture stirred vigorously for 30 min. The toluene layer was separated and washed with H_2O. Toluene was again stirred as a solution of the thiol (0.09 mmol) in MeOH/H_2O was added quickly. The solution was stirred overnight at room temperature with the thiol. A UV-Vis absorption spectrum was taken of the nanoparticles, which show a peak at 520 nm. The UV-Vis absorption spectrum demonstrated a blue shift due to **42.Eu** thiol coordination, as the TOAB interaction is an electrostatic stabilization, whereas the thiol interaction is a covalent interaction. The UV-Vis absorption spectrum shifts slightly to the red when the thiol, **42.Eu,** has reacted covalently with the surface of the particle. The solution was then stirred vigorously and a solution of $NaBH_4$ (0.2M) in H_2O was added slowly drop wise to this solution, turning the solution purple, which is an indication that the gold was reduced Au(III) - Au(0). However, after one day changes were observed in the UV-Vis absorption spectrum so this method did not provide sufficient stabilization of the particles.

3.13.5 Method 5: Modified Brust Schiffrin method

Tetrachloroaurate was dissolved in H_2O, TOAB in toluene was then added to the solution and stirred vigorously with a colour change from yellow to red, Figure 3.39 (B). To this solution, $NaBH_4$, in H_2O, was then added slowly and the solution stirred for two hours at room temperature after which the layers were allowed to separate and the toluene layer washed with H_2O, 0.1M H_2SO_4, H_2O, 0.1 NaOH and finally with water again, 0.5 mL

of this toluene solution was added to a small RBF. 0.25 mL of a 3 x 10^{-3} M solution of the complex **41*R*.Eu** in MeOH and 1 mL of H_2O was added to the solution. This was stirred vigorously overnight at room temperature causing phase transfer of particles and stabilisation with the thiols, **41.Eu** and **42.Eu,** in the H_2O layer demonstrated in Figure 3.39 (C).

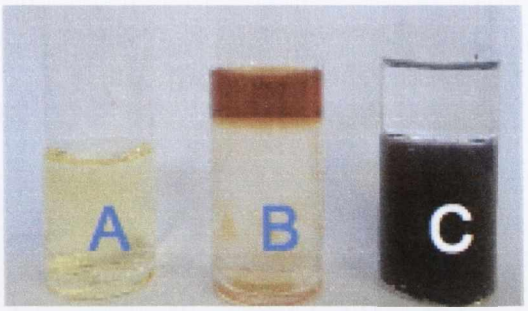

Figure 3.39: *Colour change upon phase transfer of particles for Method 5*

The UV-Vis absorption spectrum showed an SPR absorption band at 520 nm. We attribute the changes in the UV-Vis spectrum to a change in the surface dielectric constant of the nanoparticles, associated with adsorption of the thiol groups of **41.Eu** to the **AuNPs** surface. The functionalisation was carried out for each complex according to the synthesis of Method 5, adapted from Brust *et al.*,[179a] which allows the development of lanthanide luminescent **AuNPs**.

3.14: Characterisation of 41.Eu-AuNPs and 42.Eu-AuNPs

To ensure the functionalisation of the nanoparticles had occurred successfully, the UV-Vis absorption spectra were recorded. The SPR band of the nanoparticles was clearly visible centred around 530 nm, indicating that stabilisation had occurred. If the nanoparticles are not sufficiently stabilised there will be a gradual red shift over time in the SPR band showing aggregation or agglomeration which was not the case for **41.Eu-AuNPs** and **42.Eu-AuNPs**.

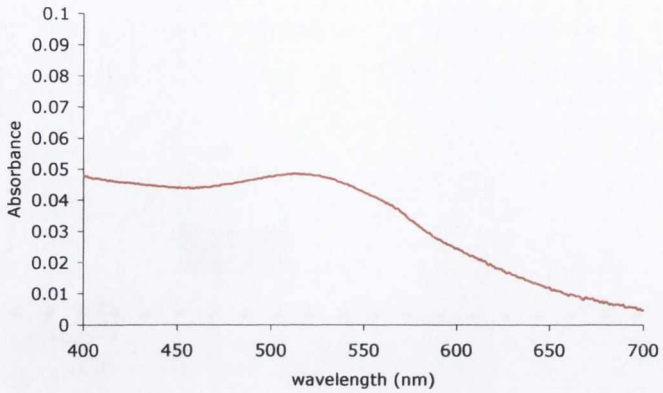

Figure 3.40: *SPR band of* ***AuNPs*** *in the UV-Vis absorption spectrum at 520 nm showing stabilization of 5 nm particles with thiol* ***42.Eu*** *in* H_2O

The samples were then analysed using Transmission Electron Microscopy (TEM) to establish the shape, size and dispersion of the particles. Different solutions of particles in H_2O were drop cast onto the grids and allowed to dry for 32 seconds and 64 seconds respectively (allowing different deposition of particles), after which the grids were blotted and the samples allowed to dry for a further 2 hours in air.

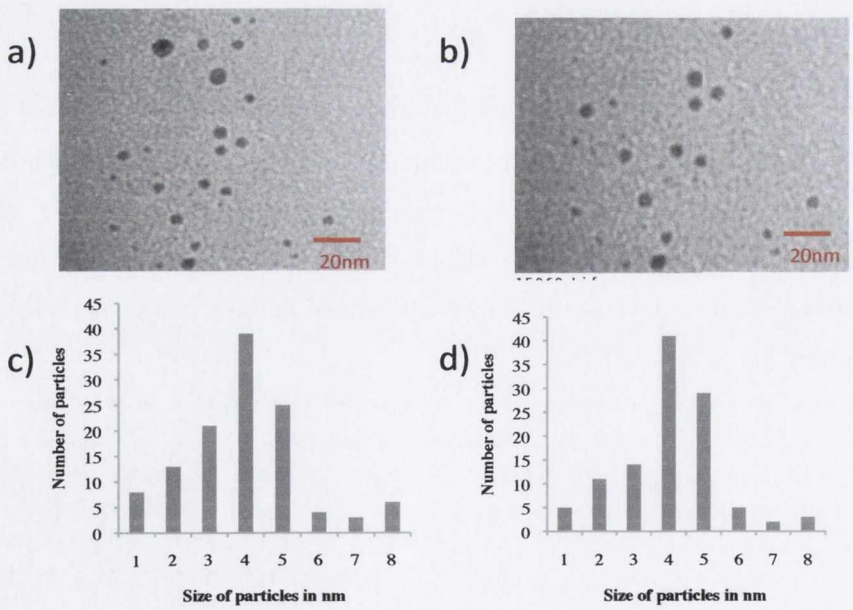

Figure 3.41: *TEM of a)* ***41S.Eu-AuNPs*** *and b)* ***41R.Eu-AuNPs*** *with a scale bar of 20 nm and distribution diagrams for both c)* ***41S.Eu-AuNPs*** *and d)* ***41R.Eu-AuNPs***

The size distribution of the nanoparticles show 5 nm particles with no aggregation or agglomeration observed. The nanoparticles are monodisperse and stabilised by the thiols which is suggested by the small size and monodispersity of the particles observed for **41.Eu**, Figure 3.41.

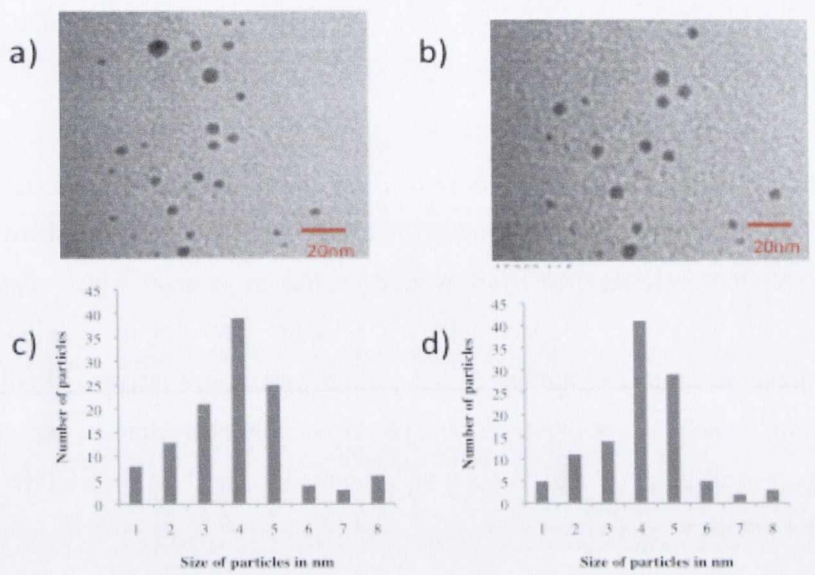

Figure 3.42: *TEM of* ***42S.Eu-AuNPs*** *and* ***42R.Eu-AuNPs*** *with a scale bar of 20 nm and distribution diagrams for both c)* ***42S.Eu-AuNPs*** *and d)* ***42R.Eu-AuNPs***

The TEM of the particles functionalised with complex **42.Eu** also show size distribution of approximately 4-5 nm, Figure 3.42. This confirms that the technique for **AuNPs** synthesis was suitable for our system, allowing the synthesis of nanoparticles of size 5-6 nm with good reproducibility.

The size and distribution of the nanoparticles in solution have also been determined. This was achieved using dynamic light scattering (DLS), as discussed in the introduction, which measures the diffusion of the particles in solution by observing the scattering of light due to brownian motion of the particles.

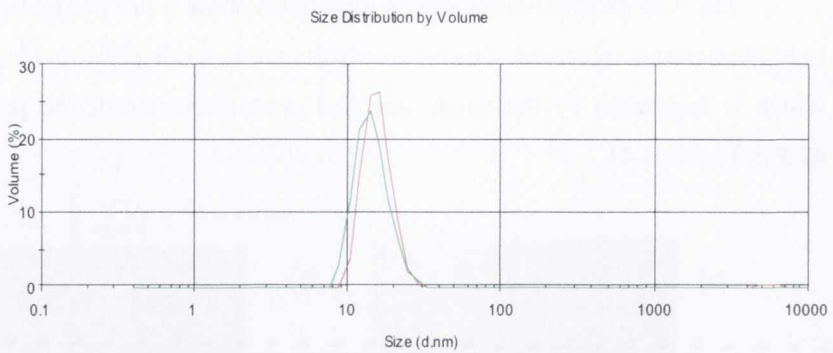

Figure 3.43: *Average hydrodynamic diameter of* ***42.Eu-AuNPs*** *in H_2O using DLS*

In this case, DLS measurements correlate with the TEM size distribution. The DLS measurement calculates the hydrodynamic radius in solution which suggests particles of 10-15 nm, which is in agreement with 5-10 nm particles in addition to the complex functionalised onto the surface of the particles causing a larger hydrodynamic radius in solution, which is not observed in TEM. Having characterised the nanoparticles the photophysical properties of the complexes functionalised on the surface of nanoparticles was important.

3.15 Spectroscopic Studies of 41.Eu-AuNPs and 42.Eu-AuNPs

Photophysical characterisation of the conjugates **41.Eu-AuNPs** and **42.Eu-AuNPs** were carried out in MeOH or HEPES buffer (pH 7.4, 0.1 M NaCl). Concentrations of the order of 10^{-7} M of nanoparticles were determined from the extinction coefficients of the Au SPR band and the concentration of complex added during the gold synthesis, were utilized to ensure the signal of complex on the gold surface would not be too high, which is compatible with measurements such as UV-Vis absorption and luminescence titrations as shown in Section 3.11. Initially a UV-Vis absorption spectrum was recorded, which again shows the distinctive three fingered absorption band at 281 nm, corresponding to the $S_0 \rightarrow \pi\pi^*$ transition for the naphthyl chromophore, Figure 3.44. The presence of the SPR band at 520 nm, indicated the absorption of the surface atoms of the particle, which demonstrated the presence of approximately 5 nm spherical nanoparticles.

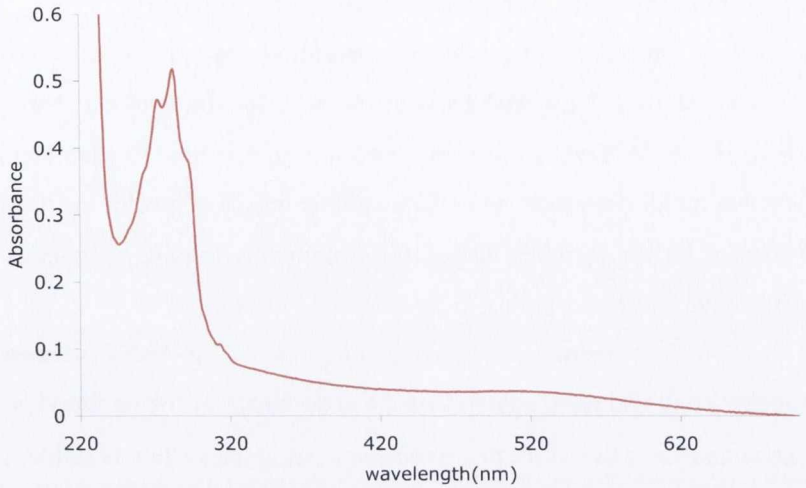

Figure 3.44: *UV-Vis absorption spectrum of* ***42.Eu-AuNPs*** *in MeOH*

Similar to the results observed for **41.Eu** and **42.Eu**, excitation of the naphthalene band at 281 nm resulted in the sensitised lanthanide emission, which demonstrated the population of the lanthanide excited state *via* energy transfer from the excited state of the naphthyl antenna to the $^5D_0$ state of the lanthanide, Figure 3.45.

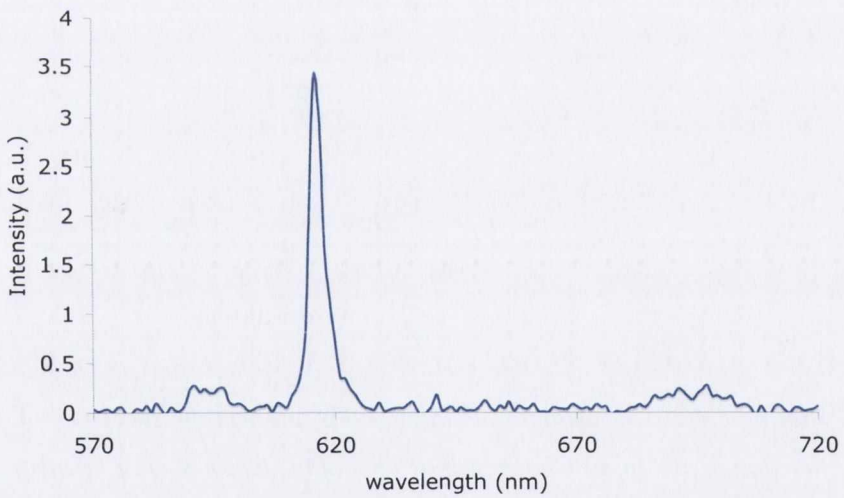

Figure 3.45*: Eu^{3+} emission spectrum of* ***41.Eu-AuNPs*** *(1 x 10^{-5} M) in MeOH, λ_{ex} = 281 nm*

As before the characteristic europium-centred emission was attributed to the $^5D_4 \rightarrow {}^7F_j$ transitions. The characterisation of the systems **41.Eu-AuNPs** and **42.Eu-AuNPs** demonstrate the properties were unchanged upon functionalisation onto the surface of the nanoparticle. The next section discusses the pH behaviour of the system **42.Eu-AuNPs** which was water-soluble and could be assessed for the behaviour as a function of pH.

3.16 Photophysical Characterisation of 42.Eu-AuNPs

Analysis of the UV-Vis absorption spectra for **42.Eu-AuNPs** showed similar behavior to the **42.Eu-AuNPs** with the λ_{max} for the naphthyl band at 281 nm. The SPR band of the **AuNPs** can also be observed at 520 nm. Excitation into the naphthyl band yielded, on all occasions, the characteristic emission spectra for the Eu^{3+} complex. As was observed for the complex alone, this system was soluble in aqueous solution allowing the pH behavior of the complex to be analysed in H_2O.

Analysis was first carried out on **42.Eu-AuNPs** using UV-Vis absorption spectroscopy and have shown that the absorbance of the naphthyl $S_0 \rightarrow \pi\pi^*$ band remains unchanged over the entire pH range, suggesting the system is stable, Figure 3.46.

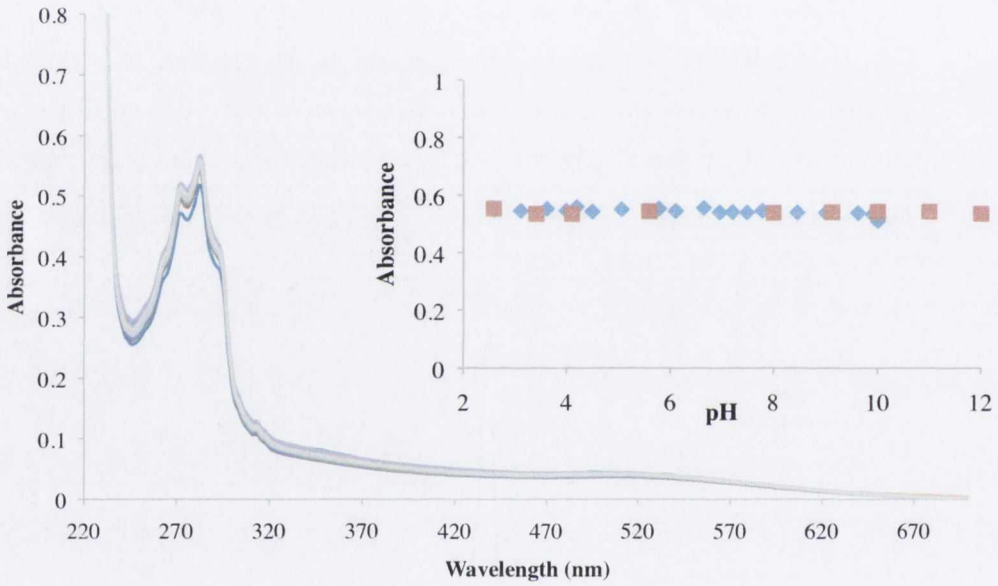

Figure 3.46: *The changes in the UV-Vis absorption spectrum of* ***42.Eu-AuNPs*** *as a function of pH. Inset: Changes at 615 nm of the luminescence intensity as a function of pH*

Similarly, the behaviour of the luminescence was also investigated over the same pH range and the results obtained for the nanoparticle conjugates were similar to those of the complexes. No major changes were recorded as a function of pH and the similar results were observed for the fluorescence emission, were relatively pH independent, showing a small steady decrease in intensity in alkaline media. These complexes are thus quite stable over a large pH range and so suitable for sensing in aqueous environments.

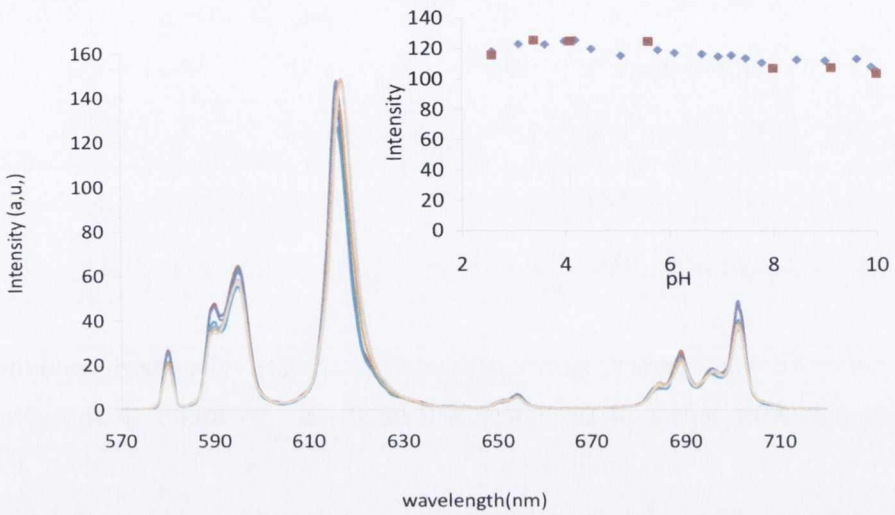

Figure 3.47: *The changes in the Eu^{3+} emission spectrum of* ***42.Eu-AuNPs*** *in aqueous solution as a function of pH.* ***Inset:*** *Plot of intensity at 615 nm as a function of pH.*

The next step is the determination of the lifetimes and q values of **41.Eu-AuNPs** and **42.Eu-AuNPs**.

3.17 Lifetimes and *q* values of 41.Eu-AuNPs and 42.Eu-AuNPs

It was important to ensure the complexes retained their photophysical properties upon functionalisation of the gold surface and so demonstrate similar lifetimes and luminescent behaviour when attached to the gold particle.

ii) $q^{Eu(III)} = 1.2\ [\ (1/H_2O - 1/D_2O) -0.25 -0.075x]$ Eq. 1

iii) $q^{Eu(III)} = 2.1\ [\ (1/H_2O - 1/D_2O)]$ Eq. 2

The lifetimes of the complexes functionalized on the surface of the particles were calculated from the deactivation of the excited state using Equation 1 for Eu^{3+} in H_2O and Equation 2 for MeOH, as discussed in Section 3.9.2, in order to determine if the complexes demonstrated the same photophysical behaviour.

Table 3.2: *Lifetimes and q values of* ***41.Eu-AuNPs and 42.Eu-AuNPs***

Complex	τ solvent (ms)	τ Deuterated solvent (ms)	q (±0.5)
41*R*.Eu -AuNPs	0.58	1.58	1.5
41*S*.Eu -AuNPs	0.79	1.55	1.3
42*R*.Eu -AuNPs	0.61	1.06	1.2
42*S*.Eu -AuNPs	0.52	1.02	1.42

The lifetimes, shown in Table 3.2, correlate quite closely with those previously calculated for the complexes alone, with slightly shorter lifetimes. This is most likely due to quenching of the luminescence by the gold surface. The q values demonstrate the binding of one or two metal bound solvent molecules, similar to that observed for the complexes so it is possible to deduce that the displacement of metal bound solvent molecules could be carried out in a similar manner to that of the complexes. The chirality of these complexes functionalised onto the gold surfaces is important, in order to determine if they retained chirality throughout the process, and for this reason, the CD and CPL of the **41.Eu-AuNPs** and **42.Eu-AuNPs** were recorded in the next section.

3.18 Circular Dichroism of **41.Eu-AuNPs and 42.Eu-AuNPs**

The CD spectra were again recorded to ensure the complex contained the chiral centres required and demonstrated the enantiomeric purity of the functionalised gold nanoparticles. The circular dichroism spectra of the complexes were again recorded on the gold surface to ensure no changes in the chirality of the system was observed.

The CD spectra were recorded for **41*R*.Eu-AuNPs** and **41*S*.Eu-AuNPs** in MeOH and are shown in Figure 3.48. The band of the $S_0 \rightarrow \pi\pi^*$ transition of **41*R*.Eu** and **41*S*.Eu** was observed to respond to polarised light with the same magnitude. It also confirms the enantiomerically pure isolation of ligands **41*R*.Eu-AuNPs** and **41*S*.Eu-AuNPs**.

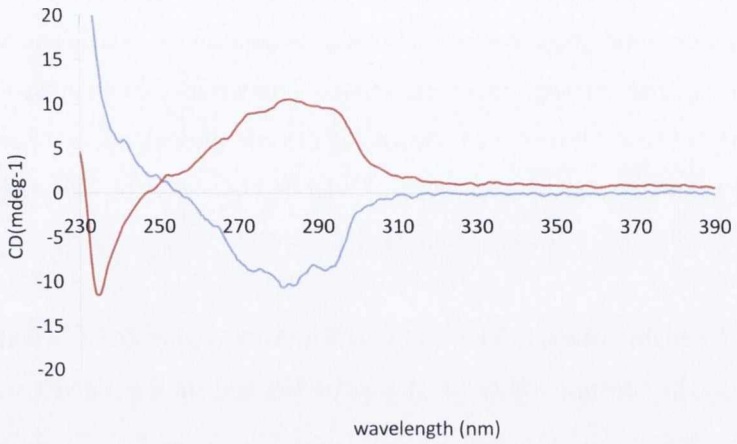

Figure 3.48**: Circular dichroism spectra of **41.Eu-AuNPs

The same result could be observed for **42*S*.Eu-AuNPs** and **42*R*.Eu-AuNPs**, which can be seen in Figure B.12, Appendix B. This demonstrates the nature of the chirality of the complexes remained unchanged during the functionalisation of these complexes onto the gold surfaces. The next step was to demonstrate the sensing ability of the **AuNPs** system. The next section discusses the CPL results of the resulting functionalised nanoparticles.

3.19 CPL of 41.Eu-AuNPs and 42.Eu-AuNPs

The CPL of the functionalised nanoparticles were carried out by Dr. Robert Peacock in Glasgow University. The CPL of the systems proved problematic as the signal of the luminescence was further decreased upon functionalisation of the nanoparticles with the complex. Although this should not show a large effect on the luminescence due to the length of the chain it is possible that the folding of the chain, proposed in Section 3.9.2, could allow the luminescence of the lanthanide to be partly quenched upon functionalisation. This fact made the CPL spectrum of the **41.AuNPs** very difficult to obtain and the intensity was very much decreased compared to that of the complex alone. Having discussed the photophysical characterisation of the complexes on the **AuNPs** we next examined the sensing ability of the complexes functionalised on the nanoparticles.

3.20 Sensing of carboxylates by 41.Eu-AuNPs and 42.Eu-AuNPs

As explained in Section 3.1 and 3.2, the purpose of this project, was to determine the sensing ability of these Eu cyclen-based chiral complexes on the surface of **AuNPs**, by the displacement of metal bound water molecules. To this end, the determination of 1:1 binding was carried out by titration with various analytes, as

discussed in section 3.15. It was demonstrated that the binding stoichiometry of the complexes remained unchanged upon formation of **41.Eu-AuNPs** and **42.Eu-AuNPs** showing that sensing could be carried out while functionalised on the surface of the **AuNPs**. These titrations, as shown for the complex alone, were carried out in MeOH for **41.Eu-AuNPs** and in a mixture of MeOH/H_2O solution for **42.Eu-AuNPs** and will be discussed in the following sections.

3.20.1 Sensing of carboxylates by 41.Eu-AuNPs and 42.Eu-AuNPs

The sensing ability of **41.Eu-AuNPs** and **42.Eu-AuNPs** was initially investigated using simple non-aromatic carboxylates, which have been shown in the literature to displace metal bound water molecules.[168] These carboxylates such as malonic acid have been shown to bind to cyclen based lanthanide complexes.[32] Aromatic carboxylates in general caused the most significant changes with the complexes alone, due to the contribution of the triplet excited state energy of the external antenna to the excited state of the lanthanide. In some cases, such as in the case of **nta** and **tta**, the antennae can more efficiently sensitise the luminescence of the lanthanide than the internal antenna provided by the complex itself.

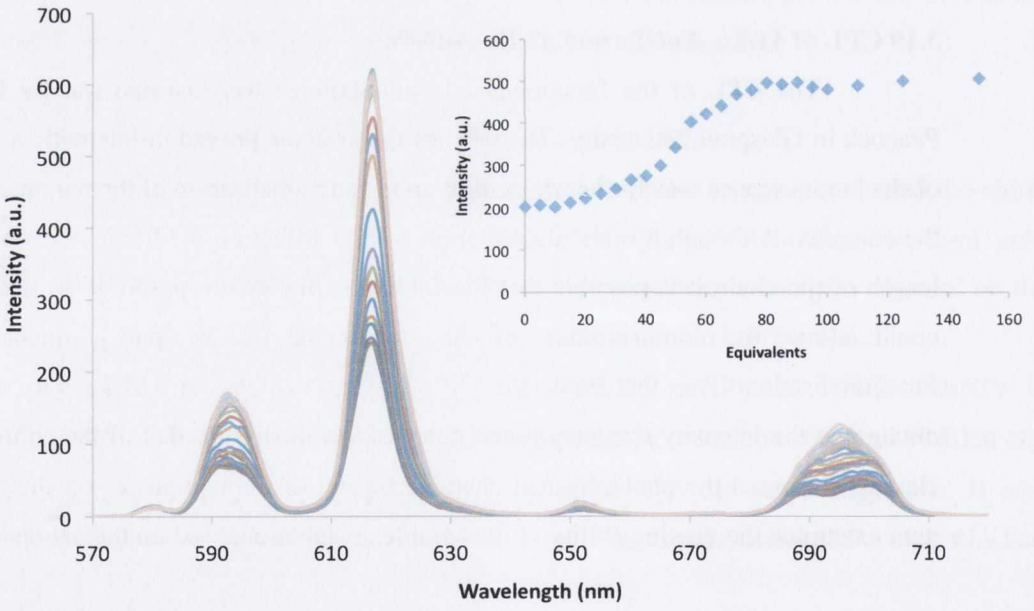

***Figure 3.49**: Changes in the Eu^{3+} emission of **41.Eu-AuNPs** (1 x 10^{-5}M), λ_{ex} at 281 nm in MeOH, upon the addition of citrate. **Inset:** Intensity at 615 nm versus the equivalents of citrate added*

A number of analytes were titrated with both **41.Eu-AuNPs** and **42.Eu-AuNPs** and were found to give varied results upon displacement of the metal bound water molecules. These results are summarised in Table 3.3 and the titration curves are shown in Appendix B. As shown for **41.Eu** and **42.Eu**, the analytes lacking a choromphore, such as lactate or succinate demonstrated only minor changes in the Eu^{3+} emission. The binding of chromophoric units, such as **nta**, **tta** or terephthalic acid, caused larger enhancements in the luminescence as shown in Table 3.3.

In contrast, titration of **42.Eu-AuNPs** in buffered solution (pH 7.4, using NaCl 0.1 M as ionic strength) demonstrated a slight quenching of the lanthanide luminescence upon addition of citrate compared to that of **41.Eu-AuNPs**, this may be due to the fact that citrate in aqueous solution has been shown to act as a strong antioxidant in aqueous solution and can potentially cause electron or charge transfer processes from the lanthanide ion excited state, thus quenching the luminescence of **42.Eu-AuNPs** by 17%.

Table 3.3**: Effect of various anions on the Eu^{3+} emission of **41.Eu-AuNPs** and **42.Eu-AuNPs

Analyte	**41.Eu-AuNPs in MeOH**	**42.Eu-AuNPs in Hepes buffer (ph 7.4, 0.1 M NaCl ionic strength)**
Citrate	Enhancement 152 %	Quenching 17 %
Ascorbate	Enhancement 10 %	Quenching 77 %
Salicylate	Enhancement 38 %	Quenching 45 %
Benzoate	Enhancement 250 %	Enhancement 49 %
Terephthalate	Enhancement 200 %	Enhancement 26 %

Benzoic acid has also been shown to be an efficient sensitiser for the luminescence of lanthanide ions, such as Eu^{3+} and Tb^{3+}.[10] Addition of benzoic acid to **41.Eu-AuNPs** and **42.Eu-AuNPs** caused a significant enhancement due to the addition of an external antenna causing excitation of the metal centred luminescence, Figure 3.50.

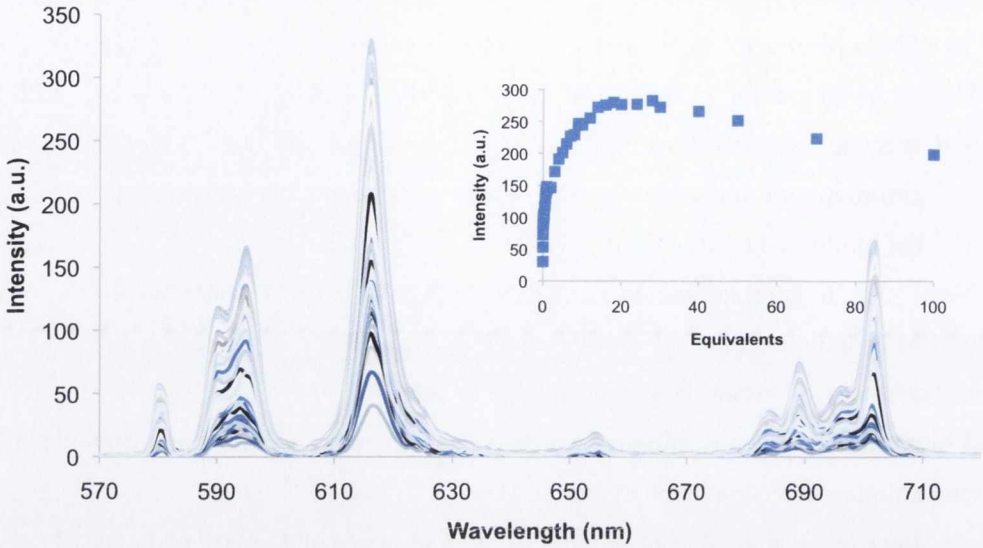

***Figure 3.50**: Changes in the Eu^{3+} emission spectrum of **42.Eu-AuNPs**, λ_{max} at 281 nm, in HEPES (0.1 M pH 7.4, ionic strength 0.1 M NaCl) upon the addition of terephthalic acid.* ***Inset:** Plot of intensity versus equivalents at 615 nm.*

Terephthalic acid, as demonstrated in Section 3.10 has been shown to cause an enhancement in the sensitisation of the excited state of the Eu^{3+}. This could possibly form ternary complexes with the formation of a 2:1 complex to analyte ratio. This was demonstrated in the isotherm, Figure 3.50, with the number of equialvents of analyte bound being 20. The results shown in Table 3.3 demonstrate the "switching on" of the luminescence due to the displacement of the metal bound water molecules by simple aromatic carboxylates. However, the extent of the enhancement has been shown to be greater with antenna such as **nta** and **tta**, which can form ternary luminescent complexes with Eu^{3+}. For this reason, titration with these antennae will be discussed in section 3.21.

3.21 Formation of ternary luminescent complexes of 41.Eu-AuNPs

As demonstrated in Section 3.16, the aromatic antennae **nta** and **tta** showed very efficient formation of ternary luminescent complexes. The changes in the photophysical properties of the **41.Eu-AuNPs** were analysed using UV-Vis absorption spectroscopy upon the addition of **nta**. As demonstrated for the complex alone, **nta** shows two strong absorption bands in the UV-Vis absorption spectrum at 245 nm and 330 nm, respectively.

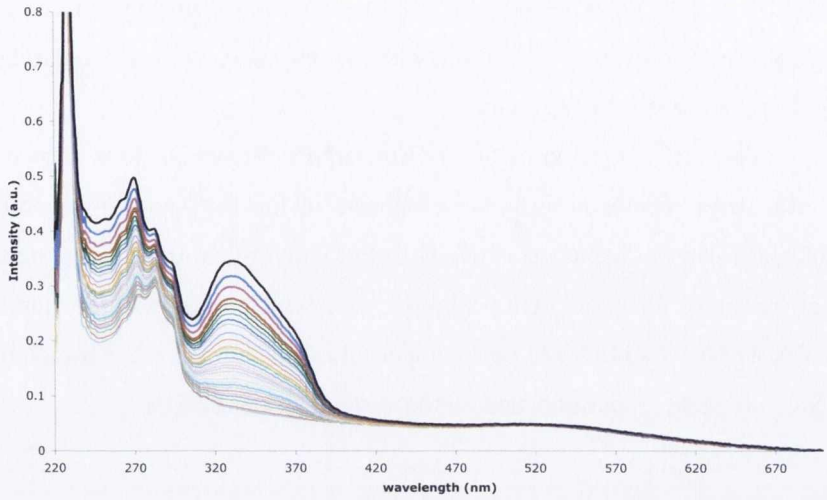

Figure 3.51: *Changes in the UV-Vis absorption spectrum of* ***41.Eu-AuNPs*** *(1 x 10^{-7} M) in MeOH upon addition of aliquots of* ***nta,*** *0-300 eqs*

Although changes for **nta** were observed, no measurable changes occurred in the SPR absorption band of the gold itself, showing the **AuNPs** were stable. Furthermore, the changes in the UV-Vis absorption spectrum for the naphthalene band were consistent with that observed for **41.Eu**.

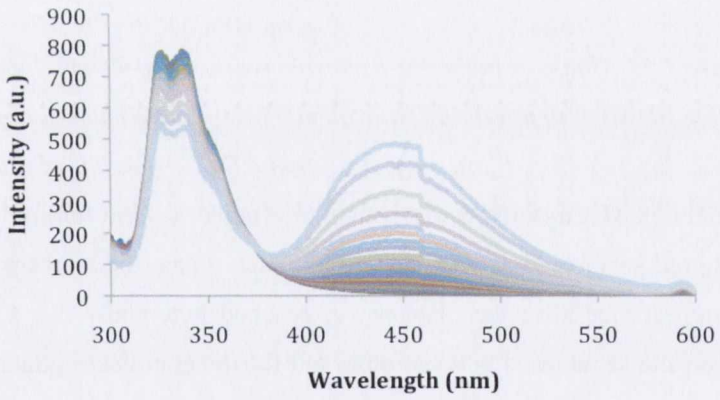

Figure 3.52: *The changes in the fluorescence emission spectrum of* ***41.Eu-AuNPs*** *(1 x 10^{-7} M), λ_{ex} 281 nm, in MeOH upon the addition of* ***nta****, with the band at 450 nm corresponding to the fluorescence of the* ***nta***

The displacement of the metal bound methanol molecules was also investigated by monitoring the changes in the fluorescence and Eu^{3+} time-delayed emission of **41.Eu-AuNPs**. Firstly, upon the addition of **nta**, the fluorescence emission of the complex experienced a decrease of approximately 40 %, characteristic of the $\pi\pi^*$ deactivation of the

naphthyl moiety, shown schematically in Figure 3.32, and indicative of the more efficient energy transfer towards the lanthanide excited state, with a concomitant increase in the band of the **nta** itself at 450 nm.

The Eu^{3+} emission of the **41.Eu-AuNPs**, Figure 3.53, as shown upon the addition of **nta**, demonstrates a significant increase in the Eu^{3+} emission confirming the solvent molecules can be displaced easily with the **AuNPs** conjugate. A plateau was observed at approximately 80 equivalents, Figure 3.54, which estimates the number of complexes, **41.Eu,** as 50-80 complexes per nanoparticle. This allows the estimation of the number of metal complexes functionalised on the surface of the **AuNPs**.

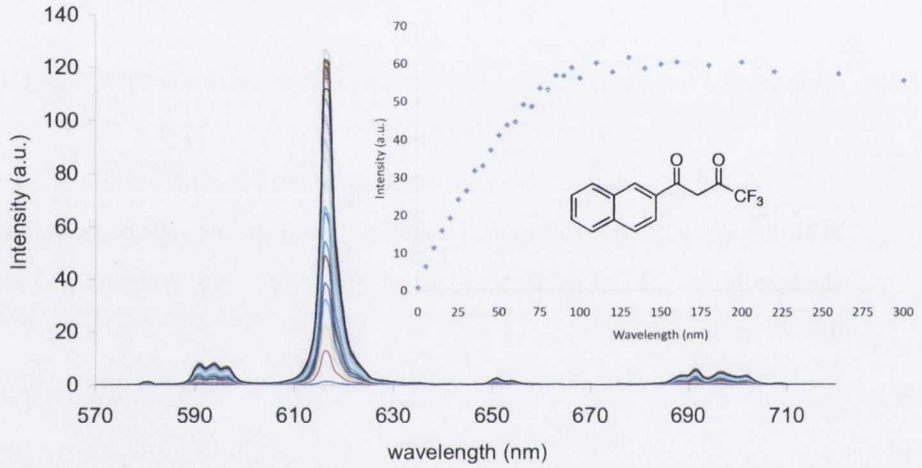

Figure 3.53**: Changes in the Eu^{3+} phosphorescence spectrum upon titrating **41.Eu-AuNPs** ($c=1 \times 10^{-7}M$) with **nta** 0-300 equivalents. Inset: Experimental binding isotherm, emission intensity at 615 nm ($^5D_0$-^7F_J) vs eqs of **nta

The complex **41.Eu-AuNPs** was shown to efficiently form luminescent ternary complexes on the gold surface. However, for the complex alone, the isotherm showed quenching of the luminescence after the plateau was reached potentially due to the inner filter effect however, the same trend was not observed for the complexes attached to the nanoparticle.

It was neccessary to determine if **3.Eu-AuNPs** behaves in the same way in more competitive media, HEPES buffered solution (pH 7.4, ionic strength-NaCl 0.1 M), which is discussed in the next section.

3.22 The formation of ternary luminescent complexes of 42.Eu-AuNPs

Both of **42.Eu-AuNPs**, **S** and ***R*** systems were also titrated with the antennae **nta** and **tta**, establishing the formation of ternary luminescent complexes with these antennae in more competititve media.

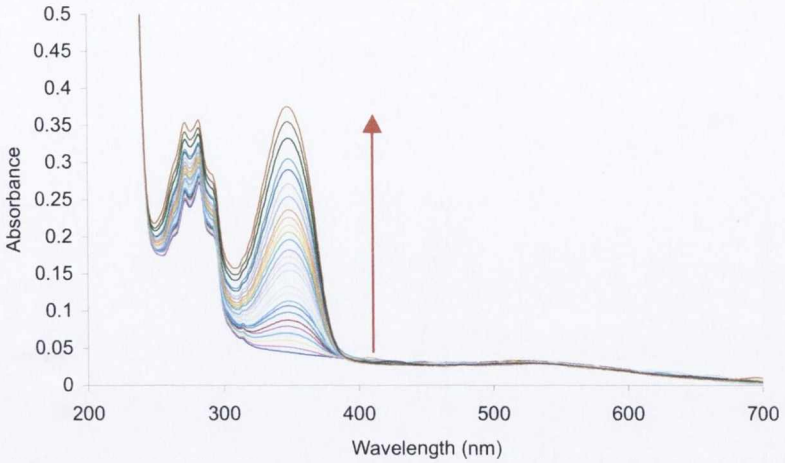

Figure 3.54: *The changes in the UV-Vis absorption spectrum of* ***42.Eu-AuNPs*** *(1 x 10^{-7} M) in HEPES (0.1 M, pH 7.4, ionic strength 0.1M NaCl) upon the addition of* ***tta***

Upon the sequential addition of **tta**, the UV-Vis absorption spectrum showed similar changes to those of **41.Eu-AuNPs**. The SPR band did not show significant changes showing that the nanoparticle surface itself was undisturbed. The changes in the fluorescence and time delayed Eu^{3+} emission were also recorded. The fluorescence spectrum demonstrated similar changes with only the band appearing indicating the presence of the **tta** at approximately 420 nm, similar to that observed for the complex alone.

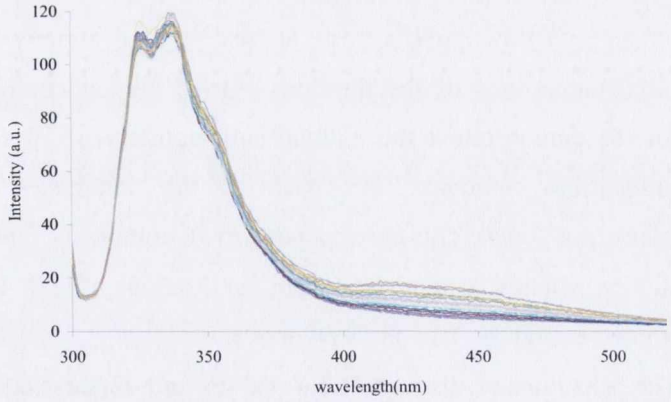

Figure 3.55: *Changes in the fluorescence emission spectrum of* ***42.Eu-AuNPs,*** λ_{max} *at 281 nm, in HEPES (0.1 M, pH 7.4 ionic strength 0.1 M NaCl) upon the additon of* ***nta***.

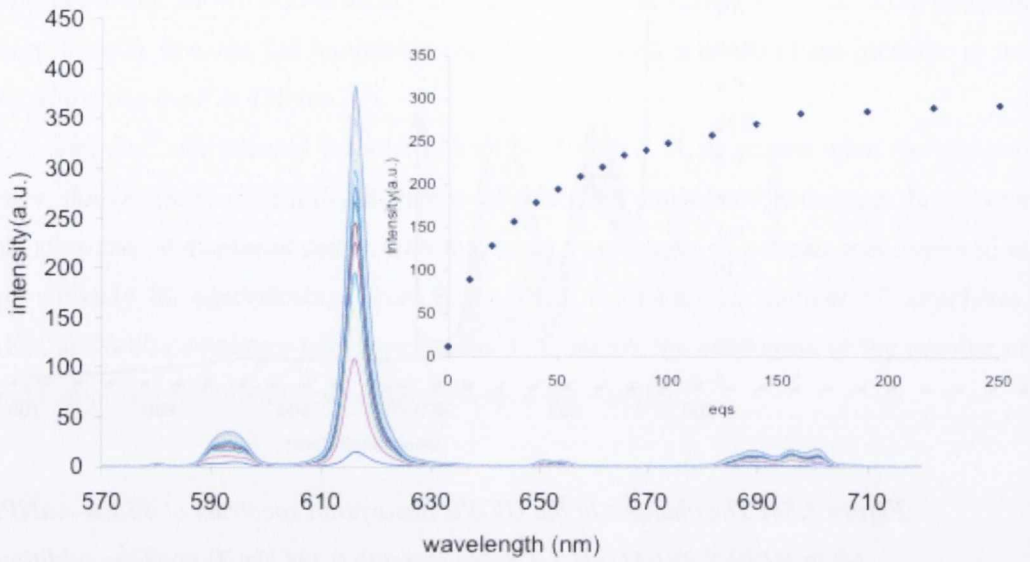

***Figure 3.56**: The changes in the Eu^{3+} emission spectrum of **42.Eu-AuNPs** in HEPES (0.1 M, pH 7.4 ionic strength 0.1 M NaCl) upon the addition of **tta**. **Inset:** Plot of intensity versus the number of equivalents of tta, 0- 250 eqs*

The presence of the J = 0 band was clearly visible in the spectrum of the complex alone. However, upon functionalisation of the particles with these complexes, the J = 0 band in the luminescence spectrum is less intense than the band observed for the complex alone. This is possibly due to the quenching of this transition by the presence of the gold SPR at 520 nm in the UV-Vis absorption spectrum, which could cause reabsorption of the excitation energy by the **AuNPs**. Also, an increase in symmetry could cause a decrease in the $^5D_0$ transition. Each of the titrations carried out on complexes **41.Eu-AuNPs** and **42.Eu-AuNPs** demonstrated the binding stoichiometry of 70 equivalents of antenna to each nanoparticle conjugate. For each of the complexes studied a 1:1 binding stiochiometry was found. This corresponded to 70 complexes functionalised on the surface of the **AuNPs**, which was confirmed from the titrations of both **41.Eu-AuNPs** and **42.Eu-AuNPs** shown in Figures 3.57 and 3.54 above.

The behaviour of systems **41.Eu-AuNPs** and **42.Eu-AuNPs** highlight the fact that these efficient sensors function quite effectively on the surface of the **AuNPs** and can be switched on with the addition of simple aromatic carboxylates and diketonates. The next section utilises the chirality of the systems **41.Eu-AuNPs** and **42.Eu-AuNPs** in order to determine if there could be interactions between the chiral centres and a possible response detected due to chiral optical changes.

3.23 Chiral Sensing

The purpose of this project was to be capable of distinguishing between chiral moieties in solution so the next step was to carry out titrations with various chiral moieties such as chiral amino acids. Titration of both *R* and *S* enantiomers were performed in MeOH in the case of **41.Eu-AuNPs** and Hepes buffered solution (pH 7.4, 0.1 M NaCl ionic strength) in the case of **42.Eu-AuNPs**. For the majority of the chiral amino acids screened, there was no change in the UV-Vis absorption spectrum or the luminescence intensity of the emission. However, in the case of two amino acids, histidine and tryptophan, significant changes were observed in the emission of the lanthanide. Upon the addition of histidine, the complex showed an enhancement in the luminescence due to displacement of the metal bound water molecules, Figure 3.57, however, the converse was observed with tryptophan with quenching of 64 % of the Eu^{3+} emission observed with up to 60 equivalents of amino acid added.

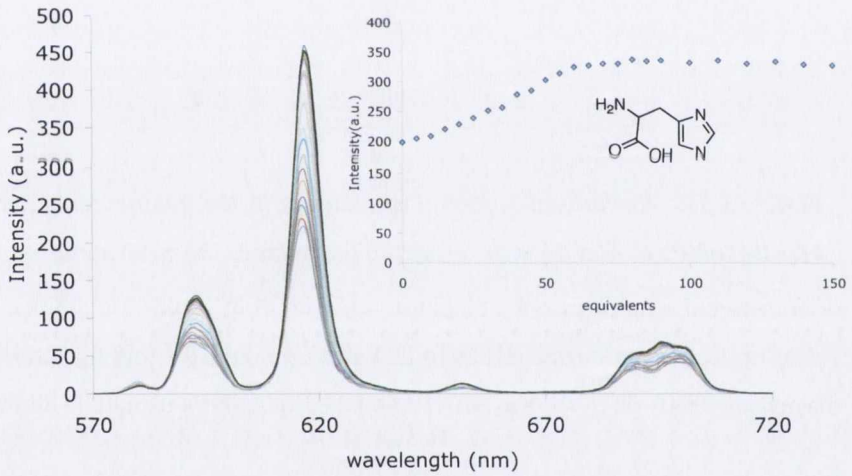

Figure 3.57: *Changes in the Eu^{3+} emission of* ***42.Eu-AuNPs*** *with addition of 0→ 150 equialvents histidine.* ***Inset:*** *The isotherm of equivalents versus intensity upon the addition of histidine*

This was due to the interaction of the amine of the tryptophan unit with the complex and can be explained by overlap of the excited singlet and triplet states causing singlet-triplet crossing between the tryptophan and the Eu^{3+} ion. This causes energy transfer from the excited state of the lanthanide to the excited state of the tryptophan unit and so can cause quenching of the luminescence. The complex showed similar behaviour upon addition of ascorbate. The plot of the normalised intensity versus the equivalents of the amino acids is

shown in Figure 3.58, demonstrating the relative enhancement in the emission of the lanthanide upon addition of each of the amino acids.

Similar titrations were carried out with **42.Eu-AuNPs** to ensure that similar responses could be obtained in buffered solution. These changes have been plotted in Figure 3.48 and show that again the histidine and tryptophan amino acids demonstrate the largest changes in the luminescence showing a specific response compared to that of the other amino acids (Appendix B). It was also possible that these chiral analytes, having

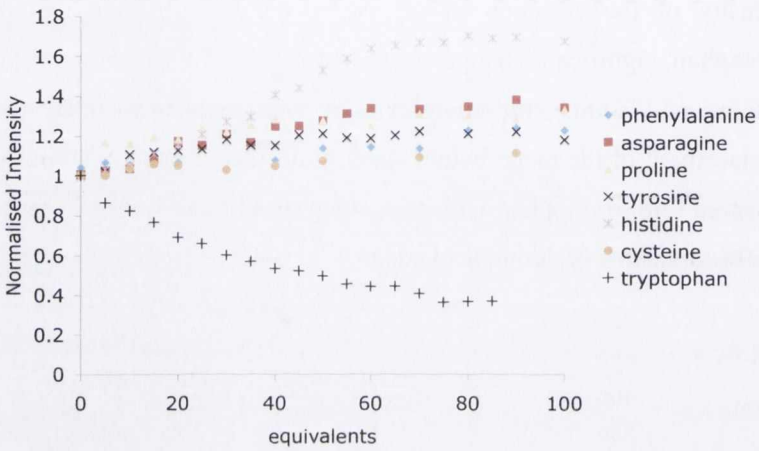

Figure 3.58: *Normalised Isotherm of changes in the luminescence intensity at 615 nm of* ***41.Eu-AuNPs*** *in MeOH with respect to the number the equivalents of each amino acid*

demonstrated a luminescence response upon binding could also show a similar response in chiral optical techniques such as in CD and CPL and for this reason the next section will discuss the analysis of **41.Eu-AuNPs** and **42.Eu-AuNPs** using CD and CPL.

3.24 Chiral sensing recorded by CD and CPL

The purpose of this project highlighted in section 3.27 is to generate chiral sensors. Utilising the characteristics discussed previously, it should be possible to initiate a chiral response upon sensing of the chiral carboxylates, particularly in the case of histidine and tryptophan, which showed the most efficient response. This response should be possible to detect using the CD or CPL. Addition of chiral amino acids, which themselves produce a response in the CD, could show changes of the naphthyl band in the CD spectrum, due to induced changes in the chirality. However, upon addition of amino acids, such as phenyalanine, the changes occurred below 250 nm, which meant it was quite difficult to determine if the changes were due to the addition of the amino acid or fluctuations in the CD spectrum itself.

The CPL was also analysed for changes in the chiral emission upon addition of an external antenna. In this case, the CPL was carried out only with the addition of **nta** as this demonstrated the greatest response in the luminescence. Further CPL studies are necessary upon the addition of amino acids in order to determine if the chiral response can be modulated with variation of the antenna and so sense the presence of chiral moieties by perturbing the chiral luminescene of the complex. The amino acids showing changes in the CD despite not effecting the signal of the chiral chromophore should demonstrate an enhancement of the chiral emission due to changes in the chirality of the system.

3.25: Conclusion

The synthesis and characterisation of **41** and **42** was carried out with the successful formation of the model compuonds **106** and **110**. The formation of these products was confirmed by ^{1}H NMR ^{13}C NMR and mass spectrometry. The corresponding Eu^{3+} were formed for each of the aforementioned ligands and characterised using ^{1}H NMR and mass spectrometry particularly the isotopic distribution pattern of the Eu^{3+} ions. Each of the complexes was studied photohphysically determining the ground and excited state behaviour and in the case of **42.Eu** the stability over a wide pH range. The number of metal bound water moelcules for each complex was found to average 2 and so the potential of these complexes to act as efficient sensors with the displacement of metal bound water molecules was demonstrated with various carboxylates. The formation of luminescent teranry complexes was also carried out with **nta** and **tta** known to form highly luminescent teranry complexes with Eu^{3+} and were found to bind in a 1:1 ratio with the complexes due to displacement of two metal bound water molecules on the lanthanide ion.

The synthesis and characterisation of **AuNPs** following the Brust-Schiffrin method was carried out followed with functionalisation with the complexes **41** and **42**. The functionalisation of the nanoparticle surface with the complexes 2, 3 was carried out and fully characterised. The **AuNPs** were then assessed for their photophysical activity and found to demonstrate the same photophysical behavior in the UV-Vis absorption, fluorescence and phosphorescence emission demonstrating the sensing of carboxylates such as citrate, succinate and were also found to bind chromphoric antennae such as **nta** and **tta** with the number of compelxes bound found to be 80 complexes per nanoparticle on average for both **41.Eu-AuNPs** and **42.Eu-AuNPs.** The sensing of chiral analytes such as amino acids was carried out and exhibited specificity for histidine and tryptophan experiencing an enhancement and a quenching, respectively. Further work can be carried out on these systems which have demonstrated efficient formation of ternary luminescent

systems with amino acids, as this could potentially allow for the formation of chiral systems, however, full studies of this could not be carried out due to time constraints. This could potentially allow the utilisation of these chiral luminescent nanoparticles which have been shown to sense the presence of chiral substrates, to sense in a chiral manner these analytes switching on the CPL signal or inducing changes in this signal.

Chapter 4

Gadolinium Contrast Agents

Chapter 4: Gadolinium contrast agents

4.1 Introduction

Since 1895, the use of lanthanides in medical imaging has become very pronounced due to the emergence of faster and more efficient technologies and novel organic ligands developed for the complexation of lanthanides.[117] There are now numerous examples of contrast agents based on Gd^{3+} macrocyclic complexes due to their enhanced stability and relaxivity, which are currently clinically available.[181] The recent incorporation of these complexes onto surfaces, such as **AuNPs** and Ag nanoparticles and supports, demonstrates the increased efficiency of the functionalised systems.[182] For this reason, the synthesis, characterisation and photophysical evaluation, followed by investigation of the relaxation potential of different cyclen Ln^{3+} complexes functionalised onto the surface of **AuNPs** are discussed in this Chapter. Building upon the success of the developments of **AuNPs** for Ln^{3+} luminescent sensors (Chapter 3), the idea was to take this further and explore the use of Gd^{3+} as an MRI contrast agent functionalised on the Au surface. To date, this is an area in which the Gunnlaugsson group has not participated in extensively. Therefore, the exploration of Gd^{3+} functionalized **AuNPs** will be discussed in this Chapter.

4.2 Magnetic Resonance Imaging (MRI):

During the past 50 years, it has been known, and exploited, that atomic nuclei, which possess spin angular momentum (*I*), can interact with an applied magnetic field, *B*.[183] The spins of such nuclei are composed of the spins of the individual protons and electrons in the nucleus; the most effective nuclei possess a spin quantum number of ½, such as ^{1}H, ^{13}C, and ^{19}F, a phenomenon well understood in NMR.

These atoms, when subjected to a magnetic field will align with this external magnetic field. However, upon the removal of the magnetic field, these spins revert to the B_0 or zero magnetisation.[183] This phenomenon is known as relaxation. Interactions between the magnetic spins in atoms and applied magnetic fields has been successfully exploited in a powerful imaging technique, called Magnetic Resonance Imaging (MRI).[129] This method is a non-invasive procedure, and is based on the magnetic fields of protons within the body, producing two-dimensional views of internal organs or tissue. An image can be generated as the protons in different tissues return to equilibrium or 'relax' at different rates giving contrast between the tissues.

There are two different mechanisms of relaxation, **longitudinal relaxation**, $\mathbf{T_1}$ (Figure 4.1) and **tranverse relaxation**, $\mathbf{T_2}$ (Figure 4.2).[117, 184] The $1/T_1$ relaxation rate is described as the longitudinal relaxation rate and is also known as the spin lattice relaxation,

which corresponds to the natural relaxation from the B_0 magnetisation. This spin lattice relaxation, as the name suggests, depends on the interaction of the spins with their surroundings and occurs with the application of the magnetization vector (M_z) in order to invert the spin and then measure the relaxation to the original state.

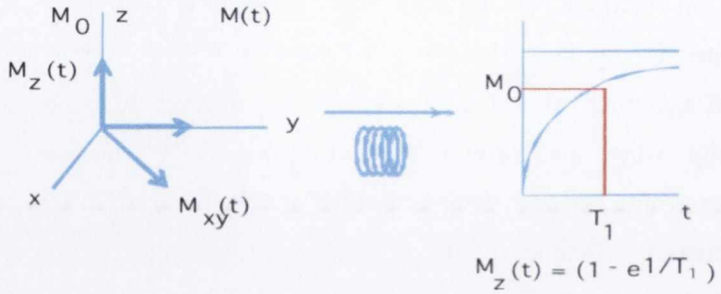

***Figure 4.1**: Longitudinal Relaxation Time (T_1)*

The transverse relaxation rate ($1/T_2$) depends on the interactions with other spins, which contribute to the relaxation of the sample. For a sample in the solution state, the magnetization in the static field remains at B_0, however, not all spins will precess at exactly the same rate and this results in a relaxation of the sample.

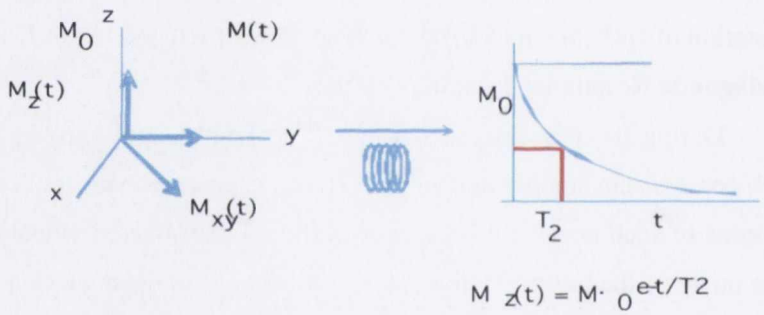

***Figure 4.2**: Transverse Relaxation Time (T_2)*

This is also described as spin-spin relaxation as it depends on the interaction of spins. These different relaxation mechanisms, T_1 and T_2, can occur simultaneously and are known as positive and negative effects, respectively. Naturally, bulk water undergoes relaxation of the water protons quite slowly and can show a difference between the tissue and the surrounding water by contrast.[117] This difference in relaxation is significant in tissues, however, in order to increase the contrast, it is necessary to enhance the local proton water relaxation, which is possible to achieve with the presence of a contrast agent. Paramagnetic metal ions, because they possess a permanent magnetic moment (μ), are ideal for the development of contrast agents and induce fast relaxation of the surrounding water protons. The Ln^{3+} ion Gd^{3+} is particularly efficient, however, others, such as Yb^{3+}, can also have an effect on the relaxation time.[129]

4.3 Relaxivity

MRI contrast agents can markedly alter the relaxation times of water protons in tissues in which they are distributed. The ability of a contrast agent to change the relaxation rate is represented quantitatively as relaxivity ($mM^{-1}s^{-1}$), given by r_1 or r_2, where the subscript refers to either the longitudinal relaxation rate ($1/T_1$) or the transverse relaxation rate ($1/T_2$).[117] Relaxivity is simply the change in the relaxation rate after the introduction of the contrast agent ($\Delta 1/T_1$) normalised to the concentration of the contrast agent or metal ion (M). As stated above, these contrast agents can be divided into two groups, depending on whether they cause a change in T_1 (longitudinal relaxation time - the time taken for the protons to realign with the external magnetic field) or T_2 (tranverse relaxation - the time taken for the protons to exchange energy with the other nuclei) relaxation rates of the water protons; known as positive or negative contrast agents, respectively. Of these, T_1 agents function in order to decrease the relaxation time of the sample, in other words a positive contrast can be observed, brightening the image in these areas, while T_2 agents are known as negative agents as they show darkening or a decrease in T_2 of the surroundings.

The ability of a contrast agent to affect the T_1 or T_2 relaxation times is characterised by the concentration normalised relaxivities r_1 and r_2.[185] These refer to the amount of increase in $1/T_1$ or $1/T_2$ per millimole of agent. The design of contrast agents requires certain characteristics, which can determine the ability of the paramagnetic ion to relate to the bulk water protons. In order to develop an efficient contrast agent the following characteristics must be taken into consideration[186]:

- **Stability - thermodynamic stability of the complex is vital for biological application in order to limit the leaching of metal ions**
- **Metal bound water molecules - the higher number of water molecules the better**
- **The rotational correlation time (τ_R), which is the time between the fluctuations in the magnetic field due to molecular motions**
- **Water exchange rate - the rate of exchange of water molecules in the environment of the paramagnetic agent**

In order to increase the number of metal bound water molecules it is important to take into account the stability, particularly with Ln^{3+} complexes, as the higher the number of water molecules bound, the more likely decomplexation can occur.[184] The

number of metal bound water molecules is important as this means the complex can exhibit similar behaviour to the molecules discussed in Chapter 3. The introduction to Ln^{3+} chemistry has already discussed the importance of metal bound water molecules in luminescent systems in Chapters 1-3, so this will not be discussed in full in this section. For the reasons discussed in Chapter 3, it can be assumed that Eu^{3+} and Tb^{3+} complexes may possess luminescent properties or at least be capable of inducing the luminescence through displacement of the metal bound water molecules, which will also be explored in this Chapter.

4.4 Contrast Agents: A Short Overview

Currently, commercially available contrast agents are based on two different systems; the first being paramagnetic Ln^{3+} ions (Section 4.5) and the second based on superparamagnetic iron oxide particles. In this thesis, the focus will be on Ln^{3+}-based systems, however there are many novel examples of iron oxide particles for MRI, due to their superparamagnetic properties.[187] Superparamagnetic nanoparticles lose their magnetisation in the absence of an external magnetic field. However, when the magnetic field is applied, they can exhibit very strong magnetisation, which can cause field inhomogeneity and activate the dephasing of the proton spins. This causes a decrease in the T_2 of the surrounding water protons.

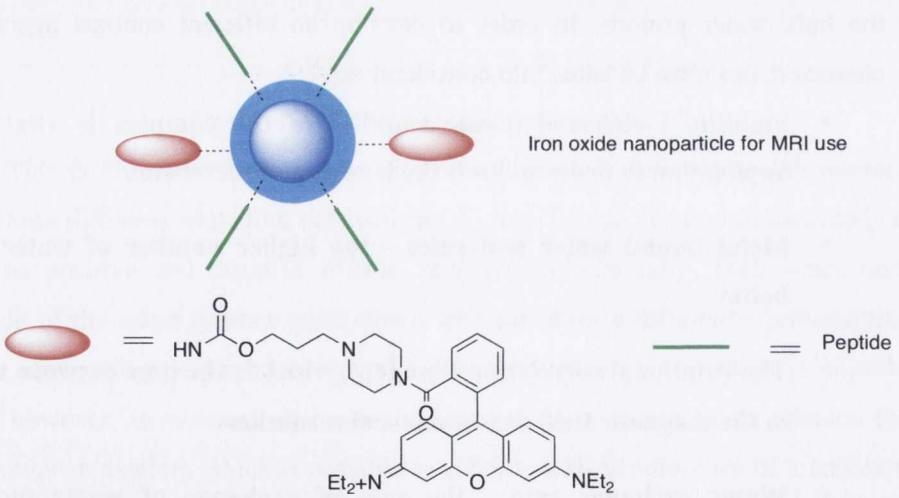

Figure 4.3: *Bombesin functionalised iron oxide nanoparticles for MRI* [188]

This approach has been utilized by Martin *et al.*,[188] for the incorporation of peptides onto the surface of the iron oxide particles in order to form selective MRI contrast agents for the imaging of the prostate for the detection of cancer, Figure 4.3. This activity was selective for PC-3 prostate, and was shown to be inhibited by the presence of the peptide alone

showing that the conjugate formed with the peptide and the iron oxide nanoparticle was responsible for the contrast enhancement.

Recently, Howes *et al.*[189] developed conjugate semi-conducting nanospheres, conjugated to four different fluorescent polymers, which demonstrated both interesting fluorescent properties and the iron oxide nanoparticles also showed magnetic properties. However, in this Chapter we will focus on the development of T_1 targeted Ln^{3+} based contrast agents. In the next section, the design, synthesis and development of contrast agents based on Ln^{3+} will be discussed.

4.5 Lanthanide-based contrast agents

This chapter will focus on the development of T_1 agents, which are broadly centred on Ln^{3+} complexes. As already discussed in Chapters 1-3, Ln^{3+} ions, due to their high coordination numbers, can bind solvent water molecules if their coordination sphere is not fully filled by the ligand. Moreover, it is known that the number of metal bound water molecules increases the potential relaxivity, Figure 4.4.[184] Of the Ln^{3+} ions, Gd^{3+} has the highest relaxivity due to the higher number of unpaired electrons, which makes it the most stable ion.[190] Gd^{3+} also possesses a symmetric S-state and so its electronic relaxation is relatively slow.

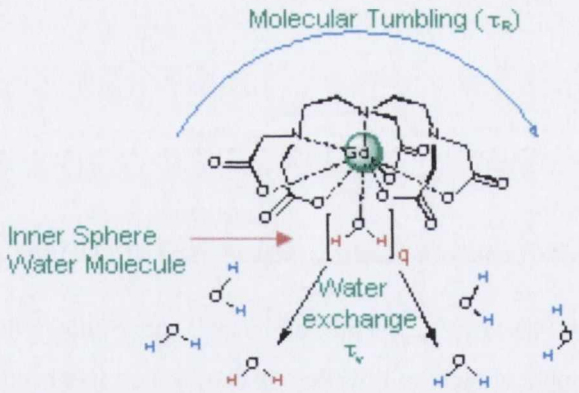

***Figure 4.4**: Gd^{3+} Contrast Agents showing inner sphere water molecules*[191]

The relaxivity, in the case of Ln^{3+} contrast agents, consists of contributions from both inner sphere, as well as outer sphere water relaxation mechanisms. The inner sphere mechanism involves the water molecules directly bound to the metal centre and has a large effect on the relaxivity of the sample. The outer sphere water molecules, are close enough to be affected by the Gd^{3+} but are not directly coordinated and so have a lesser effect on the relaxivity.

$$r_1^{IS} = \frac{q / [H_2O]}{T_{1m} + \tau_m} \qquad \textbf{Eq 4.1}$$

The inner sphere relaxivity is given by Equation 4.1, where q is the number of metal bound water molecules, T_{1m} is the T_1 of the water hydrogen in the inner sphere and $[H_2O]$ is the water concentration in mM.[192] In order to increase the relaxivity, one can increase q or decrease T_{1m} or τ_m, which is the solvent exchange rate. At least one water molecule must be bound in the inner coordination sphere of Gd^{3+} for contrast agents and this will undergo rapid exchange with the water molecules of the surrounding solution to affect the relaxation time of all the solvent protons.

As discussed in Chapter 1, recent developments in the field of MRI contrast agents have developed towards the incorporation of surfaces and nanoparticles. The design of these potential MRI contrast agents for clinical use, until now, have been centered on molecules such as Dotarem, Magnevist and Omniscan, shown in Figure 4.5, all of which have been shown to be thermodynamically and kinetically stable and possess high relaxivity mostly with one metal bound water molecule.[191]

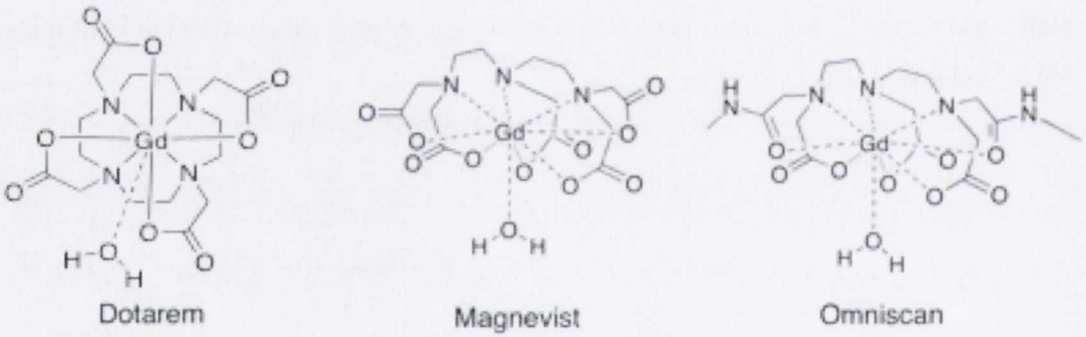

Figure 4.5: *Commercial contrast agents such as Dotarem, Magnevist and Omniscan*

Examples by Sherry *et al.*[193] and Toth *et al.*[194] have shown that anchoring these complexes on larger supports such as micelles or dendrimers has been beneficial for increasing the relaxivity due to increase in the rotational correlation time of the complex. In order to further increase this effect, many complexes have been functionalised onto surfaces[195] and onto nanoparticles and showed dramatic increases in the relaxivity.[196] Helm *et al.*[197] have recently shown the enhancement of the relaxivity upon binding of DTPA Gd^{3+} complexes to the surface of **AuNPs** by up to 3000 $mM^{-1}s^{-1}$ (Chapter 1). Molecular modeling studies were carried out in order to quantify the number of Au atoms in the nanoparticle sphere. The particles were found to yield relaxivities of 60 $mM^{-1}s^{-1}$. Recently, Meade *et al.*[198] have also developed MRI complexes based on the utilisation of click chemistry for the

incorporation of the Gd^{3+} complexes onto the surface of nanoparticles. This technique, as discussed in Chapter 1, allowed the incorporation of arms onto the complexes and a subsequent click reaction caused a number of complexes to bind to a central unit, yielding highly efficient multimetallic conjugates for MRI.

The examples cited herein highlight the potential for Ln^{3+} complexes to function as MRI contrast agents. Ln^{3+} complexes possess interesting luminescent properties as shown in the previous chapters. For these reasons, this Chapter focuses on the development of a simple ligand and it's corresponding Gd^{3+}, Eu^{3+}, and Tb^{3+} complexes, capable of functionalising the surface of **AuNPs**, the design and synthesis of which will be discussed in the following sections.

4.6 Design and Synthesis of 43

With the aim of achieving a dual functioning system capable of both the formation of ternary luminescent complexes and activity as an MRI contrast agent, ligand **43** was designed based on these properties (Scheme 4.1). Ln^{3+} complexes have previously demonstrated luminescent capabilities by selective displacement of the metal bound water molecules.[170] The Gunnlaugsson group have shown that cyclen based Ln^{3+} complexes functionalised onto **AuNPs**, underwent formation of ternary luminescent complexes with **nta** or **tta** diketonate antennae, which bind in a bidentate fashion.[113, 199] Having demonstrated that the functionalisation of nanoparticles with such complexes retained the sensing on a nanoparticle through the use of displacement assays, we set out to generate a ligand capable of demonstrating both luminescent properties and fast relaxation times as the Ln^{3+} complex. Ligand **43** was designed in order to allow functionalisation of a Ln^{3+} complex, containing two metal bound water molecules, onto a gold surface. This was ensured by employing a tetradentate macrocyclic cavity, demonstrating very strong binding constants for Ln^{3+}, ions such as Eu^{3+} and Gd^{3+} (up to 23.5 in the case of Eu^{3+}).[143] The pendant arms were chosen due to their chemical stability and their ability to wrap around the metal ion, aiding complexation. Amides have the ability to form resonance structures and as such hinder the rotation around the N=C double bond meaning they are stable towards nucleophilic attack and hydrolysis. This also makes them good donor atoms for interaction with Lewis acids. The alkane thiol chain was specifically chosen for its length and its strong affinity for the gold surface, as discussed in Chapter 3. Similar bis-aquo complexes have been previously used within the TG group for the development of highly efficient luminescent sensors whereby the sensing mechanism is due to the displacement of metal bound water molecules, by external antennae.[31] Moreover, the incorporation of two

metal bound water molecules is of great interest for the development of Gd^{3+}- based MRI contrast agents, as the inner-sphere relaxivity is proportional to the number of Gd-bound water molecules, *q*, as discussed in Section 4.5.

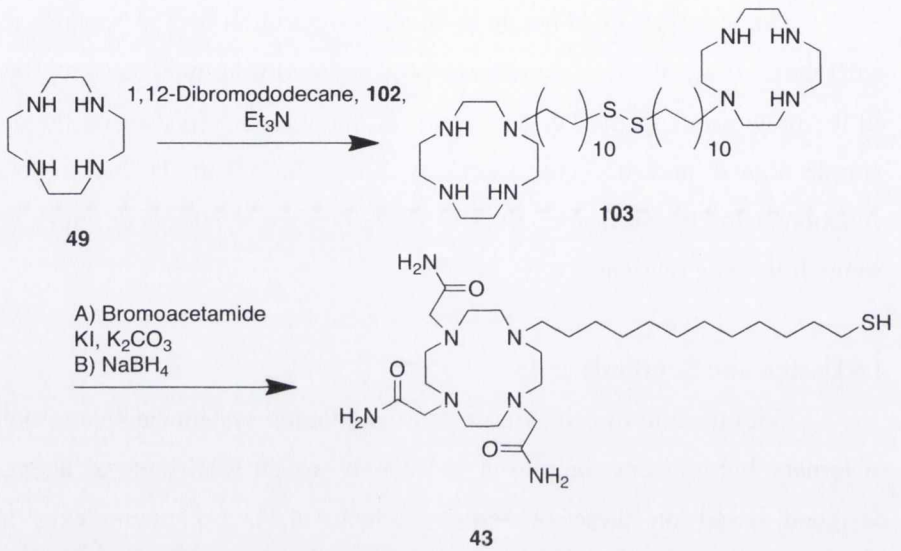

Scheme 4.1**. Synthesis of ligand **43

The synthesis of ligand **43** was carried out as outlined in Scheme 4.1. This involved the initial formation of **103** by monoalkylation of cyclen with 1,12-dodecyl sulfane, **102**, by stirring in $CHCl_3$ with Et_3N as discussed in Chapter 3. Extraction into $CHCl_3$ followed by washing with 1 M HCl and 1 M KOH yielded a yellow oil, **103**, in 70 % yield, which, upon ^1H NMR ($CDCl_3$, 400 MHz,) analysis was found to agree with the published literature values, Figure 4.6. The formation of **103** was confirmed by ^{13}C NMR ($CDCl_3$, 100 MHz) and mass spectrometry.[200] The alkylation of the remaining six amines of **103** was carried out by refluxing the compound with 6.6 equivalents of bromoacetamide, KI and K_2CO_3 overnight in CH_3CN followed by reductive cleavage of the disulfide bridge by the addition of $NaBH_4$ in H_2O. The solvent was removed under reduced pressure, the residue dissolved in $CHCl_3$ washed with 0.1 M KOH solution and the resulting oil precipitated from swirling diethyl ether and toluene which yielded **43** in 20 % yield.

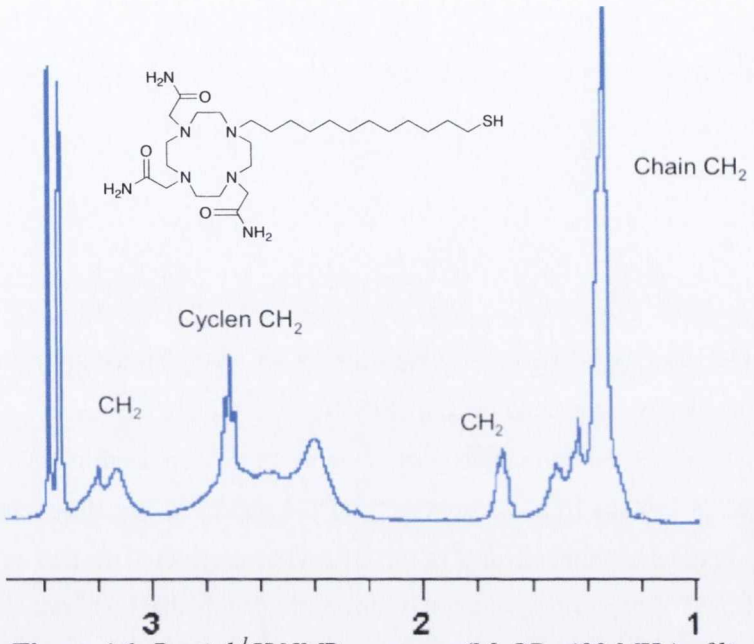

Figure 4.6**: Partial ^1H NMR spectrum (MeOD, 400 MHz) of ligand **43

The ^1H NMR spectrum (400 MHz, MeOD) of **43** showed broad peaks due to conformational equilibria that interconvert different conformations of the ring and pendant arms in solution. The 12-carbon methylene chain can be observed as a broad multiplet at 1.2 ppm. The CH_2 protons of the cyclen macrocycle and the acetamide arms were also observed as broad multiplets from 2.2 ppm to 4 ppm, however, it was difficult to assign these peaks as they appeared as broad multiplets, but could be distinguished by 2D NMR experiments. HSQC experiments allowed the determination of both the chain protons, at 1.2 and 1.6 ppm, and the cyclen CH_2 protons present at 2.5 ppm. ^{13}C NMR spectra showed the presence of the carbonyl moieties of the macrocycle, with the CH_2 arm carbons resonating at 50.19-56.8 ppm. Mass spectrometry showed a signal with exact mass 544.4026 for $C_{26}H_{54}N_7O_3S$ corresponding to the calculated value of 544.4009.

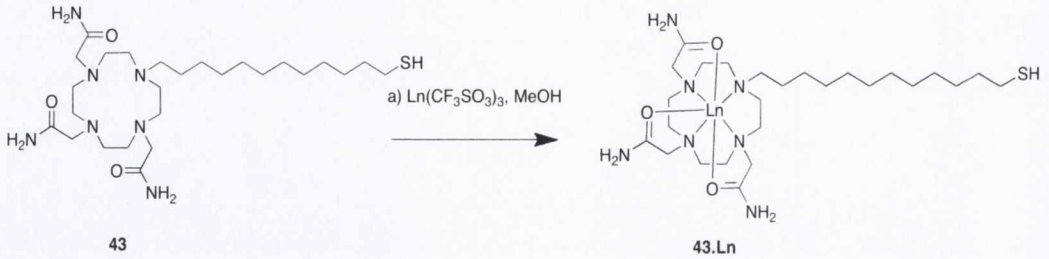

Scheme 4.2: *Complexation of* ***43*** *with* $Ln(CF_3SO_3)_3$, *(Ln =* Eu^{3+}, Tb^{3+}, Gd^{3+}, Lu^{3+}*)*

The corresponding Ln^{3+} complexes of **43** were formed by refluxing **43** with 1.1 equivalents of the corresponding $Ln(CF_3SO_3)_3$ (Ln = Eu^{3+}, Tb^{3+}, Gd^{3+}, Lu^{3+}) in MeOH for 18 hours. Many of the lanthanide shift reagents have been used in NMR spectroscopy and can cause the protons in close proximity to the paramagnetic Ln^{3+} ions to experience an enhanced magnetic field and shift in the ^1H NMR spectrum. This can be observed with the Eu^{3+} and Tb^{3+} complexes as, upon complexation with the Ln^{3+} salt, ^1H NMR spectrum (MeOD, 400 MHz) shows shifting and broadening of the axial and equatorial protons of the cyclen macrocycle significant of complexation by a Ln^{3+}, with resonances from +20 ppm to -20 ppm for the Eu^{3+} analogue as shown in Figure 4.7.

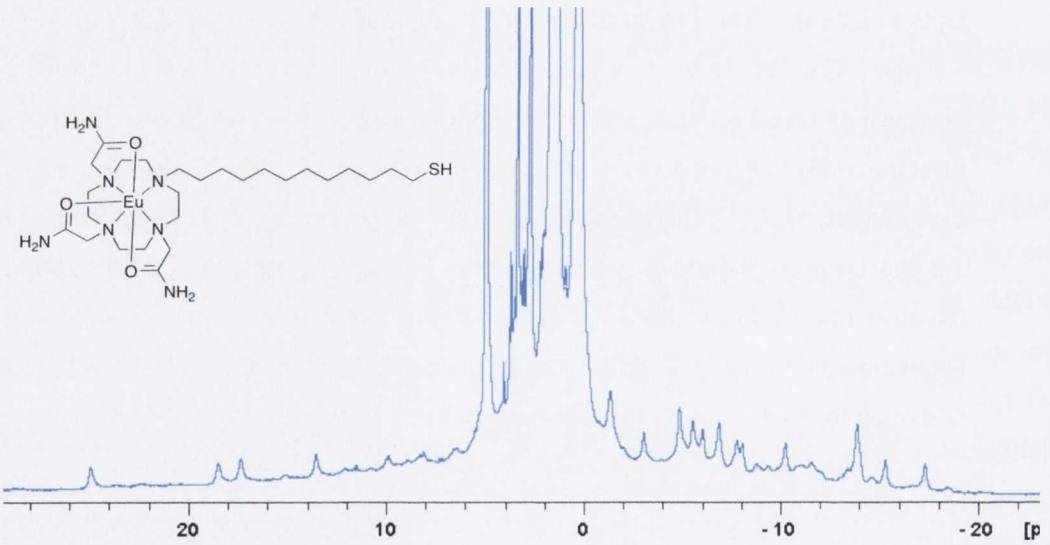

Figure 4.7*: ^1H NMR spectrum (MeOD, 400 MHz) of* ***43.Eu***

The synthesis of the CH_3 analogue, **111**, was also carried out in order to act as a control for the analysis of **43.Eu** and **43.Gd** attached to the nanoparticle. Thiol had been shown in Chapter 3 to perturb the metal bound water molecules on the surface of the complex and so this control was synthesised to compare the number of metal bound water molecules.

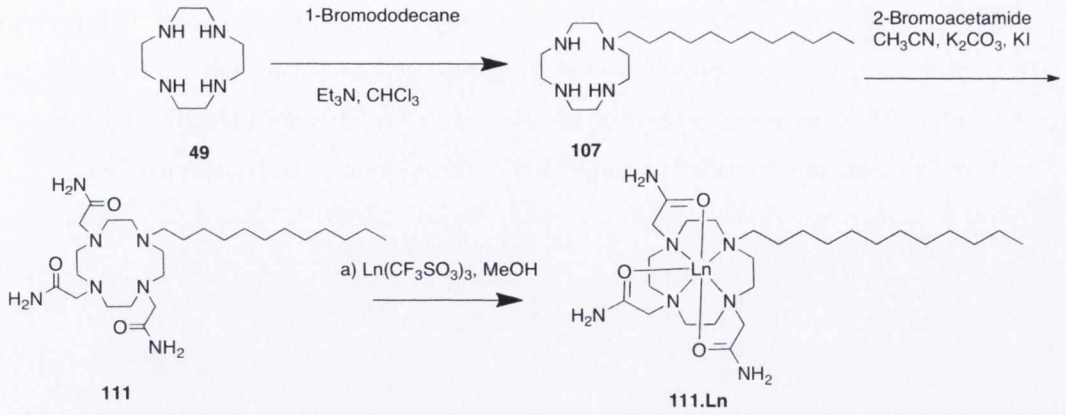

Scheme 4.3**: Synthesis of **111.Ln** (Ln = Eu^{3+}, Tb^{3+}, Gd^{3+}, Lu^{3+}) from ligand **111

The monosubstituted macrocycle, **107**, was synthesised by refluxing, in $CHCl_3$ solution, one equivalent of 1-bromododecane with cyclen overnight and one equivalent of Et_3N. The product, **107**, was extracted into $CHCl_3$ and washed with water and isolated as a yellow oil in 25% yield.

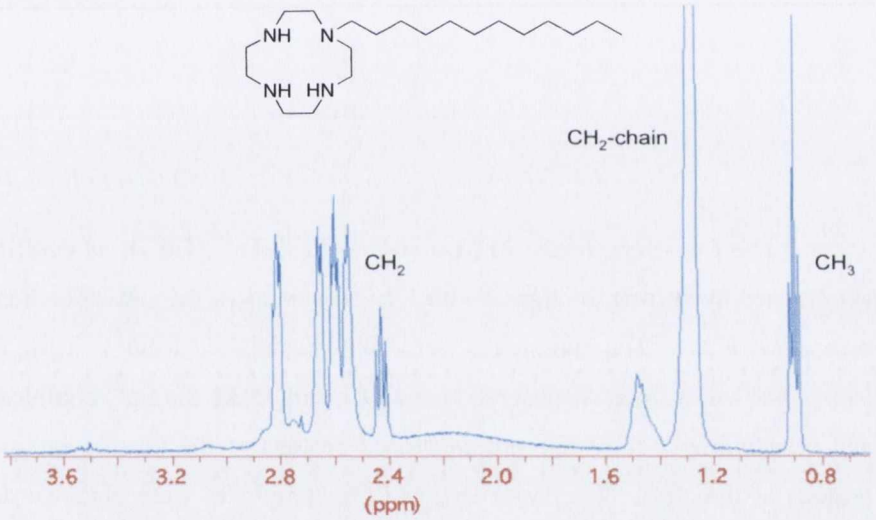

Figure 4.8:** The ^1H NMR spectrum (400MHz, $CDCl_3$) of **107

The ^1H NMR spectrum ($CDCl_3$, 400 MHz), confirmed the successful formation of the product with the CH_3 of the alkyl chain at 0.9 ppm and the cyclen CH_2 protons resonated at 2.4-2.9 ppm, shown in Figure 4.8. Mass spectrometry and ^{13}C NMR ($CDCl_3$, 100 MHz) are further evidence that the product was isolated. This product was then alkyated with 3.3 equivalents of 2-Bromoacetamide in CH_3CN in the presence of K_2CO_3, KI and stirred at reflux for 7 days. The ligand, **111**, was isolated by filtration through a plug of celite, removal of solvent, extraction into $CHCl_3$, followed by washing with water and 1 M KOH to yield **111**, as a yellow oil in 15 % yield. The ^1H NMR (MeOD, 400 MHz) spectrum of **111**, confirmed the successful synthesis with the signal of the carbon chain at

1.2 ppm, which appeared as a broad multiplet, Figure 4.9. The cyclen CH_2 protons and the protons of the corresponding arms were observed as broad multiplets at 2.34 - 2.69 ppm and 1.28 ppm, respectively. The resonances in the ^1H NMR (MeOD, 400 MHz,) spectrum of this compound was less broad than the corresponding thiol analogue, **70**.

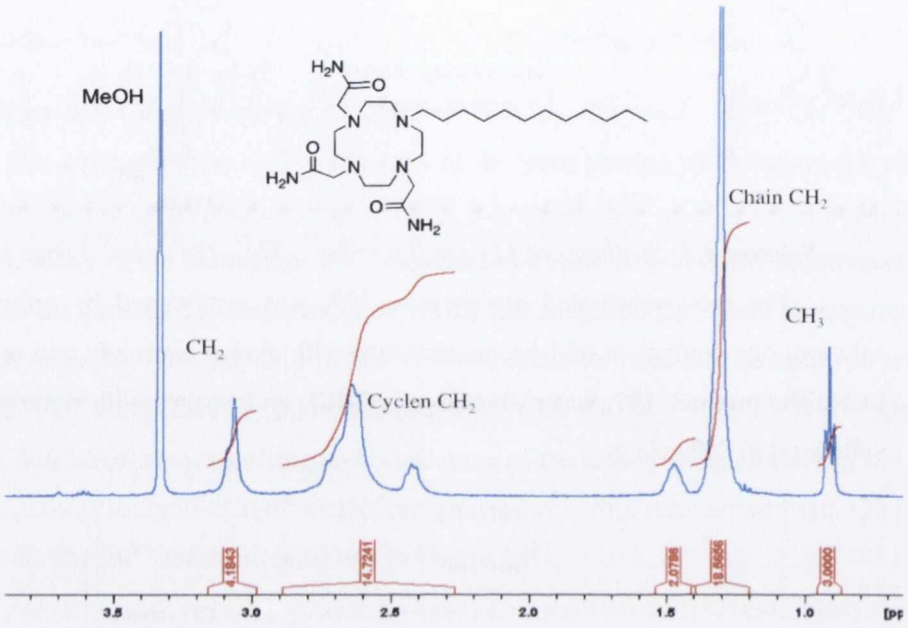

Figure 4.9**: ^1H NMR spectrum (MeOD, 400 MHz) of ligand **111

The Ln^{3+} complexes, **111.Ln** (Ln = Eu^{3+}, Tb^{3+}, Gd^{3+}), as described for **43**, were synthesised by stirring the ligand with 1.1 equivalents of the corresponding $Ln(CF_3SO_3)_3$ at reflux in CH_3CN. The complexes were then precipitated from swirling diethyl ether and isolated as yellow oils. As observed for **43.Eu** and **43.Tb** the Ln^{3+} complex showed shifting and broadening of the axial and equatorial protons of the macrocycle and the acetamide protons of the arms. The mass spectra of the complexes were obtained demonstrating the isotopic distribution pattern of the Ln^{3+} ions. The isotopic distribution pattern of **111.Eu** can be seen in the mass spectrometry with the observed mass at 812.2834 for $C_{27}H_{52}N_7O_6F_3SEu$ with the calculated mass of 812.2864 shown in Figure 4.10. Similar results were observed with the Gd^{3+} complex with the observed mass at 669.3474 for $C_{27}H_{52}N_7O_6F_3SGd$ with the calculated mass at 669.3451, also shown in Figure 4.10.

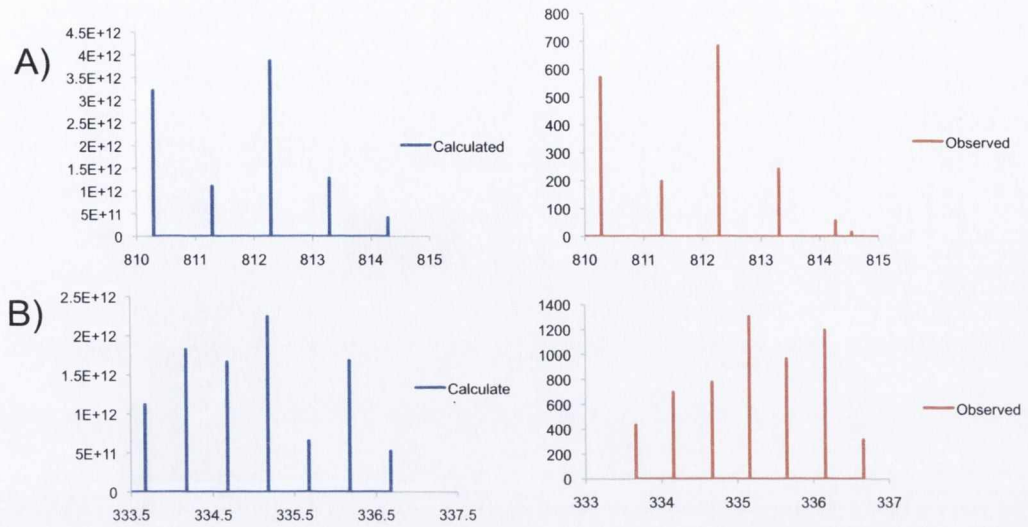

Figure 4.10: A) *MALDI of* ***111.Eu*** *calculated and observed,* ***B)*** *MALDI of* ***111.Gd****, calculated and observed*

Having successfully synthesized both **43.Ln** and **111.Ln**, the next step involved the functionalisation of the complexes onto **AuNPs** surfaces.

4.7 Synthesis and Characterisation of 43.Gd-AuNPs

The functionalisation of the surface of **AuNPs** was carried out with the complexes of **43**. The synthesis and functionalisation of the nanoparticles were carried out following an adaptation of the Brust-Schiffrin method.[50] An aqueous solution of hydrogen tetrachloroaurate ($HAuCl_4$) was mixed vigorously with a solution of tetraoctyl ammonium bromide (TOAB) in toluene. The two-phase mixture was stirred vigorously until the Au^{3+} had been transferred to the organic layer, which was indicated by a colour change from yellow to red, Figure 4.11. The Au^{3+} stabilised in toluene was then reduced in a biphasic solution with the addition of an aqueous solution of $NaBH_4$, visible due to a colour change from yellow to dark purple, Figure 4.11. After washing the solution of nanoparticles with 0.1 M HCl, 0.1 M NaOH and H_2O, an aqueous solution of **43** was then stirred vigorously with a solution of the unstabilised **AuNPs** in toluene. The phase transfer of the nanoparticles into the water layer occurred upon stabilisation of the **AuNPs** by the thiol, which was visible from a colour change of clear to purple.

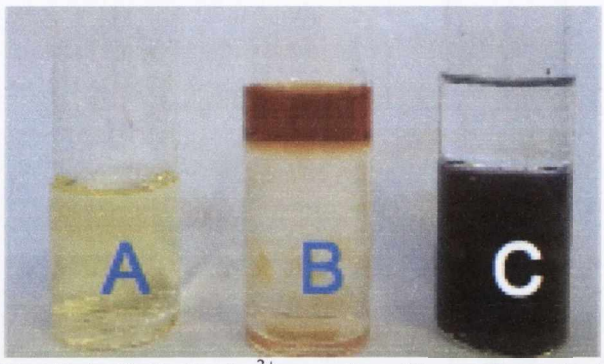

Figure 4.11: **A:** $HAuCl_4$ in H_2O, **B:** Au^{3+} transferred into toluene by TOAB, **C: AuNPs** transferred into H_2O after reduction by $NaBH_4$

of the gold in response to optical excitation. The UV-Vis absorption spectrum of the **AuNPs** in H_2O was measured, which showed the characteristic SPR band at 520 nm, demonstrating the stability and size of the nanoparticles (between 2 and 10 nm). These particles are stable over time, as the SPR band did not show significant changes over a six month period.

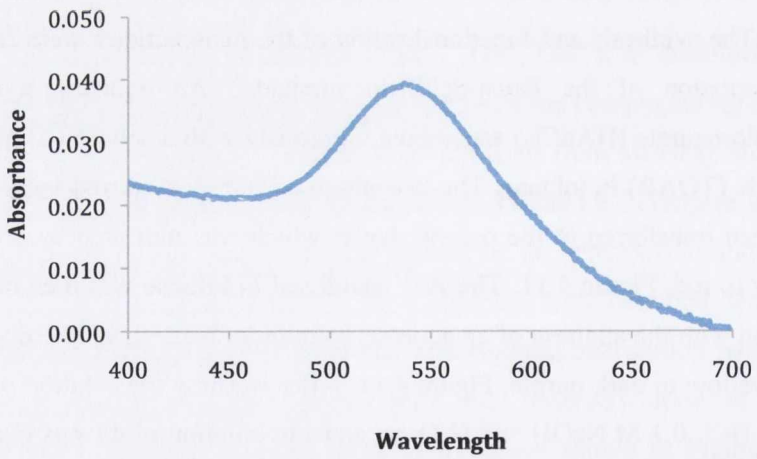

Figure 4.12: *UV-Vis absorption spectrum of* ***43-AuNPs*** *in* H_2O

In order to characterise the size and distribution profile of Ln^{3+}-stabilised nanoparticles in H_2O, a combination of Transmission Electron Microscopy (TEM) and Dynamic Light Scattering (DLS) was used, as discussed in Chapters 1 and 3. Transmission Electron Microscopy (TEM) is a technique, which measures scattering of electron beams by solid samples mounted on a grid or a background.

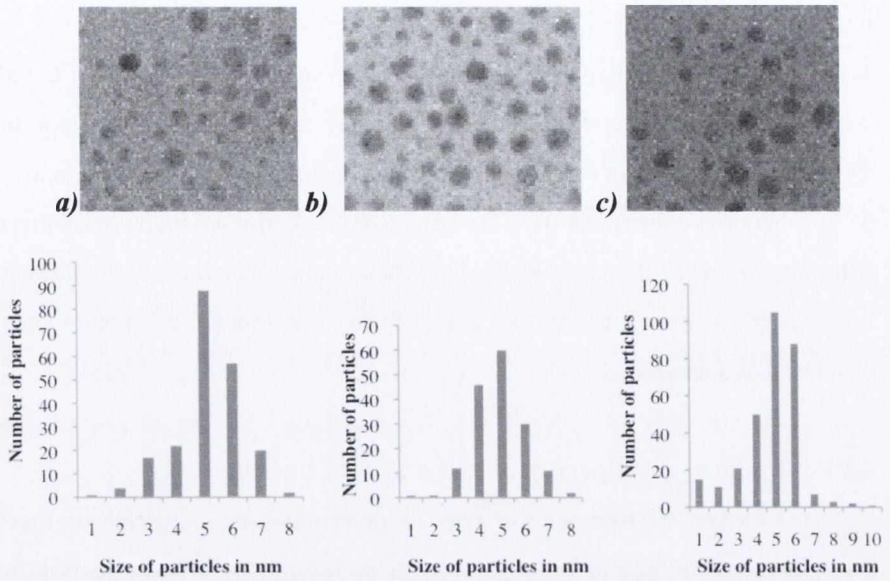

Figure 4.13**: TEM images of a) **43.Tb-AuNP, b) 43.Eu-AuNPs** and c) **43.Gd-AuNPs and size distribution diagrams corresponding to each species

Solutions of **Ln-AuNPs** in H_2O were dropcast onto the surface of the grids and allowed to dry overnight before carrying out TEM experiments. The **AuNPs** in particular, give good image contrast due to differences in composition between the non-metallic carbon background and the metallic gold nanocomposites. Characterisation of the nanoparticles by TEM, Figure 4.13, showed monodisperse stabilised particles with a size distribution of 5-6 nm, which are the size expected from the Brust method.[50]

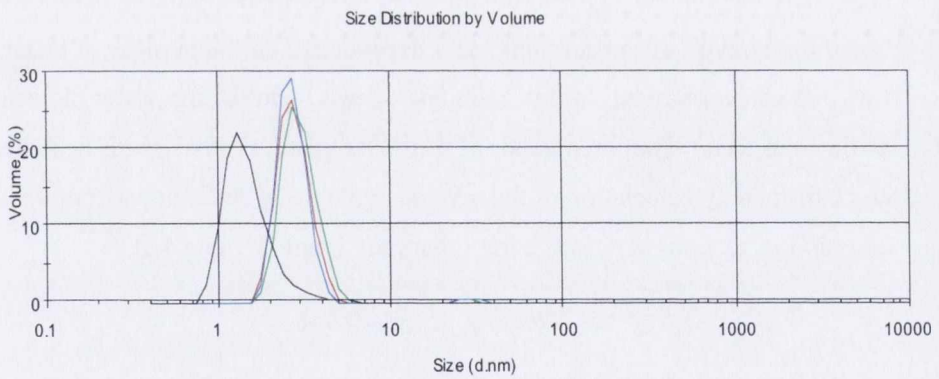

***Figure 4.14**: Hydrodynamic diameter (based on the value average particle size as measured by DLS for **43.Eu-AuNPs** (green), **43.Tb-AuNPs** (red), **43.Gd-AuNPs** (blue)*

These particles were also analysed by dynamic light scattering (DLS), which measures the backscattering of light due to the Brownian motion in solution. DLS was carried out in aqueous solutions of **43.Ln-AuNPs** to determine the size distribution and stability; the polydispersity index (PDI) gives a good indication of the stability of the

particles in aqueous solution. DLS measurements of the nanoparticle solutions (Figure 4.14) correlate with the TEM results. These solutions showed a PDI of approximately 0.095-0.199, which confirms the stability and dispersity of the nanoparticles in solution. Typically a range of up to 0.5 of PDI indicates stable solutions of particles.

Having confirmed the stability, size, and monodispersity of the nanoparticles in solution, the next step was to analyse these nanoparticulate conjugates in terms of their luminescent capabilities in the case of the Eu^{3+} and Tb^{3+} analogues, which will be discussed in section 4.8.

4.8 Photophysical Properties of 43.Ln and 43.Ln-AuNPs

The aim of this section was to determine the potential of these complexes to displace the metal bound water molecules, so the first step was to determine the number of metal bound water molecules on each complex through calculation of the luminescent lifetimes in solution.

4.8.1 Determination of the Lifetimes of 43.Eu and 111.Eu

It is important, with the synthesis of Ln^{3+} complexes (Chapter 2), to determine the number of water molecules bound to the metal centre. For the Ln^{3+} complexes, this can be achieved by calculating the luminescence lifetime or decay of the luminescence, over time, of the complex in H_2O and D_2O (discussed in Chapters 1-3). It is important to know accurately the number of metal bound water molecules as both the luminescence efficiency and the relaxivity of the solution has a dependence on the number of water molecules the Ln^{3+} ion can coordinate. In this case, one or two metal-bound water molecules are present as Eu^{3+} has a coordination number of 9 and the ligand synthesised is heptadentate. This can be confirmed by calculation of the q value, which was determined from the lifetimes of the emission in aqueous solution, using Equations 1 and 2, Table 4.1.[175]

$$q^{Tb3+} = 5[\ (1/\tau_{H2O} - 1/_{D2O}) - 0.06] \qquad \textbf{Eq. 1}$$

$$q^{Eu3+} = 1.2\ [\ (1/\tau_{H2O} - 1/_{D2O}) - 0.25 - 0.075x] \qquad \textbf{Eq. 2}$$

***Table 4.1**: Calculation of the number of metal bound water molecules*

Complex	τ_{H2O} (ms)	τ_{D2O} (ms)	q value (± 0.5)
43.Eu	0.44	0.93	1.5
111. Eu	0.52	1.14	1.7
43.Tb	2.65	1.5	1
43.Eu-AuNP	0.64	1.6	1.52
43.Tb –AuNP	2.70	1.67	0.7

Both **43.Eu** and **111.Eu** were shown to have $q > 1.0$ so it can be concluded that each complex possibly has two metal bound water molecules in its first coordination sphere, which correlates well with other compounds from the literature.[201] This hydration state was ideal for development of MRI contrast agents as it allows a high rate of water exchange directly in proximity to the Gd^{3+} centre. The lifetimes of **43.Eu-AuNPs** were also calculated and were found to correspond to the lifetimes observed for the complex alone, although it was difficult to calculate the lifetimes particularly on **AuNPs** as the intensity of the emission was lower than that of the complex alone due to quenching from the gold. Following the calculation of the luminescence lifetimes and q values the luminescent properties of these complexes were explored. These studies and the study of the behaviour of the complex in solution are discussed in Section 4.8.2. The next step was to analyse these complexes as a function of the number of equivalents of analyte to assess the potential formation of ternary luminescent complexes.

4.8.2 Photophysical Study of 43.Ln (Ln = Eu^{3+}, Tb^{3+})

As discussed in Chapter 1, in order to observe the metal centred luminescence of the complexes, there must be indirect transfer of energy to the Ln^{3+} centre by a chromophore. As can be seen in Scheme 4.1, the complex, **43.Ln**, contains no chromophore capable of sensitising the emission. Direct excitation of the Ln^{3+} ion can be carried out, however, the sensitisation of the Ln^{3+} excited state can be challenging, due to the low absorptivity, as already discussed in Chapter 1. Thus the addition of an antenna in this case is important in order to ensure sufficient energy is available for the effective sensitisation of the Ln^{3+} emission.

As discussed in Chapter 1 and 3, the excited states of Ln^{3+} ions, such as Eu^{3+} and Tb^{3+}, are known to be quenched by vibrational deactivation from O-H oscillators, such as H_2O, which are particularly prevalent in coordinatively unsaturated systems, such as in

43.Ln. However, the displacement of the two metal-bound water molecules of **43.Ln** by a suitable antennae would lead to the formation of luminescent ternary complexes upon indirect sensitization of the Ln^{3+} excited state.[199] β-diketonates and carboxylates have both been shown to form ternary complexes with Ln^{3+} ions. β-diketonates are much more efficient for Eu^{3+} sensitization, while aromatic carboxylates have been shown to sensitise Tb^{3+} luminescence more efficiently.[170] This is corresponding to the position of the triplet state level of these ligands compared to the energy levels of Eu^{3+} and Tb^{3+}. The affinity of **43.Eu** for two bidentate antennae, 4.4.4 trifluoro-1-(2-naphthyl)-1,3-butane dione (**nta**) and 4,4,4 trifluoro-1-(2-thienyl)-1,3-butanedione (**tta**), both of which have been shown to form ternary luminescent complexes with europium, have been studied as well as the luminescent properties of the ternary adducts.

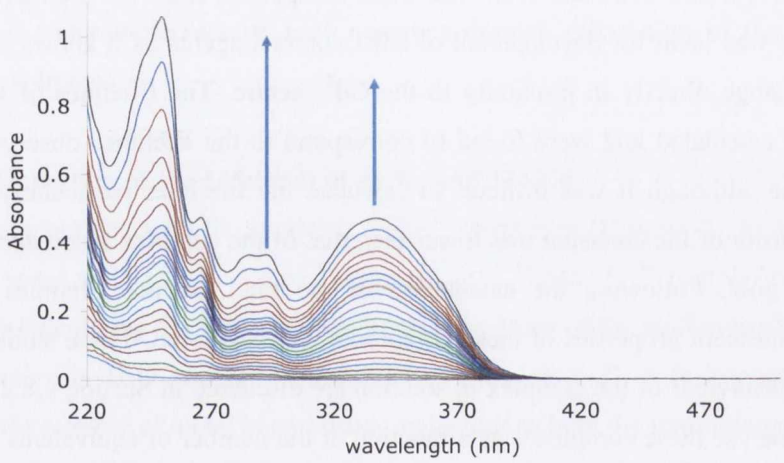

***Figure 4.15**: Evaluation of the UV-vis absorption spectrum of **43.Eu** (1 x 10^{-5}M) in HEPES buffered solution (0.1M, ionic strength 0.1M NaCl) upon addition of **nta** 0-5 equivalents.*

Initially, the UV-vis absorption spectrum of the complex was recorded and monitored upon addition of aliquots of **nta**. The **nta** possesses two strong absorption bands at 245 nm and 330 nm, which can be seen in the evolution of these bands in the UV-vis absorption spectrum, Figure 4.15.

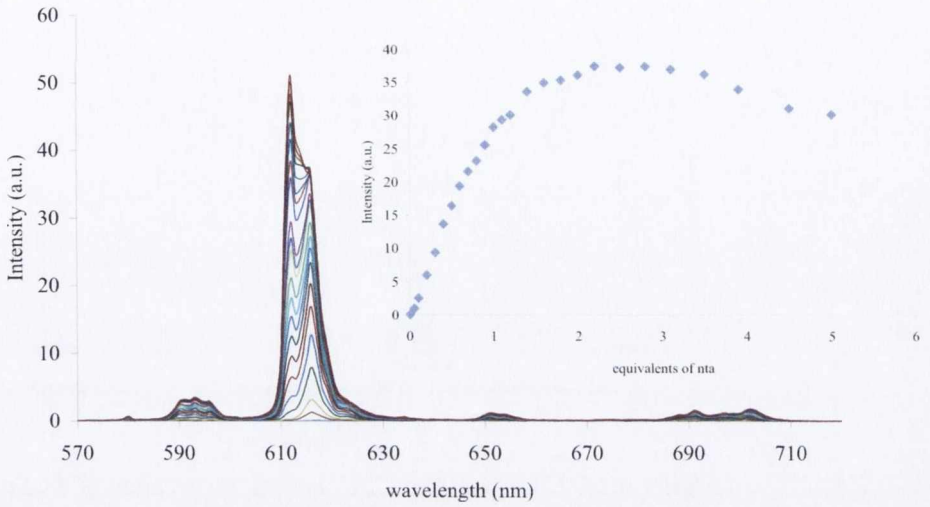

Figure 4.16: *Changes in the Eu^{3+} phosphorescence spectrum upon titrating* ***43.Eu*** *($c = 1 \times 10^{-5}$ M) with* ***nta*** *(0-6 equivalents).* ***Inset****: Experimental binding isotherm, emission intensity at 615 nm ($^5D_0$ - ^7F_J) versus equivalents of* ***nta, 0-5 eqs***

The "switching on" of the Eu^{3+} emission, upon formation of **43.Eu-nta** from **43.Eu** was also monitored by luminescence titrations using **nta** with λ_{ex} = 330 nm, Figure 4.16. Here the Eu^{3+} emission of **43.Eu-nta** was evident from the enhancement of line-like emission bands at 580, 595, 616, 650, and 700 nm, respectively, assigned to the characteristic transitions of the Eu^{3+}, $^5D_0$ - ^7F_J (J = 0, 1, 2, 3, and 4), Figure 4.11. Of these, the hypersensitive $\Delta J = 2$ transition, centered at 616 nm, gave rise to the greatest changes in the Eu^{3+} emission as this is particularly sensitive to the coordination environment of the Eu^{3+} centre, indicating the displacement of the metal bound water molecules. The binding isotherm for the formation of **43.Eu-nta** is shown as an insert in Figure 4.16. A plateau was observed after the addition of one equivalent demonstrating a 1:1 binding between the bidentate antenna and the complex displacing the two metal bound water molecules. The formation of the desired ternary complex, between the **43.Eu** and **nta**, was indicated by the dramatic enhancement of red Eu^{3+} emission that was readily visible under a UV-lamp. In a similar manner, titration of **43.Eu** with **tta** also showed a 1: 1 binding stoichiometry with the formation of a luminescent ternary complex in which the two metal-bound water molecules were displaced by the antenna, Figure 4.17.

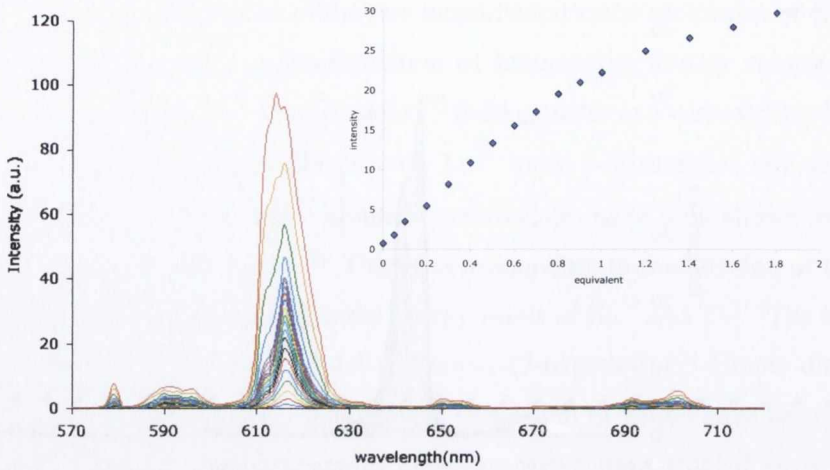

Figure 4.17: *Changes in the Eu^{3+} emission spectrum of* ***43.Eu*** *($c = 1 \times 10^{-5}$ M) in MeOH upon the addition of* ***tta*** *0-6 equivalents.* ***Inset:*** *Experimental binding isotherm, emission intensity at 615 nm ($^5D_0$ - ^7F_J) versus equivalents of* ***tta****)*

The corresponding Tb^{3+} complexes, were initially found to be non-luminescent in HEPES buffered solution (pH 7.4, NaCl 0.1 M ionic strength). However, they also gave rise to the formation of luminescent ternary adducts on titration with suitable antennae such as benzoic acid and terephthalic acid, chosen due to their triplet state levels. The titration of antenna such as benzoic acid allowed the switching on of the Tb^{3+} luminescence as shown in Figure 4.18.

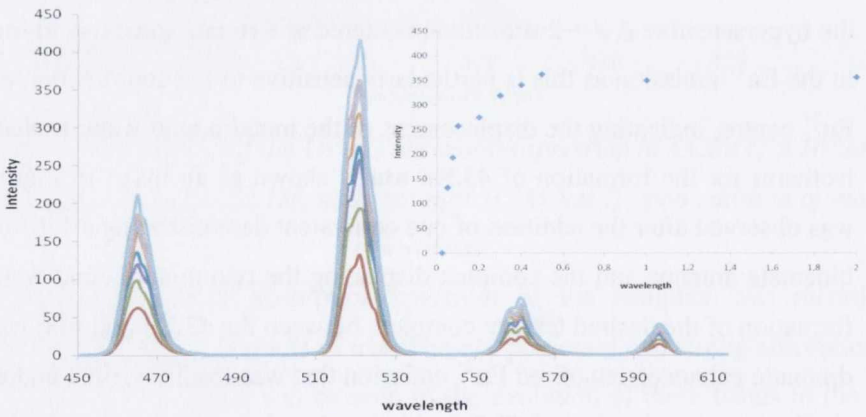

Figure 4.18: *Changes in the Tb^{3+} phosphorescence spectrum upon titrating* ***43.Tb*** *($c = 1 \times 10^{-5}$ M) with benzoic acid 0-6 equivalents.* ***Inset****: Experimental binding isotherm, emission intensity at 545 nm ($^5D_4$-$^7F_5$) versus equivalents of benzoic acid*

The excitation bands of the terbium ions at 545 nm are most sensitive to the coordination environment of the Ln^{3+} and as such show the greatest changes upon addition of the chromophore. This demonstrates that the formation of luminescent ternary complexes has been carried out for both the Eu^{3+} and Tb^{3+} analogues of **43.Ln**. The

complex **111.Eu** was also titrated with **nta** in order to determine the formation of ternary luminescent complexes utilising the alkyl-based complex.

Initially the UV-vis absorption spectrum of the complex, **111.Eu** was recorded and monitored upon addition of aliquots of **nta**. The **nta** possesses two strong absorption bands at 245 nm and 330 nm, which can be seen in the evolution of these bands in the UV-vis absorption spectrum, Figure 4.19.

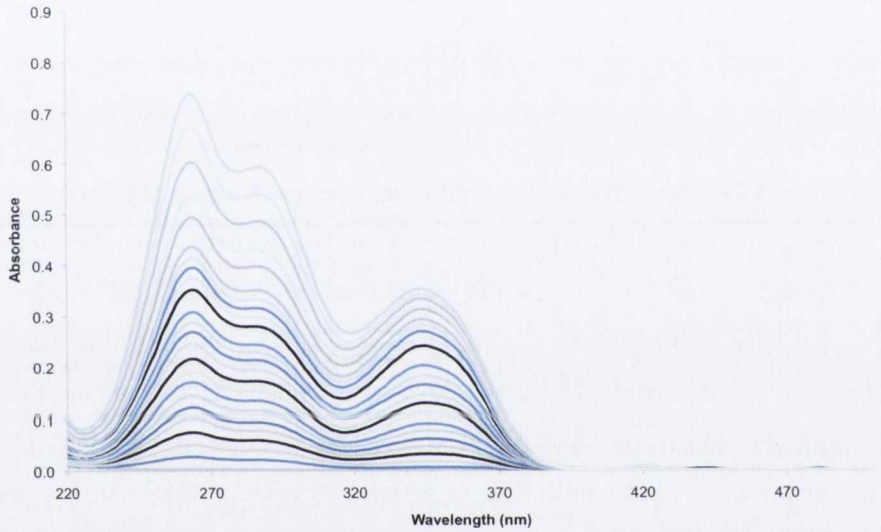

Figure 4.19: *The UV-Vis absorption spectrum of* ***111.Eu*** *($c = 1 \times 10^{-5}$ M) in HEPES (0.1M, NaCl ionic strength) upon the addition of* ***nta*** *(0-4.5 equivalents)*

The evaluation of the effect of **nta** on the complex **111.Eu** was also followed by the Eu^{3+} phosphorescence. This showed the formation of the ternary luminescent complex upon addition of one equivalent of **nta** after which a plateau was reached, Figure 4.20.

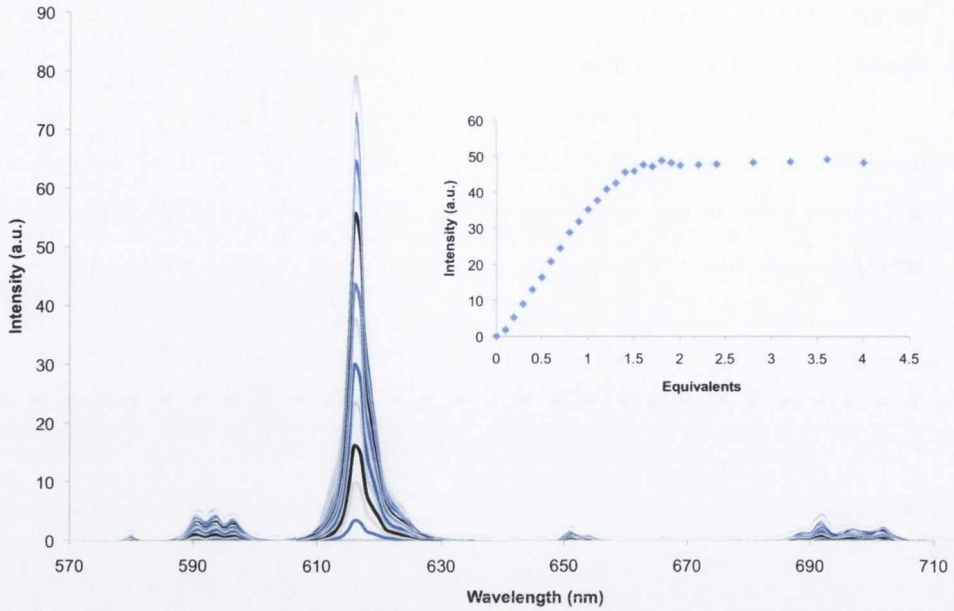

***Figure 4.20**: The changes in the Eu^{3+} emission spectrum of **111.Eu** ($c = 1 \times 10^{-5}$ M) upon the addition of **nta. Inset:** Experimental binding isotherm, emission intensity at 615 nm ($^5D_0 \rightarrow {}^7F_2$ versus eqs of **nta**)*

This highlights the possibility of using these systems for luminescent sensing. However, in this work we further developed these systems with the functionalisation of complexes **43.Ln** on **AuNPs**, which was discussed in Section 4.7, opening new perspectives to their application as efficient sensors. These sensors on the surface of **AuNPs** will be discussed in the following sections.

4.8.3 Photophysical evaluation of 43.Ln functionalised AuNPs (43.Ln-AuNPs)

The ultimate aim of this work was to functionalize the surface of **AuNPs** with Ln^{3+} complexes and determine the effect of the functionalisation of the complex on the Ln^{3+} luminescent properties. Determination of the number of complexes attached to the **AuNPs** was possible as the ternary Eu^{3+} complex, as shown in Figure 1.21, coordinates in a 1:1 ratio with the complex, therefore the binding stoichiometry would correspond to the number of complexes coordinated. Moreover, the titrations shown below, Figure 4.21 allowed the determination of the number of complexes attached to a **AuNPs** with the titration of **nta** known to bind in a 1:1 ratio, as shown by Massue *et al.*[199] Since the ternary complexes were formed in a 1:1 complex to antenna ratio with **nta** and **tta**, the binding stoichiometry would correspond to the number of complexes coordinated. From these experiments, the number of bound **43.Eu** complexes per **AuNPs** can be estimated as *ca.* 50.

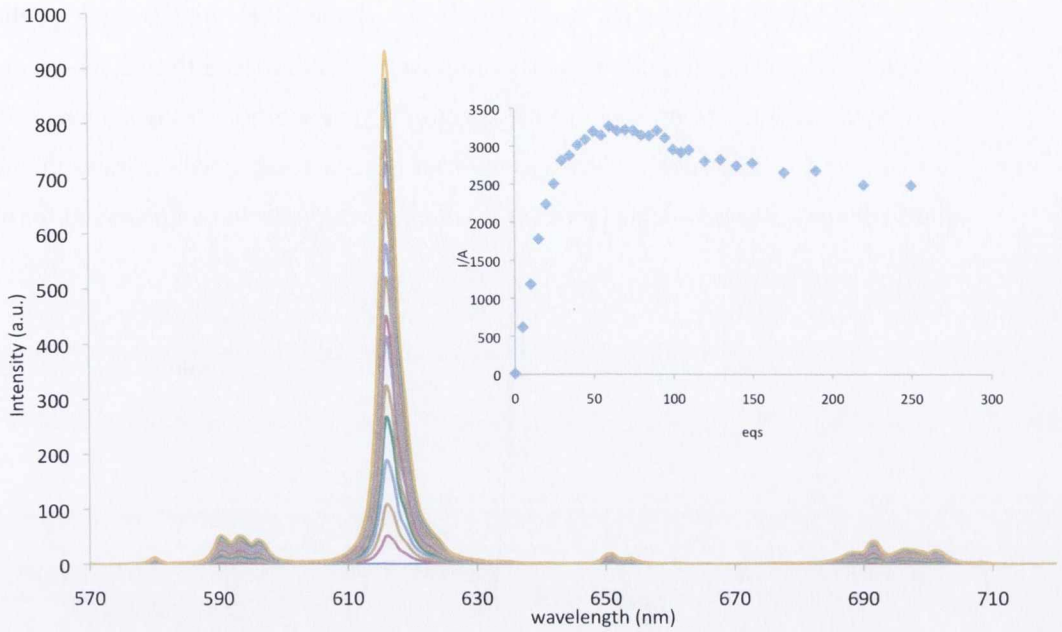

***Figure 4.21**: The changes in the Ln^{3+} centred emission of **43.Eu-AuNPs** ($1x10^{-7}M$) in HEPES (0.1M, ionic strength 0.1M NaCl) upon the addition of **nta** 0-250 equivalents.* ***Inset:** The changes in the Eu^{3+} emission at 615 nm versus the number of equivalents of **nta** added.*

The response of the complex to the addition of **tta** shows similar trends to the titration with **nta**. In this case the spectrum for the UV-vis absorption differs as the maximum absorbance is centred at 350 nm instead of 330 nm, Figure 4.22.

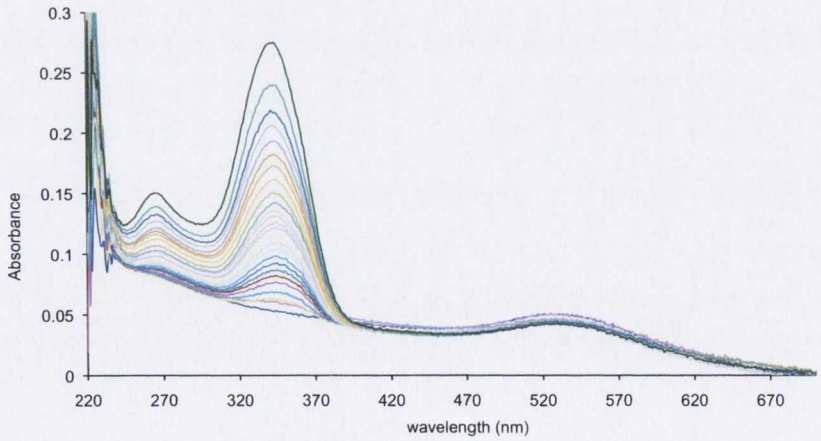

Figure 4.22: *Evaluation of the UV-vis absorption spectrum of **43.Eu-AuNPs** ($1 \times 10^{-7}M$) in HEPES buffered solution (0.1M, ionic strength 0.1M NaCl) upon addition of **tta** 0-250 equivalents.*

Excitation into the **tta** band at 350 nm yielded the luminescence of the ternary complex, as shown in Figure 4.23. This followed a similar trend to that shown previously, with an increase in the intensity of the spectrum upon addition of the antenna. The plot of intensity versus equivalents, shown as an inset in Figure 4.23, demonstrates the binding of approximately 50 equivalents of antenna, which corresponds to that observed for **nta**.

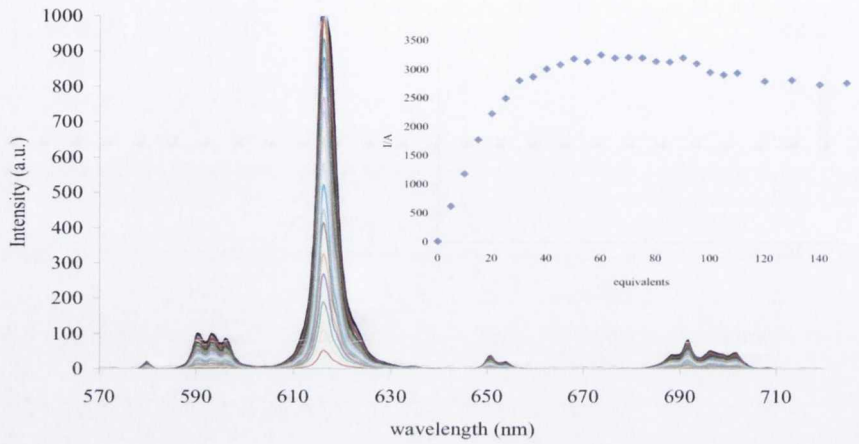

Figure 4.23: *Evaluation of the Eu^{3+} emission of* ***43.Eu-AuNPs*** *($1x10^{-7}M$) in HEPES buffered solution (0.1M, ionic strength 0.1M NaCl) upon addition of* ***tta*** *0-250 equivalents.* ***Inset:*** *shows the changes in the Eu^{3+} $^5D_0$-$^7F_2$ transition vs the number of equivalents added of* ***tta***

The Tb^{3+} complex showed similar activity to the Eu^{3+} complex allowing "switching on" of the Tb^{3+} emission upon addition of the antenna, such as benzoic or terephthalic acid. The complex showed a plateau after approximately 50 equivalents and then showed a second increase up to 100 equivalents possibly due to the luminescence of the Tb^{3+} centre itself.

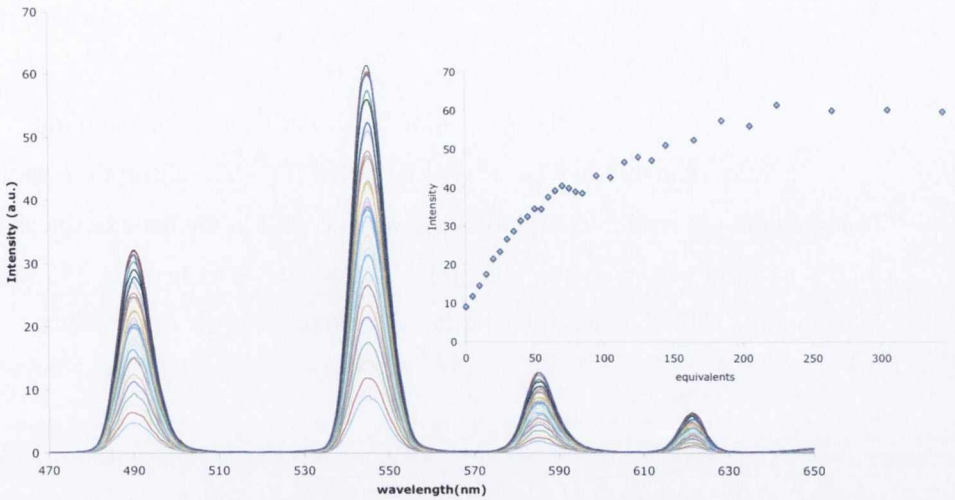

***Figure 4.25**: Evaluation of the Ln^{3+} centred emission of **43.Tb-AuNPs** ($1x10^{-7}$) in Hepes buffered solution (0.1M, ionic strength 0.1M NaCl) upon addition of benzoic acid 0-250 equivalents. **Inset:** The changes in the Tb^{3+} $^5D_4$-$^7F_5$ transition versus the number of equivalents added of benzoic acid.*

The displacement of the metal bound water molecules has been demonstrated by the switching on of the luminescent emission for the complexes, due to the formation of ternary luminescent complexes. Due to the potential of these nanoparticulate complexes to form ternary luminescent structures with appropriate antennae, it is important to determine the pH behavior of the complex on the nanoparticle surface. For this reason, the next section discusses the pH behavior of the nanoparticulate system upon the addition of the antenna.

4.8.4 pH driven self-assembly formation between 43.Eu-AuNPs and nta

As **43.EuAuNPs** was developed as a potential sensor for use in aqueous solution, it was necessary to establish the spectroscopic behaviour of the aqueous solution of **43.Eu-AuNPs** as a function of pH. The complex **43.Eu** and the complex **43.Eu-AuNPs** were analysed for their stability and behavior over a broad pH range from 2-12. However, this complex possessed very low Ln^{3+} centred emission intensity (Section 4.8), so in order to determine the behaviour upon variation of the pH, it was necessary to attach one equivalent of antenna to each complex to give the conjugate **43.Eu-AuNP-nta**. As can be seen from Scheme 4.4 the antenna experiences changes due to formation of the keto and enol forms of the **nta**.

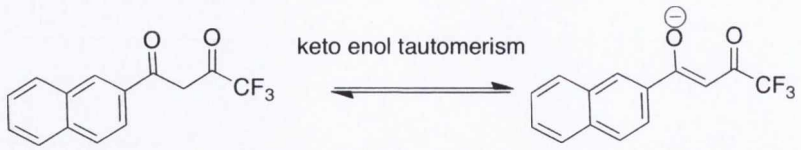

***Scheme 4.4**: Keto-enol tautomerism of the antenna* **nta**

These changes can be observed in the UV-Vis absorption spectrum, whereby changing the pH results in a small bathochromic shift in the band of the antenna at 339 nm with a concomitant hyperchromic shift, Figure 4.25. The band at 265 nm experienced a hypochromic shift. These can be attributed to changes in the **nta** antenna.

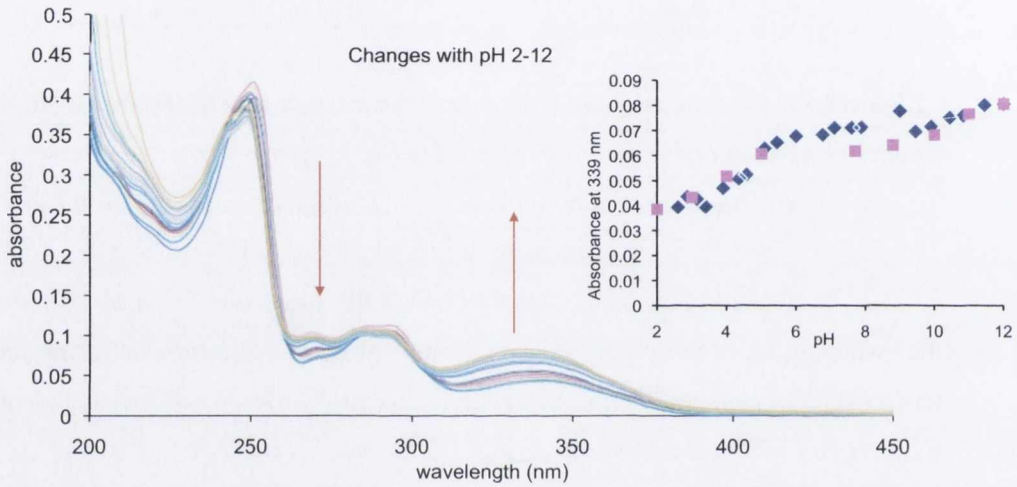

***Figure 4.25**:The changes in the UV-Vis absorption spectrum of* **43.Eu-AuNPs-nta** *as a function of pH 2-12 in H_2O.* ***Inset:** Changes in the UV-Vis absorption band at 339 nm as a function of pH with reverse titration overlaid.*

Also investigated was the pH dependent behaviour of **43.Eu-AuNPs** in the fluorescence emission spectrum, which demonstrated similar trends to that above. The antenna itself exists as a keto-enol tautomer, so the complex will exist in the most stable state on formation of the enol form, which can bind more efficiently to the Ln^{3+}. The formation of the keto form at more acidic pH, shows a dramatic decrease in the luminescence intensity due to the weaker binding of the keto form compared to the enol. The luminescence of the nanoparticulate system was found to increase at physiological pH due to binding through the enol form causing binding of the antenna more efficiently to the complex.

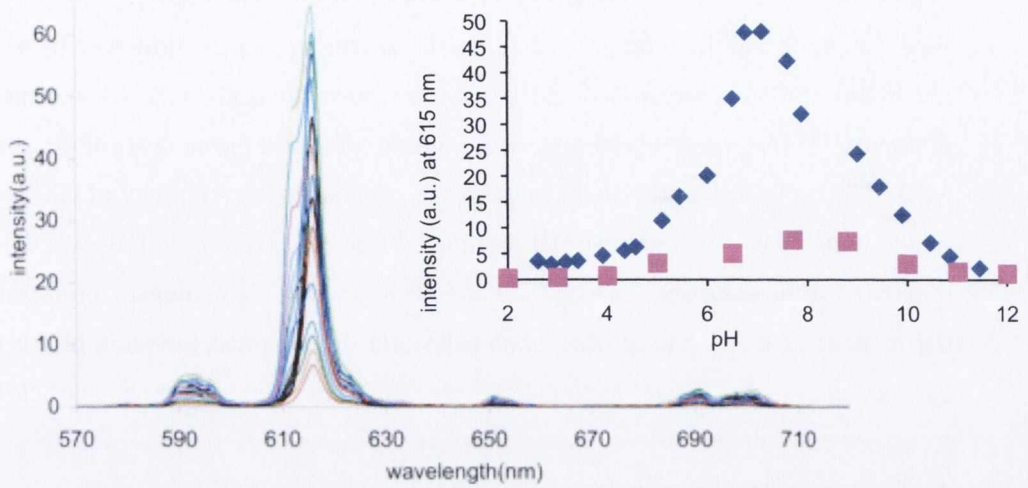

***Figure 4.28**: Evolution of the Eu^{3+} emission of **43.Eu-AuNPs-nta** with pH in H_2O*
***Inset**: Changes in the $^7F_2$ transition upon varying the pH from 12, reverse titration pH 12-2*

The pH driven self-assembly of the **AuNPs** conjugate is observed due to the formation of the enol form as shown in the titration, Figure 4.26, with the highest luminescence observed at pH 7.4. This demonstrated that the complex **43.Eu-AuNPs-nta** was most luminescent in the enol form, which is predominant at physiological pH, a behavior that has been demonstrated in similar complexes by Bonnet *et al.*[202] Having studied the complex-nanoparticulate system with regards to the luminescent behavior and the pH, the potential of this nanoparticulate system in MRI is discussed in the following sections.

4.8.5 Solution studies of complex 43.Gd and 43.Eu

Analysis of the diffusion coefficients of **43.Lu** in water (D = 2.898), found the hydrodynamic radius of the complexes **43.Eu** and **43.Lu**, to be much larger than expected for a complex of this size, R = 60 angstroms. The hydrodynamic radius was found to be 60 angstroms for both complexes, which suggests the formation of larger structure or aggregates in solution. This was further confirmed by DLS measurements carried out at the same concentration, which showed structures with diameters from 1 to 2 nm, corresponding to an average radius of 60 Å.

From this data, we can suggest that the complexes potentially organise as micelles in aqueous solution where the thiol chain acts as an hydrophobic tail and the charged Ln^{3+} complexes act as a hydrophilic head.[185] Moreover, luminescence lifetime measurements performed on **43.Eu** at the same concentration indicated that the coordination sphere of the

Eu^{3+} remained unchanged upon micelle formation and the Ln^{3+} complexes are still heptacoordinate, with one metal bound water molecule. The slow diffusion coefficients would suggest that the rotation of the micellar assembly is quite slow which, according to the Solomon-Bloembergen-Morgan theory, is known to lead to an enhancement of the relaxivity.[185] The possibility of micelle formation prompted the analysis of the potential for MRI, as micelles have previously been shown to enhance the relaxivity of Gd^{3+} complexes due to the slower rotational correlation time.[194] The next section will discuss the potential relaxivity of the complex alone and the complex-nanoparticle conjugate, prompted by both the number of metal bound water molecules and the potential lowering of the rotational correlation time due to the functionalisation of this complex onto the nanoparticle surface.

4.9 Relaxivity Measurements:

Measurements of the T_1 were carried out at both high field, 400 MHz and 600 MHz, in collaboration with Dr. John O' Brien (TCD), and at varied lower fields using the technique Nuclear Magnetic Resonance Dispersion (NMRD) in collaboration with Dr. Dermot Brougham (DCU).

The efficiency of a Gd^{3+} complex to enhance the contrast of T_1-weighted MRI is gauged by its relaxivity r_1, which is defined as the paramagnetic relaxation enhancement of the longitudinal relaxation rate of the H_2O protons as a result of the addition of a 1 mM solution of complex: $r_1 = (1/(T_1 \times [Gd]))$.

In order to calculate this relaxivity, it is first important to measure the relaxation time, T_1, of the H_2O with the Gd (III) complex added. The process of measuring the T_1 (the relaxation time) is carried out by application of a magnetic pulse, usually for an estimated duration of 5 x T_1, in order to ensure the spins are aligned with the magnetic field, Figure 4.27. Then the sample is allowed to equilibrate or relax, for time τ, after which a lower frequency pulse is applied for collection of the data, which is called the radiofrequency (RF) pulse. The NMR signal is always measured at the same detection field B_d.

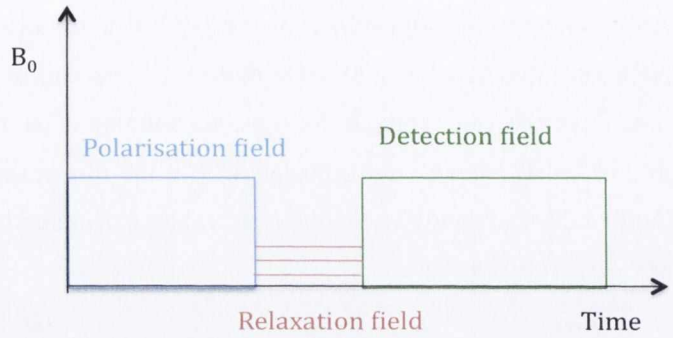

Figure 4.27: *Graphical representation of the process of T_1 measurement*

The T_1 of the sample is then obtained by analyzing the rate of decay of the H_2O signal®at various time delays. The values were then transferred to the data analysis program Origin^R and fit to a monoexponential decay using Equation 3.

$$\mathbf{Y = MO*[1 - 2*exp(-x/T_1)]} \qquad \textbf{Eq. 3}$$

-where MO is the integration of the H_2O signal, which varies depending on the length of time the sample is allowed to relax before measurement. X is the value of the delay time allowed before the measurement. The value of T_1 measures the rate of decay of the signal, which then must be compared to the values for the natural water relaxation in bulk solution. There are paramagnetic (T_{1para}) and diamagnetic (T_{1dia}) contributions to the relaxivity, which can be used to calculate the observed relaxivity, as shown in Equation 4.

$$\mathbf{1 / T_{1obs} = 1 / T_{1\,dia} + 1 / T_{1\,para}} \qquad \textbf{Eq. 4}$$

The relaxation of the sample R_1 can be calculated from $1/T_1$. However, in order to obtain the concentration normalized relaxivity of the system it is necessary to calculate the relaxivity with the concentration as shown in Equation 5.

$$\mathbf{R_1 = 1/ T_1\,[Gd]} \qquad \textbf{Eq. 5}$$

It is important to deter
value for r_1, particularly with structures such as micelles, which could contain trapped solvent. This concentration correction can be carried out using magnetic susceptibility measurements using dioxane as a reference solvent. This allows the use of the compound as a shift reagent and measures the shift of the signal of dioxane in both D_2O and a sample of the Gd^{3+} complex in D_2O.

4.10 Relaxivity Measurements of 43.Gd

The longitudinal relaxation times of the H_2O protons in solutions of **43.Gd** and **43.Gd-AuNPs** were measured at 400 MHz and 600 MHz and at 298 K (Table 4.2) by measuring the T_1 of the Gd^{3+} complex in aqueous solution. The T_1 measured for **43.Gd** solutions (at 25°C, 400 MHz), were calculated from the monoexponential fit of the plot shown in Figure 4.28, and gave rise to relaxivity values calculated using Equation 5, of r = 11.14 $s^{-1}mM^{-1}$ with T_1 = 0.034 s.

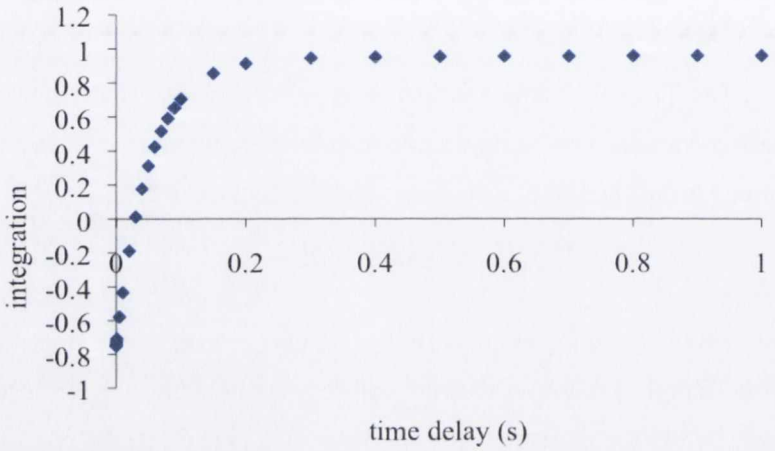

***Figure 4.28**: Plot of integration versus the time delay from ^1H NMR (400 MHz, D_2O) for the T_1 of **43.Gd** (2.67 mM)*

From these measurements, the longitudinal water proton relaxivity r_1 (H_2O), which arises from **43.Gd** can be estimated by dividing the D_2O value reported in Table 4.2 by the viscosity ratio, $h(D_2O)/h(H_2O)$ = 1.24.[203] The longitudinal relaxation times of the H_2O protons in solutions of **43.Gd**, were also measured at 10 MHz and 298 K, using NMRD studies, and the corresponding relaxivities are reported in Table 4.2 and shown in the profile in Figure 4.29.

***Table 4.2.** Longitudinal relaxivity r_1 for **43.Gd** complex*

Frequency	**10 MHz**	**400 MHz**	**600 MHz**
r_1 [$s^{-1}mM^{-1}$]	16.5	11.14	8.1

The relaxivities measured for **43.Gd** are surprisingly high in comparison to previously reported bis-aquo Gd^{3+} of similar molecular weight.[204] However, it is possible, as was discussed above, that the complex, **43.Gd**, forms micelles in aqueous solution and thus the relaxivity observed corresponds not only to one complex but to the micelle. This is also based on the fact that the complex has already been observed to consist of larger

aggregates of approximately 2 nm (see previous section); this higher relaxivity value would suggest larger particles in solution. In order to assess the rotational dynamics of the complex **43.Gd** at this concentration (C_{Gd} =2.67 mM), its hydrodynamic radius has been obtained from the measurement of its diffusion coefficient, followed by fitting to the Stokes-Einstein model.[205]

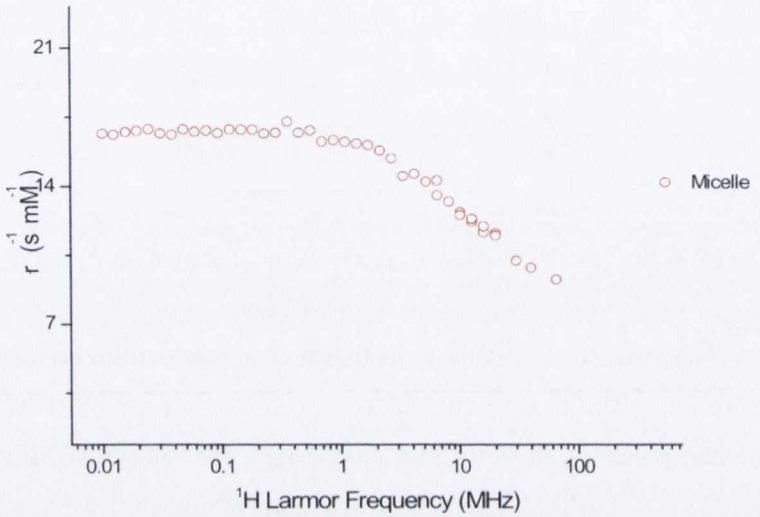

Figure 4.29: *Longitudinal relaxivity (r_1) of the H_2O protons of* ***43.Gd*** *in H_2O at 298K (2.67 mM)*

The organisation of **43.Gd** in micellar structures with slow tumbling rates together with fast water-exchange rates of the two metal-bound water molecules would be responsible for the high relaxivities measured at a concentration C_{Gd} = 2.67 mM. The europium and lutetium complexes, **111.Eu** and **111.Lu**, were used as model compounds in order to study the influence of the thiol function in the formation of the micelles. First of all, the ^{1}H NMR of the ligand showed no stacking or broadening as shown before, so it was assumed that no interactions such as that seen for **43.Ln** were observed. The DLS measurements performed on **111.Eu** and **111.Lu** in H_2O solutions confirmed the absence of the micelle in the concentration range from 0.1mM to 5 mM, with no structure observed at 1 or 2 nm in diameter in contrast to that seen for **43.Eu** and **43.Gd**. Finally, the number of metal-bound water molecules was calculated from the measurements of the luminescent lifetimes of **111.Eu** in H_2O and D_2O solutions. These values (τ_{H2O} = 0.52 ms and τ_{D2O} = 1.14 ms) are in close agreement with those obtained for **43.Eu** and are characteristic for a 1:1 complex in which two water molecules are coordinated to the metal center.

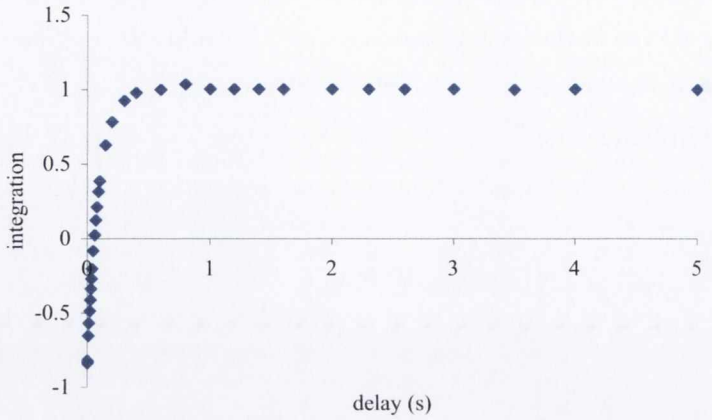

Figure 4.30**: Plot of integration vs the delay of the values from ^1H NMR for the T_1 of **111.Gd

The absence of micelle formation was further confirmed by longitudinal relaxivity measurements. The T_1 measured for **111.Gd** solutions (at 25°C, 400 MHz) calculated from the monoexponential fit of the plot Figure 4.30, gave rise to significantly lower relaxivity values of r = 5.80 $s^{-1}mM^{-1}$, compared to the **AuNPs** functionalised with **43.Gd,** in the same concentration range (r_1 = and at 400 MHz). These values are typical for a bis-aquo complex of this size.[117] As a comparison, relaxivities ranging from 5.6 to 10.5 mM^{-1} s^{-1}, at 25 °C and 20 MHz, had been measured in the same conditions for the HOPO-based Gd(III) complexes studied by Raymond, Botta, Aime and co-workers and for the DOTA analogue $[Gd(DO3A)(H_2O)_2]$ (6.0 $mM^{-1}s^{-1}$).[181, 185]

From these results, it appears that the thiol function plays a key role in the supramolecular structure formation in solution, by promoting the formation of a spherical hydrophobic pocket with the thiol in the centre of the micelle. As a comparison, the groups of Merbach, Toth and Klaveness have studied the influence of the length of the alkane chains on the micelle formation of mono-aquo Gd^{3+} complexes with DOTA derivatives and observed a significant increase of the relaxivity of the complexes upon micelle formation only for the C16-C18 functionalised derivative.[206] These results would suggest thiol-functionalised derivatives would be particularly attractive targets for the design of new micellar structures with high relaxivity.

4.11 Relaxivity Measurements of 43.Gd-AuNPs

Grafting of the **43.Gd** complexes onto the surface of **AuNPs**, was expected to give Gd-coated nanoparticles with high relaxivity. Indeed, as previously reported by Helm *et al.*,[197] the relaxivity per nanoparticle would be expected to be extremely high due to the high Gd-content (not less than 50 Gd^{3+} ions per **AuNP** in this case).

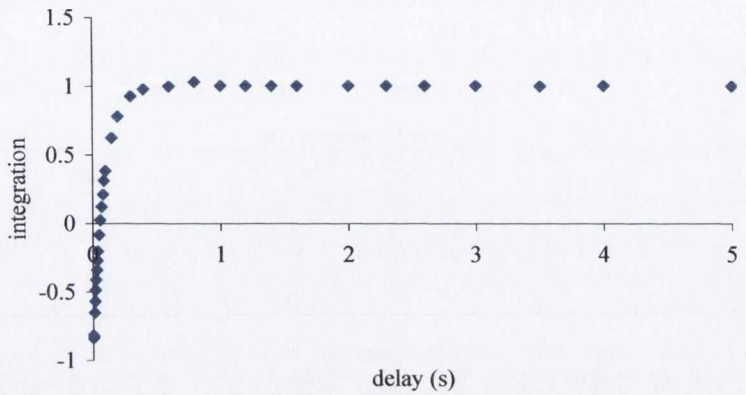

Figure 4.31: *Plot of integration versus the delay time for the T_1 of* ***43.Gd-AuNPs*** *in H_2O (2.67 mM)*

The **AuNPs** were analysed using ^1H NMR relaxation or T_1 measurements, which measures the decrease in the T_1 or the relaxation time of the bulk water solution in the presence of the complex. This was fit to a monoexponential decay, which allows the T_1 to be extrapolated from the raw data.

Table 4.4: Relaxivity calculated for 43.Gd-AuNPs

Frequency MHz	10 MHz	600 MHz	400 MHz
r_1 [$s^{-1}mM^{-1}$] per Gd	16.5	8.1	11.14
r_1 [$s^{-1}mM^{-1}$] per AuNP	-	315	416.2

An increase of the relaxivity per Gd^{3+} ion could possibly be observed for rigid nanoparticles with fast-water exchange, due to the absence of internal rotation of the Gd-chelating units and the slow rotational correlation time of the system with the relaxivity values shown in Table 4.4 and shown in the profile in Figure 4.32.

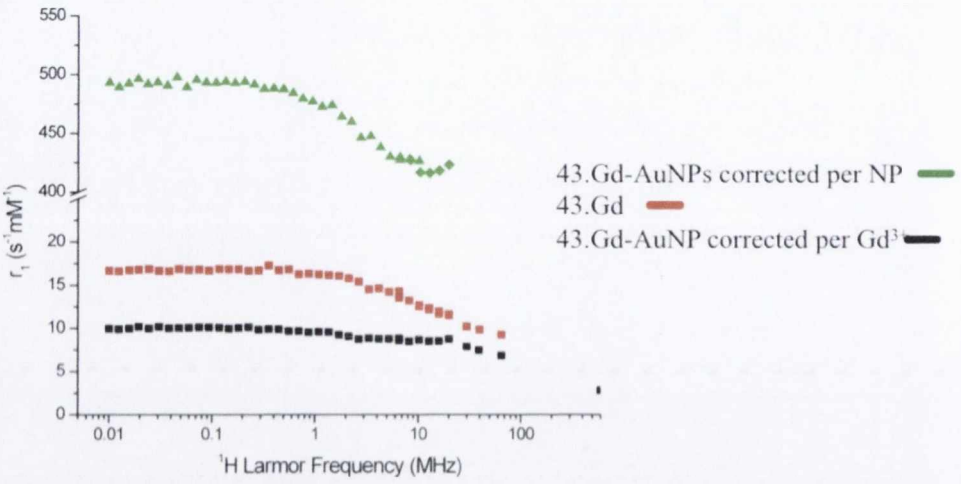

***Figure 4.33**: Longitudinal relaxivity (r_1) of the protons of H_2O with **43.Gd** and **43.Gd-AuNPs** at 298K*

However, this was not observed as the system, due to the length of the thiol chain, was seen to behave similarly to the complex alone despite being attached to the gold. This would suggest that the rotational correlation time of **43.Gd-AuNPs** is similar to that of a complex. The shape of the profile observed for the **AuNPs** was vastly different from that observed by Helm *et al.*, as no maximum was observed at medium field.[197] This could possibly be caused by the nature of the nanoparticle conjugate in this case, which possessed a long chain separating the complexes from the nanoparticle, perhaps causing the complex to behave as individual units rather than one large self assembly, in contrast to the conjugates of Helm *et al.*, which were bonded directly to the nanoparticle *via* a phenyl spacer.[197]

The nanoparticulate system still shows an overall increase in the relaxivity, giving a relaxivity of approximately 545 $mM^{-1}s^{-1}$ per particle, instead of $16mM^{-1}s^{-1}$ per Gd^{3+} ion. The longitudinal relaxation time of the H_2O protons of a 2.67 mM solution of **43.Gd-AuNP** in H_2O has been found to be T_1 = 0.081 s at 400 MHz. The Gd^{3+} content was checked by magnetic susceptibility shift measurements and elemental analysis by Internal Coupled Plasma (ICP). This established the relaxivity per Gd^{3+} ion as 2.67 $mM^{-1}s^{-1}$ in water.

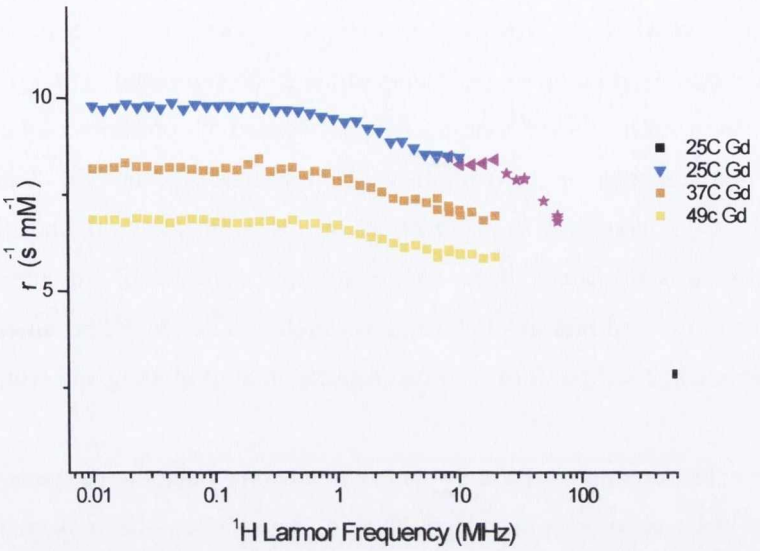

***Figure 4.33**: Longitudinal relaxivity (r_1) of the protons of **43.Gd-AuNPs** in H_2O at 25 °C, 37 °C, 49 °C*

The H_2O exchange rate and the rotational correlation time are the main limiting factors for complexes of this type. The relaxivity of the **43.Gd-AuNPs** at variable temperature was measured in order to determine the limiting factor on the relaxivity. If the limiting factor is the H_2O exchange rate, the complex should show an increase in the relaxivity observed at higher temperature.[207] However, in this case **43.Gd-AuNPs** showed a decrease in the relaxivity upon an increase in temperature shown in Figure 4.33. It is possible that as the temperature increases, the H_2O exchange becomes too fast, showing a decrease in the extent of the interaction with the Gd^{3+} ion. This suggests that the H_2O exchange rate is not limiting the relaxivity but the rotational correlation time. The potential of these compounds was demonstrated for MRI due to the formation of micellar structure of **43.Gd** giving high relaxivity values and the use of tethered nanoparticle systems to increase the loading of the contrast agent again enhancing the potential of the MRI contrast agent.

4.12: Conclusion

In summary, the synthesis and characterisation of **43**, **43.Eu**, **43.Gd** and **111.Eu** and **111.Gd** has been carried out and the ligands and complexes fully characterised. The Eu^{3+} complexes of the above ligands were shown to contain two metal-bound water molecules, which lend these complexes to the application as luminescent sensors for dicarboxylates such as **nta**, **tta** and also for carboxylates such as benzoic acid in the case of the Tb^{3+} complex. The functionalisation of the nanoparticles with the complex **43.Eu**

showed interesting characteristics, binding an estimated 50 complexes for the luminescent system showing the number of complexes per Gd^{3+} ion is 50, which allows the concentration of complex per nanoparticle to be estimated. The Eu^{3+} complex attached to the nanoparticle showed that it efficiently sensed the presence of the antenna switching on the luminescence of the complexes on the nanoparticle. The behaviour of the ternary luminescent complex as a function of pH was analysed and found to rely on the conformational change of the complex with the keto-enol tautomerism of the antenna as binding observed between pH 6 and 8, which was due to the presence of the enol isomer of the antenna. The keto form is much less efficient at binding and would result in a decrease in the luminescence of the complex.

The complex **43.Eu** displayed interesting interactions using diffusion coefficients and DLS measurements, which give information on the movement and hydrodynamic radius of the complex in solution. The complex **43.Gd** was shown to have high relaxivity compared to similar complexes in the literature. The relaxivity of the complex **43.Gd** was obtained with a T_1 of approximately 0.034 seconds with relaxivity of 11.14 $mM^{-1}s^{-1}$ at 400 MHz. Complex **111.Gd** demonstrated relaxivity of r = 5.80 $mM^{-1}s^{-1}$ in comparison to that observed for **43.Gd**. The nanoparticle based conjugate demonstrated relaxivity of 545 $mM^{-1}s^{-1}$, which corresponded to the relaxivity per nanoparticle showing the enhancement based on the functionalisation of a number of complexes on the nanoparticles, showing the benefit of high loading. These results demonstrate the potential for systems such as these to improve both the formation of luminescent ternary complexes with **43.Eu**, **111.Eu** and **43.Eu-AuNPs** and also in the development of novel MRI contrast agents with high relaxivity.

Chapter 5

Experimental

Chapter 5: Experimental Details

5.1 General Experimental Details

All chemicals were obtained from Sigma-Aldrich, Fluka, Strem, or Chematech and unless otherwise specified were used without further purification. Deuterated solvents for NMR analysis were purchased from Apollo Scientific. Dry solvents were prepared using standard procedures, according to Vogel,[208] with distillation prior to each use. Chromatographic columns were run manually using silica gel 60 (230-40 mesh ASTM) or aluminium oxide (activated, neutral, Brockman I STD grade, 150 mesh, or activated, basic, Brockman I STD grade, 150 mesh). Chromatographic columns were also run on a Teldyne Isco Combiflash Companion Automatic machine using prepacked silica or alumina columns. Solvents for synthetic purposes were used at GPR grade unless otherwise stated. Analytical TLC was performed using Merck Kieselgel 60 F_{254} silica plates or Polygram Alox N/UV_{254} Aluminium oxide plates. Visualisation was by UV light (254 nm), exposure to I_2 on silica or by immersion in aqueous alkaline $KMnO_4$ solution. NMR spectra were recorded at 400 MHz using a Bruker Spectrospin DPX-400 instrument that operates at 400.13 MHz for ^1H NMR and 100.3 MHz for ^{13}C NMR. NMR spectra were also recored at 600 MHz, using a Bruker advance II that operates at 600.13 MHz, for ^1H NMR and 150.9 MHz for ^{13}C NMR. Shifts were referenced relevant to the internal solvent signals, with chemical shifts expressed in parts per million (ppm) downfield from the standard. Multiplicities are abbreviated as follows: singlet (s), doublet (d), triplet (t), quintet (q), multiplet (m) and broad (br). All NMR analysis was performed as 293 K. Mass Spectra were determined by detection using electrospray on a Mass Lynx NT V 3.4 on a Waters 600 Controller connected to a 996 photodiode array detector with HPLC-grade methanol, water or acetonitrile as carrier solvents. Accurate molecular weights were determined by a peak-matching method, using leucine enkephaline (H-Try-Gly-Gly-Phe-Leu-OH) as the standard internal reference (m/z = 556.2771). Samples were prepared as solutions in methanol or acetonitrile. Infrared spectra were recorded on a Perkin Elmer Spectrum One FT-IR spectrometer fitted with a universal ATR sampling accessory. Elemental analysis was carried out at the microanalysis laboratory, School of Chemistry and Chemical Biology, University College Dublin. X-ray diffraction studies were carried out by Dr. Thomas McCabe, School of Chemistry, Trinity College Dublin. NMRD was carried out in DCU by Dr. Dermot Brougham. DLS measurements were performed on $1\text{-}3\times10^{-7}$ M solutions of **AuNP** in distilled water using a Zetasizer Nano Series (Malvern Instruments).

The lanthanide metal salts $Ln(CF_3SO_3)_3$ were purchased from Aldrich and were dried under high vacuum over P_2O_5 prior to use.

5.2 UltraViolet-Visible Spectroscopy

UV-Visible absorption spectra were recorded with a Varian Cary 50 spectrophotometer. The solvents used were of HPLC grade. The blank used was of the solvent system the titration was undertaken in. Baseline correction measurements were used in all spectra. All stock solutions were freshly prepared before measurement.

5.3 Luminescence Measurements

Fluorescence and luminescence measurements were recorded using a Varian Carey Eclipse Fluorimeter with a 1.0 cm path length quartz cell. The solvents used were all of HPLC grade. The concentrations of the ligands and complexes examined were the same as those used for the UV-Vis absorption measurements (Section 5.3). The settings for the Fluorimeter for the luminescence measurements carried out in Chapters 2, 3, and 4 are shown in Table 5.1.

Table 5.1: *Luminescence settings for Varian Carey Eclipse fluorimeter*

Mode: Phosphorescence	Total Decay: 0.02 ms
Flash: 1	Delay: 0.1 ms
Gate: 10 ms	PMT Voltage: Med - 900
Excitation slit width: 20 nm	Emission slit width: 1.5 -5 nm

5.4 Lifetime Determination for Ln(III) Complexes

Luminescence lifetime measurements of all europium complexes were carried out in H_2O or MeOH on a Varian Eclipse Fluorescence spectrophotometer. The settings for the Varian Carey Eclipse Fluorescence spectrophotometer are shown in Table 5.2.

Table 5.2: *General Settings for Lifetime studies*

Indirect Excitation Eu(III): 281 nm	Emission Eu(III): 615 nm
Delay time: 0.1 ms	Gate Time: 0.025 ms
Flash Count: 1	No. Cycles: 30
Total Decay: 1-10 ms	PMT Voltage: High or 900
Excitations slit width: 20 nm	Emission slit width: 5 nm

5.5 CD spectrscopy

CD spectra were recorded on a Jasco J-810-150S spectropolarimeter. All CD spectra are reported as mdeg *vs* λ (nm). The baseline solvent was taken and removed from the spectra shown. These spectra were recorded in MEOH, HPLC grade.

5.6 CPL Measurements

Circularly Polarised Luminescence spectra were recorded at the University of Glasgow. Excitation of the Eu^{3+} (560-581 nm) was accomplished using a Coherent 599 tuneable dye laser (0.03 nm resolution) with an argon ion laser as a pump source. The laser dye used in the measurement was Rhodamine 100 in ethylene glycol. Calibration of the emission monochromator (and subsequently the dye laser) was accomplished by passing scattered light from a low power He-Ne laser through the detection system. The error in the dye laser wavelength was assumed to be equal to the resolution of the emission detection. Optical detection consisted of a photoelastic modulator (PEM, Hinds Int.) operating at 50 kHz and a linear polariser, which together act as a circular analyser, followed by a long pass filter, focusing lense and a 0.2m double monochromator. The emitted light was detected by a cooled EM1-9558QB photomultiplier tube operating in photon counting mode. The output pulses from the photomultiplier tube were passed through a variable gain amplifier/ discriminator and input into a purpose built differential photon counter. The 50 kHz reference signal from the photoelastic modulator was used to direct the incoming pulses into two separate counters, an up counter which counts every photon pulse and thus is a measure of the total luminescence signal I = I left +Iright and an up/down counter, which addds pulses when the analyser is transmtting left circularyl polarised light nd substracts when the analyser is transmitting right circularly polarised light. This second counter provides a measure of the differential emission intensity I = Ileft – I right. The differential photon vounter allows for a selection of the time window for countin, which is centred around the maximum in the modulation cycle.

5.7 Tranmission Electron Micrscopy (TEM)

The instrument used was a Jeol 2100 Transmission Electron Microscope (TEM)

operating at 200kv with a Lanthanum Hexaborise emission source. Thin specimens are inserted, through an airlock system, into the high vacuum of the column. Then electrons are accelerated down the column and pass through the specimen to form an image in the beam.

5.8 Nuclear magnetic resonance

The frequency dependence of the ^{1}H relaxation for the samples was recorded over the frequency range 0.01 – 20 MHz using a Spinmaster FFC-2000 Fast Field Cycling NMR Relaxometer (Stelar SRL, Mede, Italy). The system operated at a measurement frequency of 9.25 MHz for ^{1}H, with a 90° pulse of 7 ms. T_1 measurements were performed as a function of external field, B_0, with standard pulse sequences incorporating B_0 field excursions.[209] The temperature of the samples was maintained at 25°C and controlled within ±1°C through the use of a thermostatted airflow system. All of the ^{1}H magnetisation recovery curves were mono-exponential within experimental error and the random errors in fitting T_1 were always less than 1%. measurements at 9.25 MHz, the relaxometer magnet was used. For higher frequencies a re-conditioned Bruker WP80 electromagnet was used, with the Stelar console. At higher frequency the 90° pulse was typically 5.5 ms.

5.10 Experimental

1-(prop-2-ynyl)-1,4,7,10-tetraazacyclododecane (**50**)[210]

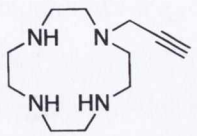

Cyclen, **49** (1.158 g, 6.72 mmoles, 4 eq.) was dissolved in $CHCl_3$ with Et_3N (0.23 mL, 6.72 mmoles, 4 eq.). Propargyl bromide (0.15 mL, 1.68 mmoles, 1 eq.) was added slowly drop wise and the solution refluxed overnight at 65 °C. The resulting solution was then extracted with $CHCl_3$, washed with 1M KOH (5 x 15 mL) solution and H_2O (2 x 15 mL), dried over $MgSO_4$, filtered and solvent removed under reduced pressure to yield a yellow oil 0.3344 g in 96 % yield. HRMS (*m/z*-ES+) Found for $C_{11}H_{23}N_4$: 211.1974, Calculated: 211.1923; δ_H ($CDCl_3$, 400 MHz): 3.67 (2H, s, CH_2), 2.69 - 2.65 (m, 16H, CH_2), 2.11 (1H, CH, alkyne). δ_C ($CDCl_3$, 100 MHz,): 78.39 (q), 76.34 (CH_2), 72.2 (CH_2), 49.5 (CH_2), 46.4 (CH_2), 45.7 (CH_2), 44.1 (CH_2), 42.7 (CH_2). ν_{max} (neat sample)/ cm^{-1}: 3431, 3372, 3284, 3239, 3183, 2921, 2841, 2820, 2311, 2092, 1648, 1613, 1550, 1461, 1401, 1343, 1263, 1257, 1155, 1122, 1054, 985, 901, 814.7, 807, 735.

2,2',2''-(10-(prop-2-ynyl)-1,4,7,10-tetraazacyclododecane-1,4,7-triyl)triacetamide (51)

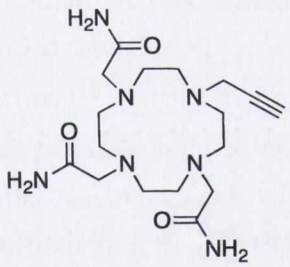

50 (0.17 g, 0.798 mmoles, 1eq.), Cs_2CO_3 (0.805 g, 2.47 mmoles, 3.1 eq.) and KI (0.41 g, 2.47 mmoles, 3.1 eq.) were dissolved in $CHCl_3$. *N*-bromoacetamide (0.34 g, 2.47 mmoles, 3.1 eq.) was added drop wise over 10 min and the resulting mixture refluxed over 7 days. The mixture was filtered through a plug of celite. The solvent was removed under reduced pressure and the residue dissolved in 1 mL of MeOH and precipitated out of swirling diethyl ether to give a yellow oil, 0.167 g in 55 % yield. HRMS (*m/z*-ES+) Found for $C_{17}H_{32}N_7O_3$ 382.1940 Required 382.2567; δ_H (MeOD, 400 MHz): 8.30 (3H, s, NH_2), 5.66 (3H, s, NH_2), 3.30 (4H, s, CH_2), 3.06 (4H, s, CH_2), 2.53 (16H, cyclen CH_2), 2.19 (1H, Alkyne CH); δ_C (MeOD, 100 MHz): 175.1 (q), 79.0 (q), 72.9 (q), 61.8 (CH_2), 58.9 (CH_2), 53.4 (CH_2), 53.0 (CH_2), 50.9 (CH_2), 50.7 (CH_2), 43.5 (CH_2), 31.1 (CH). ν_{max} (neat sample)/ cm^{-1}: 3348, 2949, 2837, 1672, 1450, 1248, 1226, 1172, 1117, 1019.

51.Eu

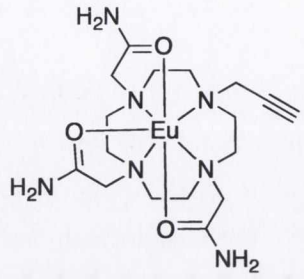

50 (0.040 g, 0.11 mmoles, 1 eq.) was dissolved in MeOH (10 mL) and $Eu(CF_3SO_3)_3$ (0.075 g, 0.126 mmoles, 1.2 eq.) added slowly dropwise to the resulting solution and refluxed overnight at 65 °C. The solvent was reduced to 1 mL under reduced pressure and precipitated from swirling diethyl ether (100 mL) to yield a yellow oil, 0.059 g, quantitative yield. HRMS (*m/z*-ES+) Found 551.1472 for $C_{17}H_{31}EuN_7O_3$ Required: 551.1701. δ_H (MeOD, 400 MHz): 30.2, 26.7, 22.5, 19.5, 13.8, 5.99, 5.69, 4.17, 2.48, 0.24, -0.28, -1.73, -1.98, -5.53, -6.33, -9.12, -11.2, -12.72, -15.25, -16.73, -18.18, -18.71, -20.41, -22.77. ν_{max} (neat sample)/ cm^{-1}: 3348, 2949, 2837, 1672, 1450, 1248, 1226, 1172, 1117, 1019.

2,2'-(4-(2-(methylamino)-2-oxoethyl)-10-(prop-2-ynyl)-1,4,7,10-tetraazacyclododecane-1,7-diyl)bis(N,N-dimethylacetamide) (52)

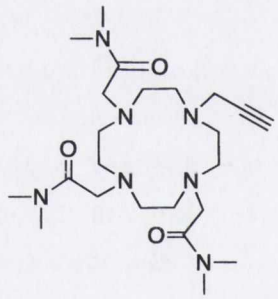

50 (0.334 g, 1.59 mmoles, 1 eq.) was dissolved in CH_3CN and KI (0.80 g, 5.25 mmoles, 3.3 eq.) and K_2CO_3 (0.726 g, 5.25 mmoles, 3.3 eq.) added to the solution. α-Chloro-*N,N*-dimethyl acetamide (0.635 g, 5.25 mmoles, 3.3 eq.) was added slowly to the solution and the solution stirred at 85 °C for 7 days. The solution was filtered and the product extracted into $CHCl_3$, washed with 1M KOH (5 x 15 mL) and H_2O (2 x 15 mL), dried over $MgSO_4$, filtered and solvent removed under reduced pressure to yield a yellow oil, 0.4292 g in 58 % yield. HRMS (*m/z*-ES+): Found for $C_{23}H_{44}N_7O_3$: 466.3484, Required: 466.3506; δ_H ($CDCl_3$, 400 MHz): 3.38 - 2.66 (m, 34 CH_2 and CH_3, CH_2), 2.13 (m, 1H, alkyne CH). δ_C ($CDCl_3$, 100 MHz): 170.9 (q) 79.1 (q), 72.59 (q), 72.5 (q), 57.9 (CH_2), 57.3 (CH_2), 52.6 (CH_2), 52.38 (CH_2), 51.98 (CH_2), 51.9 (CH_2), 51.6 (CH_2), 43.1 (CH_2), 42.3 (CH_2), 37.2 (CH_3), 37.0 (CH_3), 35.5 (CH). ν_{max} (neat sample)/ cm^{-1}: 3455, 3302, 3231, 2935, 2815, 2237, 1635, 1503, 1457, 1398, 1360, 1263, 1104, 1060, 1008, 924, 803, 751, 729, 694.

(52.Eu)

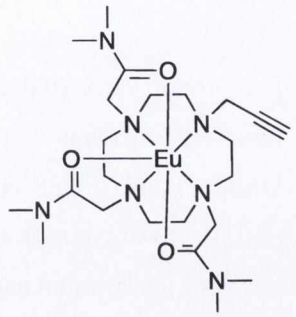

52 (0.264 g, 0.57 mmoles, 1 eq.) was dissolved in MeOH and $Eu(CF_3SO_3)_3$ (0.373 g, 0.62 mmoles, 1.1 eq.) added slowly and the solution stirred overnight at 65 °C, after which the solvent was reduced to 1 mL and the product precipitated from swirling diethyl ether (100 mL) to yield a yellow oil 0.496 g, quantitative yield. HRMS (*m/z* ES+) Found for $C_{24}H_{42}N_7O_6F_3SEu$: 766.2103, Required: 766.208; δ_H (MeOD, 400 MHz): 19.21, 18.08, 16.43, 11.90, 5.56, 4.01, 2.52, 1.70, 0.73, -1.79, -7.69, -8.62, -13.28, -16.66, -18.96. ν_{max} (neat sample)/ cm^{-1}: 3454, 3232, 2926, 1618, 1505, 1459, 1414, 1409, 1249, 1215, 1153, 1078, 1026, 957, 906, 823, 756.

(52.Tb)

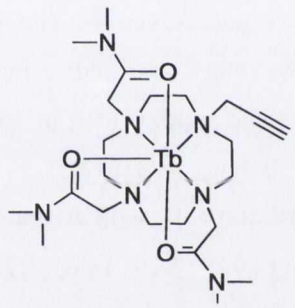

52 (0.30 g, 0.645 mmoles, 1 eq.) was dissolved in MeOH (25 mL) with $Tb(CF_3SO_3)_3$ (0.52 g, 0.71 mmoles, 1.1 eq.) and refluxed overnight. The solvent was removed under reduced vacuum dissolved in 1 mL of MeOH and precipitated out of swirling diethyl ether (150 mL) to yield a yellow oil 0.40 g, quantitative yield. HRMS (*m/z*-ES+) Found 772.2144 for $C_{24}H_{42}N_7O_6STbF_3$, Required: 772.2123; δ_H (MeOD, 400 MHz): 432.6, 391.9, 376.1, 295.1, 287.2, 247.0, 215.1, 192.9, 177.2, 145.2, 129.2, 109.6, 96.9, 89.9, 86.9, 82.2, 53.1, 16.2, 1.35, -7.4, -11.8, -12.2, -18.5, -27.9, -31.1, -2.0, -7.6, -12.5, -18.9, -28.1, -31.5, -49.6, -53.5, -55.4, -82.2, -86.9, -89.6, -94.8, 106.7, -107.3, -119.5, -148.1, -150.7, -174.8, -186.5, -219.7, -242.8, -260.6, -318.2, -338.1, -366.2, -372.3, -608.0; ν_{max} (neat sample)/ cm^{-1}: 3485, 1620, 1462, 1248, 1155, 1079, 1026, 958, 824.

(57.Eu)

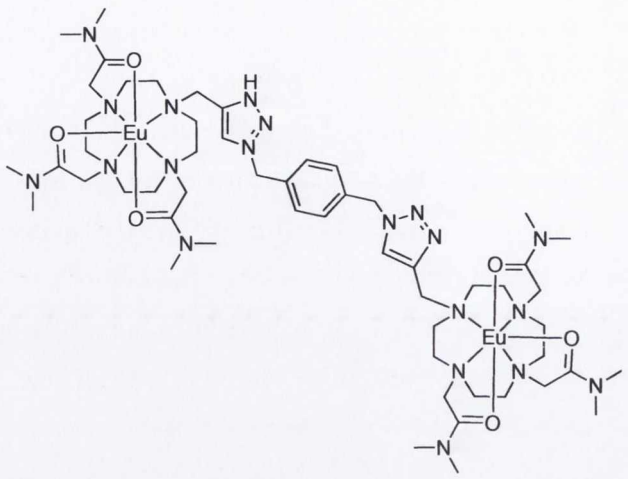

p–dibromoxylene (0.042 g, 0.16 mmoles, 1eq.) was dissolved in DMF (5 mL) and Na azide (0.031 g, 0.48 mmoles, 3 eq.) added to the solution and stirred overnight at 25°C. The complex **52.Eu** (0.20 g, 0.32 mmoles, 2 eq.) was then added with sodium ascorbate (0.0032 g, 0.016 mmoles, 0.1 eq.) and $CuSO_4.5H_2O$ (0.04 g, 0.016 mmoles, 0.1 eq.) and stirred for a further 48 hours before extracting the solution with ether to remove excess xylene starting material. The solvent was removed from the aqueous layer and the product redissolved in MeOH to and triturated with ether to yield a green solid. This was then purified using column chromatography to give the product as a yellow hygroscopic solid, 0.11 g in 46 % yield. HRMS (m/z - MALDI) 1909.5112 [M + $(CF_3SO_3)_3$ + $(H_2O)_2$ + H_2] for $C_{57}H_{100}Eu_2F_9N_{20}O_{17}S_3$, Required: 1909.5018. δH (MeOH, 400 MHz): 36.40, 34.90, 30.56, 29.01, 27.46, 26.78, 25.41, 22.43, 21.27, 19.34, 17.99, 16.92, 14.79, 13.63, 12.38, 9.28, 8.12, 7.54, 6.77, 5.03, 4.54, 3.58, 2.90, 2.20, 1.45, 0.48, -0.58, -1.35, -2.80, -3.26, -4.45, -5.22, -6.00, -7.64, -9.57, -10.73, -11.41, -12.76, -13.44, -14.31, -16.64, -18.57, -19.15, -20.02. ν_{max} (neat sample)/ cm^{-1}: 3415, 2141, 2060, 1621, 1610, 1449, 1283, 1234, 1183, 1155, 1131, 1032, 767, 638.

(57.Tb)

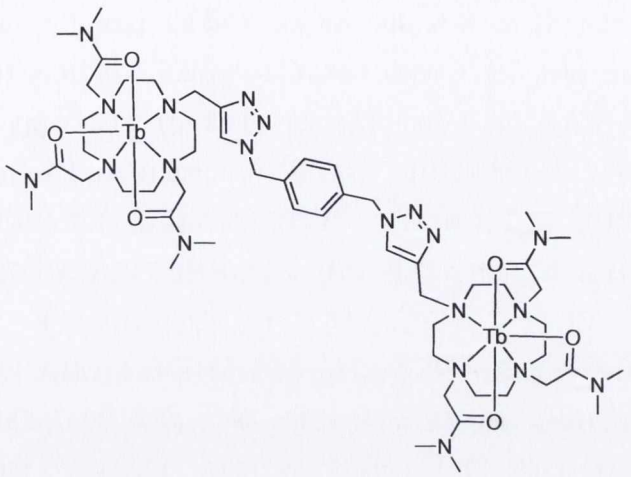

p–dibromoxylene (0.040 g, 0.015 mmoles, 1eq.) was dissolved in DMF (5 mL) and Na azide (0.020 g, 0.03 mmoles, 2 eq.) was added to the solution and stirred overnight at 25 °C. The complex **52.Tb** (0.19 g, 0.30 mmoles, 2 eq.) was then added with sodium ascorbate (0.003 g, 0.015 mmoles, 0.1 eq.) and $CuSO_4.5H_2O$ (0.0037 g, 0.015 mmoles, 0.005g, catalytic) and stirred for a further 48 hours before extracting the solution with ether to remove excess xylene starting material. The solvent was removed from the aqueous layer and the product redissolved in MeOH and triturated with ether to yield a yellow oil 0.11 g in 51% yield. HRMS (m/z MALDI): Found: 2031.4130 for $C_{58}H_{93}N_{20}O_{18}F_{12}S_4Tb_2$, Required: 2031.4175; δH (MeOD, 600 MHz): 306.7, 254.7, 174.3, 167.0, 150.8, 99.9, 85.0, 82.6, 65.6, 63.6, 61.0, 45.7, 4.83, 3.69, 3.33, 1.32, 0.92 -19.73, -16.44. ν_{max} (neat sample)/ cm^{-1}: 3659, 3556, 3475, 2942, 2923, 2850, 2091, 1619, 1540, 1500, 1458, 1406, 1374, 1255, 1231, 1169, 1035, 958, 907, 821, 823, 765, 698.

2,2'-(4-(2-(1-(naphthalen-1-yl)ethylamino)-2-oxoethyl)-10-(prop-2-ynyl)-1,4,7,10-tetraazacyclododecane-1,7-diyl)bis(N-methyl-N-(1-(naphthalen-1-yl)ethyl)acetamide) (53)

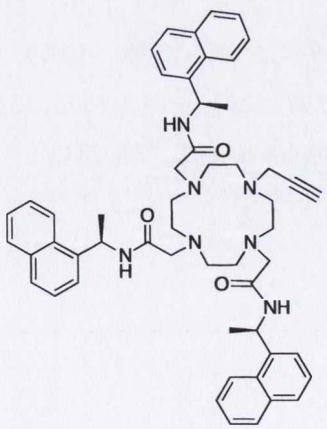

50 (0.1059 g, 0.504 mmoles, 1eq.) was dissolved in CH_3CN with K_2CO_3 (0.23 g, 1.66 mmoles, 3.3 eq.) and KI (0.276 g, 1.66 mmoles, 3.3 eq.). 2 chloro-*N*-[(1S)-(1-naphthalenylethyl)] acetamide (0.412 g, 1.66 mmoles, 3.3 eq.) was added and the solution refluxed over 7 days. The solution was filtered through a plug of celite and the solvent removed under vacuum. The compound was redissolved in $CHCl_3$ and extracted with 0.1 M KOH

solution. The organic layers were combined, dried over $MgSO_4$ filtered and the solvent removed to yield a cream oil which was purified column chromatography using 95:5 CH_2Cl_2 / MeOH to yield 0.1588 g, 37 % yield. HRMS (*m/z* ES+) Found for $C_{53}H_{62}N_7O_3$ 844.4911 Required: 844.4914; δ_H ($CDCl_3$, 400 MHz): 7.29-8.1 ppm (br, m, 21 CH naphthyl) 1.28-3.0 ppm (br m, 34H, CH_2-Cyclen, CH_3, CH-alkyne). δ_C ($CDCl_3$, 100 MHz): 170.40 (q) 169.90 (q), 169.19 (q), 137.9 (q), 137.6 (q), 133.8 (q), 133.81 (q), 131.5(q), 131.3(q), 128.7 (CH), 128.6 (CH), 128.5 (CH), 126.7 (CH), 126.6 (CH), 126.5 (q), 126.0 (CH), 125.9 (CH), 125.5 (CH), 125.2 (CH), 125.0 (CH), 123.6 (CH), 123.4 (CH), 122.8 (CH), 122.6 (CH), 78.0 (CH), 77.2 (CH), 77.0 (CH), 76.7 (CH), 73.1 (CH), 72.5 (CH), 58.6 (CH_2), 56.1 (CH_2), 55.2 (CH_2), 54.9 (CH_2), 54.6 (CH_2), 52.6 (CH_2), 51.8 (CH_2), 51.7 (CH_2), 51.6 (CH_2), 50.8 (CH_2), 43.8 (CH), 43.7 (CH_2), 43.5 (CH), 43.4 (CH_2), 19.9 (CH_3), 19.7 (CH_3), 19.5 (CH_3). ν_{max} (neat sample)/ cm^{-1}: 3280, 3040, 2966, 2927, 2810, 2235, 1646, 1597, 1508, 1446, 1396, 1368, 1323, 1293, 1246, 1237, 1170, 1107, 1101, 1087, 1000, 961, 905, 799, 777, 724.

53.Eu

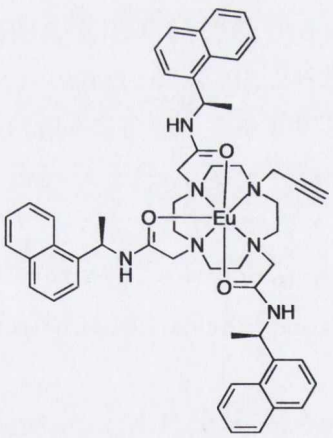

53S (0.0455g, 0.0527 mmoles, 1eq.) was dissolved in MeOH with $Eu(CF_3SO_3)_3$ (0.035 g, 0.0579 mmoles, 1.1 eq.) and refluxed overnight. The product was isolated by preciptation from ether to give a clear oil 0.0573 g in quantitative yield; δ_H (MeOD, 400 MHz) 19.21, 18.42, 9.76, 9.52, 9.39, 9.13, 8.38, 8.23, 8.15, 7.74, 7.69, 7.45, 7.43, 7.07, 6.65, 6.49, 6.30, 6.02, 5.73, 5.52, 3.66, 3.50, 3.16, 3.09, 2.48, 2.28, 2.18, 1.59, 1.42, 1.31, 1.20, 0.97, 0.00, -0.41, -2.26, -4.51, -4.96, -5.88, -7.01, -7.99, -9.12, -9.64, -10.36, -11.35, -12.20, -12.98, -15.19, -19.62, -20.00. ν_{max} (neat sample)/ cm^{-1}: 3494.9, 3253.9, 3095, 2977, 2870, 1615, 1575, 1511, 1454, 1379, 1362, 1261, 1237, 1162, 1079, 1027, 957, 927, 899, 861, 801, 779, 731.

53.Eu

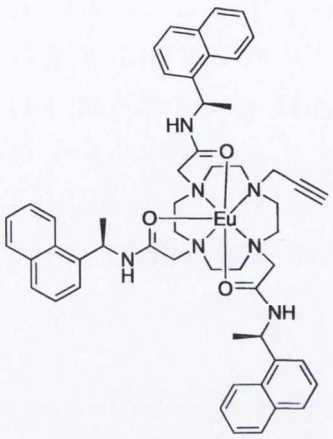

53*R* 0.1637 g, 0.194 mmoles, 1eq.) was dissolved in MeOH with $Eu(CF_3SO_3)_3$ (0.128 g, 0.213 mmoles, 1.1 eq.) and the resulting solution was refluxed overnight. The product was isolated by precipitation from swirling diethyl ether to give **53.Eu** as a clear oil, 0.20 g, quantitative yield. HRMS (m/z–MALDI) Found m/z 1144.3439 for $[M\text{-}H^+ + CF_3SO_3^-]^+$ Calculated m/z: 1144.3495, δ_H (MeOD, 400 MHz) 19.21, 18.42, 9.76, 9.52, 9.39, 9.13, 8.38, 8.23, 8.15, 7.74, 7.69, 7.45, 7.43, 7.07, 6.65, 6.49, 6.30, 6.02, 5.73, 5.52, 3.66, 3.50, 3.16, 3.09, 2.48, 2.28, 2.18, 1.59, 1.42, 1.31, 1.20, 0.97, 0.00, -0.41, -2.26, -4.51, -4.96, -5.88, -7.01, -7.99, -9.12, -9.64, -10.36, -11.35, -12.20, -12.98, -15.19, -19.62, -20.00. ν_{max} (neat sample)/ cm^{-1}: 3494.9, 3253.9, 3095, 2977, 2870, 1615, 1575, 1511, 1454, 1379, 1362, 1261, 1237, 1162, 1079, 1027, 957, 927, 899, 861, 801, 779, 731.

58.Eu

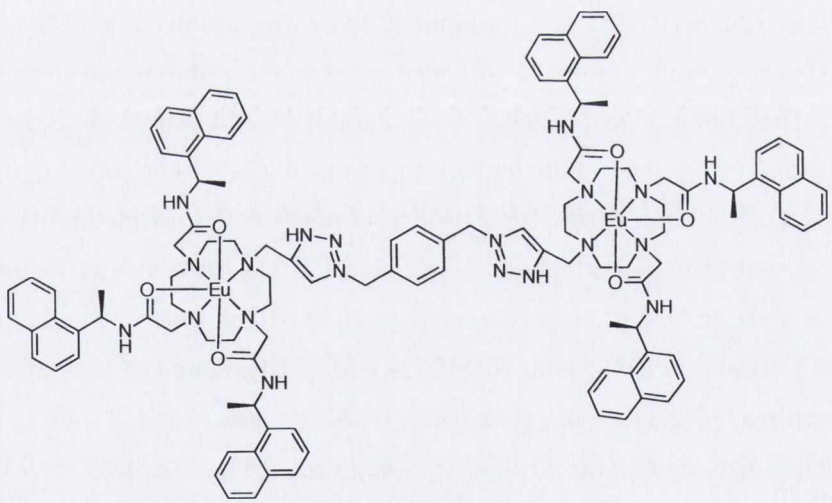

p–dibromoxylene (0.050 g, 0.26 mmoles, 1eq.) was dissolved in DMF (5 mL) and Na azide (0.034 g, 0.52 mmoles, 2 eq.) was added to the solution and stirred overnight at 25 °C. The complex **53*S*.Eu** (0.52 g, 0.52 mmoles, 2 eq.) was then added with sodium ascorbate (0.005 g, 0.026 mmoles, 0.1 eq.) and $CuSO_4.5H_2O$ (0.0038 g, 0.015 mmoles, catalytic) and stirred for a further 48 hours before extracting the solution with ether to

remove excess xylene starting material. The solvent was removed from the aqueous layer and the product redissolved in MeOH and triturated with ether to yield a yellow oil 0.30 g in 53% yield. HRMS (m/z-MALDI): Found for 11423.3512 for [M - 4H + K^+], Required 1142.3495. δH (MeOH, 600 MHz): 27.49, 25.51, 24.20, 22.77, 22.38, 9.93, 9.22, 8.78, 8.45, 8.07, 7.79, 7.57, 7.08, 6.80, 6.53, 6.09, 5.60, 5.43, 4.94, 4.44, 3.84, 3.40, 3.13, 2.91, 2.30, 1.87, 1.43, 1.10, 0.05, -0.06, -1.65, -2.63, -3.24, -4.17, -5.49, -7.19, -8.17, -8.72, -9.93, -11.16, -11.62, -12.74, -14.93, -15.75, -16.92, -177,88. ν_{max} (neat sample)/ cm^{-1}: 3419, 2997, 2909, 2061, 1617, 1540, 1463, 1387, 1254, 1171, 1083, 1031, 957, 901, 804, 780.

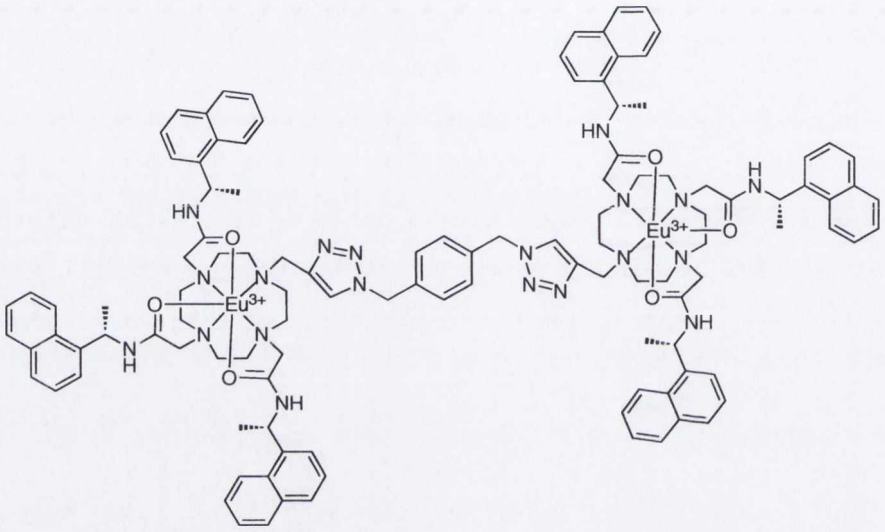

p–dibromoxylene (0.0282 g, 0.15 mmoles, 1eq.) was dissolved in DMF (5 mL) and Na azide (0.020 g, 0.30 mmoles, 2 eq.) was added to the solution and stirred overnight at 25 °C. The complex ***7S*** (0.299 g, 0.30 mmoles, 2 eq.) was then added with sodium ascorbate (0.003 g, 0.015 mmoles, 0.1 eq.) and $CuSO_4.5H_2O$ (0.0037 g, 0.015 mmoles, 0.005g, catalytic) and stirred for a further 48 hours before extracting the solution with ether to remove excess xylene starting material. The solvent was removed from the aqueous layer and the product redissolved in MeOH and triturated with ether to yield a green oil 0.169 g in 51% yield. HRMS (m/z-MALDI): Found 1142.3426 for [M + H + K], Required 1142.3495. δH (MeOD, 600 MHz): 306.7, 254.7, 174.3, 167.0, 150.8, 99.9, 85.0, 82.6, 65.6, 63.6, 61.0, 45.7, 4.83, 3.69, 3.33, 1.32, 0.92 -19.73, -16.44. ν_{max} (neat sample)/ cm^{-1}: 3279, 3118, 2989, 2928, 1746, 1617, 1599, 1516, 1484, 1461, 1413, 1365, 1244, 1166, 1081, 1027, 960, 903, 829, 803, 780, 735.

2,8-*Bis*(methyl)-6H, 12H-5,11-methanodibenzo[b,f][1,5] diazocine (68)[211]

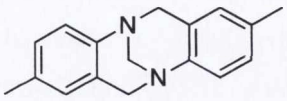

p-Toluidine (0.50g, 4.7 moles, 1 eq.) was dissolved in TFA (5 mL) and paraformaldehyde (0.21 g, 7 mmoles, 1.5 eq.) was added dropwise to the solution and stirred at 25 °C for 16 h. The volume of TFA was reduced to 2 mL, H_2O (10 mL) added and the solution basified to pH 10. The product was extracted into $CHCl_3$ (3 x 10 mL), washed with H_2O (2 x 10 mL), dried over $MgSO_4$, filtered and the solvent removed under reduced pressure to yield an orange solid, 0.837 g, 71 %. HRMS (*m/z* -ES): Found: 251.1700 for $C_{17}H_{18}N_2$, Required: 251.1548. δ_H ($CDCl_3$, 400 MHz); 2.29 (s, 6H, CH_3-4), 4.23 (d, J = 16.6 Hz, 2H, CH_2-H_a), 4.67 (s, 2H, CH_2- H_c), 4.87 (d, J = 16.6 Hz, 2H, CH_2-H_b), 6.84 (s, 2H, Ar-CH-3), 7.12 (d, J = 8.5 Hz, 2H, Ar-1), 7.30 (d, J = 8.5 Hz, 2H, Ar-CH-2). δ_C (100 MHz, $CDCl_3$) 138.9 (q), 136.6 (q), 129.1 (q), 127.1 (CH), 124.4 (CH), 123.8 (CH), 66.2 (CH_2), 57.0 (CH_2), 20.5 (CH_3). ν_{max} (neat sample)/cm^{-1}: 2920, 2081, 1634, 1496, 1445, 1415, 1327, 1305, 1267, 1178, 1025, 993, 962, 925, 874, 821, 796, 751, 718, 708, 686.

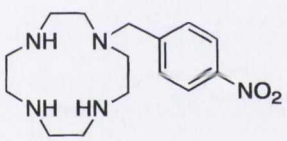

1-[(4-nitrophenyl) methyl]-1,4,7,10-tetraazacyclododecane[212] (72)

Cyclen (1.0 g, 5.8 mmoles, 4 eq.) was dissolved in $CHCl_3$ (50 mL) with Et_3N (0.25 mL, 5.8 mmoles, 4 eq.) and 4-nitrobenzyl chloride (0.31 g, 1.8 mmoles, 1eq.) and the resulting solution was stirred overnight at 65 °C. The reaction mixture was then washed with 0.1 M NaOH (4 x 15 mL) and H_2O (2 x 15 mL), the organic layers combined, dried over $MgSO_4$ and the solvent removed under reduced volume to give **72**, as a yellow oil, 0.41 g in 74 % yield. HRMS (*m/z*-ES+) Found 308.2086 for $C_{15}H_{26}N_5O_2$, Required: 308.2087; δ_H ($CDCl_3$, 400 MHz): 8.19 (d, J = 9.04 Hz, 2H, Ar-H), 7.50 (d, J = 9.04 Hz, 2H, Ar-H), 3.71 (s, 2H, CH_2), 2.82 (m, 4H, cyclen CH_2), 2.69 (m, 4H, cyclen CH_2), 2.58 (m, 8H, Cyclen CH_2). δ_C (100 MHz, $CDCl_3$): 146.7 (q), 129.0 (CH), 123.3 (CH), 58.3 (CH_2), 51.12 (CH_2), 46.5 (CH_2), 45.7 (CH_2), 44.5 (CH_2). ν_{max} (neat sample)/ cm^{-1}: 3643, 3294, 2926, 2821, 1603, 1556, 1515, 1459, 1446, 1408, 1350, 1271, 1256, 1224, 1184, 1160, 1112, 1102, 1084, 1054, 1042, 1032, 1015, 975, 949, 933, 920, 896, 849, 803, 789, 772, 758, 739, 706, 645, 627.

1-[(4-nitrophenyl) methyl]-1,4,7,10-tetraazacyclododecane-4,7,10 triacetamide (73)[213]

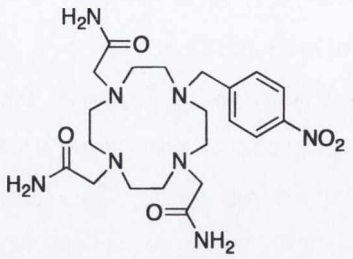

72 (0.444 g, 1.44 mmoles, 1eq.) was dissolved in $CHCl_3$ with KI (0.747 g, 4.5 mmoles, 3.1eq.) and Cs_2CO_3 (1.46 g, 4.5 mmoles, 3.1eq.). Bromoacetamide (0.62 g, 4.5 mmoles, 3.1 eq.) as then added slowly to the reaction mixture and the mixture then refluxed at 65 °C over 7 days. The reaction mixture was filtered to remove inorganic salts and the solvent removed under reduced vacuum. The product was then triturated with $CHCl_3$ and MeOH to yield the product **73** as a white hydroscopic solid 0.1 g, 15% yield. HRMS (m/z-ES+) Found: 501.4297 for $C_{21}H_{34}N_8O_5$ Required: 501.2550; δ_H ($CDCl_3$, 400 MHz): 8.12 (d, *J*= 8.52 Hz, 2H, Ar-H), 7.39 (d, J= 8.52 Hz, 2H, Ar-H), 3.57 (2H, s, CH_2), 3.45 (4H, s, CH_2), 3.33 (2H, m, CH_2), 3.29 (2H, s, CH_2), 3.04- 2.94 (4H, m, CH_2), 2.59 (10H, m, CH_2). δ_C ($CDCl_3$, 100 MHz): 172.8 (q), 172.7 (q), 147.7 (q), 146.4 (q), 129.7 (CH_2), 123.3 (CH_2), 58.6 (CH_2), 58.0 (CH_2), 57.6 (CH_2), 53.5 (CH_2), 53.1 (CH_2), 53.0 (CH_2), 52.6 (CH_2). ν_{max} (neat sample cm^{-1}): 3300, 1668, 1515, 1406, 1344, 1083, 1006.

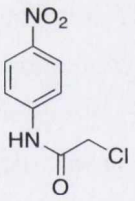

2-chloro-*N*-(4-nitrophenyl)acetamide

0.50 g, 3.36 mmoles, 1 eq.) was stirred in the presence of NaOH (0.18 g, 4 mmoles, 1.1 eq.) in CH_2Cl_2, at 0 °C. Chloroacetyl chloride (0.32 mL, 4 mmoles, 1.1 eq.) was added drop wise over 1 hour and the resulting solution was stirred overnight followed by extraction into $CHCl_3$, washing with 1M HCl (2 x 10 mL) and 1M NaOH (2 x 10 mL) and finally with H_2O (2 x 10 mL), dried over $MgSO_4$ filtered and solvent removed under reduced pressure to yield a brown oil, 0.67 g 85 % yield. HRMS (m/z-ES^+); Found: 213.0058 for $C_8H_6N_2O_3Cl$, Required: 213.0067. δ_H ($CDCl_3$, 400 MHz): 10.92 (s, 1H, NH), 8.24 (d, J = 7.0 Hz, 2H, Ar-H), 7.83 (d, J = 7.0 Hz, 2H, Ar-H), 4.35 (s, 2H, CH_2). δ_C ($CDCl_3$, 400 MHz): 165.6 (q), 144.6 (q), 142.6 (q), 125.1 (CH), 119.1 (CH), 43.6 (CH_2). ν_{max} (neat sample cm^{-1}): 3275, 3228, 3163, 3105, 2988, 2942, 1683, 1623, 1597, 1566, 1496, 1405, 1379, 1332, 1294, 1254, 1198, 1173, 1112, 967, 923, 871, 849, 828, 772, 718, 687.

[N_1-(4-nitrophenyl)]-1,4,7,10-tetraazacyclododecane-acetamide (78)[214] [212]

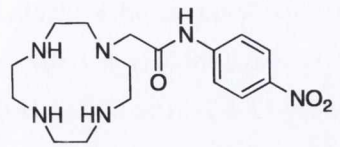

Cyclen (0.96 g, 5.6 mmoles, 4 eq.) was dissolved in $CHCl_3$ with Et_3N (0.78 mL, 5.6 mmoles, 4eq.) and stirred as the acetamide (0.3 g, 1.4 mmoles, 1 eq.) was added slowly drop wise to the solution and was then stirred at 65 °C overnight. The product was then extracted into $CHCl_3$ and washed with 0.1 M KOH solution, H_2O, dried over $MgSO_4$, filtered sovent removed to yield a yellow oil 0.485 g, quantitative yield. HRMS (*m/z*-ES+): Found: 351.2133 for $C_{16}H_{27}N_6O_3$, Required: 351.2145; δ_H ($CDCl_3$, 400 MHz): 8.20 (d, J = 9.2 Hz, 2H, Ar-H), 7.99 (d, J = 9.2 Hz, 2H, Ar-H), 3.50 (s, 2H, CH_2), 2.76 (m, 16H, Cyclen CH_2). δ_C ($CDCl_3$, 400 MHz): 171.1 (q), 144.5 (q), 143.2 (q) 125.0 (CH), 119.0 (CH), 60.1 (CH_2), 53.88 (CH_2), 47.43 (CH_2), 47.18 (CH_2), 46.02 (CH_2). ν_{max} (neat sample cm^{-1}): 3449, 3322, 3199, 2945, 2821, 1694, 1594, 1510, 1498, 1406, 1325, 1298, 1170, 1107, 1076, 994, 935, 850, 748, 690, 691.

[N_1,N_1,N_4,N_4,N_7,N_7-hexamethyl-N_{10}-(4-nitrophenyl)]-1,4,7,10-tetraazacyclododecane-4,7,10 tetraacetamide (79)[214]

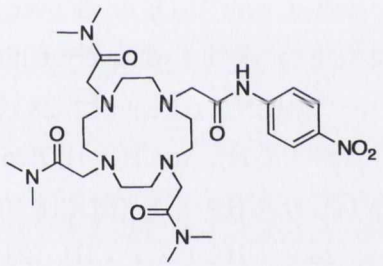

78 (0.30 g, 0.86 mmoles, 1eq.) was dissolved in $CHCl_3$ with KI (0.47 g, 2.83 mmoles, 3.3 eq.) and K_2CO_3 (0.39 g, 2.83 mmoles, 3.3 eq.). α-Chloro-*N*,*N*-dimethyl acetamide (0.34 g, 2.83 mmoles, 3.3 eq.) was added and the solution refluxed overnight. The product was then extracted into $CHCl_3$ and washed with water to yield the product as a brown oil 0.39 g, 75 % yield. HRMS (m/z-ES+) Found for $C_{28}H_{48}N_9O_6$ 606.3728 Required 606.3734; δ_H ($CDCl_3$, 400 MHz): 7.32 (d, J = 8.52 Hz, 2H, Ar-H), 6.46 (d, J = 8.52 Hz, 2H, Ar-H), 2.76 - 3.5 ppm (m, 19H, Cyclen CH_2). δ_C ($CDCl_3$, 100 MHz): 171.8 (q), 170.41 (q), 170.21 (q), 145.21 (q), 142.11 (q), 123.87 (CH), 119.04 (CH), 57.15 (CH_2), 54.64 (CH_2), 54.50 (CH_2), 53.04 (CH_2), 49.72 (CH_2), 35.75 (CH_2), 35.63 (CH_2), 35.22 (CH_3), 35.13 (CH_3). ν_{max} (neat sample)/ cm^{-1}: 3434, 2966, 2821, 1648, 1554, 1504, 1174, 1104.

[N_1,N_1,N_4,N_4,N_7,N_7-hexamethyl-N_{10}-(4-aminophenyl)]-1,4,7,10-tetraazacyclododecane-4,7,10 tetraacetamide (80)[214]

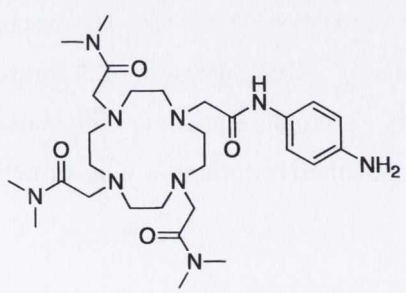

79 (0.078 g, 0.129 mmol) and Pd/C (10 %) were dissolved in EtOH (3 mL), and a solution of $N_2H_4.H_2O$ (0.052 g, 1.032 mmol) in EtOH (5 mL) was added dropwise. The reaction mixture was then refluxed overnight, under an

argon atmosphere. The brown solution was filtered through celite and the solvent was removed under reduced pressure to yield the product as a brown oil, 0.065 g, 88% yield. HRMS for $C_{28}H_{50}N_9O_4$: Observed 576.3996, Calculated 576.3986; δ_H ($CDCl_3$, 400 MHz): 10.07 (s, 1H, NH), 7.57 (d, J= 8.0 Hz, 2H, Ar-H,), 6.54 (d, J = 8.5 Hz, 2H, Ar-H,), 3.4-2.4 (m, 42H, CH_2CONCH_3 + CH_2 Cyclen); δ_C (100 MHz, $CDCl_3$): 170.97 (q), 170.72 (q), 169.80 (q), 142.55 (q), 130.74 (q), 121.15 (CH), 114.93 (CH), 57.99 (CH_2), 54.95 (CH_2), 53.46 (CH_2), 52.42 (CH_2), 50.90 (CH_2), 36.25 (CH_2), 36.09 (CH_2), 35.65 (CH_3), 35.53 (CH_3). ν_{max} (neat sample)/ cm^{-1}: 3434, 2966, 2821, 1648, 1554, 1504, 1174, 1104.

4-Nitrobenzylphthalimide (89)[215]

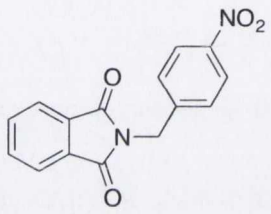

Potassium phthalimide (4.77 g, 25.7 mmoles, 1.1 eq.) and nitrobenzyl bromide (5.0 g, 23 mmoles, 1 eq.) were dissolved in DMF (200 mL) and stirred overnight at room temperature. The reaction mixture was then dissolved in H_2O and the product extracted into a mixture of EtOAc and toluene 2:1. The organic extracts were combined, washed with H_2O, dried over $MgSO_4$, filtered and the solvent removed under reduced pressure to yield a white crystalline solid, 4.64 g, 64 %. HRMS (m/z ES^+): Found: 283.0713 for $C_{15}H_{11}N_2O_4$, Required: 283.0719. δ_H ($CDCl_3$, 400 MHz) 8.18 (d, J=9.0 Hz, 2H, Ar-CH-7); 7.88 (m, 2H, Ar-CH-1,4), 7.76 (m, 2H, Ar-CH-2,3) 7.59 (d, J= 9.0 Hz, 2H, Ar-CH-6), 4.95 (s, 2H, CH_2-5). δ_C ($CDCl_3$, 100 MHz) 167.2 (q), 147.1 (q), 142.8 (q), 133.9 (q), 131.4 (q), 128.9 (CH), 123.5 (CH), 123.2 (CH), 40.42 (CH_2). ν_{max} (neat sample)/ cm^{-1}: 3075, 2162, 1767, 1695, 1600, 1509, 1465, 1423, 1392, 1345, 1327, 1205, 1186, 1168, 1100, 1087, 1012, 976, 964, 943, 868, 858, 833, 801, 791, 744, 724, 693.

4- Aminobenzylphthalimide (90)[215]

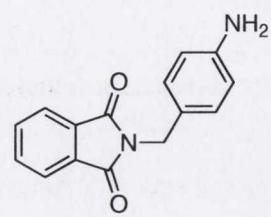

4-Nitrobenzylphthalimide (0.272 g, 0.962 mmoles, 1eq.) was dissolved in a mixture of $CHCl_3$ and MeOH (15/10 mL), with 10% Pd/C catalyst and placed in the hydrogenation apparatus. The flask was evacuated of air and then placed under a pressure of 3 atmospheres. The solution was then shaken overnight under this H_2 pressure at room temperature. The flask was then emptied of hydrogen and the solution filtered through a plug of celite in a

sintered glass funnel. The solvent was removed under reduced pressure to give yellow crystals, 0.233 g in 96 % yield. HRMS (*m/z*-ES+) Found: 253.1700 for $C_{15}H_{12}N_2O_2$, Requires: 253.0977; δH (DMSO-d_6, 400MHz) 7.83 (m, 2H, Ar-CH), 7.69 (m, 2H, Ar-CH), 7.15 (d, J = 8.5 Hz, 2H, Ar-CH), 6.83 (d J = 8.5 Hz, 2H, Ar-CH), 4.66 (s, 2H, CH_2); δC (DMSO-d_6, 100 MHz) 167.7 (q), 141.4 (q), 134.5 (q), 131.6 (CH), 128.7 (CH), 123.2 (CH), 117.6 (CH), 40.7 (CH_2); ν_{max} (neat sample)/ cm^{-1}: 3449, 3363, 2922, 2852, 2586, 1769, 1709, 1609, 1531, 1512, 1465, 1423, 1393, 1368, 1333, 1290, 1204, 1184, 1176, 1116, 1087, 1069, 1018, 980, 956, 928, 835, 791, 748, 724, 681.

2,8-Bis(phthalyl)-6H,12H-5,11- methanodibenzo[b,f][1,5] diazocine[215]

4-Amino benzylphthalimide, **90** (0.47 mmoles, 0.1194 g, 1 eq.), was dissolved in TFA (10 mL) and formaldehyde (0.1 ml, 0.95 mmoles, 2 eq.) was added drop wise to the solution. This was stirred at 25 °C overnight. The volume of TFA was reduced to 2 mL under reduced pressure and the product was dissolved in H_2O, basified up to pH 9 and extracted into $CHCl_3$ (3 x 15 mL). The organic layers were combined and the solution washed with H_2O (2 x 15 mL), dried over $MgSO_4$, filtered and the solvent removed to yield a brown oil, 0.077 g, 30 % yield. HRMS (*m/z*-ES+) Found for $C_{33}H_{25}N_4O_4$: 541.1876, Required 541.2746; δ_H ($CDCl_3$, 400 MHz) 7.80 (m, 2H, Ar-CH), 7.68 (m, 2H, Ar-CH), 7.24 (d, J = 8 Hz, 2H, Ar-CH), 7.06 (d, J = 8 Hz, 2H, Ar-CH), 6.98 (s, 2H, Ar-CH), 4.70 (d, J = 4.5 Hz, 2H, CH_2), 4.62 (d, J = 16.6 Hz, 2H, CH_2), 4.23 (s, 2H, CH_2), 4.10 (d, J = 16.6 Hz, 2H, CH_2); δ_C ($CDCl_3$, 100 MHz): 167.6 (q), 165.6 (q), 144.6 (q), 142.6 (q), 133.5 (CH), 131.6 (CH), 127.4 (CH), 125.1 (CH), 119.1 (CH), 66.2 (CH_2), 57.9 (CH_2), 43.6 (CH_2); ν_{max} (neat sample)/cm^{-1}; 2923, 2843, 1763, 1613, 1519, 1493, 1465, 1430, 1389, 1333, 1310, 1298, 1262, 1210, 1184, 1103, 1087, 1068, 955, 938, 891, 843, 831, 799, 773, 760, 721, 710, 660.

2,8-Bis(methanamine)-6H, 12H-5,11- methanodibenzo[b,f][1,5] diazocine (87)[215]

91 (0.8588 g, 1.6 mmoles, 1 eq.) was dissolved in neat hydrazine. The solution was refluxed at 80 °C overnight. The hydrazine was partly removed under reduced pressure and the solution dissolved in 20 mL H_2O. The product was then extracted into $CHCl_3$ (4 x 15 mL), washed with H_2O (2 x 10 mL), dried over $MgSO_4$ and solvent removed under reduced pressure to yield a pale yellow oil, 0.382 g in 86 %. HRMS (*m/z*-ES) Found 281.1611 for $C_{17}H_{21}N_4$ Calculated: 281.1766; δ_H

($CDCl_3$, 400 MHz) 7.09 (s, 4H, Ar-CH), 6.85 (s, 2H, Ar-CH), 4.65 (d, J = 16.6 Hz, 2H, CH_2), 4.29 (s, 2H, CH_2), 4.13 (d, J = 16.6 Hz, 2H, CH_2), 3.71 (s, 4H, CH_2). δ_C ($CDCl_3$, 100 MHz): 146.2 (q), 138.5 (q), 127.3 (q), 125.9 (CH), 125.1 (CH), 124.7 (CH), 66.5 (CH_2), 58.3 (CH_2), 45.5 (CH_2). ν_{max} (neat sample/cm^{-1}): 3367, 2916, 1609, 1491, 1440, 1366, 1345, 1298, 1207, 1159, 1113, 1097, 1061, 961, 944, 884, 739, 689.

2,8-Bis(acetamide)-6H,12H-5,11-methanodibenzo [b,f][1,5] diazocine (92)

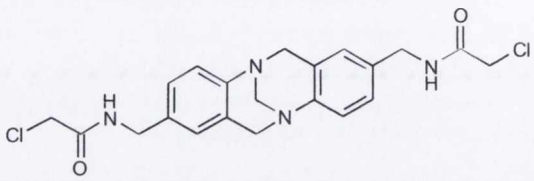

87, (0.4829 g, 1.72 mmoles, 1 eq.) and NaOH (0.137 g, 3.44 mmoles, 2 eq.) were dissolved in CH_2Cl_2 and cooled to -10 °C. Chloroacetyl chloride (0.4 mL, 3.44 mmoles, 2 eq.) was dissolved in CH_2Cl_2 (50 mL) and added dropwise to the solution over 1 hour. The resulting solution was stirred at room temperature overnight after which the precipitate was dissolved in H_2O (30 mL) and extracted into CH_2Cl_2 (3 x 20 mL). The aqueous solution was dried under reduced pressure and MeOH added to yield an orange precipitate. This was re-extracted with $CHCl_3$ and washed with H_2O. The yellow solid obtained was dissolved in MeOH with heating and allowed to precipitate upon cooling to yield a white solid, 0.017 g in 2 %. HRMS (*m/z*-ES): Found: 433.1675 for $C_{21}H_{22}N_2O_2Cl_2$, Requires: 433.1198. δ_H (DMSO-d_6, 400 MHz); 8.6 (s, 2H, Ar-CH), 7.01 (m, 4H, Ar-CH), 6.82 (s, 2H, Ar-CH), 4.57 (d, J = 16.5 Hz, 2H, CH_2), 4.20 (s, 2H, CH_2), 4.13 (d, J = 6.0 Hz, 2H, CH_2), 4.07 (s, 2H, CH_2), 4.03 (d, J = 16.5 Hz, 2H, CH_2); δ_C (DMSO-d_6, 100 MHz); 165.8 (q), 147.0 (q), 133.8 (q), 127.9 (q), 126.4 (CH), 125.8 (CH), 124.7 (CH), 66.3 (CH_2), 58.3 (CH_2), 42.6 (CH_2), 42.2 (CH_2); ν_{max} (neat sample)/ cm^{-1}: 3288, 3049, 2923, 2896, 2847,1652, 1539, 1493, 1462, 1423, 1360, 1334, 1305, 1229, 1208, 1164, 1146, 1112, 1097, 1063, 1016, 1003, 954, 901, 884, 834, 784, 686.

2-(4,10-Bis-dimethylcarbamoylmethyl-1,4,7,10-tetraaza-cyclododec-1-yl)-*N,N*-dimethyl-acetamide (77)[216]

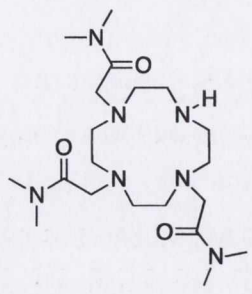

Cyclen (1.0 g, 5.8 mmoles, 1 eq.) was dissolved in CH_3CN (200 mL) in the presence of K_2CO_3 (2.68 g, 19.4 mmoles, 3.3 eq.) and KI (3.22 g, 19.4 mmoles, 3.3 eq.) α-Chloro-*N,N*-dimethyl acetamide (2.3 g, 19.4 mmoles, 3.3 eq.) was added slowly dropwise over one hour and the resulting solution was refluxed over 3 days. The reaction mixture was filtered through a plud of celite, the solvent removed under reduced pressure, the product redissolved in $CHCl_3$ and washed with 1M KOH (3 x 25 mL) and H_2O (3 x 25 mL), dried over

$MgSO_4$, filtered, solvent removed under reduced pressure to give a brown oil which was purified using column chromatography on alumina with CH_2Cl_2/MeOH 98:2 gradient to yield the product as a yellow oil, 0.87 g in 35 % yield. HRMS (m/z-ES^+): Found: 428.3349 for $C_{20}H_{42}N_7O_3$, Calculated: 428.3344; δ_H($CDCl_3$, 400 MHz) 9.98 (broad s, 1H, N–H), 3.59 (s, 2H, CH_2–acetamide), 3.56 (s, 4H, CH_2-acetamide), 3.08 (s, 8H), 3.03 (s, 3H), 2.95 (s, 6H), 2.88 (s, 10H), 2.83 (s, 7H); δ_C ($CDCl_3$, 100 MHz): 170.3 (q), 170.2 (q), 55.5 (CH_2), 53.8 (CH_2), 51.7 (CH_2), 50.6 (CH_2), 49.7 (CH_2), 46.7 (CH_2), 36.4 (CH_2), 35.3 (CH_3); 34.4 (CH_3); ν_{max} (neat sample)/ cm^{-1}: 2927, 2852, 1637, 1508, 1475, 1402, 1338, 1261, 1103, 1064, 1022, 881, 806, 769, 667, 649, 574, 484.

2,8-Bis(methylenediol)-6H, 12H-5,11- methanodibenzo[b,f][1,5] diazocine (96)[211]

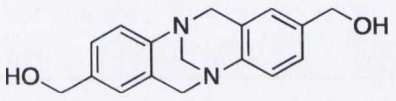

4-Amino benzyl alcohol (0.5 g, 4.1 mmoles, 1 eq.), was dissolved in TFA (10 mL) with paraformaldehyde (0.211 g, 8 mmoles, 2 eq.) and stirred overnight at 25 °C. The reaction mixture was basified to pH 10 using 1 M NaOH solution and then extracted with CH_2Cl_2, washed with H_2O (5 x 10 mL), dried over $MgSO_4$, filtered and solvent removed under reduced pressure to yield a brown oil in 0.32 g in 27 % yield. HRMS (*m/z*-ES^+) Found for $C_{17}H_{19}N_2O_2$: 283.1439, Required: 283.1447; δ_H (DMSO-d_6, 400 MHz); 7.07 (4H, s, Ar-H), 6.86 (2H, s, Ar-H), 4.99 (2H, bs, OH), 4.56 (d, J =16.64, 2H, TB-CH_2), 4.31 (s, 4H, CH_2), 4.21 (s, 2H, TB-CH_2), 4.04 (d, J = 16.64, 2H, CH_2); δ_C (DMSO-d_6, 100 MHz); 146.7 (q), 137.5 (q), 127.6 (q), 125.6 (CH), 125.0 (CH), 124.3 (CH) 66.4 (CH_2), 62.6 (CH_2), 58.4 (CH_2). ν_{max} (neat sample)/ cm^{-1}: 2917, 1668, 1613, 1515, 1491, 1347, 1324, 1111, 1096, 1064, 950, 898, 825, 804, 747, 664.

4-amino methyl benzoate (95)

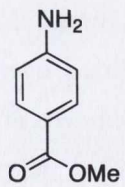

4-Amino benzoic acid (2.0 g, 14.6 mmoles, 1 eq.) was dissolved in MeOH (25 mL). This was stirred vigorously. Sulfuric acid (2 mL, 29.2 mmoles 2 eq.) was added drop wise to the solution and this was stirred overnight at 80 °C. The solvent was removed under reduced pressure and the product extracted into $CHCl_3$ (10 x 20 mL) and the organic layers combined and washed with H_2O (5 x 25 mL), dried over $MgSO_4$ filtered and the solvent removed to yield a cream/pink solid, 1.41 g, 65 % yield. δ_H: ($CDCl_3$, 400 MHz); 3.86 (s, 3H, CH_3-3), 6.63 (d, J= 8.6 Hz, 2H, Ar-CH-1), 7.85 (d, J = 8.6 Hz, 2H, Ar-CH-2). δC ($CDCl_3$, 100 MHz) 166.8 (q), 150.6 (q), 131.1 (CH), 119.1 (q), 113.3 (CH), 51.2 (CH_3).

ν_{max} (neat sample)/ cm^{-1}: 3406, 3336, 3228, 2987, 2944, 2844, 1681, 1636, 1596, 1574, 1514, 1433, 1341, 1312, 1198, 1174, 1117, 1077, 1012, 974, 850, 841, 824, 767, 697.

2,8-Bis(carboxymethyl)-6H, 12H-5,11- methanodibenzo[b,f][1,5] diazocine (96)[211]

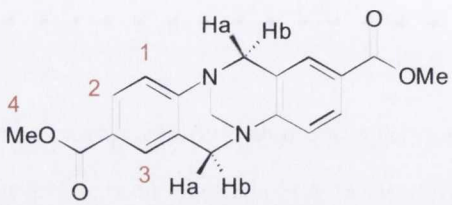

4-Aminomethylbenzoate (0.41 g, 2.7 mmoles, 1 eq.) was dissolved in TFA (10 mL). Formaldehyde (0.43 mL, 5.4 mmoles, 1.5 eq.) was added dropwise and the solution was stirred overnight at room temperature. The volume of TFA was then reduced to 5 mL under reduced pressure and the remaining reaction mixture dissolved in H_2O (10 mL). The product was extracted into $CHCl_3$ (5 x 15 mL), the organic layers combined and washed with H_2O (2 x 15 mL), dried over $MgSO_4$, filtered and the solvent removed under reduced pressure to give a yellow solid, 0.60 g, 66 % yield. HRMS (*m/z* -ES) Found: 339.1706 for $C_{19}H_{18}N_2O_4$ Requires: 339.1345; δ_H ($CDCl_3$, 400 MHz): 7.84 (d, J = 8.6 Hz, 2H, Ar-CH-2), 7.66 (s, 2H, Ar-CH-3), 7.2 (d, J = 8.6 Hz, 2H, Ar-CH-1), 4.75 (d, J = 16.6 Hz, 2H, CH_2-H_b), 4.35 (s, 2H, CH_2-H_c), 4.26 (d, J = 16.5 Hz, 2H, CH_2-H_a), 3.9 (s, 3H, CH_3); δ_C (100 MHz, $CDCl_3$): 166.1 (q), 151.9 (q), 128.4 (q), 128.0 (q), 126.9 (CH), 125.3 (CH), 124.5 (CH), 66.2 (CH_2), 58.2 (CH_2), 51.6 (CH_3); ν_{max} (neat sample) cm^{-1}: 2952, 2904, 1606, 1570, 1519, 1489, 1434, 1354, 1333, 1275, 1251, 1238, 1210, 1193, 1170, 1123, 1107, 1064, 1020, 986, 963, 942, 890, 876, 843, 813, 798, 786, 768, 736, 709, 679.

2,8-Bis(carboxylic acid)-6H, 12H-5,11- methanodibenzo[b,f][1,5] diazocine[211]

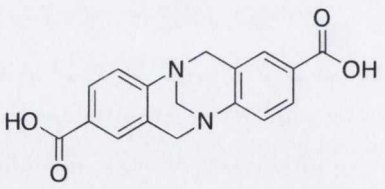

Compound **96** (0.50 g, 1.5 mmoles, 1eq.) was dissolved in 1 M NaOH (2 mL). This was refluxed overnight under inert atmosphere. The ethanol was removed under reduced pressure, H_2O added (20 mL), and the solution neutralised using 1 M HCl until a cream precipitate settled out of solution. The precipitate was filtered under suction and dried to yield a off white solid, 0.32 g in 70 % yield. HRMS (*m/z*-ES+) Found for $C_{17}H_{18}N_2$: 311.1439, Required: 311.1032; δ_H (DMSO-d_6, 400 MHz): 7.69 (d, J = 8 Hz, 2H, Ar-CH-2), 7.57 (s, 2H, Ar-CH-3), 7.19 (d, J = 8 Hz, 2H, Ar-CH-1), 4.68 (d, J = 16.6 Hz, 2H, CH_2-H_b), 4.26 (d, J = 16.6 Hz, 4H, CH_2-H_a),

4.24 (s, 2H, CH_2-H_c); δ_C (DMSO-d_6, 100 MHz): 167.0 (q), 152.3 (q), 128.5 (q), 128.1 (q), 128.0 (CH), 125.8 (CH), 124.8 (CH), 65.8 (CH_2), 58.0 (CH_2); ν_{max} (neat sample) cm^{-1}: 2912, 2527, 1979, 1680, 1605, 1574, 1517, 1492, 1387, 1350, 1332, 1278, 1251, 1206, 1127, 1094, 1060, 965, 944, 889, 844, 819, 773, 736, 708, 665.

(97)

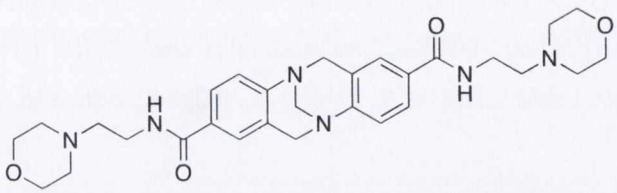

87 (0.20 g, 0.645 mmoles, 1eq.) was dissolved in THF under inert atmosphere. 1 (2-aminoethyl) morpholine (0.177 ml, 0.00129 mmoles, 2eq.) was added with HOBt (0.182 g, 0.129 mmoles, 2eq.). The solution was then stirred vigorously for 15 min at 0°C. EDCI.HCl (0.258 g, 0.129 mmoles, 2 eq.), Et_3N (0.188 mL, 0.129 mmoles, 2 eq.) and DMAP (0.165 g, 0.129 mmoles, 2 eq.) were then added to the solution and stirred for 30 min at 0 °C and then overnight at 25 °C. The solution was filtered, the solvent removed under reduced pressure. The resulting residue was dissolved in CH_2Cl_2, extracted with 1M HCl, the aqueous layer was then basified with KOH and extracted with $CHCl_3$ (3 x 15 mL), dried over $MgSO_4$, filtered, and the solvent removed under reduced pressure to yield an off-white oil, 0.132 g, 38% yield. HRMS (*m/z*-ES^+) Found for $C_{29}H_{39}N_6O_4$: 535.3039, Required: 535.3033. δ_H (DMSO-d_6, 400 MHz): 7.52 (d, J = 8.36 Hz, 2H, Ar-H), 7.44 (s, 2H, Ar-H), 7.19 (d, J = 8.36 Hz, 2H, Ar-H), 4.75 (d, J = 16.72 Hz, 2H, CH_2-TB), 4.35 (s, 2H, CH_2-TB), 4.25 (d, J = 16.72, 2H, CH_2-TB), 3.73 (m, 8H, CH_2-ethyl), 3.49 (m, 4H, morpholine-CH_2), 2.56 (t, J = 5.92 Hz, 4H, CH_2), 2.49 (s, 8H, CH_2). δ_C (DMSO-d_6, 400 MHz): 166.3 (q), 150.5 (q), 129.8 (q), 127.4 (q), 126.0 (CH), 125.2 (CH), 124.6 (CH), 66.5 (CH_2), 66.3 (CH_2), 58.4 (CH_2), 56.4 (CH_2), 52.8 (CH_2), 35.5 (CH_2). ν_{max} (neat sample)/ cm^{-1}: 3309, 2814, 1633, 1607, 1538, 1484, 1442, 1297, 1208, 1184, 1143, 1111, 1067, 1034, 1007, 964, 946, 913, 844, 798, 769, 733.

98

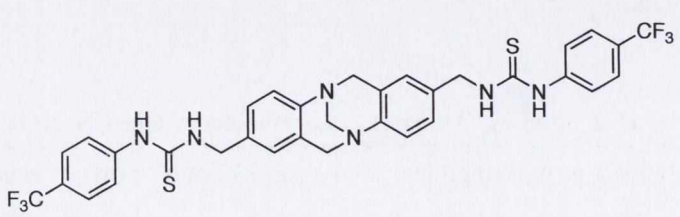

87 (0.2468 g, 0.88 mmoles, 1eq.) was dissolved in $CHCl_3$ with Et_3N and stirred vigorously while α,α,α-trifluorophenyl isothiocyanate (0.358 g, 1.76 mmoles, 2eq.) was added drop wise in $CHCl_3$ over one hour. The solution was

refluxed overnight at 65° C, after which the product was then isolated by suction filtration to yield a white solid, 0.26 g in 43% yield. HRMS (*m/z*- MALDI): Found for $C_{33}H_{29}N_6F_6S_2$: 687.1801, Required: 687.1799; m.p. 212 °C; δ_H (DMSO-d_6, 600 MHz): 9.81 (s, 2H, NH), 8.32 (s, 2H, NH), 7.71 (d, J = 5.64, 2H, CH), 7.63 (d, J = 5.72, 2H, CH), 7.09 (m, 4H, CH), 6.92 (s, 2H, CH), 4.60 (d, J = 11.2 Hz, 2H, CH_2), 4.59 (s, 4H, CH_2), 4.08 (d, J = 11.2 Hz, 2H, CH_2); δ_C (DMSO-d_6, 100 MHz): 180.3 (q), 147.1 (q), 143.3 (q), 133.4 (q), 127.8 (q), 126.6 (CH), 125.9 (CH), 125.6 (CH), 125.2 (CH), 124.7 (CH), 123.5 (q), 121.9 (CH), 66.3 (CH_2), 58.3 (CH_2), 46.8 (CH_2). δF (DMSO-d_6, 162 MHz): -60.8; ν_{max} (neat sample)/ cm^{-1}: 3250, 1616, 1543, 1493, 1462, 1422, 1321, 1266, 1209, 1166, 1121, 1066, 1016, 978, 962, 942, 888, 836, 744, 670.

99

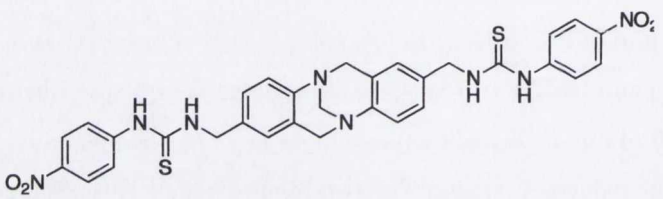

87 (0.19 g, 0.68 mmoles, 1eq.) was dissolved in $CHCl_3$ with Et_3N (0.2 mL, 1.43 mmoles, 2eq.). 4-nitrophenyl isothiocyanate (0.257 g, 1.43 mmoles, 2 eq.) was added drop wise in $CHCl_3$ over one hour. The solution was filtered and the orange precipitate washed with $CHCl_3$, dried under vacuum to yield 0.17 g, 40 % yield. HRMS (*m/z*-ES) Found for $C_{31}H_{29}N_8O_4S_2$: 641.1740, Calculated 641.1753; m.p. 216 °C; δ_H (DMSO-d_6, 400 MHz): 10.12 (s, 2H, NH), 8.56 (s, 2H, NH), 8.16 (d, J = 6.12 Hz, 4H, CH), 7.83 (d, J = 6.04, 4H, CH), 7.08 (m, 4H, CH), 6.93 (s, 2H, CH), 4.23 (s, 2H, CH_2), 4.61 (d, J = 11.64, 2H, CH_2), 4.59 (s, 2H, CH_2), 4.08 (d, J = 11.16, 4H, CH_2). δ_C (DMSO-d_6, 400 MHz): 179.8 (q), 147.0 (q), 145.8 (q), 141.7 (q), 133.0 (q), 127.8 (q), 126.5 (CH), 125.9 (CH), 124.6 (CH), 124.5 (CH), 123.2 (CH), 120.2 (CH), 66.09 (CH_2), 58.2 (CH_2), 46.7 (CH_2). ν_{max} (neat sample)/ cm^{-1}: 3295, 3082, 2979, 1597, 1495, 1453, 1327, 1319, 1257, 1231, 1171, 1111, 144, 969, 875, 849, 751, 725, 721.

Thioacetic Acid S-(12-bromododecyl) Ester[217] (**100**)

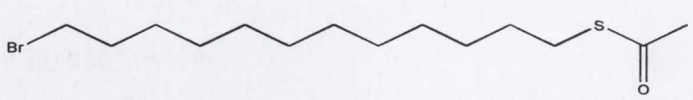

Bromododecane (5.00 g, 15.2 mmoles, 3.45 eq) was refluxed in CH_3CN (100 mL) with potassium thioacetate (0.5015 g, 4.39 mmoles, 1 eq.) for 72 hours. Solvent was removed under reduced pressure, H_2O was added and the solution extracted with CH_2Cl_2 (3 x 25mL), washed with H_2O (3 x 20 mL) to yield a brown solid, which was purified using

column chromatography hexane: ethyl acetate 95:5 gradient as eluent to yield a white oil, 0.7578 g, 53% yield. HRMS (m/z- ES^+): Found: 345.0864 for $C_{14}H_{27}BrOSNa$, Required: 345.0865. δ_H ($CDCl_3$, 400 MHz) 3.42 (2H, t, $J = 7$ Hz, CH_2-Br) 2.87 (2H, t, $J = 7$ Hz, CH_2-S), 2.34 (3H, s, CH_3) 1.84 (q, 2H, CH_2-CH_2-Br), 1.54 (2H, m, CH_2-CH_2-S), 1.28 (16H, m, CH_2-Chain). δ_C ($CDCl_3$, 100 MHz) 33.67 (CH_2), 32.39 (CH_2), 30.23 (CH_3), 29.05 (CH_2), 28.65 (CH_2), 28.31 (CH_2), 27.73 (CH_2). ν_{max} (neat sample)/ cm^{-1}: 2915, 1685, 1469.

1-Bromo-12-(12-bromododecyldisulfanyl)dodecane[217] (101)

MeOH (80 mL) was cooled to 0 °C in an acetone ice bath and acetyl chloride (9.7 g, 123 mmoles, 25 eq.) was added dropwise to the stirring solvent, which formed a cloudy suspension. **101** (1.6 g, 4.95 mmoles, 1eq.) was added dropwise in methanol (70 mL) over 1.5 hours and the solution stirred at 25 °C for 2 days. The solvent was removed under reduced vacuum. H_2O was added and the product extracted into CH_2CL_2 (3 x 20 mL), dried over $MgSO_4$, filtered and the solvent removed under reduced vacuum to give a white solid 1.2275 g, 88% yield. m.p. 35-37 °C. δ_H ($CDCl_3$, 400 MHz): 3.33 (2H, t, CH_2Br), 2.43 (2H, q, CH_2S), 1.75 (2H, q, CH_2CH_2Br), 1.50 (2H, q, CH_2-CH_2-S), 1.20 (10H, m, CH_2 chain). δ_C ($CDCl_3$, 100 MHz): 33.67 (CH_2), 33.60 (CH_2), 32.38 (CH_2), 29.07 (CH_2), 29.05 (CH_2), 28.97 (CH_2), 28.61 (CH_2), 28.31 (CH_2), 27.93 (CH_2), 27.73 (CH_2), 24.23 (CH_2). ν_{max} (neat sample)/ cm^{-1}: 2914, 2567, 1469.

1-Bromo-12-(12-bromododecyldisulfanyl)dodecane (102) [217]

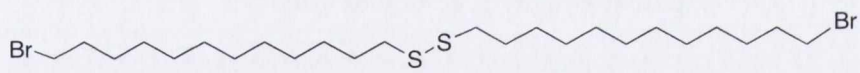

101 (1.23 g, 4.36 mmoles, 1 eq.) was dissolved in CH_2Cl_2 (50 mL) and refluxed overnight with iodine (0.33g, 1.31 mmoles, 0.3 eq.) (catalytic). The resulting solution was washed with H_2O (3 x 20 mL), dried over $MgSO_4$, filtered and the solvent removed under reduced pressure to yield a cream crystalline solid 1.15 g, 47% yield. m.p. 48-50 °C. δ_H ($CDCl_3$, 400 MHz): 3.41 (4H, t, CH_2-Br), 2.68 (4H, t, CH_2-S), 1.84 (4H, m, CH_2-CH_2-S), 1.65 (4H, m, CH_2CH_2S), 1.36(8H, m, CH_2 chain) 1.29 (24H, m, CH_2 chain). δ_C ($CDCl_3$, 100 MHz): 38.72 (CH_2), 33.65 (CH_2), 32.39 (CH_2), 29.09 (CH_2), 29.07 (CH_2), 29.04 (CH_2), 28.99 (CH_2), 28.78 (CH_2), 28.77 (CH_2), 28.32 (CH_2), 28.07 (CH_2), 27.03 (CH_2). ν_{max} (neat sample)/cm^{-1}: 2930, 2849, 1687, 1646, 1542, 1471, 1461, 1353, 1324, 1271, 1220, 1133, 958, 802, 777, 719.

[1,2 bis (dodecyl)-1,4,7,10 tetraazacyclododecane] 12-disulfane (103)[218]

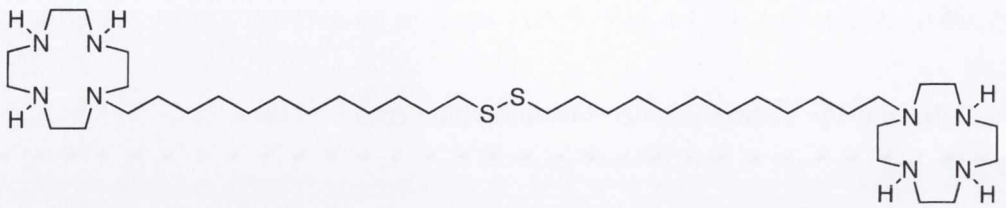

Cyclen (0.44g, 2.55 mmoles, 8 eq.), bromo dodecyl sulfide (0.1787g, 0.319 mmoles, 1 eq.) and Et_3N (0.2576g, 2.55 mmoles, 8 eq.) were dissolved in $CHCl_3$ (30 mL) and stirred at 65°C overnight. H_2O (20 mL) was added to the solution and the product extracted into $CHCl_3$ (2 x 20 mL) and washed with 1M NaOH solution (3 x 20 mL) and again with H_2O (20 mL), dried over $MgSO_4$, filtered and solvent removed to yield a yellow oil 0.1784 g, 0.24 mmoles, 79 %. HRMS (*m/z*-ES+) Found: 743.6529 for $C_{40}H_{86}N_8S_2$, Required: 743.6532; δ_H ($CDCl_3$, 400 MHz) 1.2 (36H, m, disulfide chain), 1.6 (4H, m, CH_2-disulfide chain), 2.33 (40H, m, cyclen and disulfide chain). δ_C ($CDCl_3$, 100 MHz): 54.00 (CH_2), 51.03 (CH_2), 46.52 (CH_2), 45.62 (CH_2), 44.65 (CH_2), 38.67 (CH_2), 29.47 - 26.84 (Chain CH_2). ν_{max} (neat sample)/cm^{-1}: 2925, 2825, 1464, 1352, 1263, 1113, 908, 798, 750, 702.

2 Chloro-*N*-[(1*S*)-(1-naphthalenylethyl)] acetamide (105) [219]

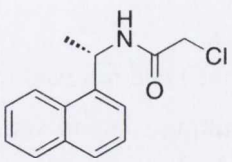

(*S*)-(+)-α-(1-Naphthyl)-ethyl amine (1.0 g, 5.84 mmoles, 1eq) was dissolved in $CHCl_3$ (100 mL) with Et_3N (1.66 mL, 11.7 mmoles, 2 eq.) and cooled to 0° C in an acetone ice bath. Chloroacetyl chloride (0.698 mL, 8.76 mmoles, 1.5 eq.) was added dropwise in $CHCl_3$ to the cooled solution over an hour. After addition the flask was warmed to room temperature and stirred overnight at 25° C. H_2O (50 mL) and the product extracted into $CHCl_3$ (2 x 20 mL) washed with H_2O (20 mL), aqueous citric acid (3 x 20 mL) and then again with H_2O (20 mL), dried over $MgSO_4$, solvent removed under reduced pressure to yield a brown solid, 1.16 g, 80 % yield. HRMS (*m/z*-ES+) Found for $C_{14}H_{14}ClNO$: 270.0662, Required: 270.0662. δ_H ($CDCl_3$, 400 MHz): 8.08 (2H, d J = 8.32 Hz, naphthyl-H). 7.90 (1H, d J =7.8 Hz , naphthyl- H), 7.84 (1H, d, J = 8.0 naphthyl-H), 7.48 (4H, m, Ar-napthyl), 6.83 (1H, bs,

NH) 5.94 (1H, m, CH-NH) 4.05 (2H, q =m, 2H), 1.72 (3H, d, J= 6.8 CH_3). δ_C ($CDCl_3$, 100 MHz) 164.4 (q), 137.0 (q), 133.5 (q), 130.5 (q), 128.5 (CH), 128.2(CH), 126.2(CH), 125.5(CH), 124.8(CH), 122.6(CH), 122.1(CH), 45.2 (CH-NH), 42.1 (CH_2-Cl), 20.8 (CH_3). ν_{max} (neat sample)/cm^{-1} : 3293, 2976, 2876, 1706, 1646, 1601, 1538, 1510, 1454, 1400, 1372, 1341, 1219, 1175, 1117, 1089, 999, 961, 912, 867, 800, 791, 780, 672.

2 chloro-N-[(1R)-(1-naphthalenylethyl)] acetamide (105) [219]

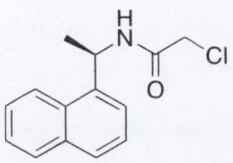

(R)-(-)-α-(1-naphthyl)-ethyl amine (1.0 g, 5.84 mmoles, 1eq) was dissolved in $CHCl_3$ (100 mL) with Et_3N (1.66 mL, 11.7 mmoles, 2 eq.) and cooled to 0° C in an acetone ice bath. Chloroacetyl chloride (0.698 mL, 8.76 mmoles, 1.5 eq.) was added dropwise in $CHCl_3$ to the cooled solution over an hour. After addition the flask was warmed to room temperature and stirred overnight at 25° C. H_2O (50 mL) and the product extracted into $CHCl_3$ (2 x 20 mL) washed with H_2O (20 mL), aqueous citric acid (3 x 20 mL) and then again with H_2O (20 mL), dried over $MgSO_4$, solvent removed under reduced pressure to yield a brown solid, 1.05 g, 73 % yield. HRMS (m/z-ES+) Found for $C_{14}H_{14}ClNO$: 270.0662, Required: 270.0343. δ_H ($CDCl_3$, 400 MHz): 8.08 (d, J = 8.32 Hz, 2H, naphthyl-H). 7.90 (d, J = 7.8 Hz, 1H, naphthyl- H), 7.84 (d, J = 8.0, 1H, naphthyl-H), 7.48 (m, 4H, Ar-naphthyl), 6.83 (bs, 1H, NH) 5.94 (m, 1H, CH-NH) 4.05 (m, 2H, CH_2), 1.72 (d, J = 6.8, 3H, CH_3). δ_C ($CDCl_3$, 100 MHz) 164.4 (q), 137.0 (q), 133.5 (q), 130.5 (q), 128.5 (CH), 128.2 (CH), 126.2 (CH), 125.5 (CH), 124.8 (CH), 122.6 (CH), 122.1 (CH), 45.2 (CH-NH), 42.1 (CH_2-Cl), 20.8 (CH_3). ν_{max} (neat sample)/cm^{-1} : 3293, 2976, 2876, 1706, 1646, 1601, 1538, 1510, 1454, 1400, 1372, 1341, 1219, 1175, 1117, 1089, 999, 961, 912, 867, 800, 791, 780, 672.

(41*S*) 2,2'-(4-(12-mercaptododecyl)-10-(2-(1-(naphthalen-1-yl)ethylamino)-2-oxoethyl)-1,4,7,10-tetraazacyclododecane-1,7-diyl)bis(N-methyl-N-(1-(naphthalen-1-yl)ethyl)acetamide)

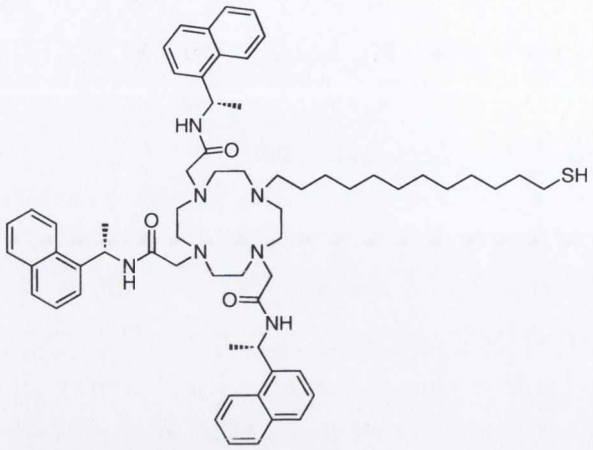

103 (0.126 g, 0.17 mmoles, 1 eq.), KI (0.186 g, 1.12 mmoles, 6.6 eq.), K_2CO_3 (0.155 g, 1.12 mmoles, 6.6 eq.) were dissolved in $CHCl_3$ and cooled to 0 °C followed by slow addition of 2-chloro-*N*-[(*S*)(1-naphthalenylethyl)]-acetamide (0.277 g, 1.12 mmoles, 6.6 eq.) to the solution. The solution was then stirred at 70° C for 7 days followed by reductive cleavage with $NaBH_4$ (0.013 g, 0.34 mmoles, 2 eq.). Removal of solvent followed by washing with acid extraction into $CHCl_3$, basification of the acid layer followed by extraction into $CHCl_3$ and washing with water yielded the product. Column chromatography gradient 95:5 CH_2Cl_2/MeOH separated excess starting material to yield the product as a brown/yellow oil 0.091g, 53 % yield. HRMS Found for $C_{62}H_{84}N_7O_3S$: 1006.6348 Required: 1006.6356; δ_H (DMSO-d_6, 400 MHz): 8.63 (1H, s, NH), 8.26 (Ar-Naph-H), 7.98 (Ar-Naph-H), 7.90(Ar-Naph-H), 7.78 (Ar-Naph-H), 7.50 (Ar-Naph-H), 5.70 (3H, s, CH), 2.60 (16H, m, cyclen CH_2), 1.48 (9H, m, CH_3), 1.19 (24H, m, Chain CH_2). δC (DMSO-d_6, 100 MHz): 169. 6 (q), 140.0 (CH), 133.8 (CH), 130.8 (CH), 129.1 (CH), 127.8 (CH), 126.6 (CH), 126.0 (CH), 125.8 (CH), 123.5 (CH), 122.9 (CH), 53.75 (Cyclen CH_2). ν_{max} (neat sample)/ cm^{-1}: 3273, 3046, 2969, 2925, 2852, 1652, 1512, 1451, 1375, 1305, 1242, 1122, 1037, 1004, 800, 777, 751, 665.

41*S*.Eu

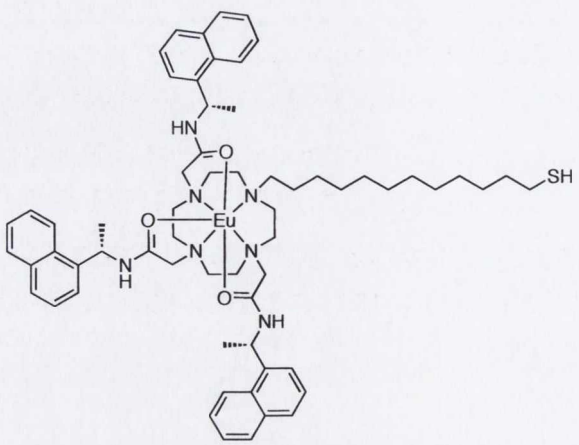

41 (0.019g, 0.019 mmoles, 1eq.) was dissolved in CH_3CN (10 mL) and heated at reflux overnight with $Eu(CF_3SO_3)_3$ (0.012g, 0.02 mmoles, 1.1eq.) followed by precipitation of the complex from ether to yield a yellow oil 0.015 g, 70 % yield.

HRMS: Found 1158.5535 for $C_{62}H_{83}EuN_7O_3S$, Required: 1158.5491; δ_H (MeOD, 400 MHz): 22.74, 21.02, 19.18, 9.44, 8.70, 8.08, 8.02, 7.55, 6.68, 6.4, 6.14, 5.82, 5.48, 4.94, 3.85, 3.80, 3.48, 3.5, 2.50, 0.018, -0.05, -1.39, -1.82, -5.16, -6.84, -7.20, -9.00, -10.26, -0.66, -12.61, -14.5, -19.34, -19.90.. ν_{max} (neat sample)/ cm^{-1}: 3421.9, 3249.9, 3085.9, 3054.9, 2962.9, 2924.9, 2851.6, 1615.7, 1573.8, 1511.9, 1452.9, 1364.9, 1243.6, 1160.7, 1080.8, 1028.6, 957.1, 897.9, 800.8, 777.6, 730.8.

41*R* 2,2'-(4-(12-mercaptododecyl)-10-(2-(1-(naphthalen-1-yl)ethylamino)-2-oxoethyl)-1,4,7,10-tetraazacyclododecane-1,7-diyl)bis(N-methyl-N-(1-(naphthalen-1-yl)ethyl)acetamide)

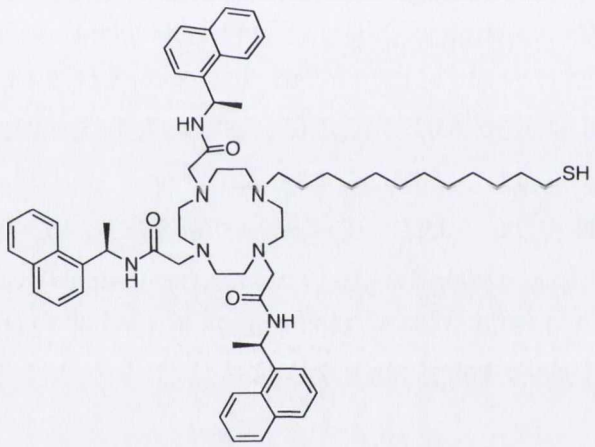

103 (0.2843 g, 0.38 mmoles, 1 eq.), KI (0.415 g, 2.5 mmoles, 6.6 eq.) and K_2CO_3 (0.345 g, 2.5 mmoles, 6.6 eq.) were dissolved in $CHCl_3$ and stirred at 0°C with dropwise addition of **105** (0.625 g, 2.5 mmoles, 6.6 eq.) to the solution. The solution was stirred for 2 weeks at reflux 65 °C, after which $NaBH_4$ (0.029 g, 7.6 mmoles, 2 eq.) was added to the solution and stirred at room temperature overnight. The solution was filtered to remove inorganic salts and extracted with 1M HCl, the aqueous layer was then basified using 1M KOH solution and extracted into $CHCl_3$. The solvent was removed under reduced pressure and the product purified using column chromtography with 95:5 CH_2Cl_2/MeOH gradient to give a brown oil, 0.2749 g, 0.27 mmoles, 72 % yield. HRMS (*m/z*-MALDI) Found: 1005.6278 for $C_{124}H_{164}N_{14}O_6S_2$, Required: 1005.6254. δ_H (DMSO-d_6, 400 MHz): 8.63 (1H, s, NH), 8.26 (Ar-Naph-H), 7.98 (Ar-Naph-H), 7.90(Ar-Naph-H), 7.78 (Ar-Naph-H), 7.50 (Ar-Naph-H), 5.70 (3H, s, CH), 2.60 (16H, m, cyclen CH_2), 1.48 (9H, m, CH_3), 1.19 (24H, m, Chain CH_2). δC (DMSO-d_6, 100 MHz): 169. 6 (q), 140.0 (CH), 133.8 (CH), 130.8 (CH), 129.1 (CH), 127.8 (CH), 126.6 (CH), 126.0 (CH),

125.8 (CH), 123.5 (CH), 122.9 (CH), 53.75 (Cyclen CH_2). ν_{max} (neat sample)/ cm^{-1}: 3264, 3057, 2927, 2853, 1653, 1537, 1513, 1451, 1375, 1239, 1123, 801, 777, 751.

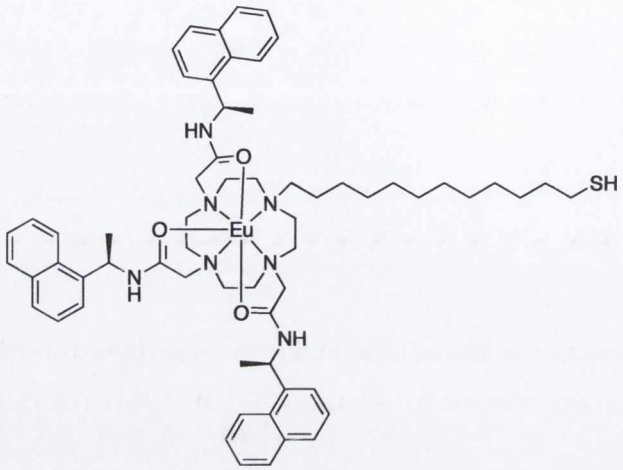

41*R*.Eu

41 (0.1078 g, 0.118 mmoles, 1eq.) was dissolved in 5 mL CH_3CN and refluxed overnight with $Eu(OCF_3SO_3)_3$ (0.706 g, 0.107 mmoles, 1.1 eq.) at 85 °C. Subsequent reduction of solvent to 2 mL and precipitation from swirling ether yielded the product as a yellow oil 0.114 g, 86 % yield. HRMS *(m/z*-ES+) Found for $C_{62}H_{83}EuN_7O_3S$: 1158.5491, Required: 1158.5535; δ_H (MeOD, 400 MHz): 22.01, 20.11, 19.43, 9.51, 9.17, 9.01, 8.80, 8.46, 8.31, 8.13, 7.89, 7.81, 7.48, 7.36, 6.94, 6.81, 6.71, 6.64, 6.36, 6.03, 5.95, 5.69, 5.51, 4.94, 4.15, 4.03, 3.62, 3.58, 3.49, 3.36, 3.32, 3.15, 3.06, 2.86, 2.69, 2.68, 2.66, 2.44, 2.30, 1.66, 1.40, 1.34, 1.04, 0.88, 0.11, 0.009, -0.24, -0.51, -1.00, -1.38, -1.85, -2.40, -4.56, -4.76, -5.25, -5.46, -7.35, -7.66, -9.45, -9.98, -10.66, -11.59, -12.53, -15.04, -18.40, -19.65. ν_{max} (neat sample)/ cm^{-1}: 3282.7, 3083.8, 2924.8, 2852.9, 1617, 1573.8, 1511.9, 1453.8, 1375.0, 1262.0, 1241.0, 1223.0, 1157.0, 1081.8, 1027.4, 957.0, 899.9, 800.7, 778.6, 720.0.

1-dodecyl-1,4,7,10-tetraazacyclododecane (107)

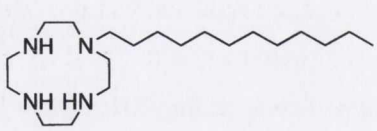

Cyclen (0.5 g, 2.90 mmoles, 4 eq.) and Et_3N (0.294 g, 2.9mmoles, 4 eq.) were dissolved in $CHCl_3$ followed by slow addition of bromododecane (0.181 g, 0.725 mmoles, 1 eq) at 0° C. Refluxing overnight at 65° C followed by washing with NaOH (0.1 M) and H_2O, dried over $MgSO_4$, filtered and solvent removed under reduced vacuum to yield a yellow oil 0.336 g, 49 % yield. HRMS (*m/z*-ES+) Found for $C_{20}H_{45}N_4$: 341.3639, Required: 341.3644; δ_H (400 MHz, $CDCl_3$): 2.38 (16H, br m, Cyclen), 1.44 (2H, d, J = 6.52 Hz, CH_2), 1.35 (18H, CH_2, Chain), 0.86 (3H, t, J = 6.52 Hz, CH_3). δC ($CDCl_3$, 400 MHz): 56.1 (CH_2), 53.9 (CH_2), 51.2 (CH_2), 50.7 (CH_2), 48.2 (CH_2), 48.1 (CH_2), 47.9 (CH_2), 46.2 (CH_2), 45.2 (CH_2), 44.4 (CH_2), 31.5 (CH_2), 29.23 (CH_2), 29.21 (CH_2), 28.9 (CH_2), 27.0 (CH_2), 26.9 (CH_2), 26.5

(CH_2), 26.3 (CH_2), 22.2 (CH_2), 13.7 (CH_3); ν_{max} (neat sample)/ cm^{-1}: 3378, 3334, 2920, 2850, 2350, 1647, 1537, 1465, 1405, 1346, 1281, 1216, 1109, 1067, 1028, 930, 897, 793, 765, 720, 659.

2,2'-(4-dodecyl-10-(2-(1-(naphthalen-1-yl)ethylamino)-2-oxoethyl)-1,4,7,10-tetraazacyclododecane-1,7-diyl)bis(N-methyl-N-(1-(naphthalen-1-yl)ethyl)acetamide) (106)

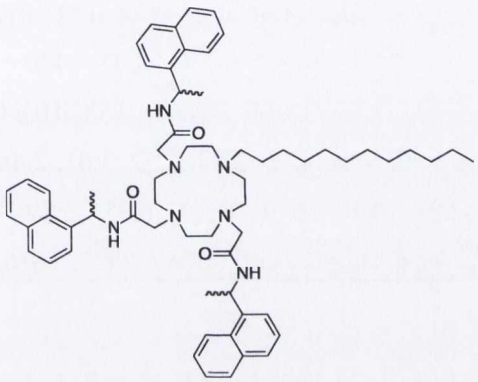

107 (0.1151g, 0.338 mmoles, 1eq), KI (0.186g, 1.12 mmoles, 3.3eq) K_2CO_3 (0.155g, 1.12 mmoles, 3.3 eq.) were dissolved in CH_3CN (30 mL) cooled to 0° C. (S)-(+)-α-(1-naphthyl)-acetamide (0.278g, 1.12 mmoles, 3.3eq) was added slowly drop wise and subsequently refluxed for 7 days at 85 °C. The solution was then filtered through celite to remove inorganic salts and the solvent removed. The product was extracted with $CHCl_3$ washed with KOH and H_2O dried over $MgSO_4$, filtered and solvent removed under reduced vacuum to yield a brown oil 0.1092g in 33 % yield. HRMS (*m/z*-ES^+): Found for $C_{62}H_{83}N_7O_3Na$: 996.6447, Required: 996.6455; δ_H: 7.33-8.40 (br m, 21H, naphthyl CH), 5.80 (s, 3H, CH), 2.38-3.47 (m, 20H, Cyclen CH_2), 1.64-1.68 (m, 8H, CH_2), 1.13- 1.34 (m, 16H, Chain CH_2), 0.85-0.89 (m, 9H, CH_3). δ_C ($CDCl_3$, 100 MHz): 170.2 (q), 169.0 (q), 140.0 (q), 139.3 (q), 133.7(q), 133.6 (q), 127.7 (CH), 126.3 (CH), 126.2 (CH), 125.7 (CH), 125.6 (CH), 125.5 (CH), 123.4 (CH), 123.1 (CH), 58.2 (CH_2), 57.7 (CH_2), 53.9 (CH_2), 53.6 (CH_2), 53.4 (CH_2), 52.5 (CH_2), 51.6 (CH_2), 50.1 (CH_2), 44.7(CH) 31.9 (CH_2) 29.3 (Cyclen CH_2) 26.6 (CH_2) 22.7 (CH_2) 21.3 (CH_3), 14.1 (CH_3). ν_{max} (neat sample)/ cm^{-1}: 3196, 3046, 2924, 2852, 1649, 1597, 1543, 1511, 1449, 1396, 1375, 1263, 1238, 1178, 1121, 1087, 1031, 1002, 950, 860, 799, 777, 730, 699.

106*R*.Eu

106 (0.060 g, 0.062 moles, 1 eq.) was dissolved in CH_3CN with 1.1 eq of europium triflate

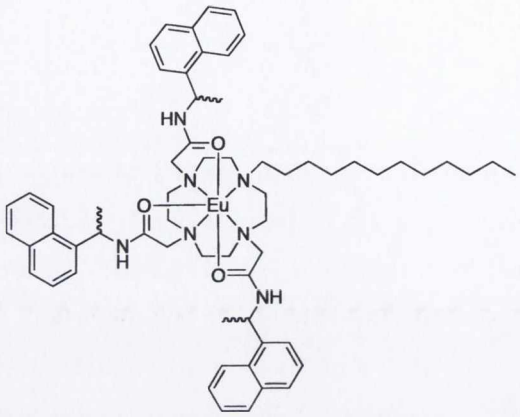

(0.041 g, 0.068 mmoles, 1.1 eq.) and refluxed overnight. The reaction mixture was reduced to 2 mL under reduced pressure and precipitated out of ether (100 mL) to yield a yellow oil 0.016 g, 23 % yield. HRMS (m/z-ES+) Found for $C_{62}H_{83}N_7O_3NaEu$: 1124.5651, Required: 1124.5613; δ_H (MeOD, 400 MHz): 25.53, 22.24, 20.60, 19.53, 10.64, 9.96, 8.70, 8.46, 8.03, 7.81, 7.57, 7.50, 6.66, 6.35, 5.86, 5.34, 4.20, 3.84, 3.52, 3.01, 2.49, 1.61, 1.29, 1.07, 0.92, -0.20, -1.27, -2.06, -2.45, -3.38, -4.10, -5.01, -6.17, -6.45, -6.89, -7.20, -8.15, -8.65, -9.9, -12.11, -13.24, -20.68; ν_{max} (neat sample)/ cm^{-1}: 3269, 2927, 1616, 1454, 1238, 1164, 1082, 1027, 959, 801, 778.

N-[(1*S*)-1-(1-Naphthalenyl)ethyl] 1,4,7,10 tetraazacyclododecane-1-acetamide (108)[219]

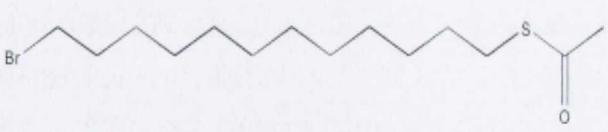

Cyclen (1.625 g, 9.43 mmoles, 4.1 eq) and Et_3N (0.279g, 2.76 mmoles, 1.2 eq) were dissolved in $CHCl_3$ cooled and 2 chloro-N-[(1S)-(1-naphthalenylethyl)] acetamide (0.57g, 2.3 mmoles, 1 eq) added slowly and the reaction mixture refluxed at 65° C overnight. H_2O added to the reaction mixture and the product extracted into $CHCl_3$ (2 x 15 mL) washed with H_2O (15 mL) and 1M NaOH (3 x 20 mL) and then again with H_2O (15 mL), dried over $MgSO_4$ filtered and the solvent removed under reduced pressure to isolate the desired product as a brown oil, quantitative yield. HRMS (m/z-ES+) Found for $C_{22}H_{34}N_5O$: 384.2755 Required 384.2763. δ_H ($CDCl_3$, 400 MHz): 8.06 (1H, d, Naphthyl), 8.5 (1H, d, NH), 7.79 (2H, m, Naphthyl), 7.48 (4H, m, Naphthyl), 5.90 (1H, t, CHNH), 3.13 (4H, q, CH_2), 2.21 (16H, m, Cyclen, CH_2), 1.71 (3H, d, CH_3). δ_C ($CDCl_3$, 100 MHz): 170.2 (q), 137.8 (q), 133.2(q),

130.9 (q), 128.2 (CH), 127.7 (CH), 126.1 (CH), 125.5 (CH), 124.8 (CH), 123.2 (CH), 122.5 (CH), 58.7 (CH_2), 53.0 (CH_2), 46.5 (CH_2), 46.3 (CH_2), 45.8 (CH_2), 45.3 (CH_2), 43.6 (CH_2), 19.6 (CH_3), 11.2 (CH). ν_{max} (neat sample)/cm^{-1}: 3236, 3047, 2932, 2834, 1650, 1597, 1544, 1510, 1449, 1398, 1373, 1263, 1179, 1060, 939, 801, 778, 699, 660.

(**42*S***)

2,2'-(4-(12-mercaptododecyl)-10-(2-(1-(naphthalen-1-yl)ethylamino)-2-oxoethyl)-1,4,7,10-tetraazacyclododecane-1,7-diyl)bis(N,N-dimethylacetamide) (42)

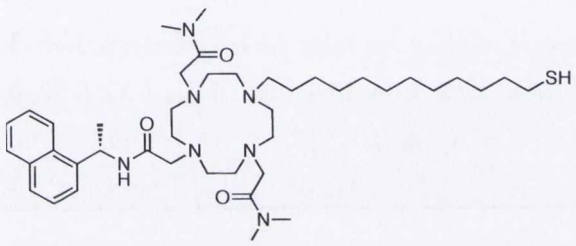

108 (0.50 g, 1.3 mmoles, 2 eq.) was dissolved in $CHCl_3$ in the presence of Et_3N (0.18 mL, 1.3 mmoles, 2 eq.) and **102** (0.36 g, 0.65 mmoles, 1 eq.) was added slowly dropwise and stirred for four days at reflux 85 °C. The solution was then washed with 1 M KOH solution (2 x 10 mL) and H_2O (2 x 10 mL), dried over $MgSO_4$, filtered and the solvent removed under reduced pressure to yield a brown oil, which was purified on column chromatography (CH_2Cl_2/ MeOH) to yield **109** as a yellow oil. This was used without further purification as an intermediate and was dissolved in CH_3CN and (*S*)-(+)-α-Chloro-*N,N*-dimethyl acetamide (0.31 g, 2.6 mmoles, 4 eq.) added slowly dropwise in the presence of K_2CO_3 (0.36 g, 2.6 mmoles, 2 eq.) and KI (0.43 g, 2.6 mmoles, 4 eq.). The resulting solution was refluxed for 1 week after which $NaBH_4$ (0.0098 g, 2.6 mmoles, 2 eq.) was added and stirred overnight. The solvent was removed under reduced vacuum and the product dissolved in $CHCl_3$ and washed with H_2O (5 x 10 mL). Column chromatography with 95:5 CH_2Cl_2/MeOH was carried out on the reulting oil and size exclusion chromatography yielded the product 0.025 g, 5 % yield. HRMS (m/z-ES+) Found for $C_{42}H_{71}N_7O_3SNa$: 776.5214: Required: 776.5237; δ_H ($CDCl_3$, 400 MHz) 8.11 (1H, m, Ar-H), 7.67 (3H, m, Ar-H), 7.46 (4H, m, Ar-H), 5.90 (1H, s, CH), 2.66 (34H, br m, Cyclen and arm CH_2), 1.59 (9H, m, CH_2) 1.27 (29H, m, CH_3 and CH_2). δ_C ($CDCl_3$, 100 MHz): 172.2 (q), 171.6 (q), 134.5 (CH), 129.0 (CH), 128.9 (CH), 127.5 (CH), 126.3 (CH), 125.7 (CH), 123.1 (CH), 122.5 (CH), 57.1, 55.2 (CH_2), 55.20 (CH_2), 54.6 (CH_2), 48.8 (CH_2), 45.2 (CH_2), 35.5 (CH_2), 35.0 (CH_2), 34.8 (CH_2), 34.7 (CH_2), 29.6 (CH_2), 29.3 (CH_3), 29.2 (CH_2), 28.4 (CH_2). ν_{max} (neat sample)/ cm^{-1}: 3284, 2962, 2926, 2847, 1723, 1644, 538, 1510, 1448, 1398, 1298, 1259, 1101, 1062, 1022, 946, 902, 864, 800, 781, 759, 701, 662.

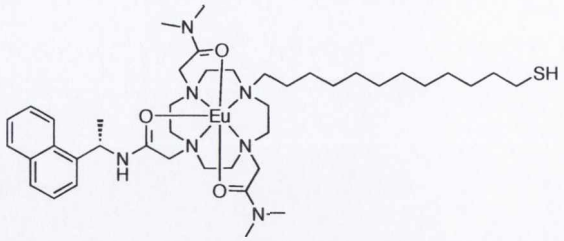

(42*S*.Eu)

42*S* (0.043 g, 0.057 mmoles, 1eq.) was refluxed in CH_3CN with 1.1eq of $Eu(OCF_3SO_3)_3$ (0.038 g 0.063 mmoles, 1.1 eq.) overnight. The solvent was reduced to 2 mL under reduced pressure and precipitated out of swirling ether (100 mL) to yield a yellow oil, 0.23 g, 45 % yield. δ_H (MeOD, 400 MHz): 11.81, 10.01, 9.59, 8.34, 8.13, 7.92, 7.83, 7.54, 6.51, 6.17, 5.90, 5.51, 4.92, 4.38, 3.79, 3.66, 3.56, 3.49, 3.32, 3.24, 3.22, 3.15, 3.03, 2.99, 2.69, 2.17, 2.03, 1.69, 1.55, 1.41, 1.33, 0.92, 0.45, 0.28, 0.11, -0.34, -1.04, -1.41, -1.79, -2.76, -5.79, -6.41, -7.17, -12.67, -13.29, -13.76, -14.57, -16.16, -16.39; ν_{max} (neat sample)/ cm^{-1}: 3382.0, 2945.6, 1620.7, 1265.1, 1171.5, 1028.4, 743.1, 704.7.

2,2'-(4-(2-(1-(naphthalen-1-yl)ethylamino)-2-oxoethyl)-10-tridecyl-1,4,7,10-tetraazacyclododecane-1,7-diyl)bis(N,N-dimethylacetamide) (42)

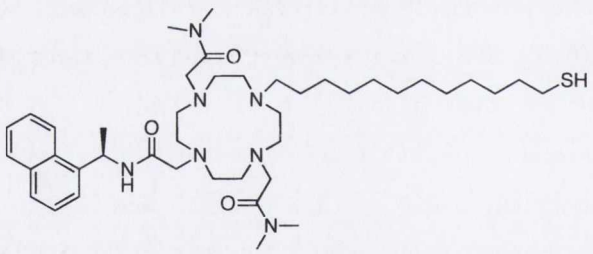

103 (0.157 g, 0.21 mmoles, 1eq.) was dissolved in dry CH_3CN (100 mL) in an RBF with addition of K_2CO_3 (0.064 g, 0.464 mmoles, 2.2 eq.) followed by slow addition of (R)-(-)-α-(1-naphthyl)-acetamide (0.105 g, 0.423 mmoles, 2 eq.). The mixture was stirred for 2 days at 65 °C, after which K_2CO_3 (0.10 g, 0.84 mmoles, 4 eq.) and KI (0.14 g, 0.84 mmoles, 4 eq.) were added followed by slow addition of (R)-(-)-α-Chloro-*N,N*-dimethyl acetamide (0.105 g, 0.42 mmoles, 2. eq.) and stirred for a further 8 days at 65 °C. The reaction mixture was filtered through a plug of celite and the solvent removed under reduced pressure. The resulting residue was dissolved in $CHCl_3$ and washed with 1 M HCl, then basified to pH 10 with 1 M KOH and extracted into $CHCl_3$ to give a yellow oil 0.024 g in 15 % yield. HRMS (*m/z*-ES+) Found for $C_{42}H_{71}N_7O_3S$: 753.5369, Required: 753.5339. δ_H ($CDCl_3$, 400 MHz): 8.11 (1H, m, Ar-H), 7.67 (3H, m, Ar-H), 7.46 (4H, m,

Ar-H), 5.90 (1H, s, CH), 2.66 (34H, br m, Cyclen and arm CH_2), 1.59 (9H, m, CH_2) 1.27 (29H, m, CH_3 and CH_2). δ_C ($CDCl_3$, 100 MHz) 172.2 (q), 171.6 (q), 134.5 (CH), 129.0 (CH), 128.9 (CH), 127.5 (CH), 126.3 (CH), 125.7 (CH), 123.1 (CH), 122.5 (CH), 57.1 (CH_2), 55.2 (CH_2), 55.20 (CH_2), 54.6 (CH_2), 48.8 (CH_2), 45.2 (CH_2), 35.5 (CH_2), 35.0 (CH_2), 34.8 (CH_2), 34.7 (CH_2), 29.6 (CH_2), 29.3(CH_3), 29.2 (CH_2), 28.4 (CH_2). ν_{max} (neat sample)/ cm^{-1} 2929.2, 1654.1, 1421.5, 1264.6, 895.8, 743, 703.63.

42R.Eu

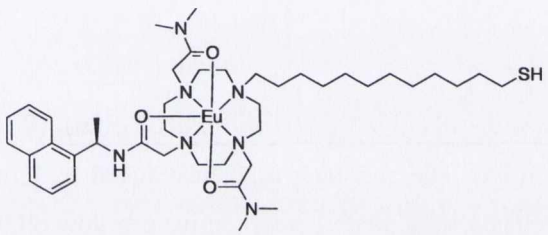

42*R* (0.114g, 0.15 mmoles, 1eq.) was dissolved in acetonitrile (20 mL) and refluxed overnight with $Eu(CF_3SO_3)_3$ (0.0966g, 0.166 mmoles, 1.1eq) at 85°C after which the formation of a clear yellow solution was observed. Subsequent reduction of solvent to 2 mL followed by precipitation out of swirling ether yielded the product as a yellow oil, 0.1712 g, quantitative yield. δ_H (MeOD, 400 MHz): 11.81, 10.01, 9.59, 8.34, 8.13, 7.92, 7.83, 7.54, 6.51, 6.17, 5.90, 5.51, 4.92, 4.38, 3.79, 3.66, 3.56, 3.49, 3.32, 3.24, 3.22, 3.15, 3.03, 2.99, 2.69, 2.17, 2.03, 1.69, 1.55, 1.41, 1.33, 0.92, 0.45, 0.28, 0.11, -0.34, -1.04, -1.41, -1.79, -2.76, -5.79, -6.41, -7.17, -12.67, -13.29, -13.76, -14.57, -16.16, -16.39. ν_{max} (neat sample)/ cm^{-1}: 3310, 2942, 2831, 1448, 1272, 1114, 1023, 737.

110*R*

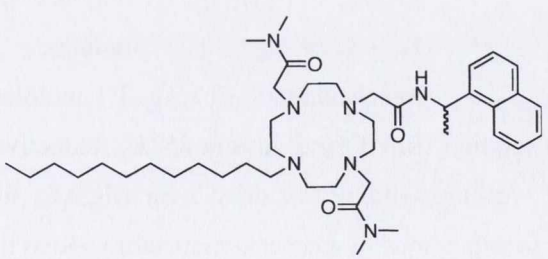

107 (0.129 g, 0.38 mmoles, 1 eq.), K_2CO_3 (0.058 g, 0.42 mmoles, 1.1eq.), KI (0069 g, 0418 mmoles, 1.1 eq.) were dissolved in CH_3CN (50 mL). (R)-(-)-α-Chloro-*N,N*-dimethyl acetamide (0.103 g, 0.418 mmoles, 1.1 eq.) was added slowly and the solution refluxed at 85 °C. After 2 days K_2CO_3 (0.11g, 0.76 mmoles, 2 eq.) KI (0.126 g, 0.76 mmoles, 2 eq.) and α-chloro-*N,N*-dimethylacetamide (0.092 g, 0.76 mmoles, 2.2 eq.) were added and stirred for a further 5 days after which the mixture was filtered through a plug of celite, solvent removed extracted with $CHCl_3$,

washed with a 1M solution of KOH and water, dried over $MgSO_4$, filtered, solvent removed to yield the product as a yellow oil, 0.22 g, 80 % yield. HRMS (m/z-ES^+) Found 722.5695 for $C_{42}H_{71}N_7O_3$, Required: 722.5697. δH ($CDCl_3$, 400 MHz): 7.44-8.37 (m, 7H, CH-naphthyl), 5.91 (s, 1H, CH), 1.90-3.39 (m, Cyclen and CH_2), 1.65 (CH_2), 1.27 (CH_2 chain, CH_3), 0.891 (CH_3). δC ($CDCl_3$, 100 MHz): δ_C ($CDCl_3$, 100 MHz): 170.2 (q), 169.0 (q), 140.0 (q), 139.3 (q), 133.7(q), 127.7 (CH), 126.2 (CH), 125.6 (CH), 125.5 (CH), 123.4 (CH), 123.1 (CH), 58.2 (CH_2), 57.7 (CH_2), 53.9 (CH_2), 53.6 (CH_2), 53.4 (CH_2), 52.5 (CH_2), 51.6 (CH_2), 50.1 (CH_2), 44.7(CH) 31.9 (CH_2) 29.3 (Cyclen CH_2) 26.6 (CH_2) 22.7 (CH_2) 21.3 (CH_3), 14.1 (CH_3). ν_{max} (neat sample)/ cm^{-1}: 3227, 3048, 2923, 2852, 1645, 1511, 1453, 1399, 1262, 1239, 1209, 1178, 1102, 1059, 1038, 1003, 958, 905, 860, 801, 777, 750, 666.

110*R*.Eu

110*R* (0.20 g, 0.28 mmoles, 1 eq.) was dissolved in MeOH with $Eu(CF_3SO_3)_3$ (0.18 g, 0.30 mmoles, 1.1 eq.) and refluxed overnight. The solvent was then reduced to 1 mL under reduced pressure and precipitated from swirling diethyl ether to give a yellow oil, 0.19 g in 81% yield. HRMS (m/z- MALDI) Found: 1022.4272 for $C_{43}H_{70}N_7O_6F_3SEu$, Required: 1022.4273; δH: 24.3, 20.5, 14.2, 8.9, 7.7, 4.9, 3.3, 1.5, -1.2, -2.1, -4.1, -5.5, -6.0, -8.2, -9.8, -10.4, -11.7, -17.7, -21.7. ν_{max} (neat sample)/ cm^{-1}: 3316, 2926, 1618, 1222, 1161, 1081, 1026, 901, 778.

2,2',2''-(10-(12-mercaptododecyl)-1,4,7,10-tetraazacyclododecane-1,4,7-triyl)triacetamide (43)

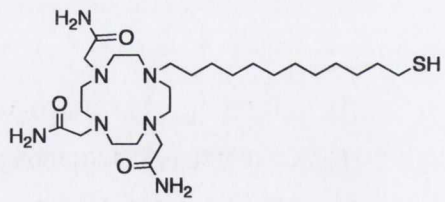

Dodecanyl tetraazacyclododecane (0.2468 g, 0.332 mmoles, 1eq.) was dissolved in CH_3CN with K_2CO_3 (0.151 g, 1.1 mmoles, 3.3 eq.) and KI (0.176 g, 1.1 mmoles, 3.3 eq.). Bromoacetamide (0.15 g, 1.1 mmoles, 3.3 eq.) was added to the solution and the solution stirred for 5 days at 85 °C. Reductive cleavage with $NaBH_4$ (2eq.), followed by washing with water, dried over $MgSO_4$, filtered and solvent removed followed by two precipitations in ether and methanol yielded the product as a yellow clear oil 0.090 g, 51% yield. HRMS (*m/z*-ES+) Found for $C_{26}H_{54}N_7O_3S$: 544.4026, Required 544.4009; δ_H (MeOD, 400 MHz): 3.26 (CH_2), 3.18 (CH_2), 3.02 (CH_2), 1.70 (CH_2), 1.51 (CH_2), 1.30 (CH_2 chain). δ_C (MeOD, 100 MHz): 175.7(q), 175.1(q), 169.3 (), 160.3, 56.8 (Cyclen CH_2), 56.5 (Cyclen CH_2), 54.6 (Cyclen CH_2), 54.4 (CH_2),

51.3(CH_2), 51.2 (CH_2), 50.7 (CH_2), 50.1 (CH_2), 38.8 (CH_2), 29.8 (CH_2), 29.7 (CH_2), 29.6 (CH_2), 29.64 (CH_2), 29.58 (CH_2), 29.3 (CH_2), 29.2 (CH_2), 29.1 (CH_2), 28.4 (CH_2), 28.3 (CH_2), 27.9 (CH_2), 27.8 (CH_2), 25.2 (CH_2), 7.1 (CH_2). ν_{max} (neat sample)/ cm^{-1}: 3361, 3314, 3170, 2924, 2853, 2820, 1697, 1680, 1446, 1371, 1332, 1284, 1256, 1102, 1008, 907, 811, 722, 675.

General Procedure for the synthesis of 43.Ln

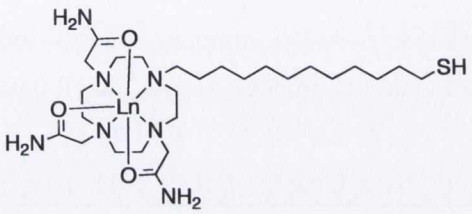

43 was dissolved in MeOH with 1.1 eq. of Ln $(CF_3SO_3)_3$ and refluxed overnight under argon. Solvent was removed under reduced pressure and the resulting residue was precipitated out of swirling diethyl ether to yield xx.Ln as yellow oils.

43.Gd

43 (0.016 g, 0.0294 mmoles, 1 eq.) was refluxed in MeOH with $Gd(CF_3SO_3)_3$ (0.019 g, 0.032 mmoles, 1.1 eq.) to give a yellow oil, 0.0398 g, 47 % yield. HRMS (MALDI): Found 1186.14 for [**43.Gd** + $(CF_3SO_3)_3$ + K^+] Calculated: 1186.6786. ν_{max} (neat sample)/ cm^{-1}: 3350, 3334, 2924, 2853, 1659, 1621, 1457, 1367, 1272, 1246, 1166, 1085, 1029, 915, 878, 834, 766, 720, 650.

43.Eu

1 (0.016 g, 0.0294 mmoles, 1eq.) was refluxed in MeOH with $Eu(CF_3SO_3)_3$ (0.019g, 0.0324 mmoles, 1.1eq.) to yield 0.0157 g, 77 % yield. δ_H (MeOD, 400 MHz): -17.4, -15.35, -13.89, -11.6, -10.3, -8.7, -8.09, -7.8, -6.9, -5.5, -4.90, -3.05, -1.35, 0.29, 0.90, 1.34, 1.69, 2.02, 2.16, 2.70, 3.01, 3.14, 3.32, 3.35, 3.49, 3.63, 3.64, 3.69, 3.75, 4.05, 4.94, 5.5, 6.4, 8.1, 9.83, 13.53, 17.32, 18.45. ν_{max} (neat sample)/ cm^{-1}: 3353, 3187, 2928, 2856, 1660, 1597, 1466, 1248, 170, 1083, 1028, 918, 832.

43.Lu

43 (0.028 g, 0.05 mmoles, 1 eq.) was dissolved in CH_3CN (10 mL) and the solution stirred with slow addition of $Lu(CF_3SO_3)_3$ (0.035 g, 0.056 mmoles, 1.1 eq.) to the solution

followed by heating at reflux overnight. The solvent was reduced to 1 mL and the product precipitated out of ether to yield the product as a yellow oil 0.033 g, 92 % yield. δ_H (MeOD, 400 MHz): 3.86, 3.68, 3.48, 3.32, 3.19, 3.04, 2.99, 2.90, 2.83, 2.68, 2.20, 1.98, 1.69, 1.41, 1.30, 1.14; ν_{max} (neat sample)/ cm^{-1}: 3385, 3322, 3255, 2929, 2859, 1672, 1603, 1469, 1226, 1171, 1081, 1028, 917, 884, 837, 764.

43.Tb

43 (0.029g, 0.0537 mmoles, 1eq.) was dissolved in CH_3CN (20 mL) and stirred under reflux overnight with $Tb(CF_3SO_3)_3$ (0.0358 g, 0.059 mmoles, 1.1eq.) followed by precipitation from swirling diethyl ether to yield the product as a yellow oil 0.0353g, 93.5 % yield. δ_H (MeOD, 400 MHz): -155.1, -141.7, -116.1, -85.34, -55.9, -24.15, -15.0, -14.4, -13.7, -10.28, -9.6, -5.40, -2.77, -2.73, -1.46, -0.47, 0.04, 0.19, 0.49, 0.99, 1.19, 1.38, 1.49, 2.09, 2.31, 2.49, 3.33, 3.78, 4.85, 7.01, 15.52 302.6, 304.6, 306.0. ν_{max} (neat sample)/ cm^{-1}: 3348, 3174, 2927, 2855, 1657, 1596, 1463, 1249, 1173, 1081, 1029, 919, 833.

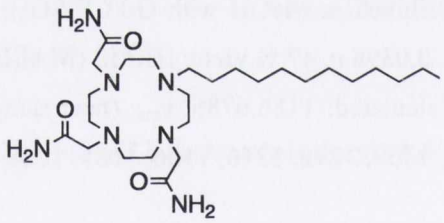

2,2',2"-(10-dodecyl-1,4,7,10-tetraazacyclododecane-1,4,7-triyl)triacetamide **(111)**

107 (0.336 g, 0.98 mmoles, 1eq.) was dissolved in $CHCl_3$ with K_2CO_3 (0.45 g, 3.3 mmoles, 3.3 eq.) and KI (0.541 g, 3.3 mmoles, 3.3 eq.) and stirred with addition of bromoacetamide (0.45 g 3.2 mmoles, 3.3 eq.) at 0 °C. The mixture was stirred for 7 days at 65 °C before filtration through a plug of celite and removal of solvent. Extraction into $CHCl_3$ followed by washing with base, dried over $MgSO_4$, filtered and solvent removed under reduced pressure, yielded a white solid 0.0751 g, 15 % yield. HRMS (m/z-MALDI) Found for $C_{27}H_{55}N_3O_3$: 534.4103, Required: 534.4108; δ_H (MeOD, 400 MHz): 8.39 (1H, s, NH_2), 8.02 (2H, s, NH_2), 7.11 (1H, s, NH_2), 6.17 (1H, s, NH_2), 5.96 (2H, s, NH_2), 5.48 (2H, s, NH_2), 3.06 (6H, m, CH_2) 2.34 - 2.69 (16H, m, Cyclen), 1.28 (22H, m, CH_2), 0.89 (3H, m, CH_3). δ_C (MeOD, 100 MHz): 77.5 (CH_2). 77.2 (CH_2), 77.2 (CH_2), 77.1 (CH_2), 50.3 (CH_2), 50.0 (CH_2), 49.8 (CH_2), 49.6 (CH_2), 49.4 (CH_2), 49.3 (CH_2), 49.0 (CH_2), 31.9 (CH_2), 29.6 (CH_2), 29.5 (CH_2), 22.6 (CH_2), 14.1 (CH_2). ν_{max} (neat sample)/ cm^{-1}: 3356, 3257, 3167, 2919 (sharp), 2849, 1673, 1449, 1404, 1360, 1348, 1294,

1261, 1202, 1152, 1116, 1087, 1068, 1046, 1032, 1002, 979, 959, 923, 880, 803, 718, 669. CHN: Observed for C: 57.83, H: 9.98, N: 17.81 calculated C: 61.02 H: 10.44 N: 19.16.

General procedure for synthesis of 111.Ln

111 was dissolved in MeOH and $Ln(CF_3SO_3)_3$ added to the mixture slowly. The solution was then refluxed overnight followed by reduction of the solvent to 1 mL under reduced pressure and precipitation out of swirling diethyl ether, which yielded the product as a yellow oil.

111.Eu

111 (0.0144 g, 0.028 mmoles, 1 eq.) and $Eu(CF_3SO_3)_3$ (0.0185 g, 0.031 mmoles, 1.1 eq.) 0.0097 g, 52 % yield. HRMS (m/z-MALDI) Found for $C_{27}H_{52}N_7O_6F_3SEu$, 812.2834, Required: 812.2864; δ_H (MeOD, 400 MHz): 23.90, 21.56, 19.87, 19.09, 8.15, 7.92, 4.92, 3.69, 3.66, 3.49, 3.32, 3.05, 2.78, 2.66, 2.54, 2.05, 1.30, 0.92, 0.10, -.47, -1.19, -1.42, -1.70, -2.30, -2.60, -5.04, -5.44, -6.36, -7.95, -8.44, -9.17, -9.67, -11.24, -11.49, -12.01, -13.79, -16.97, -18.01, -18.66; ν_{max} (neat sample)/ cm^{-1}: 3357, 2926, 2856, 1666, 1600, 1467, 1235, 1217, 1165, 1082, 1025, 914, 880, 831, 762.

111.Gd

111 (0.0642 g, 0.125 mmoles, 1eq.) with $Gd(CF_3SO_3)$ (0.0462 g, 0.138 mmoles, 1.1 eq.) yielded a white oily solid, 0.398 g, 47 % yield. HRMS (*m/z*-ES+) Found for $C_{27}H_{52}N_7O_6F_3SGd$ 669.3474, Required: 669.3451. ν_{max} (neat sample)/ cm^{-1}: 3367, 2930, 2856, 1603, 1467, 1237, 1217, 1164, 1079, 1025, 917, 880, 829, 764.

AuNPs

General Procedure: Tetrachloroaurate trihydrate was dissolved in Millipore water and stirred vigorously on addition of toluene containing tetraoctylammonium bromide (TOAB). The mixture was stirred vigorously at room temperature for 10 mins followed by addition of $NaBH_4$ slowly. The mixture was then stirred at room temperature for 2 hours. On cessation of stirring the product separated into the toluene layer as a dark purple solution. The product was extracted into toluene, washed with 0.1 M HCl, and 0.1 M NaOH followed by washing with H_2O. UV-vis absorption spectrum showed the characteristic SPR band of the **AuNPs** at 530 nm.

Eu.AuNP –General Synthesis

A 1 x 10^{-3} solution of complex in $MeOH/H_2O$ was stirred vigorously on addition of toluene solution of nanoparticulate gold. The resulting water layer upon transfer of the gold to the complex solution turned deep purple showing stabilisation by the complex of the nanoparticle in the aqueous layer. The layers were then separated and the aqueous layer filtered through a 0.2 μm pore syringe filter in order to remove possible aggregates. The resulting pink / purple solution (colour dependent on concentration of gold) contained the stabilized nanoparticles and the SPR in the UV-vis absorption spectrum could be seen to shift to approximately 520 nm.

References

6.0 References

1. (a) Matsumoto, K., Yuan, J., *Metal Ions in Biological Systems*. New York, 2003, Vol. 40; (b) Faulkner, S., Pope, S. J. A., Burton-Pye, B. P., *Appl. Spectrosc. Rev.* **2005,** *41* (1); (c) Kido, J., Okamoto, Y. , *Chem. Rev.* **2002,** *102*, 2357.
2. (a) Harte, A. H., Trinity College Dublin, 2005; (b) Murray, N. S., Trinity College Dublin, 2008.
3. Bunzli, J.-C. G., Piguet, C., *Chem. Soc. Rev.* **2005,** *34*, 1048.
4. (a) Bunzli, J.-C., *Acc. Chem. Res.* **2006,** *39*, 53; (b) Cotton, S., *Lanthanides and Actinides*. 1991.
5. Piguet, C., Bunzli, J-C., *Chem. Soc. Rev.* **1999,** *28*, 347.
6. Binnemans, K., *Chem. Rev.* **2009,** *109*, 4283.
7. Parker, D., Dickins, R. S., Puschmann, H., Crossland, C., Howard, J. A. K., *Chem. Rev.* **2002,** *102*, 1977.
8. Beer, P. D., Dent, S. W., West, T. J., *J. Chem. Soc. Dalton Trans.* **2001**, 2341.
9. Bunzli, J.-C. G., Comby, S., Chauvin, A-S., Vandevyer, C. D. B., *J. Rare Earth.* **2007,** *25*, 257.
10. Parker, D., Williams, J. A. G., Marcel Dekker Inc.: New York, 2003; Vol. 40.
11. Dos Santos, C. M. G., Harte, A. J., Quinn, S. J., Gunnlaugsson, T., *Coord. Chem. Rev.* **2008,** *252*, 2512.
12. Forster, T., *Discuss Faraday Soc.* **1959,** *27*, 7.
13. Dexter, D., *J. Phys. Chem.* **1953,** *21*, 836.
14. (a) Horrocks, W. D. J., Sudnick, D. R., *J. Am. Chem. Soc.* **1979,** *101*, 334; (b) Horrocks, W. D. J., Sudnick, D. R., *Acc. Chem. Res.* **1981,** *14*, 384; (c) Supowski, R. M. H., W. D., *Inorg. Chim. Acta,* **2002,** *340*, 44.
15. (a) Beeby, A. C., I. M.; Dickins, R. S.; Faulkner, S.; Parker, D.; Royle, L.; Sousa, A. S. D.; Williams, J. A. G.; Woods, M., *J. Chem. Soc., Perkin Trans.* **1999,** *2*, 493; (b) Beeby, A., Dickins, R. S., Faulkner, S., Parker, D., Williams, J. A. G., *Chem. Commun.* **1997**, 1401.
16. McMahon, B., Mauer, P., McCoy, C. P., Lee, T. C., Gunnlaugsson, T., *J. Am. Chem. Soc.* **2009,** *131*, 17542.
17. Renaud, F., Piguet, C., Bernardinelli, G., Hopfgartner, G., Bunzli, J-C. G. , *Chem. Commun.* **1999**, 457.
18. Bunzli, J.-C. G., *Acc. Chem. Res.* **2006,** *39*, 53.
19. dos Santos, C. M. G., Gunnlaugsson, T., *Dalton Trans.* **2009**, 4712.
20. Moore, D., Trinity College Dublin, 2009.
21. Nonat, A. G., M.; Gateau, C.; Fries, P. H.; Helm, L.; Mazzanti, M., *Dalton Trans.* **2009**, 8033.
22. Santos, C. M. G. D., Trinity College Dublin, 2007.
23. Leonard, J., Trinity College Dublin, 2003.
24. Stomeo, F., Trinity College Dublin, 2006.
25. Fanning, A.-M., Trinity College Dublin, 2005.
26. Nwe, K. A., C. M.; Morrow, J. R.,. *J. Am. Chem. Soc.* **2008,** *130*, 14861.
27. Thompson, M. K., Lough, A. J., White, A. J. P., Williams, D. J., Kahwa, I. A., *Inorg. Chem.* **2003,** *42*, 4828.
28. Harte, A., Trinity College Dublin, 2006.
29. Tei, L., Gugliotta, G., Avedano, S., Giovenzana, G. B., Botta, M., *Org. Biomol. Chem.,* **2009,** *17*, 4406.
30. Shiraishi, Y., Furubayashi, Y., Nishimura, G., Hirai, T., *J. Lumin.,* **2007,** *127*, 623.

31. Harte, A. J. J., P.; Plush, S. E.; Kruger, P. E.; Gunnlaugsson, T., *Inorg. Chem.*, **2006,** *45*, 9465.
32. Plush, S. E., Gunnlaugsson, T., *Org. Lett.*, **2007,** *9*, 1919.
33. Natrajan, L. S., Villaraza, A. J. L., Kenright, A. M., Faulkner, S., *Chem. Commun.* **2009**.
34. Jauregui, M. P., W. S.; Allain, C.; Vidler, L. R.; Willis, M. C.; Kenright, A. M.; Snaith, J. S.; Stasiuk, G. J.; Lowe, M. P.; Faulkner, S., *Dalton Trans.* **2009**, 6283.
35. (a) Elharibi, M., Hamacek, J., Humbert, N., Bunzli, J-C., Albrecht-Gary, A-M., *New J. Chem., 28*, 1096; (b) Deiters, E., Song, B., Chauvin, A-S., Vandevyver, C. D. B., Gumy, F., Bunzli, J-C. G., *Chem. Eur. J.* **2009,** *15*, 885.
36. Albrecht, M., Scmid, S., Dehn, S., Wickleder, C., Zhang, S., Bassett, A. P., Pikramenou, Z., Frohlich, R., *New J. Chem.*, **2007,** *31*, 1755.
37. Torelli, S., Delayhaye, S., Hauser, A., Bernardinelli, G., Piguet, C., *Chem. Eur. J.* **2004,** *10*, 3503.
38. Leonard, J. P., Jensen, P., McCabe, T., O'Brien, J. E., Peacock, R. D., Kruger, P. E., Gunnlaugsson, T., *J. Am. Chem. Soc.* **2007,** *129*, 10986.
39. Stomeo, F., Lincheneau, C., Leonard, J. P., O'Brien, J. E., Peacock, R. D., McCoy, C. P., *J. Am. Chem. Soc.* **2009,** *131*, 9636.
40. (a) Lincheneau, C., Peacock, R. D., Gunnlaugsson, T., *Chem. Asian. J.* **2010,** 5, 500; (b) Comby, S., Stomeo, F., McCoy, C. P., Gunnlaugsson, T., *Helv. Chim. Acta* **2009,** *92*, 2461.
41. De, M., Ghosh, P. S., Rotello, V. M., *Adv. Mater.* **2008,** *20*, 4225.
42. Jang, S. S., Jang, Y. H., Kim, Y-H., Goddard, W. A. III., Flood, A. H., Laursen, B. W., Tseng, H-R., Stoddart, J. F., Jeppesen, J. O., Wook Choi, J., Steuerman, D. W., Delonna, E., Heath, J. R., *J. Am. Chem. Soc.* **2005,** *127*, 1563.
43. Simon de Diaz, A., Diaz-Garcia, M. E., *Anal. Chim. Acta* **2010,** *666*, 1.
44. Huang, X., Neretina, S., El-Sayed, M. A, *Adv. Mater.*, **2009,** *21*, 1.
45. Biju, V., Itoh, T., Anas, A., Sujith, A., Ishakawa, M., *Anal. Bioanal. Chem.* **2008,** *391*, 2469.
46. Nishi, H., Asahi, T., Kobatake, S., *J. Phys. Chem. C* **2009,** *113*, 17359.
47. Wilson, R., *Chem. Soc. Rev.* **2008,** *37*, 2028.
48. Parker, J. P., Fields-Zinna, C. A., Murray, R. W., *Acc. Chem. Res.*, **2010**.
49. (a) Boisselier, E., Astruc, D., *Chem. Soc. Rev.* **2009**; (b) Daniel, M.-C., Astruc, D., *Chem. Rev.* **2004,** *104*, 293.
50. Brust, M. W., M.; Bethell, D.; Schriffin, D. J.; Whyman, R.,. *J. Chem. Soc., Chem. Commun.*, **1994**, 801.
51. Turkevitch, J., Stevenson, P. C., Hillier, J. , *Discuss. Faraday Soc.* **1951,** *11*, 55.
52. Gittins, D. I., Caruso, F., *Angew. Chem. Int. Ed.*, **2001,** *40*, 3001.
53. Kimling, J., Maier, M., Okenve, B., Kotaidis, V., Ballot, H., Plech, A., *J. Phys. Chem. B.*, **2006,** *110*, 5700.
54. Lin, Y.-C. Y., B-Y.; Lin, W-C.; Lee, S-H.; Kuo, C-H.; Shyue, J-J., *J. Colloid Interf. Sci.*, **2009,** *340*, 126.
55. Yockell-Lelievre, H., Gingras, D., Vallee, R., Ritcey, A. M., *J. Phys. Chem. C.* **2009**.
56. Sharma, R., Holland, G. P., Solomon, V. C., Zimmermann, H., Schiffenhaus, S., Amin, S. A., Buttry, D. A., Yarger, J. L., *J. Phys. Chem. C.* **2009,** *113*, 16387.
57. Park, J.-H., Ganbold, E. O., Uuriintuya, D., Lee, K., Joo, S.-W. , *Chem. Commun.* **2009**, 7354.
58. Kundu, S., Wang, K., Liang, H., *J. Phys. Chem. C.* **2009**, 113, 14390.
59. Sperling, R. A. G., P. R.; Zhang, F.; Zanella, M.; Parak, W. J., *Chem. Soc. Rev.* **2008,** *37*, 1896.
60. Kim, K.-H., Kim, J. U., Cha, S-H., Lee, J-C., *J. Am. Chem. Soc.* **2009**, 131, 7482.

61. Vignolle, J., Tilley, T. D., . *Chem. Commun.* **2009**, 7230.
62. Sobhan, M. A., Withford, M. J., Goldys, E. M., *Langmuir* **2010**, 26, 3156.
63. Chen, G., Wang, Y., Huey Tan, L., Yang, M., Siew Tan, L., Chen, Y., Chen, H., *J. Am. Chem. Soc.* **2009,** *131*, 4218.
64. Tu, C., li, G., Shi, Y., Yu, X., Jiang, Y., Zhu, Q., Liang, J., Gao, Y., Yan, D., Sun, J., Zhu, X., *Chem. Commun.* **2009**, 3211.
65. Reimer, L., Kohl, H., *Transmission Electron Microscopy Physics of Image Formation* Springer: Atlanta, 2008; Vol. 36.
66. Perrault, S. D., Chan, W. C. W., *J. Am. Chem. Soc.* **2009,** 131, 17042.
67. Jans, H., Liu, L., Austin, L., Maes, G., Huo, Q., *Anal. Chem.* **2009,** *81*, 9425.
68. Katayama, K., Nomura, H., Ogata, H., Eitoku, T., *Phys. Chem. Chem. Phys.* **2009,** *11*, 10494.
69. (a) Klajn, R., Coskun, A., Olson, M. A., Wesson, P. J., Stoddart, J. F., Gryzbowski, B. A., *J. Am. Chem. Soc.* **2009,** *131*, 4233; (b) Kim, T., Huh, Y-M., Haam, S., Lee, K., *J. Mate. Chem.* **2010,** *20*, 8194.
70. Thomas, K. G. K., P. V., *Acc. Chem. Res.* **2003,** *36*, 888.
71. Gryko, D. T., Clausen, C., Lindsey, J. S., *J. Org. Chem.*, **1999,** *64*, 8635.
72. Imahori, H., Arimura, M., Hanada, T., Nishimura, Y., Yamazaki, I., Sakata, Y., Fukuzumi, S., *J. Am. Chem. Soc.*, **2001,** *123*, 335 .
73. Dulkeith, E., Morteani, A. C., Niedereichholz, T., Klar, T. A., Feldmann, J., Levi, S. A., VanVegel, F. C. J. M.; Reinhoudt, D.; Moller, M.; Gittins, D. I., *Phys. Rev. Lett.* **2002,** *89*, 203002.
74. Park, M.-H., OFir, Y., Samanta, B., Rotello, V. M. , *Adv. Mater.* **2009,** *21,* 22, 2323.
75. Stemmler, M., Stefani, F. D., Bernhardt, S., Bauer, R. E., Kreiter, M., Mullen, K., Knoll, W. , *Langmuir Lett.*, **2009,** *25*, 12425.
76. Shi, X., Wang, S. H., Van Antwerp, M. E., Chen, X., Baker Jr., J. R., *Analyst* **2009,** *134*, 1373.
77. Ghosh, P., Han, G., De, M., Kim, C. K., Rotello, V. M., *Adv. Drug Del. Rev.* **2008,** *60*, 1307.
78. Murphy, C. J., Gole, A. M., Stone, J. W., Sisco, P. N., Alkilany, A. M., Goldsmith, E. C., Baxter, S. C., *Acc. Chem. Res.* **2008,** *41*, 1721.
79. Agasti, S. S., Chompoosor, A., You, C-C., Ghosh, P., Kim, C. K., Rotello, V. M., . *J. Am. Chem. Soc.* **2009**, 131, 5728.
80. Nakanishi, J., Nakayama, H., Shimizu, T., Ishida, H., Kikuchi, Y., Yamaguchi, K., Horiike, Y., *J. Am. Chem. Soc.* **2009,** *131*, 3822.
81. (a) Lin, Q.; Huang, Q.; Li, C.; Bao, C.; Liu, Z.; Li, F.; Zhu, L., *J. Am. Chem. Soc.*, **2010,** *132*, 10645; (b) Skrabalak, S. E., Chen, J., Sun, Y., Lu, X., Au, L., Cobley, C. M., Xia, Y., *Acc. Chem. Res.* **2008**, 41, 1587.
82. Kim, C. K., Ghosh, P., Pagliuca, C., Zhu, Z-J., Menichetti, S., Rotello, V. M., *J. Am. Chem. Soc.* **2009**.
83. Hwu, J. R., Lin, Y. S., Josephrajan, T., Hsu, M. H., Cheng, F-Y., Yeh, C.-S., Su, W.-C., Shieh, D.-B., *J. Am. Chem. Soc.* **2009,** *131*, 66.
84. Peng, G., Tisch, O., Hakim, M., Shehada, N., Broza, Y. Y., Billan, S., Abdah-Bortnyak, R., Kuten, A., Haick, H., *Nat. Nanotechnol.* **2009,** *4*, 669.
85. Sperling, R. A., Gil, P. R., Zhang, F., Zanella, M., Parak, W. J., *Chem. Soc. Rev.* **2008,** *37*, 1896.
86. (a) Velu, R.; Ramakrishnan, V. T.; Ramamurthy, P., *Tetrahedron Lett.*, **2010,** *51* 33, 4331; (b) Lin, C.-Y.; Yu, C.-J.; Lin, Y.-H.; Tseng, W.-L., *Anal. Chem.* **2010,** *82*, 16, 6830.
87. Wang, L.; Li, T.; Du, Y.; Chen, C.; Li, B.; Zhou, M.; Dong, S., *Biosens. Bioelectron.* **2010,** *25*, 12, 2622.

88. Aili, D., Enander, K., Rydberg, J., Nesterenko, I., Bjorefors, F., Baltzer, L., Liedberg, B., *J. Am. Chem. Soc.*, **2008**, 130, 5780.
89. Lisowski, C. E., Hutchinson, J. E., *Anal. Chem.* **2009,** *81*, 10246.
90. Durocher, S., Rezaee, A., Hamm, C., Rangan, C., Mittler, S., Mutus, B., *J. Am. Chem. Soc.* **2009,** *131*, 7, 2475.
91. Shang, L., Yin, J., Li, J., Jin, L., Dong, S., *Biosens. Bioelectron.* **2009,** *25*, 269.
92. Shang, L., Jin, L., Dong, S., *Chem. Commun.* **2009**, 3077.
93. Ai, K., Liu, Y., Lu, L., *J. Am. Chem. Soc.* **2009,** *131*, 9496.
94. Chen, W., Tu, X., Guo, X., *Chem. Commun.* **2009**, 1736.
95. Jiang, X., Waterland, M., Blackwell, L., Wu, Y., Jayasundera, K. P., Partridge, A., *Steroids* **2009,** *74*, 819-824.
96. Shiang, Y.-C., Huang, C-C., Chang, H-T., *Chem. Commun.* **2009**, 3437.
97. Mao, X., Xu, H., Zeng, Q., Zeng, L., Liu, G., *Chem. Commun.* **2009**, 3065.
98. Paciotti, G. F., Kingston, D. G. I., Tamarkin, L., *Drug Develop. Res.* **2006,** *67*, 47.
99. Wilton-Ely, J. D. E. T., *Dalton Trans.* **2008**, 25.
100. Cao, R. J., Diaz-Garcia, A. M., Cao, R., *Coord. Chem. Rev.;* **2009,** *253*, 1262.
101. Bonomi, R., Selvestrel, F., Lombardo, V., Sissi, C., Polizzi, S., Mancin, F., Tonellato, U., Scrimin, P., *J. Am. Chem. Soc.* **2008**, 130, 15744.
102. Cormode, D.; Davis, J.; Beer, P., *J. Inorg. and Organomet. P. Mater.* **2008,** *18*, 1, 32.
103. Beer, P. D., Cormode, D. P., Davis, J. J., *Chem. Commun.* **2004**, 414.
104. Mayer, C. R., Cucchiaro, G., Jullian, J., Dumur, F., Marrot, J., Dumas, E., Secheresse, F., *Eur. J. Inorg. Chem.* **2008**, 3614.
105. Mayer, C. R., Dumas, E., Secheresse, F., *J. Colloid Interf. Sci.* **2008**, 328, 452.
106. Hallet, A. J., Christian, P., Jones, J. E., Pope, S. J. A. , *Chem. Commun.* **2009**, 4278.
107. Sheng, K., Yan, B., *J. Mater. Sci: Mater. Electron* **2010,** *21*, 65.
108. Wang, Y., Zhou, X., Wang, T., Zhou, J., *Mater. Lett.* **2008,** *62*, 3582.
109. Gu, J. Q., Sun, L-D., Yan, Z-G., Yan, G-H., *Chem. Asian. J.* **2008,** *3*, 1857.
110. Ai, K., Zhang, B., Lu, L., *Angew. Chem. Int. Ed.* **2009,** *48*, 304.
111. Ipe, B. I., Yoosaf, K., Thomas, K. G., *J. Am. Chem. Soc.* **2006,** *128*, 1907.
112. Lewis, D. J., Day, T. M., MacPherson, J. V., Pikramenou, Z., *Chem. Commun.* **2006**, 1433.
113. Murray, N. S., Jarvis, S. P., Gunnlaugsson, T., *Chem. Commun.* **2009**, 4959.
114. Massue, J., *J. Am. Chem. Soc.* **2008,** *130*, 6900.
115. Bonnet, C. S., Massue., J., Quinn, S. J., Gunnlaugsson, T., *J. Am. Chem. Soc.* **2008,** *130*, 6900.
116. Merbach, A. E. T., E., *The Chemistry of Contrast Agents in Medical Magnetic Resonance Imaging*. Wiley: 2001.
117. Caravan, P., *Chem. Soc. Rev.* **2006,** *35*, 512.
118. Terreno, E., Castelli, D. D., Viale, A., Aime, S., *Chem. Rev.* **2010,** *110*, 3019.
119. Debouttiere, P.-J., Roux, S., Vocanson, F., Billotey, C., Beuf, O., Favre-Reguillon, A., Lin, Y., Pellet-Rostaing, S., Lamartine, R., Perriat, P., Tillement, O., *Adv. Funct. Mater.* **2006,** *16*, 2330.
120. Rieter, W. J., Kim, J. S., Taylor, K. M. L., An, H., Lin, W., Tarrant, T., Lin, W., *Angew. Chem. Int. Ed.* **2007,** *46*, 3680.
121. Tsai, Z.-T., Wang, J -F., Kuo, H-Y., Shen, C-R., Wang, J-J., Yen, T-C. , *J. Magn. Magn. Mater.* **2010,** *322*, 208.
122. Meledrandi, C. J. S., J. K.; Ghosh, S.; Brougham, D. F., *Langmuir* **2008,** *24*, 14159.

123. Corr, S. A., Byrne, S. J., Tekoruite, R., Meledandri, C. J., Brougham, D. F., Lynch, M., Kerskens, C., O' Dwyer, L., Gun'ko, Y. K., . *J. Am. Chem. Soc.* **2008,** *130*, 4214.
124. Van Kasteren, S. I., Campbell, S. J., Serres, S., Anthony, D. C., Sibson, N. R., Davis, B. G., *PNAS* **2009,** *106*, 1, 18.
125. Mulder, W. J. M., Strijkers, G. J., Van Tilborg, G. A. F., Cormode, D. P., Fayad, Z. A., Nicolay, K., *Acc. Chem. Res.,* **2009,** *42*, 7, 904.
126. Villaraza, A. J. L., Bumb, A., Brechbiel, M. W.,. **2010**, 21, 1014.
127. Torres, S., Martins, J. A., Andre, J. P., Geraldes, C. F. G. C., Merbach, A. E., Toth, E. , *Chem. Eur. J.* **2006,** *12*, 940.
128. Song, Y., Kohlmeir, E. K., Meade, T. J., *J. Am. Chem. Soc.* **2008**, 130, 6662.
129. Bottril, M., Kwok, L., Long, N. J., *Chem. Soc. Rev.* **2006,** *35*, 557.
130. Alric, C., Taleb, J., LeDuc, G.; Mandon, C.; Billotey, C.; Le Meur-Herland, A.; Brochard, T.; Vocanson, F.; Janier, M.; Perriat, P.; Roux, S.; Tillement, O. , *J. Am. Chem. Soc.* **2008,** *130*, 5908.
131. Song, Y., Xu, X., MacRenaris, K. W., Zhang, X-Q., Mirkin, C. A., Meade, T. J., *Angew. Chem. Int. Ed.* **2009,** *48*, 1.
132. Park, J.-A., Reddy, P. A. N., Kim, H. K., Kim, I-S., Kim, G-C., Chang, Y., Kim, T-G., *Bioorg. Med. Chem. Lett.,* **2008,** *18*, 6135.
133. Moriggi, L., Canizzo, C., Dumas, E., Mayer, C. R., Ulianov, A., Helm, L., *J. Am. Chem. Soc.* **2009,** *131*, 10828.
134. Marradi, M., Alcantara, D., Martinez de la Fuente, J., Garcia-Martin, M. L., Cerdan, S., Penades, S., *Chem. Commun.* **2009**, 3922.
135. Bonnet, C. S.; TÛth, v., *Comptes Rendus Chimie, 13*, 700.
136. Bunzli, J.-C. G., *Chem. Rev.* **2010,** *110*, 2729.
137. (a) Nonat, A. M.; Allain, C.; Faulkner, S.; Gunnlaugsson, T., *Inorg. Chem.* **2010,** *49*, 8449; (b) Pope, S. J. A.; Coe, B. J.; Faulkner, S.; Laye, R. H., *Dalton Trans.,* **2005,** 8, 1482.
138. (a) Stasiuk, G. J.; Lowe, M. P., *Dalton Trans.* **2009**, 9725; (b) Jauregui, M., Perry, W. S., Allain, C., Vidler, L.R., Willis, M. C., Kenright, A. M., Snaith, J. S., Stasiuk, G. J., Lowe, M. P.., Faulkner, S., *Dalton Trans.* **2009**, 6283.
139. (a) dos Santos, C. M. G.; Fernandez, P. B.; Plush, S. E.; Leonard, J. P.; Gunnlaugsson, T., *Chem. Commun.* **2007**, 3389; (b) Leonard, J. P.; Gunnlaugsson, T., *J. Fluoresc.* **2005,** *15* 4, 585.
140. Harte, A. J.; Jensen, P.; Plush, S. E.; Kruger, P. E.; Gunnlaugsson, T., *Inorg. Chem.,* **2006,** *45*, 9465.
141. Murray, B. S., Parker, D., dos Santos, C. M. G., Peacock, R. D., *Eur. J. Inorg. Chem.* **2010**, 2663.
142. Mamedov, I., Parac-Vogt, T. N., Logothetis, N. K., Angelovski, G., *Dalton Trans.* **2010,** *39*, 5721.
143. Szilgyi, E.; Toth, E.; Kovacs, Z. n.; Platzek, J.; Radchel, B.; Brcher, E., *Inorg. Chim. Acta* **2000,** *298*, 226.
144. Kolb, H. C. F., M. G.; Sharpless, B., *Angew. Chem. Int. Ed.* **2001,** *40*, 2004.
145. Gil, M. V. A., M. J.; Lopez, O., *Synth.* **2007,** *11*, 1589.
146. Rostovstev, V. V., Green, L. G., Fokin, V. V., Sharpless, K. B. , *Angew Chem. Int. Ed.* **2002,** *41*, 2596.
147. (a) Aucagne, V.; Berne, J.; Crowley, J. D.; Goldup, S. M.; Hanni, K. D.; Leigh, D. A.; Lusby, P. J.; Ronaldson, V. E.; Slawin, A. M. Z.; Viterisi, A. l.; Walker, D. B., *J. Am. Chem. Soc.,* **2007,** *129*, 11950; (b) Kumar, A. P., P. S., *Org. Lett.* **2008,** *10* 2, 165.
148. Chow, H.-F., Lau, K-N., Ke, Z., Liang, Y., Lo, C-M., *Chem. Commun.* **2010,** *46*, 3437.

149. Viguier, R. F. H., Hulme, A. N., *J. Am. Chem. Soc.* **2006,** *128*, 11370.
150. Massue, J.; Plush, S. E.; Bonnet, C. S.; Moore, D. A.; Gunnlaugsson, T., *Tetrahedron Lett.* **2007,** *48*, 8052.
151. Rodger, A. N., B. , Circular Dichroism and Linear Dichroism. **1997**.
152. Koeller, S.; Bernardinelli, G.; Bocquet, B.; Piguet, C., *Chem. Eur. J.,* **2003,** *9*, 1062.
153. Valik, M. S., R. M., Kral, V., , *Supramol. Chem.,* **2005,** *17*, 347.
154. (a) Bag, B. G., *Curr. Sci.* **1995,** *68*; (b) Dolensky, B. E., J.; Kral, V.; Pardo, C.; Valik, M., *Adv. Heterocyclic Chem.* **2007,** *93*, 1.
155. Spielman, M. A., *J. Am. Chem. Soc.* **1935,** *57*, 583.
156. Wilcox, C. S., *Tetrahedron Lett.* **1985,** *26*, 5749.
157. Bresson, C.; Luhmer, M.; Demeunynck, M.; Kirsch-De Mesmaeker, A.; Pierard, F., *Tetrahedron Lett.,* **2004,** *45*, 2863.
158. (a) Veale, E., Frimannsson, D. O., Lawler, M. Gunnlaugsson, T. , *Org. Lett.* **2009,** *11,* 4040; (b) Veale, E., Gunnlaugsson, T. , *J. Org. Chem.* **2010**.
159. Abella, C. A. M.; Benassi, M.; Santos, L. S.; Eberlin, M. N.; Coelho, F., *J. Org. Chem.,* **2007,** *72*, 4048.
160. Chappell, L. L.; Voss, D. A.; Horrocks, W. D.; Morrow, J. R., *Inorg. Chem.* **1998,** *37*, 3989.
161. (a) Duke, R. M., Veale, E. B., Pfeffer, F. M., Kruger, P. E., Gunnlaugsson, T., *Chem. Soc. Rev.* **2010,** *39*, 3936; (b) Boyle, E. M., McCabe, T., Gunnlaugsson, T. , *Supramol. Chem.* **2010,** *22*, 586.
162. (a) Nishiyabu, R., Aime, C., Gondo, R., Kaneko, K., Kimizuka, N., *Chem. Commun.* **2010,** *46*, 4333; (b) Accorsi, G.; Armaroli, N.; Parisini, A.; Meneghetti, M.; Marega, R.; Prato, M.; Bonifazi, D., *Adv. Func. Mater.* **2007,** *17*, 2975.
163. (a) Massue, J. Q., S. J.; Gunnlaugsson, T., *J. Am. Chem. Soc.* **2008,** *130*, 6900; (b) Montalti, M.; Zaccheroni, N.; Prodi, L.; O'Reilly, N.; James, S. L., *J. Am. Chem. Soc.* **2007,** *129*, 2418.
164. (a) Bruce, J. I. D., R. S.; Govenlock, L, J.; Gunnlaugsson, T.; Lopinski, S.; Lowe, M. P.; Parker, D.; Peacock, R, D.; Perry, J. J. B.; Aime, S.; Botta, M. , *J. Am. Chem. Soc.* **2000,** *122*, 9674; (b) dos Santos, C. M. G.; Gunnlaugsson, T., *Supramol. Chem.,* **2009,** *21*, 173.
165. Muller, G.; Maupin, C.; Riehl, J.; Birkedal, H.; Piguet, C.; Bünzli, J. C., *Eur. J. Inorg. Chem.,* **2003**, 4065.
166. Cantuel, M.; Lincheneau, C.; Buffeteau, T.; Jonusauskaite, L.; Gunnlaugsson, T.; Jonusauskas, G.; McClenaghan, N. D., *Chem. Commun.* **2010,** *46*, 2486.
167. (a) Murray, N. S. Jarvis, S. P.; Gunnlaugsson, T. , *Chem. Commun.* **2009**, 4959; (b) Massue, J., Quinn, S. J., Gunnlaugsson, T., *J. Am. Chem. Soc.* **2008,** *130*, 6900.
168. Bruce, J. I.; Dickins, R. S.; Govenlock, L. J.; Gunnlaugsson, T.; Lopinski, S.; Lowe, M. P.; Parker, D.; Peacock, R. D.; Perry, J. J. B.; Aime, S.; Botta, M., *J. Am. Chem. Soc.* **2000,** *122*, 9674.
169. S. Dickins, R.; Gunnlaugsson, T.; Parker, D.; D. Peacock, R., *Chem. Commun.* **1998**, 1643.
170. Parker, D. Williams, J. A. G., *Responsive Luminescent Lanthanide Complexes* Marcel Dekker Inc.: New York, 2003.
171. Muller, G., *Dalton Trans.* **2009**, 9692.
172. Bunzli, J. C. G., *Acc. Chem. Res.* **2006,** *39*, 53.
173. Yokokawa, S., Tamada, K., Ito, E., Hara, M., *J. Phys. Chem. B.* **2003,** *107*, 3544.
174. Massue, J., Plush, S. P., Bonnet, C.S., Gunnlaugsson, T., *Tetrahedron Lett.* **2007,** *48*, 8052.

175. Beeby, A.; M. Clarkson, I.; S. Dickins, R.; Faulkner, S.; Parker, D.; Royle, L.; S. de Sousa, A.; A. Gareth Williams, J.; Woods, M., *J. Chem. Soc., Perkin Trans. 2* **1999,** *0*, 493.
176. Rodger, A. N., B. , *Circular Dichroism and Linear Dichroism*. Oxford Chemistry Press: New York, Tokyo, 1997.
177. Field, J. E.; Muller, G.; Riehl, J. P.; Venkataraman, D., *J. Am. Chem. Soc.* **2003,** *125*, 11808.
178. (a) Dickins, R.; Gunnlaugsson, T.; Parker, D.; D. Peacock, R., *Chem. Commun.* **1998,** 1643; (b) Parker, D. Williams., J. A. G., *Metal Ions in Biological Systems* **2003**.
179. (a) Brust, M., Walker, M.; Bethell, D.; Schriffin, D. J.; Whyman, R. , *J. Chem. Soc., Chem. Commun* **1994**, 801; (b) Wu, X.; Thrall, E. S.; Liu, H.; Steigerwald, M.; Brus, L., *J. Phys. Chem. C,* **2010,** *114*, 12896.
180. Laaksonen, P.; Kivioja, J.; Paananen, A.; Kainlauri, M.; Kontturi, K.; Ahopelto, J.; Linder, M. B.,. *Langmuir* **2009,** *25*, 5185.
181. Chan, K. W.-Y., Wong, W-T, *Coord. Chem. Rev.* **2007,** *251*, 2428.
182. Na, H. B., Song, I. C., Hyeon, T., *Adv. Mater.* **2009,** *21*, 2133.
183. Derome, A. E., *Modern NMR Techniques for Chemistry Research,* Pergamon: 1987; Vol. 6.
184. Sherry, A. D., Caravan, P., Lenkinski, R. E., *J. Magn. Res. Imaging* **2009,** *30*, 1240.
185. Terreno, E. C., D. D.; Viale, A.; Aime, S., *Chem. Rev.* **2010,** *110*, 3019.
186. Sherry, A. D. C., P.; Lenkinski, R. E., Primer of Gadolinium Chemistry. *J. Magn. Reson. Imaging* **2009,** *30*, 1240.
187. Eibofner, F.; Steidle, G.; Kehlbach, R.; Bantleon, R.; Schick, F., *Magnet. Reson. Med.* **2010,** *64*, 1027.
188. Martin, A.; Hickey, J.; Ablack, A.; Lewis, J.; Luyt, L.; Gillies, E., *J. Nanopart. Res.* **2010,** *12*, 1599.
189. Howes, P.; Green, M.; Bowers, A.; Parker, D.; Varma, G.; Kallumadil, M.; Hughes, M.; Warley, A.; Brain, A.; Botnar, R., *J. Am. Chem. Soc.* **2010,** *132*, 9833.
190. Merbach, A. E., Toth, E., *The Chemistry of Contrast Agents in Medical Magnetic Resonance Imaging*. Wliey: 2001.
191. Werner, E., Datta, A., Jocher, C. J., Raymond, K. N., *Angew. Chem. Int. Ed.* **2008,** *47*, 8568.
192. Frullano, L., Meade, T. J., *J. Biol. Inorg. Chem.* **2007,** *12*, 939.
193. Meser Ali, M., Woods, M., Caravan, P., Opina, A. C. L., Spiller, M., Fettinger, J. C., Sherry, A. D., *Chem. Eur. J.,* **2008,** *14*, 7250.
194. Torres, S. M., J. A.; Andre, J. P.; Geraldes, C. F. G. C.; Merbach, A. E.; Toth, E.,. *Chem. Eur. J.* **2006,** *12*, 940.
195. Ahren, M. S., L.; Klasson, A.; Soderlind, F.; Abrikossova, N.; Skoglund, C.; Bengtsson, T.; Engstrom, M.; Kall, P.- O.; Uvdal, K. , *Langmuir* **2010,** *26*, 5753.
196. park, J. A. R., A. N.; Kim, H-K.; kim, I-S.; Kim, G-C.; Chang, Y.; Kim, T-J.,. *Bioorg. Med. Chem. Lett.* **2008,** *18*, 6135.
197. Moriggi, L. C., C.; Dumas, E; Mayer, C. R.; Ulianov, A.; Helm, L., *J. Am. Chem. Soc.* **2009,** *131*, 10828.
198. Song, Y. X., X.; MacRenaris, K. W.; Zhang, X-Q.; Mirkin, C.A.; Meade, T. J. , *Angew. Chim. Int. Ed.* **2009,** *48*, 1.
199. Massue, J., Quinn, S.J., Gunnlaugsson, T., *J. Am. Chem. Soc.,* **2008,** *130*, 6900.
200. Massue, J., Plush, S.P., Bonnet, C.S., Gunnlaugsson, T., *Tetrahedron Lett.* **2007,** *48*, 8052.
201. dos Santos, C. M. G., Harte., A. J., Quinn, S. J., Gunnlaugsson, T., *Coord. Chem. Rev.* **2008,** *252*, 2512.

202. Bonnet, C. S., Massue, J., Quinn, S. J., Gunnlaugsson, T. , *Org. Biomol. Chem.* **2009,** *7*, 3074.
203. Nonat, A., Fires, P. H., Pecaut, J., Mazzanti, M., *Chem. Eur. J.* **2007,** *13*, 8489.
204. Powell, D. H.; Dhubhghaill, O. M. N.; Pubanz, D.; Helm, L.; Lebedev, Y. S.; Schlaepfer, W.; Merbach, A. E., *J. Am. Chem. Soc.* **1996,** *118*, 9333.
205. Lycknert, K., Rundlof, T., Widmalm, G., *J. Phys. Chem. B.,* **2002,** *106*, 5275.
206. Torres, S. M., J. A.; Andre, J. P.; Geraldes, C. F. G. C.; Merbach, A. E.; Toth, E., *Chem. Eur. J.* **2006,** *12*, 940.
207. Ali, M. M., Woods, M., Caravan, P., Opina, A.C.L., Spiller, M., Fettinger J. C., Sherry, A. D., *Chem. Eur. J.* **2008,** *14*, 7250.
208. Vogel, A. I.; Tatchell, A. R.; Furnis, B. S.; Hannaford, A. J.; Smith, P. W. G., *Vogel's Textbook of Practical Organic Chemistry*. 5th ed.; Prentice Hall: New York, 1996.
209. Kimmich, R. A., E., *Prog. Nucl. Magn. Reson. Spec.* **2004,** *44*, 257.
210. Boldrini, V.; Giovenzana, G. B.; Pagliarin, R.; Palmisano, G.; Sisti, M., *Tetrahedron Lett.* **2000,** *41*, 6527.
211. Jensen, J.; Tejler, J.; Warnmark, K., *J. Org. Chem.,* **2002,** *67*, 6008.
212. Baykal, U.; Akkaya, M. S.; Akkaya, E. U., *J. Incl. Phenom. Macro.* **1999,** *35*, 311.
213. Amin, S.; Voss, D. A.; Horrocks, W. D.; Morrow, J. R., *Inorg. Chem.* **1996,** *35*, 7466.
214. Plush, S. E.; Clear, N. A.; Leonard, J. P.; Fanning, A.-M.; Gunnlaugsson, T., *Dalton Trans.* **2010,** *39,* 3644.
215. Wilcox, C. S., *Tetrahedron Lett.* **1985,** *26*, 5749.
216. Gunnlaugsson, T.; Leonard, J. P.; Mulready, S.; Nieuwenhuyzen, M., *Tetrahedron* **2004,** *60*, 105.
217. Yokokawa, S.; Tamada, K.; Ito, E.; Hara, M., *J. Phys. Chem. B.,* **2003,** *107*, 3544.
218. Massue, J.; Plush, S. E.; Bonnet, C. S.; Moore, D. A.; Gunnlaugsson, T., *Tetrahedron Lett.,* **2007,** *48*, 8052.
219. Aime, S., Botta, M., Dickins, R. S., Maupin, C. L., Parker, D., Riehl, J. P., Williams, J. A. G.,. *J. Chem. Soc. Dalton Trans.,* **1998**, 881.

Appendices

Appendix A

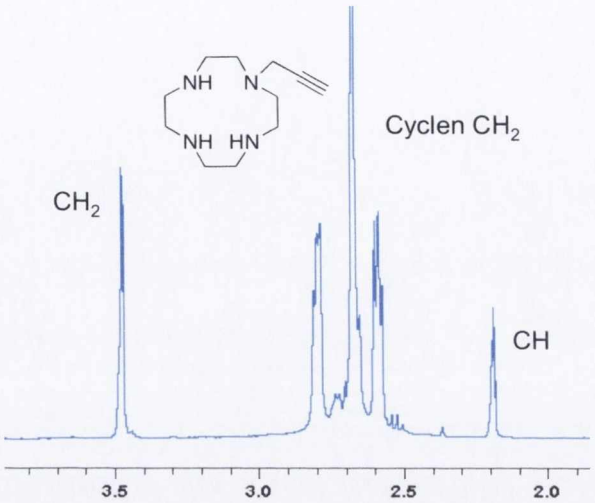

Figure A.1: *The ^{1}H NMR spectrum ($CDCl_3$, 400 MHz) of* ***46***

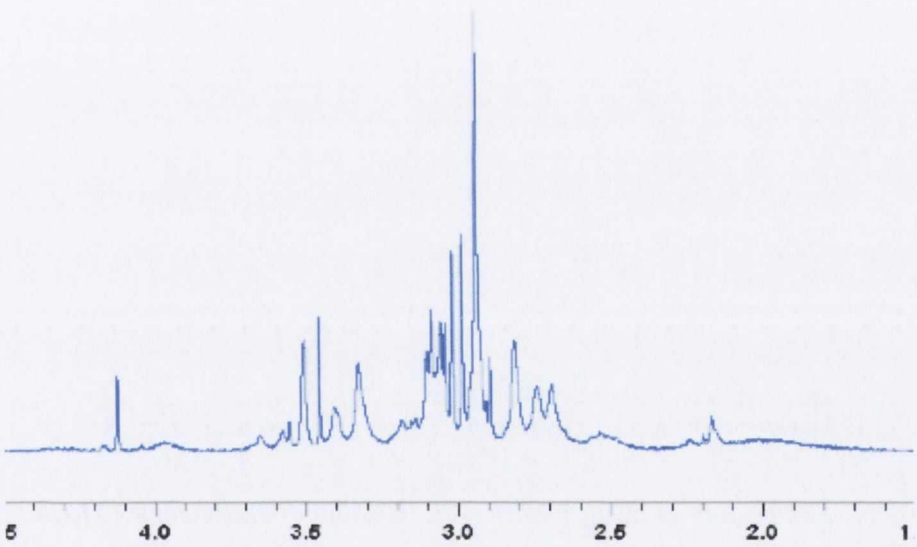

Figure A.2*: The ^{1}H NMR spectrum (MeOD, 400 MHz) of ligand* ***46***

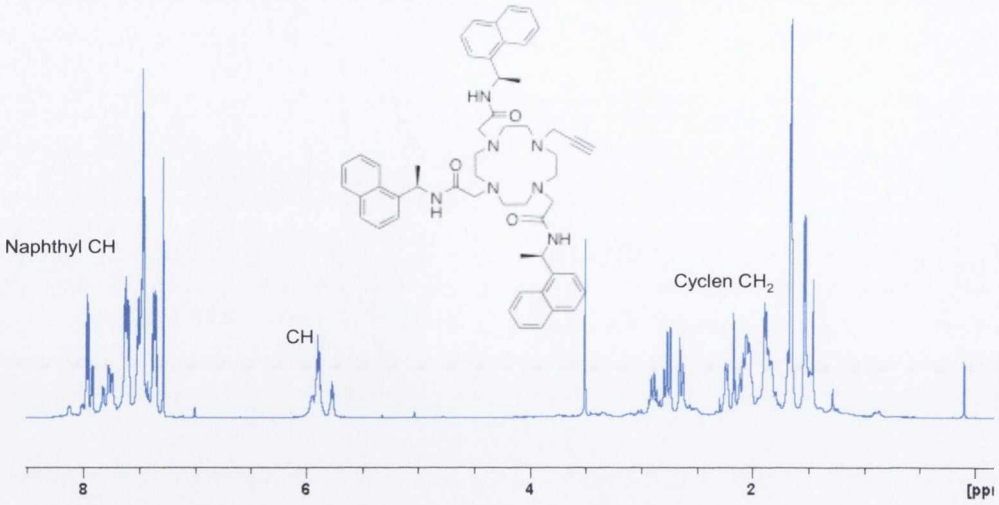

Figure A.3**: ^1H NMR ($CDCl_3$, 400 MHz) of ligand **53S

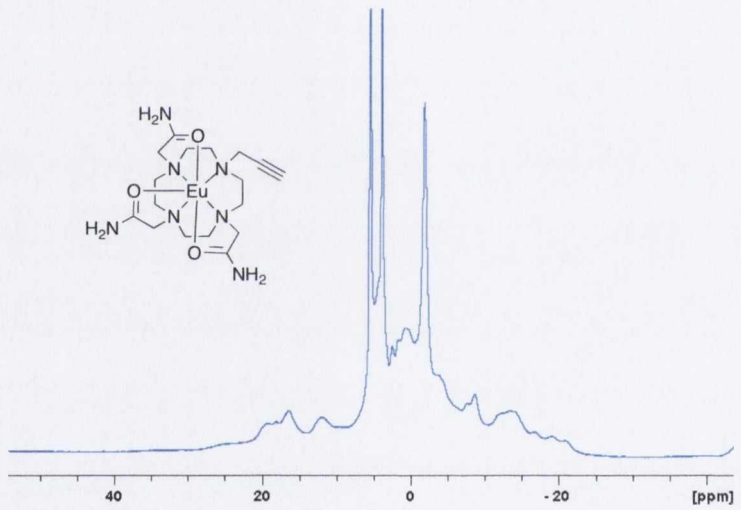

Figure A.4**: ^1H NMR spectrum (MeOD, 400 MHz) of complex **51.Eu

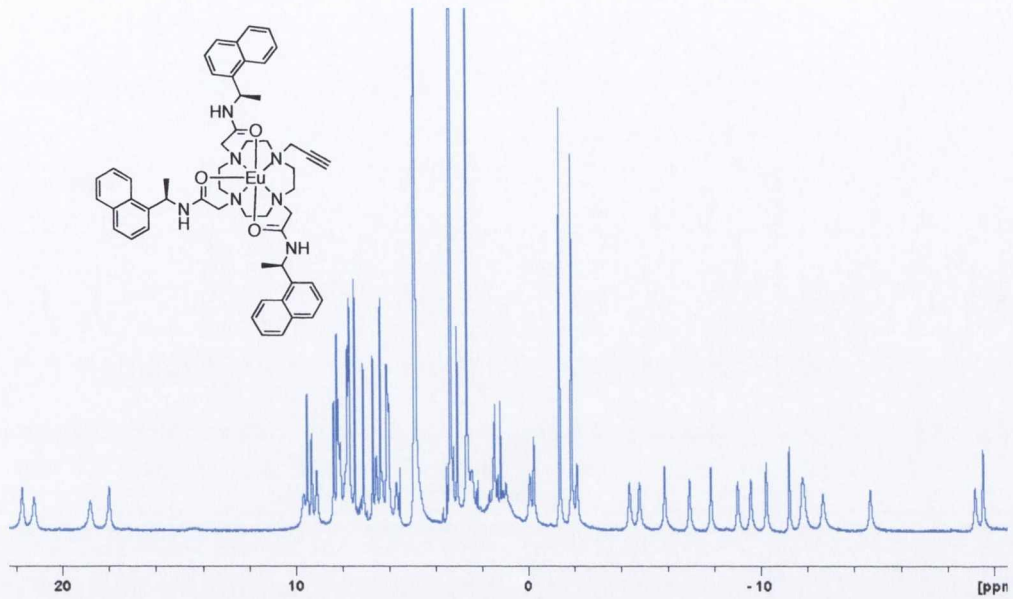

Figure A.5: *^{1}H NMR spectrum (MeOD, 400 MHz) of* ***53S.Eu***

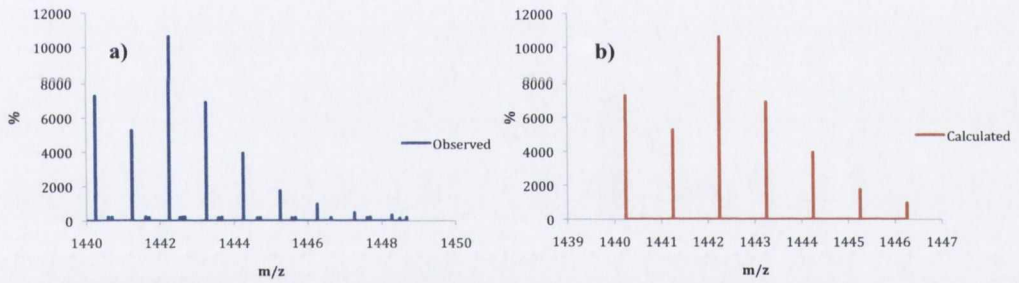

Figure A.6*: Mass spectroscopic analysis showing* ***a)*** *complex* ***58.Eu*** *b) Calculated spectrum*

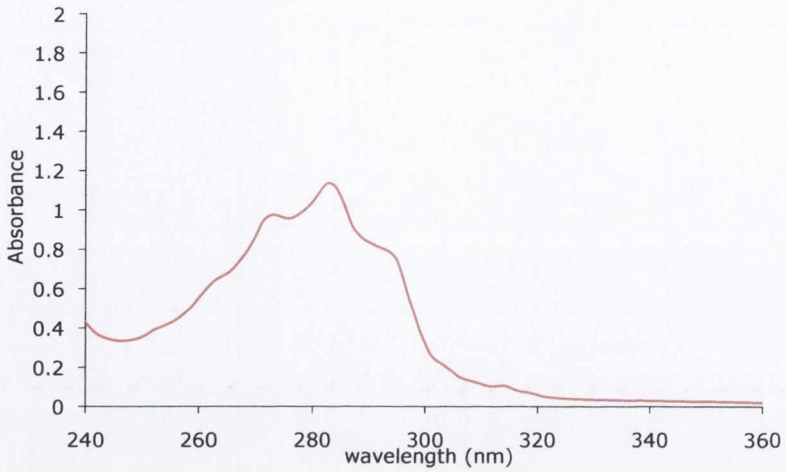

Figure A.7**: UV-vis absorption spectrum of **53.Eu

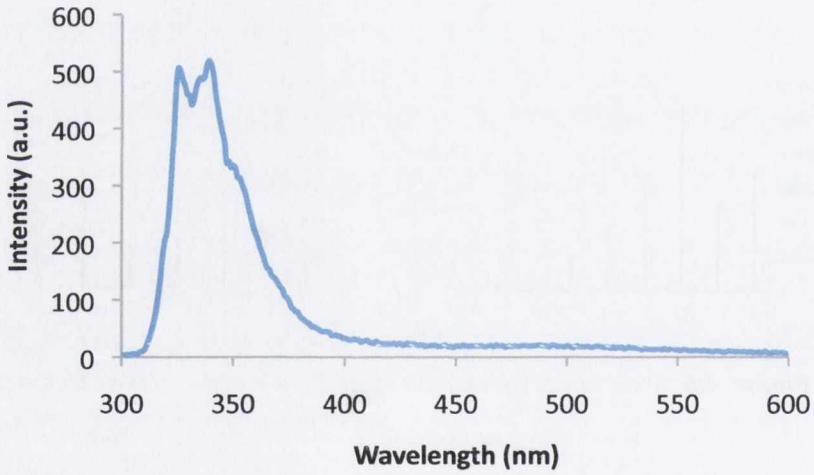

***Figure A.8:** Fluorescence emission spectrum of **53R.Eu** in MeOH with excitation at 281 nm*

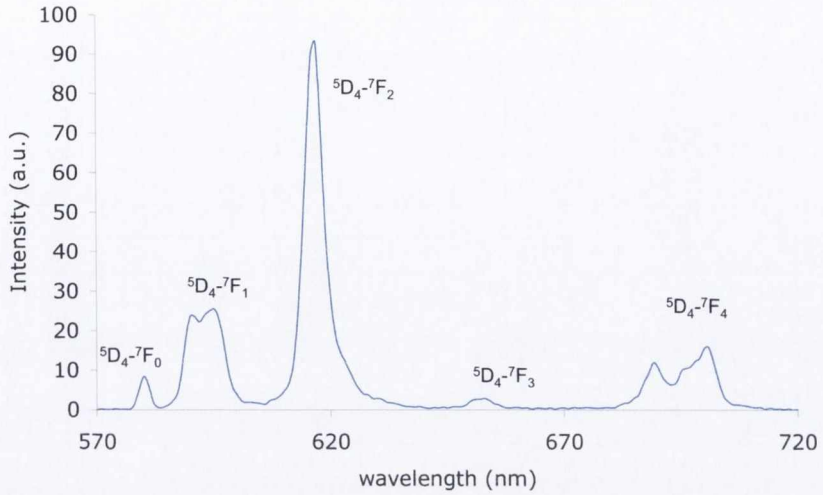

***Figure A.9**: Eu^{3+}centred emission of the complex **49.Eu** excited at 281 nm*

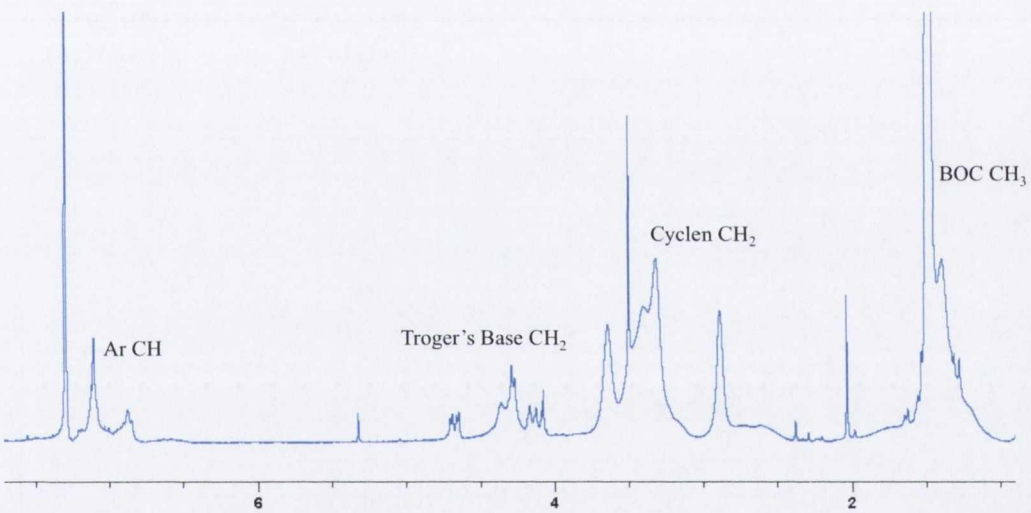

***Figure A.10**: ^1H NMR of product formed from functionalisation of triBOC cyclen with the acetamide*

Table A.1: Selected bond angles for 83

Bond	Length (Å)	Bond	Length (Å)
C(9) O(2) C(21)	115.62(15)	C7 C15 C18	121.82(17)
C(18) O(4) C(25)	115.56(15)	C14 C15 C18	118.94(16)
C(24) N(1) C(23)	110.51(15)	C8 C16 C12	119.26(17)
C(24) N(1) C(13)	112.65(14)	C8 C16 C9	118.86(17)
C(23) N(1) C(13)	107.84(15)	C12 C16 C9	121.86(17)
C(10) N(6) C(23)	111.58(15)	C8 C17 C10	118.80(17)
C(10) N(6) C(20)	112.49(14)	C8 C17 C13	120.67(17)
C(23) N(6) C(20)	107.08(14)	C10 C17 C13	120.48(17)
C(15) C(7) C(22)	121.24(17)	O1 C18 O4	122.98(18)
C(17) C(8) C(16)	121.37(17)	O1 C18 C15	124.70(18)
O(3) C(9) O(2)	122.65(17)	O4 C18 C15	112.31(16)
O(3) C(9) C(16)	124.99(18)	C14 C19 C24	120.51(18)
O(2) C(9) C(16)	112.35(16)	N6 C20 C22	110.89(15)
C(17) C(10) C(11)	119.97(17)	C7 C22 C24	118.62(17)
C(17) C(10) N(6)	121.68(17)	C7 C22 C20	119.97(16)
C(11) C(10) N(6)	118.35(16)	C24 C22 C20	121.33(17)
C(12) C(11) C(10)	120.72(18)	N1 C23 N6	111.59(15)
C(11) C(12) C(16)	119.80(18)	C19 C24 C22	120.10(17)
N(1) C(13) C(17)	111.57(15)	C19 C24 N1	118.71(16)
C(19) C(14) C(15)	120.26(17)	C22 C24 N1	121.18(16)
C(7) C(15) C(14)	119.23(17)		

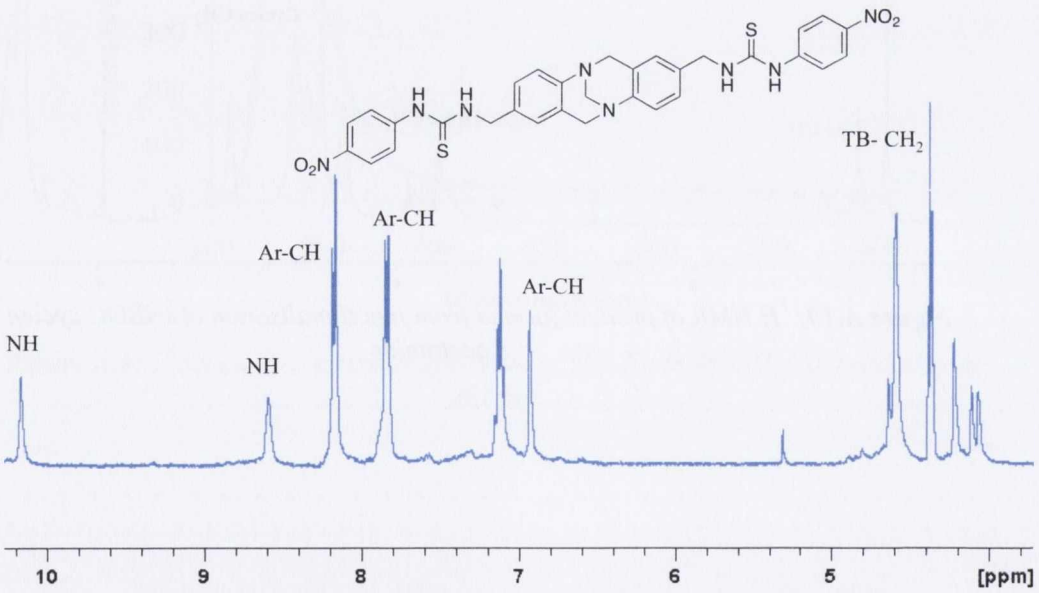

Figure A.11**: The ^{1}H NMR spectrum (DMSO-d_6, 400 MHz) of **99

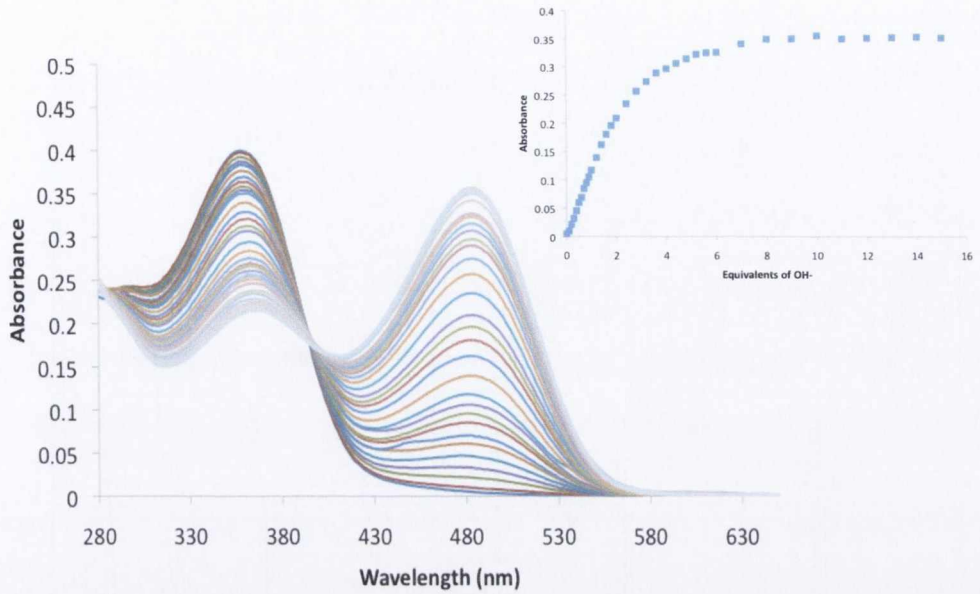

***Figure A.12**: Changes in the UV-Vis absorption spectrum of **99** upon addition of OH^-.*
***Inset:** Plot of Absorbance versus equivalents*

Appendix B

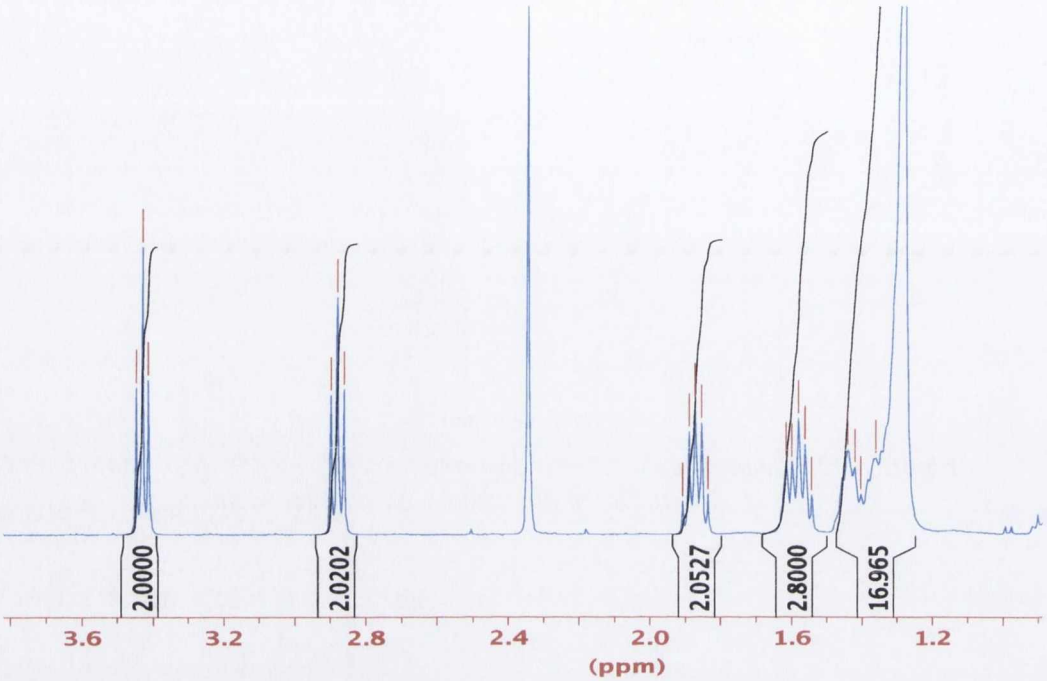

Figure B.1: *^{1}H NMR ($CDCl_3$, 400MHz) of* ***101***

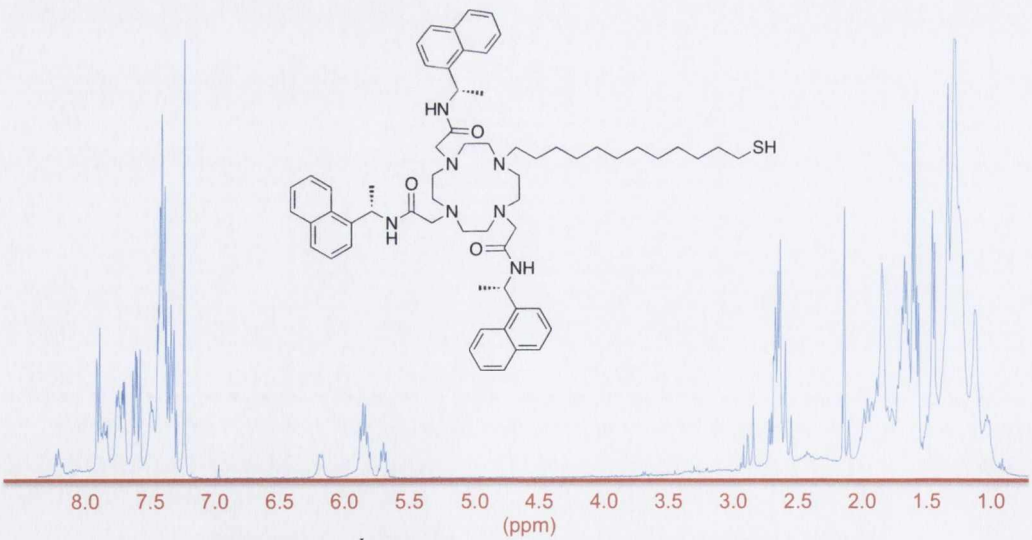

Figure B.2*: ^{1}H NMR spectrum ($CDCl_3$, 400 MHz) of* ***41S***

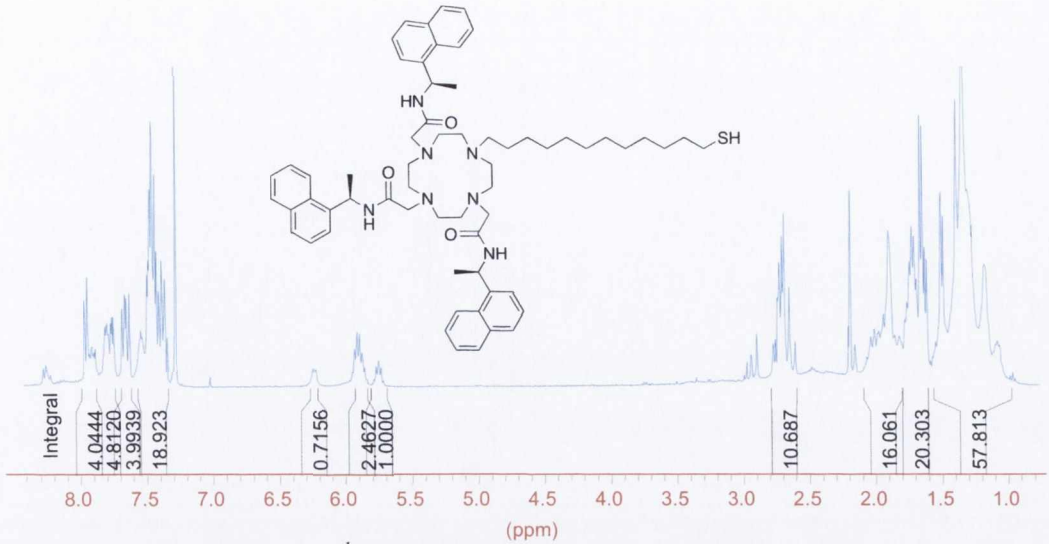

Figure B.3: *^{1}H NMR spectrum ($CDCl_3$, 400 MHz) of* ***41R***

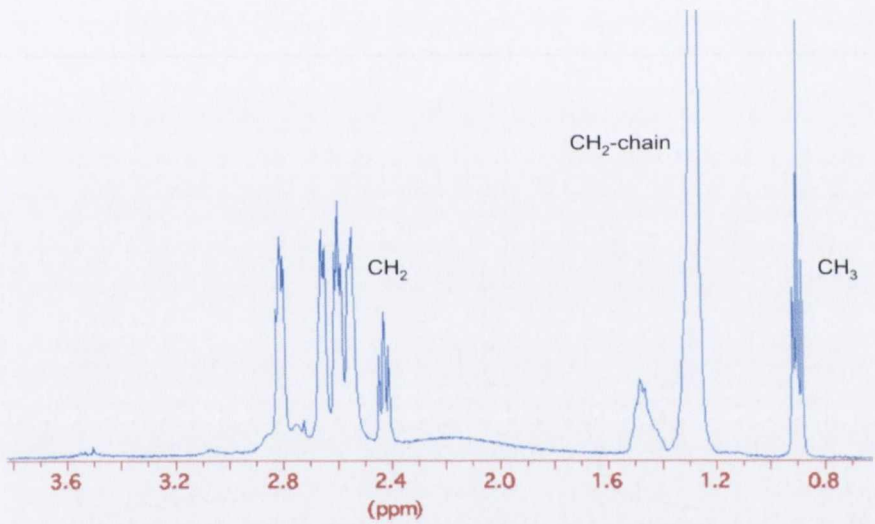

Figure B.4: *^{1}H NMR spectrum ($CDCl_3$, 400 MHz) of* ***107***

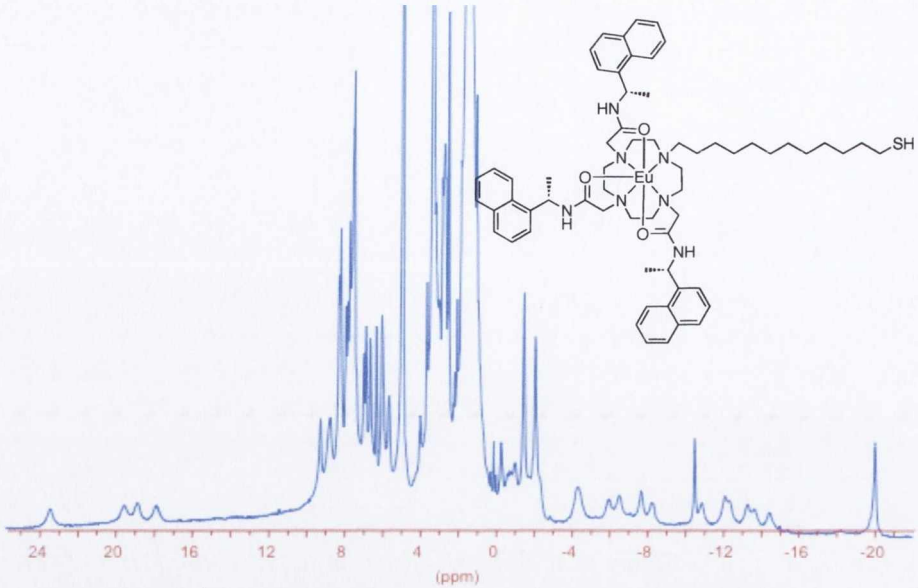

Figure B.5**: ^{1}H NMR spectrum ($CDCl_3$, 400 MHz) of **41R.Eu

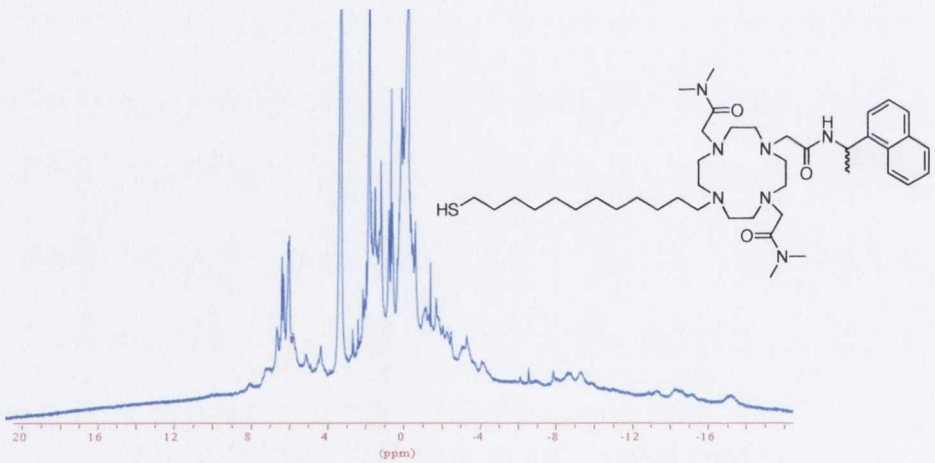

Figure B.6**: 1H NMR spectrum (MeOD, 400 MHz) of **42R.Eu

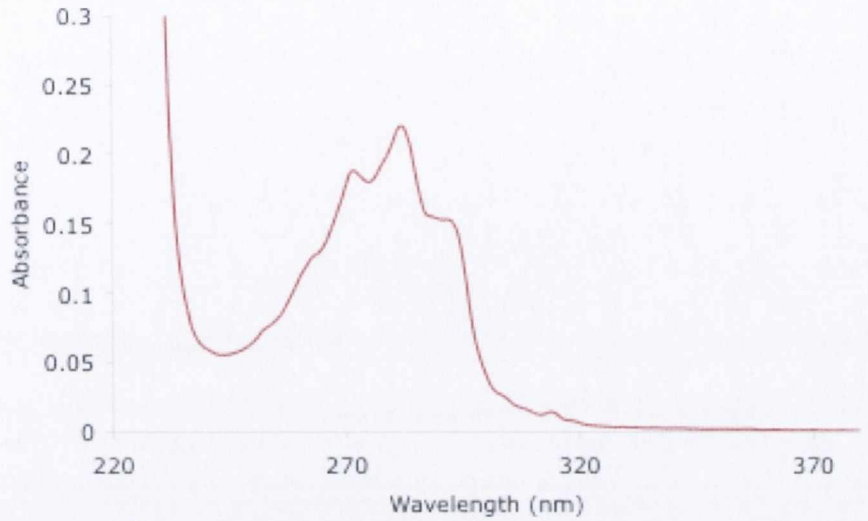

***Figure B.7**: The UV-Vis absorption spectrum of **42R.Eu** (1 x 10^{-5}M) in MeOH*

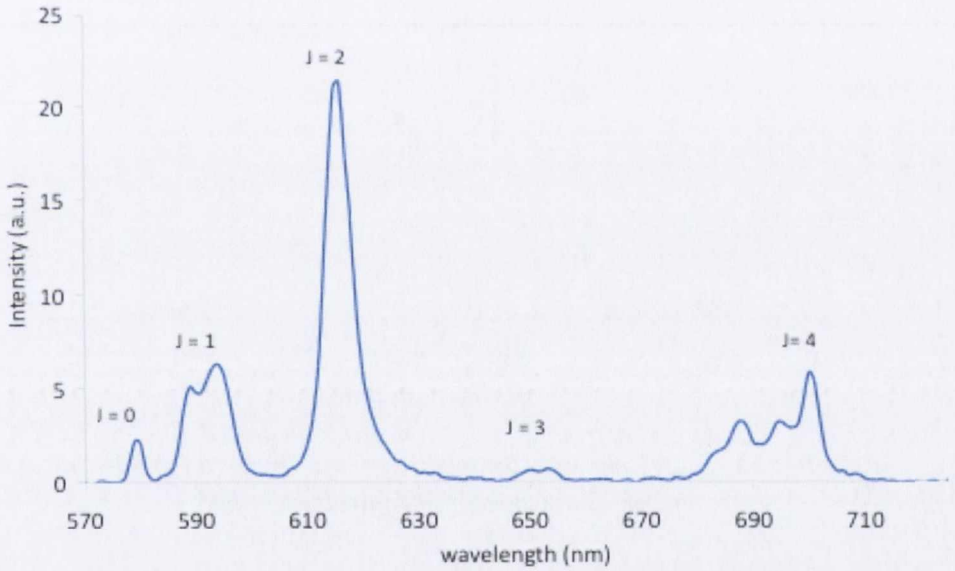

***Figure B.8**: The Eu^{3+} emission spectrum of **42R.Eu** (1 x 10^{-5}M) in MeOH*

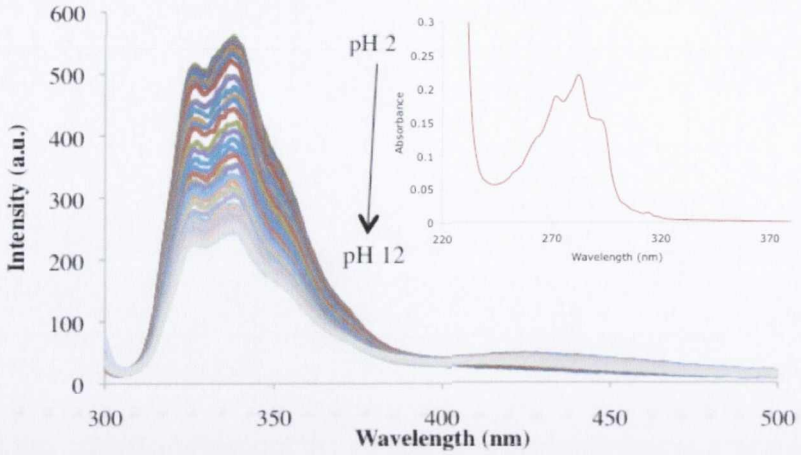

***Figure B.9**: Changes in the fluorescence emission spectrum of **42.Eu** (1 x 10^{-5}M) in TEAP (0.1 M), λ_{max} at 281 nm, upon changes in pH. **Inset:** Plot of changes in the intensity at 338 nm versus pH*

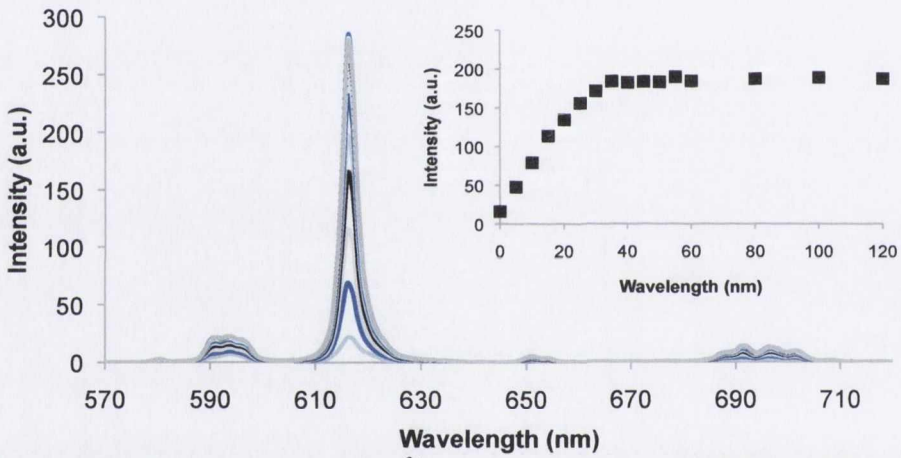

Figure B.10**: The changes in the Eu^{3+} emission spectrum of **41R.Eu-AuNPs** (1 x 10^{-7}M) in MeOH, λ_{max} at 281 nm upon the addition of **tta. Inset**:Plot of intensity at 615 nm versus the number of equivalents of **tta

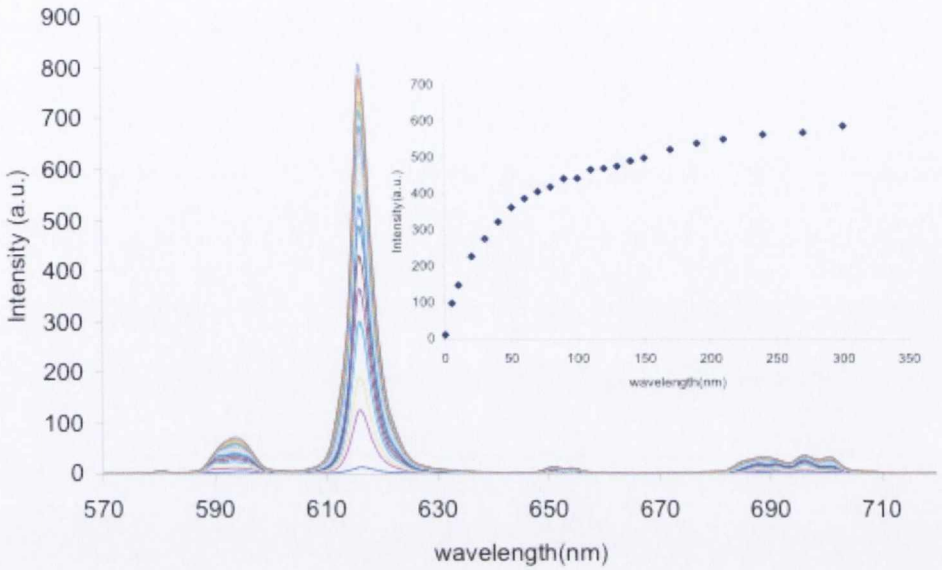

***Figure B.11**: The changes in the Eu^{3+} emission spectrum of **42.Eu-AuNPs** (1×10^{-7} M) in MeOH, λ_{max} at 615 nm upon the addition of **nta**. **Inset**: Plot of intensity at 615 nm versus the number of equivalents of nta added.*

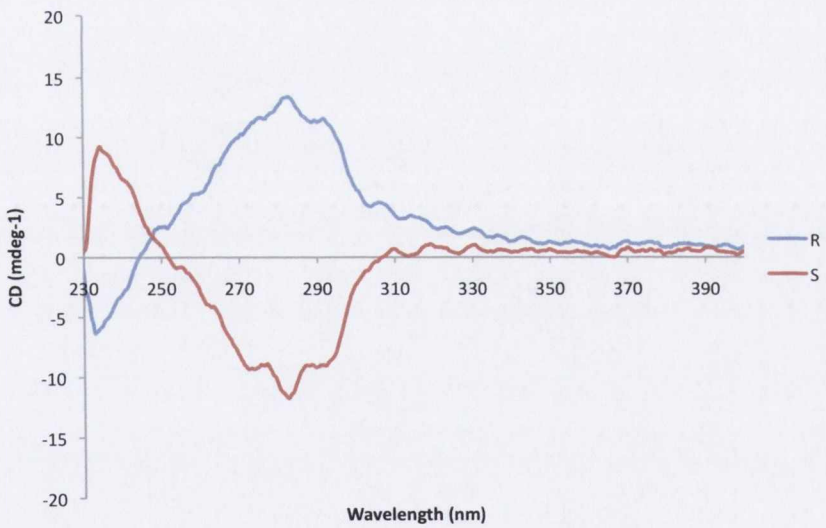

***Figure B12**: CD spectra of **42.Eu-AuNPs R** and **S** enantiomers in MeOH*

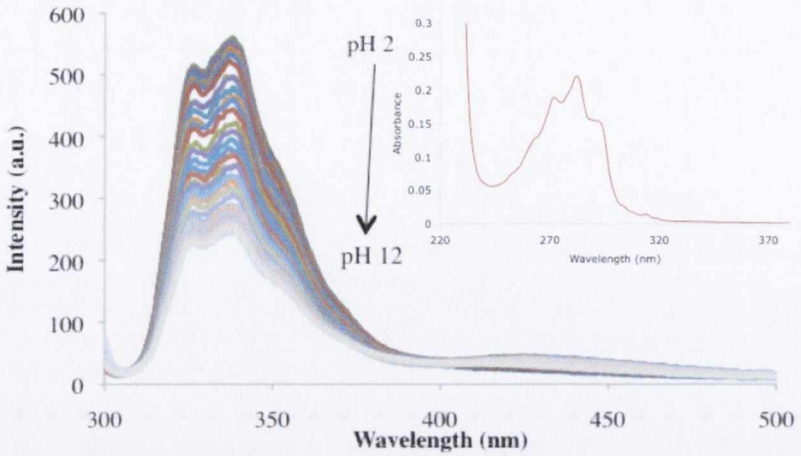

***Figure B.9**: Changes in the fluorescence emission spectrum of **42.Eu** (1 x 10^{-5}M) in TEAP (0.1 M), λ_{max} at 281 nm, upon changes in pH. **Inset:** Plot of changes in the intensity at 338 nm versus pH*

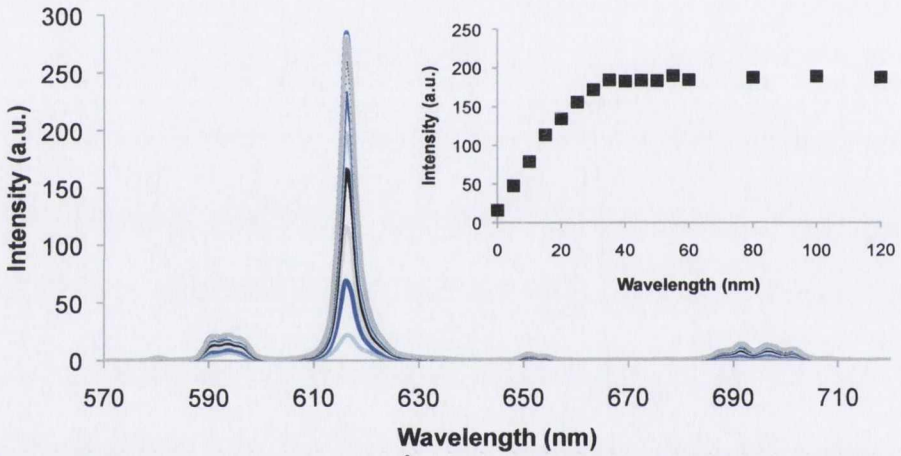

Figure B.10**: The changes in the Eu^{3+} emission spectrum of **41R.Eu-AuNPs** (1 x 10^{-7}M) in MeOH, λ_{max} at 281 nm upon the addition of **tta. Inset**:Plot of intensity at 615 nm versus the number of equivalents of **tta

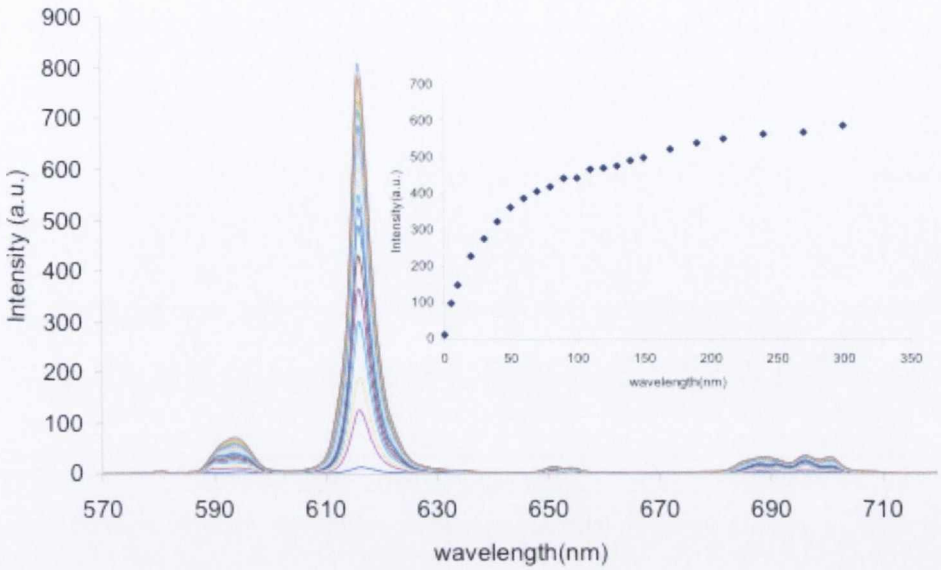

Figure B.11: *The changes in the Eu^{3+} emission spectrum of* ***42.Eu-AuNPs*** *(1×10^{-7}M) in MeOH, λ_{max} at 615 nm upon the addition of* ***nta***. ***Inset***: *Plot of intensity at 615 nm versus the number of equivalents of nta added.*

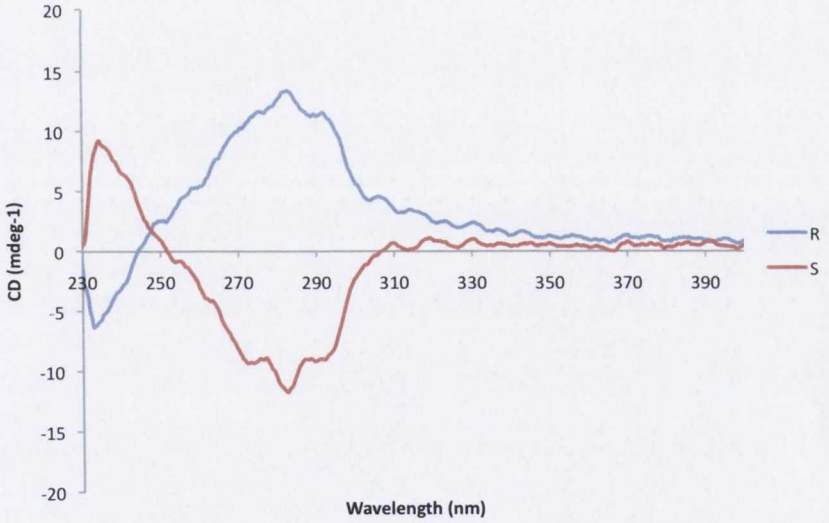

Figure B12: *CD spectra of* ***42.Eu-AuNPs R*** *and* ***S*** *enantiomers in MeOH*